Understanding the measurement of forests with waveform lidar

Steven Hancock

Departments of

Space & Climate Physics

and Geography

University College London

Thesis submitted for the degree of Doctor of Philosophy

13^{th} March 2010

A tree. Mckinnley Grove, Sierra Nevada, California

"That's just virtual tree hugging"

Mr. Andy Vass - Vulcan Restoration Trust

Abstract

The measurement of forests is essential for monitoring and predicting the role and response of the land surface to global climate change. Globally consistent and frequent measurements can only be made by satellites; unfortunately many current system's measurements saturate at moderate canopy densities and are not directly related to forest properties, requiring tenuous empirical relationships that are insensitive to many of the Earth's most important, Carbon rich forests.

Lidar (laser radar) is a relatively new technology that offers the potential to make direct measurements of forest height, vertical density and, when ground based, explicit measurements of structure. In addition measurements do not saturate until much higher forest densities.

In recent years there has been much interest in the measurement of forests by lidar, with a number of airborne and terrestrial and one spaceborne lidar developed. Measuring a forest leaf by leaf is impractical and very tedious, so more rapid ground based methods are needed to collect data to validate satellite derived estimates. These rapid methods are themselves not directly related to forest properties causing uncertainty in any validation of remotely sensed estimates.

This thesis uses Monte Carlo ray tracing to simulate the measurement of forests by full waveform lidars over explicit geometric forest models for both above and below canopy instruments. Existing methods for deriving forest properties from measurements are tested against the known truth of these simulated forests, a process impossible in reality. Causes of disagreements are explored and new methods developed to attempt to overcome any shortcomings. These new methods include dual wavelength lidar for correcting satellite based measurements for topography and a voxel based method for more directly relating terrestrial lidar signals to forest properties.

Contents

List of Tables

List of Figures

Chapter 1: Introduction

Global climate change has become one of the most discussed and important issues of recent years. There have been many high profile scientific studies, including the inter governmental panel on climate change (Alley *et al.* 2007), which shared the Nobel peace prize with Al Gore in 2007. All agree that understanding global change and the climate should be one of the major goals of science over the coming years.

The flow of Carbon dioxide into the atmosphere from the burning of fossil fuels is well known and the amount currently in the atmosphere is also easily measured, any difference between these must be due to the natural world. At present the natural world seems to be removing more than it is emitting, a net sink (Pitman 2003), but where exactly this is being absorbed and the mechanisms are not fully understood (Rodell *et al.* 2004). Many processes for emitting and absorbing greenhouse gases are known, but which of these is the dominant factor is unknown.

Many of these mechanisms are dependent on the climate and human activity, for example the rate of photosynthesis depends upon temperature (Williams 1996) whilst the total rate is very much affected by deforestation and subsequent burning (Brown *et al.* 1995) and there is a fear that these negative and positive feedbacks may become unbalanced, leading to runaway climate change (Cox *et al.* 2004). The quantification of these feedback loops, through better understanding of physical processes (Walker *et al.* 1981) and models that can make use of a variety of data sources are needed (Williams 1996, Rayner *et al.* 2005). The consensus is that accurate data on the current and past state of the world and realistic models describing the basic processes are needed to fully understand the contribution and reaction of the natural world to climate change (Alley *et al.* 2007).

One of the great unknowns is the amount of standing above ground biomass, both woody and foliar. This foliar biomass provides the interface between the atmosphere and 90% of the Earth's land based biomass (Ozanne *et al.* 2003) and so an accurate figure for it now is vital when quantifying the Carbon cycle. Around a quarter of the Earth's land surface is covered in forest (Pfeifer *et al.* 2004) and they are by far the largest stores of above ground Carbon (Waring *et al.* 1995b) and so a proper measure of forest extent and properties is vital to understanding climate.

Currently there are large uncertainties in all estimates of forest biophysical parameters, even something as easy to collect for small plots as above ground biomass (Pitman 2003, Hurtt *et al.* 2004), let alone something as hard to measure as foliar biomass (Bréda 2003). Without an accurate map of current biomass it is very difficult to monitor changes, whether due to climate or human land use change (deforestation or reforestation) whilst models cannot reliably be calibrated (or spun up) for past data to predict the future.

An emerging field in modelling is that of "data assimilation", that is a model that can be periodically updated by real observations, preventing it from deviating from the truth and so provide a better understanding of the processes involved (Williams *et al.* 2005). This process requires frequent observations to keep the model on track. Any bias in guiding measurements will pull the model away from the truth and so give an inaccurate picture of the current and future world state. Therefore it is very important that the data used to guide a model, or start of a stand alone model, does not include any bias (Williams *et al.* 2005).

This thesis intends to examine current methods for measuring forest properties and, using a state of the art computer simulator, explore the possibilities of future instruments to overcome the present shortcomings and uncertainties.

1.1 Layout of the thesis

The second chapter will review the various methods for modelling the interaction of light and vegetation. Chapter three will present techniques used to measure forests, both directly, ground based optical methods and remotely sensed signal using the theory described in chapter two.

Chapter four will describe the simulator used to generate lidar signals throughout the thesis and the steps taken to ensure realism. The forest models used will also be presented. Chapter five will use this simulator to generate data sets of existing and future spaceborne instruments. Current methods for inverting forest properties from remote sensing signals will be tested on these simulated datasets and various improvements suggested, leading to a proposal for an ideal canopy lidar capable of measuring the majority of the Earth's forests.

Chapter six will examine the measurement of forests by terrestrial lidar needed to validate

spaceborne measurements. The simulator will be used to generate data of terrestrial full waveform lidars. The current method for extracting canopy properties from these instruments and a new, more direct, method will be implemented and tested. Finally conclusions are presented in chapter seven.

1.2 Definitions

Some terms commonly used throughout the thesis are defined here.

LAI; leaf area index, half the total leaf surface area per unit ground area.

PAI; plant area index, half the total plant (leaf, wood and flowers) surface area per unit ground area.

LAD; leaf angle distribution, a function to describe the orientation of leaves.

PAD; plant angle distribution, a function to describe the orientation of all vegetation elements.

Gap fraction; the fraction of visible area that light can pass through.

Contact frequency; fraction of visible area taken up by objects. Equal to one minus the gap fraction.

Foliage profile; vertical distribution of gap fraction.

dbh; diameter at breast height. The diameter of a tree's trunk 1.3m above the ground.

brdf; bidirectional reflectance, the proportion of energy incident from a given direction reflected in another direction, given per unit solid angle.

Phase function; throughout this thesis, "phase function" will be used to mean the ratio of the observed reflectance to that if the visible surface area were flat and normal to the view directions over all view angles.

A note on LAI Originally it was defined as the one sided area (Watson 1947 cited in (Bréda 2003)) but that is not appropriate for needles. It has no real biological significance (Jonckheere *et al.* 2004) so it has been suggested that the total projected area of foliage elements be used instead (Chen and Black 1992).

1.3 List of mathematical symbols

P_{gap} - gap fraction η_λ - apparent reflectance at a wavelength λ A_p - projected area A_f - lidar footprint area

A_s - surface area $G(\theta)$ - Ross G function $g(\theta)$ - fraction of leaves with normals in direction θ. $\Gamma(\theta)$ - Phase function θ - zenith angle

α - angle of incidence

ρ_e - element reflectance

ρ_l - leaf reflectance

ρ_w - wood reflectance

ρ_c - canopy reflectance

Chapter 2: Mathematical modelling of trees

To understand the measurement of vegetation by optical instruments, mathematical models are needed to relate the recorded signal to forest parameters. These models allow both simulations of remote sensing signals given a set of scene parameters or inversion of scene parameters from a measured signal. Allen *et al.* (1970b) came up with one of the first practical canopy reflectance models. This was based upon the earlier work of Duntley (1942) and Kubelka and Munk (1931), describing the interaction of light with plastics and paints respectively. These models treat the object as a layer of small scattering elements bounded on top by the atmosphere and underneath by a substrate (whether ground for forests, air or metal) and are referred to as "turbid medium" models.

2.1 Turbid media

In a turbid medium model light enters through the top, being scattered by the diffuse media and finally reflected from the ground. The radiation field is normally split into the down-welling (from the sun and scattering) and upwelling flux (reflected from the ground and scattered from the canopy); these are known as two stream models. The turbid layer is treated as semi-infinite, so that the fluxes into and out of the edges are negligible, making them 1-D models. Some variants allow the properties to change with height, with multiple layers of turbid media (Suits 1972).

One of the key values for radiative transfer is the probability that a ray of light will interact with the vegetation layer rather than passing right through, known as the contact frequency (which is one minus the gap probability, P_{gap}) introduced by Monsi and Saeki (1953) (cited in (Lang and Xiang 1986)). If it is assumed that scattering elements are arranged randomly the probability can be given by the Poisson distribution; know as Beer-Lambert's law;

$$P_{gap} = e^{-k.A_p} \tag{1}$$

Where A_p is the fractional area of canopy material up along the path length p and k is a constant. The integral of A_p for a vertical transect through the full canopy is equal to the plant area index (PAI). If a transect is taken along zenith θ, then $A_p = \frac{PAI}{\cos\theta}$. This forms the core of

turbid medium models.

There are many limitations to such a model, one of the most obvious being that it assumes that the canopy looks the same (other than path length) from all viewing angles. Often the elements of a canopy will preferentially lie at certain zenith angles, such as eucalyptus leaves hanging vertically so that more leaf area is visible when looking horizontally than vertically. This will cause the contact frequency to vary with angle (Wilson 1959).

Figure 1: Eucalyptus leaves to show non random orientation

2.1.1 Leaf Angle Distribution

This property can be described by a leaf angle distribution (LAD) (Ross and Nilson 1965). This describes the probability of a leaf surface normal (or part of for curving leaves) lying with its normal in a given direction, generally denoted by $g(\theta, \phi)$, where θ is zenith angle and ϕ azimuth. Obviously the integral over all angles is unity. Most authors believe that the leaves' azimuth distribution is random (Fuchs *et al.* 1984), therefore the distribution is assumed to be independent of azimuth, reducing to the function $g(\theta)$. When Strebel *et al.* (1985) attempted to explicitly model certain crops' azimuth distributions, they found that a Poisson distribution (random) would suffice for most cases as more complex distributions were no more statistically significant. Whilst some authors still believe the azimuthal distribution to be significant (Teh *et al.* 2000), because of the results of Strebel *et al.* (1985) and the overwhelming assumption of uniform azimuth in the literature (Weiss *et al.* 2004), only the zenith dependence will be examined for the rest of this

review.

The LAD allows the fraction of total surface area projected in a given direction to be calculated. This factor is given by the "Ross G" function, $G(\theta)$ (Ross 1981). This is the integral of the leaf angle distribution multiplied by the area projected in the direction of interest over all angles.

$$G(\theta) = \int_{-\pi}^{\pi} g(\theta)u(\theta)cos(\alpha)d\alpha \tag{2}$$

Where $u(\theta)$ is the total surface area of leaves with surface normals in direction θ. Note that the integral is from $-\pi$ to π as leaves do not tend to grow with their top surfaces facing downwards (Ross 1981). Several authors report that the total intersected light is fairly insensitive to $G(\theta)$ (Goudriaan 1988); This view is not shared by all, indicated by the amount of work being done to measure and characterise LAD (Kuusk 1995, Wang *et al.* 2007). The assumption of insensitivity of $G(\theta)$ to angular distribution is most appropriate for sparse (LAI<1) canopies, giving factors of two differences in G for LAIs above 3.

To combine measurements from different viewing angles a mathematical model is needed to describe $g(\theta)$. Wilson (1960) carried out some of the earliest work with the aim of finding the optimum angle for LAI measurements with his inclined point quadrats. It was assumed that all leaves in a canopy had a single zenith angle, much like the curved surface of a cone. This is obviously an unrealistic model but was the first attempt to quantify the effects of foliage angle on measured LAI and highlighted the well known cross over point of projected LAI at a viewing zenith angle of 57.5^o. This was furthered with a set of with slightly more likely, but still idealised, cases (de Wit 1965). These special cases described LADs that could easily be represented analytically, including canopies where all leaves stand vertically (erectophile), horizontally (planophile), at an angle of 45^o (plagiophile), an even mixture of horizontal and vertical (extremophile) and uniformly pointing in all directions (spherical). These special cases avoid the numerical integration required by Wilson (1960) and the results are elegant but, other than the spherical distribution, are rarely observed in reality. Fuchs *et al.* (1984) attempted to use a fixed leaf angle distribution (the same as used by Wilson (1960)) but found that it could not model the observed projected area across a range of zeniths, a spherical distribution being a better description.

Suits (1972) included a leaf angle distribution in his early canopy reflectance model, leaf areas were projected onto the vertical and horizontal planes, equivalent to an extremophile canopy with varying proportions of vertical and horizontal leaves. This leads to unrealistic effects as viewing angle changes (particularly around 45^o) and cannot match many real situations (Verhoef 1984), however it was one of the first, practical attempts to make an invertible canopy reflectance model. Verhoef (1984) went on to refine the angular distribution by allowing fixed leaf angles (in the style of Wilson (1960)) or uniform distributions (spherical (de Wit 1965)) to create the popular SAIL model.

Since the work of Wilson (1959), de Wit (1965) and Suits (1972), other functions have been put forward to describe leaf angle distributions. Most importantly it has been shown that real leaf canopies show continuous angular distributions rather than the discrete distributions of earlier models (Thomas and Winner 2000b). One of the most popular is the spheroidal distribution of Campbell (1986), also referred to as the ellipsoidal distribution. This is a generalisation of de Wit's spherical distribution in which the probability of leaf normals lying in each zenith are allowed to vary, following the surface of an ellipsoid (an ellipse rotated about one axis to form a 3D object, see figure 2). The two horizontal radii are the same, b, ensuring uniform azimuthal distribution and these can be different to the vertical radius, a. The ratio of b to a describes the variation of leaf area with zenith. If the three radii are equal the distribution becomes spherical.

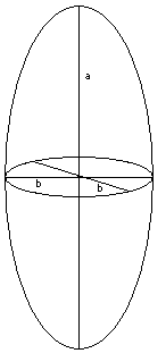

Figure 2: Illustration of an ellipsoid

Ross (1975) described an equivalent model where a factor was used to describe the deviation from a perfect spherical distribution. This has not found as wide an appeal as the ellipsoidal

distribution, perhaps because it was created to reduce computational expense which is no longer an issue (Wang *et al.* 2007).

For the ellipsoidal distribution the LAD can be found by integrating the projected surface area for each zenith ring divided by the total area to get equation 3 (Campbell 1990).

$$g(\theta) = \frac{2\chi^2 sin\theta}{\Lambda(cos^2\theta + \chi^2 sin^2\theta)^2} \tag{3}$$

Where $\chi = \frac{b}{a}$, a measure of the eccentricity, θ is zenith angle and Λ is related to the ellipsoid's surface area, which depends upon its eccentricity.

If $\chi = 1$, $\Lambda = 2$,

if $\chi < 1$ the spheroid is prolate, $\Lambda = \chi + \frac{\arcsin(\epsilon)}{\epsilon}$ where $\epsilon = \sqrt{1-\chi^2}$,

if $\chi > 1$ the spheroid is oblate, $\Lambda = \chi + \frac{ln(\frac{1+\epsilon}{1-\epsilon})}{2\epsilon\chi}$ where $\epsilon = \sqrt{1-\chi^{-2}}$.

Note that because the elemental area is rotated about the vertical axis the surface area decreases with zenith by the factor $sin(\theta)$, reaching zero at nadir. This is an artifact of fitting the LAD to a convex geometric primitive. This limitation was picked up by Thomas and Winner (2000b) who pointed out that in certain canopies the projected leaf area shows a maximum at nadir rather than the minimum predicted by an ellipsoid. With an ellipsoids $G(\theta)$ may still have a maximum at nadir, only $g(\theta)$ cannot.

To allow a maximum at nadir they rotated the surface zenith by 90^o at each point, effectively changing the sines to cosines and vice versa to give;

$$g(\theta) = \frac{2\chi^2 cos\theta}{\Lambda(sin^2\theta + \chi^2 cos^2\theta)^2} \tag{4}$$

Where χ, θ and Λ are the same as in equation 3.

However, the data they used to justify this model was for the angular distribution of pine needle shoots rather than of the pine needles themselves. Pine shoots tend to lie horizontally (depending on species) whilst the needles protrude from the shoots at a range of angles, some flatter (white fir at $\pm 30^o$) and others equally in all directions (Ponderosa pine, from unpublished measurements taken during the course of this PhD). However if shoots rather than leaves are

taken as the elementary scattering units, as many authors believe (Chen *et al.* 1997, Smolander and Stenberg 2003, Rochdi *et al.* 2006), this model may be more appropriate, although at the same time some studies suggest that there are very few leaves laying horizontally (Wang *et al.* 2007). It will, however, model the shoot twig's angular distribution; shoots are far from flat (as assumed in the Beer-Lambert law (Jupp *et al.* 2009)), so the leaf angle distribution will still not be captured by the twig angle distribution.

These distributions have the great advantage for inversion of being described by only a single parameter, χ, and this has earned them a wide following, they are constrained by forcing them to fit to the outside of a convex geometric primitive, enforcing a gradually varying value of $G(\theta)$ with a single maximum preventing them from describing a bimodal canopy, such as an extremophile (de Wit 1965).

To overcome this limitation Goel and Strebel (1984) suggested using a two parameter beta distribution. This was phrased by Wang *et al.* (2007) as;

$$g(t) = \frac{1}{\beta(\mu,\nu)}(1-t)^{(\mu-1)}t^{(\nu-1)} \tag{5}$$

Where t is a parametrised form of zenith angle, θ; $t = \frac{2\theta}{\pi}$.

$$\beta(\mu,\nu) = \int_0^1 (1-x)^{(\mu-1)}x^{(\nu-1)}dx \tag{6}$$

The parameters μ and ν are set by the mean and variance of the observed leaf angle distribution;

$$\nu = \overline{t}\left(\frac{\sigma_0^2}{\sigma_t^2} - 1\right) \tag{7}$$

$$\mu = (1-\overline{t})\left(\frac{\sigma_0^2}{\sigma_t^2} - 1\right) \tag{8}$$

Where σ_0 is the maximum standard deviation of t ($\sigma_0 = \overline{t}(1-\overline{t})$), σ_t is the variance of t and $\overline{t}$ is the mean of t. Such a model requires more data than the simpler, single parameter models but allows a more detailed leaf angle distribution (Cescatti 1997a).

Wang *et al.* (2007) tested the ability of each of the above models to describe observed leaf angle distributions of a variety of species, from trees to small shrubberies and herbaceous plants. They found that the beta distribution gave the best fits in terms of surface normal direction and gap

fraction the majority of the time, although the spheroidal and Verhoef's spherical or fixed angle both performed well. The discontinuous Suits and de Wit methods did not represent reality well, which is not surprising given the continuous nature of real LADs. The rotated ellipsoidal method (Thomas and Winner 2000b) also gave poor fits, this is most probably because the measured LADs used did not have maxima at zenith angles of 90^o, a condition enforced by rotated surfaces. This adds weight to the suggestion that the rotated ellipsoidal is only suitable if pine shoots are taken as the elementary scattering unit rather than actual leaves.

From the study of Wang *et al.* (2007) it would seem that the beta distribution is the best, at least when data to fit to is plentiful (available from all view directions); they did not attempt to fit to less detailed data. The ellipsoidal distribution fairly accurately predicts the projected area, although consistently underestimates near nadir (due to the $\sin\theta$ factor). Therefore it is an attractive model for data limited situations common in remote sensing.

One simple way to arrive at a single parameter model that avoids forcing zero at either end would be to implicitly model a uniform azimuth distribution. This would allow a model that is not constrained by a convex geometric primitive, which will always have projected areas of zero at nadir and allow the azimuthal probability to be independent of the zenithal probability. An elliptical model of leaf zenith was proposed by Kuusk (Kuusk 1996), however when the fractional projection of leaf area, $G(\theta)$, was calculated, it was rotated about one axis to make an ellipsoid, reintroducing the factor of $\sin\theta$.

If an ellipse rather than an ellipsoid is used to describe the angular distribution we arrive at equation 9.

$$g(\theta) = \frac{\chi}{2\pi\Lambda(\cos^2\theta + \chi^2\sin^2\theta)^{\frac{3}{2}}} \tag{9}$$

Where Λ is a constant relating to surface area, θ is leaf zenith angle and $\chi = \frac{b}{a}$, as in equation 3.

This has no factor of $\sin\theta$ or $\cos\theta$ and so is never forced to zero. It is like an ellipsoid except that every zenith ring has equal surface area. In three dimensions it can be thought of as a cylinder with the surface rotated an amount depending on the height from the centre, 0^o at the centre, 90^o at the top and -90^o at the bottom.

The spheroidal functions above cannot be solved analytically and so numeric integration must be used. This can be very computationally expensive, prohibitively so, especially when dealing with high resolution data. To reduce the computational expense Jupp *et al.* (2009) suggested a linear approximation for use with their very high resolution instrument. This takes the vertical projected leaf area, L_v and the horizontally projected leaf area, L_h, in a similar manor to Suits (1972), but with some smoothing to make it continuous, avoiding the non-physical features of the earlier model.

$$G(\theta) = L_h \cos\theta + L_v \frac{2}{\pi} \sin\theta \tag{10}$$

Figure 3 shows that the approximation matches the spheroidal distribution reasonably well, though it works better for extreme eccentricities than near spherical.

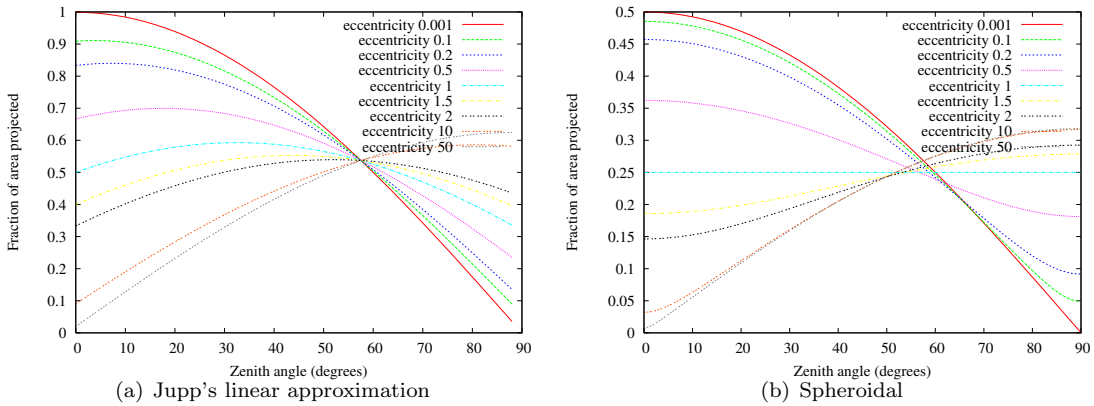

(a) Jupp's linear approximation (b) Spheroidal

Figure 3: Ross G function calculated with the spheroidal model and the linear approximation of Jupp et al (2009)

Kuusk (1996) further generalised the ellipsoidal model by allowing the axes to tilt, turning it into a two parameter function; this way the zero value can be moved from nadir and the maximum placed wherever the canopy requires. This extra complication was not backed up with data and nor was it compared to the equally complex beta distribution.

Another suggestion to account for LAD was to add up the projected leaf area in discrete bins (Goudriaan 1988) but this would not allow calculation of total surface area from observations from a set of view angles, samples would be needed at every view angle.

With the leaf angle distribution functions described above the fraction of surface area projected in a given direction, $G(\theta)$, can be calculated from equation 2. This modifies the Beer-Lambert law to;

$$P_{gap} = e^{-G(\theta).A_p} \tag{11}$$

This allows the canopy's gap fraction to vary from different view directions.

2.1.2 Opposition effect

The functions described in section 2.1.1 go some way to recreating the angular reflectance of a vegetation canopy, however it does not fully account for all the effects. The bidirectional reflectance curve in figure 4 shows that there is a sharp peak in reflectance when the viewer looks in the same direction as the illumination (at a zenith of 60^o). This is known as the opposition or hotspot effect. It was first observed in the rings of Saturn (Seeliger (1895), cited in Hapke *et al.* (1996)) and has been well documented in laboratory conditions.

A lidar detector (described in section 3.5) always looks in the hotspot direction, so fully explaining the bidirectional reflectance is not necessary to understand the signal; in fact the signal is easier to understand when views are limited to the hotspot (Strahler and Jupp 1990). Whilst it is not essential for inversion, if the lidar data is to be fused with passive optical measurements or is to be used to create a canopy model to predict off-hotspot reflectance, an appreciation of the issue is needed.

The hotspot is primarily caused by shadow hiding (Liang 2004, Hapke *et al.* 1996), when the viewer is looking along the the same vector as the illumination, all shadows are cast behind objects and so hidden from the viewer. As the vectors move apart shadows appear, reducing the measured reflectance.

A ray of light that passes any distance through a canopy will always be able to reflect back along the same path as there must be a gap for it to have got in. In a turbid medium model the path length is used to calculate the probability of a light ray interacting with the canopy (with equation 11) and so gaps are not remembered. There is a chance that a returning ray will interact

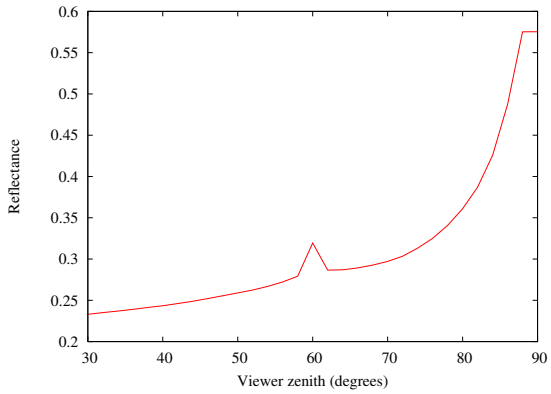

Figure 4: Sample bidirectional reflectance of a sparse Sitka spruce canopy from Monte Carlo ray tracer simulation

with elements that were not there on the way in. This forgetting of gaps is unrealistic and prevents the hotspot effect from being modelled.

In a typical forest canopy there are two different scales of shadow casting, leaves and crowns. Efforts have been made to account for both within radiative transfer models.

Crown scale shadows Except for very dense canopies a horizontally homogeneous model is not sufficient to capture all the details (Ross 1981). Within a vegetation canopy scattering elements are arranged or clumped into crowns. Shadows cast by these crowns will contribute to the hotspot effect as well as altering the visible area of foliage (also known as effective LAI, more on this later).

One method to account for the hotspot is to clump the turbid medium into geometric primitives with free space between and a layer of ground below. From a defined crown size and density the proportion of directly sunlit crown and ground, shaded crown and ground for a given viewing and illumination direction can be determined. From this the reflectance can be calculated, treating the sunlit and shaded areas of crown as 1-D turbid media. This technique was pioneered by Li and Strahler (1985) and has been refined over the years (Li and Strahler 1988, Li and Strahler 1992, Li *et al.* 1995) leading to the "GORT" model (Ni *et al.* 1999) which has been applied to a wide range of problems, including lidar (Ni-Meister *et al.* 2001).

This approach is known as a hybrid geometric model as it combines geometric optics for the discrete crowns with turbid media for canopy. With GORT type models the locations of individual

crowns is never explicitly defined, only the density and distribution through stochastic means. This level of abstraction reduces the number of model parameters, greatly easing inversion (Woodcock *et al.* 1997) but may cause problems when the detector's field of view approaches the scale of heterogeneity. The "FOREST" model (Cescatti 1997a) was created to extend the hybrid geometric approach to irregular crowns, greatly increasing the complexity of the model. The model has been shown to perform well when inverting above canopy measurements (Cescatti 1997b) but the additional complexity was not justified by comparison of inverted parameter accuracies with simpler models (those with fewer unkowns). Certain models exist that do explicitly define the locations of geometric primitives (North 1996) however these tend to use the Monte Carlo method and so will be covered later.

Kimes and Kirchner (1982) included a further level of detail where instead of geometric primitives of turbid media with a bounding plane, the scene was split into voxels (volumetric pixels or cubes). Each was filled by either a plane (for ground, trunks or buildings) or some turbid medium (for crowns). This is also known as the "discrete ordinate" method. The approach is very similar to geometric primitives with explicit locations except that the crowns are not constrained to fit into simple shapes. The light reaching and reflected by each voxel can be calculated, leading to a complete picture of the radiation regime within the canopy. The method has been refined to create the DART model (Gastellu-Etchegorry *et al.* 1996, Gastellu-Etchegorry *et al.* 2004).

Splitting the scene up into voxels increases the computational load compared to geometric primitives, but it is questionable whether real tree crowns can be represented as such simple, hard edged objects as cones and ellipses (Parker and Brown 2000).

Myneni proposed a rigorous and spatially explicit solution of the radiative transfer equations (Myneni *et al.* 1992). In practise computational limits would cause this to be similar to the voxel based methods of (Gastellu-Etchegorry *et al.* 1996).

Leaf scale shadows Turbid medium models were first developed for diffuse gases common in astrophysics (Chandrasekhar 1960). The scattering elements are treated as point particles with no size and so cast no shadows. This model is not appropriate for vegetation canopies where elements have finite size and cast shadows (Ross 1981, Knyazikhin *et al.* 1992).

There are far more leaves in a crown than there are crowns in a canopy (for a single pixel), therefore it is much more computationally expensive to explicitly define leaf scale gaps and elements than it is for crown scale shadows (Ni *et al.* 1999, Gastellu-Etchegorry *et al.* 2004). This approach of remembering all gaps has been used (Knyazikhin *et al.* 1992, Disney *et al.* 2006) but more abstract approaches are more common as they require fewer parameters, easing inversion.

One conceptually simple approach is to treat gaps and leaves as circles of a set diameter, so that a ray penetrating into a canopy can be described by a cylinder (Verstraete *et al.* 1990). The increased probability of a ray returning along the same path is accounted for by modifying the optical thickness by the fraction of overlap of the incoming and outgoing cylinders (see figure 5).

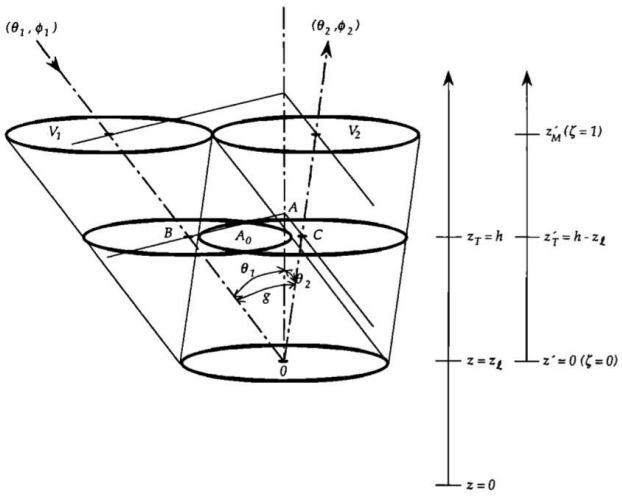

Figure 5: Illustration of the modelling of hotspot by overlapping cylinders from Verstraete et al (1990)

Jupp and Strahler (1991) used statistics to describe the probability of returning rays passing through existing gaps; the optical thickness either being zero (gap) or the same as for the turbid medium (canopy). This was an extension of earlier work to describe crown scale shadows (Strahler and Jupp 1990). It was later generalised to to use rectangular rather than circular gaps (Qin and Xiang 1994), although it was found that the hotspot is dominated by leaf size and distribution and the effect of leaf shape could be accounted for by modifying leaf size.

Kuusk (1995) used a similar approach, but with Markov chain theory rather than Boolean statistics. The probability of an interaction in a canopy layer is modified from the standard turbid medium case by whether or not there have been interactions in higher layers and a correlation fac-

tor. These three methods are mathematically equivalent (Liang 2004), requiring only an additional leaf size factor and can adequately recreate the hotspot.

Knyazikhin *et al.* (1992) gave a more rigorous, but more complicated, solution in which the canopy is taken as a random collection of leaves (turbid medium) and gaps. Interactions are remembered and influence the probability of a ray returning in the hotspot direction.

Coherent backscatter Another potential contribution to increased reflectance in the hotspot direction is a phenomenon known as "coherent backscatter". Some believe it to be significant factor in lidar reflectance (Harding, DJ, 2008, pers comm.).

Coherent backscatter, as its name suggests, results from light scattered from the target interfering with itself constructively, increasing the intensity (Stephen and Cwilich 1986). Ordinarily scattered light will be completely incoherent, so no enhanced reflectance is observed. In the hotspot direction, when the illumination source and viewer are co-aligned, an interesting effect is observed. For every photon path from the illumination source to the viewer, a reversed path can be traced from the viewer to the illumination. As these two are co-aligned, photons from both of these paths will contribute to the measured signal and as they have travelled exactly the same distance they will constructively interfere. This was first noticed by Kuga and Ishimaru (1984) and for a disordered medium, such as vegetation, is the only significant interference effect (Stephen and Cwilich 1986).

The scale of the target's roughness controls the magnitude of the effect (partially from shadows). Scenes with many elements around the size of the light's wavelength show more coherent backscatter than scenes with larger elements. Experiments found that for a typical forest canopy, where objects are generally larger than the light's wavelength, the contribution to the hotspot from coherent backscatter is insignificant compared to that from shadow hiding (Hapke *et al.* 1996). It was found to be important for dry soils and some fine structure vegetation, such as mosses.

Hapke's study focused on the visible region, where foliage reflectance is low. As coherent backscatter depends upon multiple scattering it is especially sensitive to element reflectance. Therefore it may be slightly more important to the hotspot in the near infra-red, with higher foliage reflectance. However, for the visible it was found to be such a small effect that increasing the

reflectance (from around 0.1 to 0.6) is not likely to make coherent backscatter more important than shadow hiding. It would seem to be an unnecessary level of detail although a quantitative analysis has not, as far as he author is aware aware, been performed in the near infra-red.

2.1.3 Clumping

Forest canopies are not uniform, elements are arranged into different scales from pine needle shoots up to tree crowns. Early attempts to model this heterogeneity were driven by the desire to model the hotspot (covered in section 2.1.2), but clumping also affects radiative transfer in other ways.

In a turbid medium elements are assumed to be infinitely small and completely randomly distributed. The attenuation, or shadowing, is taken into account by Beer-Lambert's law (equation 11). However, the clumping of scattering elements into crowns, whorls, branches, shoots and leaves cause deviations from complete randomness and changes the distribution of shadows.

The spatially heterogeneous models, GORT (Ni *et al.* 1999) and DART (Gastellu-Etchegorry *et al.* 1996) explicitly take crown scale clumping into account and, depending on the voxel size used, DART can deal with the branch scale. This explicit modelling is necessary if the scale of clumping is around the size of an instrument pixel (or half the size to ensure Nyquist sampling). For an instrument like Landsat with its 25m footprints, this is the crown scale. The number and density of shoots, whorls and leaves would it make it too computationally expensive to model them explicitly and, as they are not resolved by most instruments, there is little point, an implicit treatment will suffice.

The idea of a clumping factor, Ω, to scale account for the non-randomness was introduced by Nilson (1971) as a modification to Beer-Lambert's law (equation 12).

$$P_{gap} = e^{-G(\theta).A_p.\Omega} \tag{12}$$

Conifers show marked shoot scale clumping, leading to underestimates of LAI from increased self shadowing, so a decreased "apparent LAI" (Chen *et al.* 1997). Oker-Blom and Smolander (1988) (cited in (Stenberg 1996)) used the "silhouette to total surface area" or $STAR$ to scale between true and effective LAI. It appears that Gower and Norman (1991) arrived at the same

correction term independently. This factor is equal to the average projected shoot area over four different view angles divided by the total projected needle area (found by pulling the needles off and laying them flat). Stenberg (1996) noted that earlier attempts had only looked at the silhouette area perpendicular to the shoot's twig, leading to an overestimate of the projected area and so an underestimate of clumping index. Independent observations also reported an underestimate but were unsure of the cause (Fassnacht *et al.* 1994). Stenberg (1996) proposed a spherically averaged version, $\overline{STAR}$, rotating the shoot in all possible directions (assuming that the angular distribution of shoots is spherical). Cauchy's theorem (Lang 1991) was then applied to calculate the convex surface area of a shoot from $\overline{STAR}$.

For larger footprint instruments (such as AVHRR with 1.1km pixels) an implicit factor can be used to describe crown scale clumping (Chen and Cihlar 1995). This allows a 1-D model to be used, greatly streamlining computation. In this case the clumping factor, Ω is split into two components, the crown scale clumping, Ω_e, and the shoot scale clumping, γ_e which is equal to $\overline{STAR}$. Ω_e is found from the ratio of LAI assuming a non-random distribution of scattering elements (taking shoots as the basic scatterers) to the LAI assuming a random distribution. Methods to measure these two factors will be covered in section 2.4. Beer-Lambert's law then becomes;

$$P_{gap} = e^{-G(\theta).A_p.\frac{\gamma_e}{\Omega_e}} \tag{13}$$

Clumping of scattering elements into leaves actually increases the effective LAI, as leaves do not shadow themselves (Sinoquet *et al.* 2005). However the reported underestimate of LAI by the uncorrected Beer-Lambert law shows that this effect is negligible compared to other scales of clumping. Crown scale clumping, down to around a metre, is the dominant form (Lacaze *et al.* 2002, Cescatti 1997b), but in conifers, the clumping of leaves into shoots is not negligible, becoming increasingly important as canopy density increases and Ω_e approaches unity (Chen and Cihlar 1996) .

2.1.4 Woody correction

All the equations for contact probability so far have been in terms of plant area index, PAI, from the fractional projected surface areas of leaf and wood ($A_p = \frac{PAI}{\cos\theta}$). Ecological models need leaf area index as it is this surface that performs photosynthesis and other biological processes (Gower *et al.* 1999).

A canopy is typically composed of some proportion of wood, α, and leaf, $1-\alpha$. The factor, $1-\alpha$, also known as the "woody correction", can be included in Beer-Lambert's law to scale between PAI and LAI (Chen and Cihlar 1996). The gap probability then becomes;

$$P_{gap} = e^{-G(\theta).(1-\alpha).\frac{LAI}{\cos\theta}.\frac{\gamma_e}{\Omega_e}} \tag{14}$$

Canopies can also contain flowers, seeds and other organs (Ross 1981) but most authors tend to ignore these, either treating them as wood or else assuming that their impact is negligible.

2.1.5 Polarisation

The polarisation of reflected light should provide more information to aid understanding. Multiple reflection within leaves completely depolarises light whilst specular surface reflection preserves incoming polarisation (Grant *et al.* 1993). Thus different wavelengths of light will tell us something about leaf structure, but according to Kuusk (1991) there is little polarisation in reflected light from vegetation, therefore it would be unsuitable for measurement from a spaceborne instrument due to low signal strength.

2.1.6 Final Solution of the turbid media problem

So far the chapter has given the equation to calculate the gap fraction at different view angles (and so contact frequency) from vegetation properties. Certain corrections are needed to account for all affects (the hotspot, described in section 2.1.2), but otherwise equation 14 will give an acceptable answer. This allows us to calculate the fraction of light hitting the canopy and the fraction passing straight through, when combined with the canopy and ground reflectances and a phase function (to account for angular reflectance) this gives an exact solution for the singly scattered light (light

that has only interacted with the scene once). However light can interact many times with the scene, adding to the measured reflectance; this is known as the multiple scattering contribution.

The earliest attempts to account for multiple scattering were the differential equations introduced by Kubelka and Munk (1931) to describe the intensity of colour of paint. These have become know as the "Duntley equations" (Duntley 1942); they treat the radiation field as being made of down-welling light and upwelling light and so are known as two stream models. A third stream was added to account for directional illumination (the two stream model assuming isotropic diffuse light) to create a three stream model (Allen *et al.* 1970b). Another stream was added to account for the viewer direction, allowing estimates of bidirectional reflectance (Suits 1972). This approach has been refined (with leaf angle distribution, multiple layers and the hotspot) to give the SAIL model (Verhoef 1984) whilst GORT, a more complex model that uses geometric primitives to more accurately calculate the singly scattered reflectances, uses the same two stream approach to calculate multiple scattering (Ni *et al.* 1999).

The two stream approach assumes that multiple scattered light is isotropic, and the scattering certainly reduces a lot of the directional effects (Liang and Strahler 1993), but it is not an ideal solution. Some models calculate the light scattered in a discrete number of directions, such as SAIL++ (Verhoef 2002) and DART (Gastellu-Etchegorry *et al.* 2004). For horizontally homogeneous canopies (which SAIL++ assumes) only zenith directions need be taken into account, reducing the number of calculations required. This better accounts for angular effects (such as LAD) but increases the computational load.

Differential equations are set up in these directions (whether two, four or more) and loaded into matrices. As light scattered into an area can be scattered back, an exact solution of the radiative transfer equations would require an iterative approach, adding up all the different orders of multiple scattering until absorption at each interaction makes the intensity negligible. This requires a significant amount of computation and complicates inversion, but by clever manipulation of the matrices and by re-expressing the infinite sums, the computation can be brought down to a manageable level (Verhoef 2002). These approaches tend to ignore scattering between the ground and canopy and so are known as "black soil" approximations.

These attempts to produce analytical solutions for radiative transfer allow inversion, but large assumptions need to be made as a vegetation canopy is too complex for a perfect analytical solution (Widlowski *et al.* 2007). More comprehensive reviews, complete with equations, are available for the interested reader (Ross 1981, Myneni and Ross 1989) (indeed they are incredibly comprehensive with as much detail as anyone could want).

2.1.7 Turbid medium conclusions

With equation 14 a turbid medium can account for the effect of canopy structure on radiative transfer and has found favour for inverting estimates of LAI from optical measurement (Law *et al.* 2001). However, whilst the 1-D turbid medium models can recreate all the basic elements of canopy reflectance, they achieve this through effective parameters which are not necessarily directly related to physical features. These effective parameters can be fudged to accurately match measured angular reflectances whilst issues such as the contribution of wood and multiple scattering are not dealt with in a physical manner (Smolander and Stenberg 2003). Thus the LAI and other variables predicted by the model may not be the true values (Widlowski *et al.* 2005)

Of course a model cannot be inverted with any accuracy if there are more unknowns than measurements to constrain them, so abstract models such as turbid media are necessary. Care must be taken when using models to explore physical processes to make sure that assumptions do not hide the truth.

2.2 Explicit methods

The assumptions in and reliance on effective parameters of turbid medium models means that they are not ideal for understanding the measurement of forests through simulations. Therefore more detailed models that do not need effective parameters are needed. Models exist that explicitly define the position, orientation and spectral properties of all elements in the scene then calculate the radiation field by a form of numeric integration, though these are far more computationally expensive than the more abstract turbid medium methods. A complete description of a vegetation scene contains far too many variables to allow direct inversion (attempts have been made using fitting to look up tables of simulated waveforms, but with slightly abstracted forests (Koetz *et al.*

2006)) but it also minimises assumptions, allowing physically realistic simulations of remote sensing signals.

In the beginning the computational expense of explicit methods limited their use (Myneni *et al.* 1992), users tending towards more abstract volumetric methods (Kimes and Kirchner 1982). The simulation of optical remote sensing signals has much in common with computer graphics; both produce light signals (or images if a 2D array) from given objects, also known as rendering. This synergy with computer graphics and the explosive growth in computer power, graphics hardware and the increasing sophistication of rendering algorithms in the late 1980s and 1990s made explicit simulations of vegetation feasible (Borel *et al.* 1991). Care must be taken when employing computer graphics acceleration methods as these tend to be designed to produce a "psycho-physical" result, one that looks right to a human eye rather that a physically accurate result obeying energy conservation required for remote sensing images (Koenderink and van Doorn 1996).

2.2.1 Radiosity

One popular computer graphics method is known as the "radiosity" technique (Cohen and Wallace 1993). These calculate how much light reflects between every surface in the scene, producing a set of "form factors" that can be used to calculate the radiance measured by a detector from an illumination source placed anywhere within the scene. This is ideal for films since each frame can be quickly rendered from the form factors, though the initial calculation is computationally expensive and the set of form factors can be large if there are many elements in the scene (which there invariably are in forests).

They were first used for remote sensing of vegetation in the early 1990s (Borel *et al.* 1991) and thus far only scenes with relatively sparse canopies have been modelled with radiosity methods (for example scrub in semi-desert regions with a ground cover of $<25\%$ (Qin and Gerstl 2000) and, more recently, short crops (Liu *et al.* 2007)) and the scaling of computational and memory expense with scene complexity and size has been cited as a major disadvantage of the technique (Disney *et al.* 2000, Liang 2004). The computer requirements can be reduced by splitting the scene into repeatable subsections, but these units cannot be smaller than the scale of heterogeneity (Qin and Gerstl 2000), limiting its applicability to forests.

It is questionable whether it would be practical to use radiosity methods with scenes as complex as a coniferous forest (they being one of the most structurally complex biomes). Also radiosity models do not typically record the path length of light and so it has been suggested than they are not suitable for simulating the range resolved signals required for lidar (Disney *et al.* 2000).

2.2.2 Monte Carlo ray tracing

Monte Carlo techniques are a form of numeric solution whereby a finite number of samples are made of a complex system, building up a picture of the system's behaviour (Metropolis and Ulam 1949). They are very popular for problems that have no analytic solution (such as radiative transfer), without making many assumptions and whose complexity makes alternate methods slow. Previous uses include electron microscopy (Shimizu and Ze-Jun 1992), neutron diffusion for nuclear fission (Metropolis and Ulam 1949) and CO_2 flux (Hollinger *et al.* 2004) and they are an obvious choice for solving radiative transfer.

2.2.3 Details of operation

For radiative transfer the process is called Monte Carlo ray tracing and has been used for many years, including optical instrument design on the very first electronic and mechanical computers (Comrie 1940). It can work in two modes, the most physically intuitive of which is forwards ray tracing. In this mode rays of light are traced from an illumination source (whether it be the sun, a laser or a diffuse sky) towards the target. At the first object it reaches it is either absorbed, reflected or transmitted depending on a randomly drawn number, the probability and direction of each is set by the bidirectional reflectance and transmittance spectra of the object struck. Using a probability distribution to choose either reflection or transmission prevents the ray from splitting into two, both of which would need to be traced, doubling the computational load with each interaction. This process is repeated until the ray is either absorbed, leaves the scene, undergoes a maximum number of interactions or reaches the detector, in which case its intensity is added to the signal. By this process a "ray tree" is generated, a set of intensities throughout the target. This is repeated for many (typically tens of thousands to millions) rays until a representative signal from the target is reached.

All interactions occur in the geometric domain (Houstoun 1938) so that no diffraction or refraction effects have to be calculated. Any features smaller than the radiation's wavelength are taken into account by the element bidirectional reflectance and transmittance.

The alternative mode is reverse ray tracing, where rays are traced from the detector back to the scene. This ensures that every ray has a chance to contribute to the signal (Lewis 1999). For cases when the field of view of the detector is smaller than the field of illumination (which is generally the case for passive optical sensors with slightly diffuse sky conditions) reverse ray tracing is more efficient than forwards as with forwards it would be possible for a ray traced from the illumination to never enter the detector's field of view, wasting computer time (Disney *et al.* 2000). However, if the field of view is smaller than the field of illumination the opposite is true and a ray traced from the detector might never enter the field of illumination. Therefore in these cases, which include most lidar detectors (Schutz *et al.* 2005), forwards ray tracing would be more efficient.

How many rays to sample the scene with and what to limit the maximum number of interactions to depend upon the scene. Often the maximum number of iterations is set as the number of interactions after which the ray's contribution to the total intensity is negligible (found from test runs) and the number of rays is set as the number after which the fractional change in recorded radiance (from one new ray to another) drops below a certain level. Limiting the maximum number of interactions can cause a small truncation in energy but the effect is small and can be corrected by a small factor (Disney *et al.* 2000). Obviously if only a psycho-physical result is needed, as is the case for computer graphics, less physically stringent limits can be set, using enough rays and interactions to ensure a human observer will not notice the difference.

Finding which object a ray strikes through intersection tests is the most computationally expensive process in ray tracing, especially if the scene contains many elements. Methods to increase the efficiency have been introduced such as using hierarchical "bounding boxes" around objects (Glassner 1989). This way many millions of elements can be grouped into relatively few boxes which can be tested for intersection, then only test the elements within intersected boxes.

One obvious short coming of the individual photon tracing method described above is that if a photon is absorbed, it makes no contribution to the signal and all the computational effort has

been in vain. A more computationally efficient method is to attenuate a ray at each interaction rather than completely absorb it. Rays are then "bundles of photon paths" rather than individual photons (Lewis 1999).

Another acceleration method is known as "fictitious flight". With this, rather than waiting for a ray to happen to scatter back to the detector, at each interaction a line is traced to the detector and if the point is visible a contribution is added (Ross and Marshak 1988). If reverse ray tracing is to be used exactly the same process is carried out but with lines back to the illumination at each interaction, a slightly more complex process (Disney *et al.* 2000).

This concept was further developed into the "ray spreading" method to speed calculations of bidirectional reflectance (Thompson and Goel (1998) cited in Liang (2004)). Periodically an interaction is spread out into a wavefront travelling in all directions. This contributes to the reflectance across the whole hemisphere making calculation of the brdf faster than with traditional ray tracers. It is not clear whether this technique would be of any benefit to simulations of lidar, where the illumination and detector are highly directional.

2.2.4 Ray tracing of plants

Monte Carlo methods were first suggested for solving radiative transfer in vegetation canopies in the late 1960s and early 1970s, seemingly independently by Smith and Oliver (1974) and Tanaka (1969) (cited in Ross and Marshak (1988)). Due to the computational expense of the method the early work represented plant canopies with turbid media, the Monte Carlo sampling dealing with multiple scattering.

As computers became more powerful, simulations with explicit geometric models models became possible (Ross and Marshak 1988). One major advantage Monte Carlo ray tracing has over other explicit 3-D methods is that the number of rays to be traced and the maximum number of interactions are set independently of the scene. This means that computation time does not scale directly with complexity as it does for radiosity (Liang 2004) making it preferable for complex or dense canopies.

2.3 Forest models

Explicit plant models allow physically realistic simulations of remote sensing signals, however a large amount of data is required to describe the location, shape, orientation and optical properties of every element in the scene. For us to have confidence in the results the scene must be a realistic representation of reality (Pinty *et al.* 2001). There have been many studies to describe accurate plant structure (a review is given in Godin and Sinoquet (2005)). These have ranged from look alike for computer graphics (Glassner 1986) to full cytological models to explore plant community biology (Chelle 2005).

For remote sensing instruments only the optical properties are important, that is the structure and bidirectional reflectance of each element. More detailed, cell scale, detail is not necessary; though such biological considerations can help in the creation of structural models (Allen *et al.* 2005).

2.3.1 Geometry

The process of measuring the exact location of points of interest on a plant in order to produce an accurate 3-D model is well developed (Godin *et al.* 1999). These use 3-D coordinate recording devices such as electromagnetic digitisers (Raab *et al.* 1979), photogrammetry (Innes and Koch 1998) or sonic digitisers (Mack and Pyke 1979) to manually record each coordinate along with the element type (trunk, leaf etc) so that little processing is needed after the data has been collected. Making such direct measurement of plant structure is a laborious and time consuming process, so is not suitable for creating the stand scale models necessary for remote sensing simulations (Godin *et al.* (1999) took 24 worker days to digitise eight relatively small trees).

A much quicker method to build up a set of plant models required for a stand is to use mathematical models to "grow" them on a computer. This idea was pioneered by Lindenmeyer (1968a) (with the sister paper Lindenmeyer (1968b)) who showed that small adjustments of simple growth rules could lead to complex and vastly different structures that can mimic real organisms. A similar method of simple rules was used (seemingly independently) to produce 3-D tree-like structures (Honda 1971).

These early attempts were only plant-like as they were not based on real plants; just made to look similar. Gradually the methods were refined so that plants could be represented to a high degree of realism (Prusinkiewicz and Lindenmeyer 1990, Allen *et al.* 2005). Some take biological factors into account to predict how plants of the same species develop in different environments (Chelle 2005). As an interesting aside it has been found that the algorithms represent reality better if chosen to optimise light exposure (for light liking species (Honda 1978)) or mechanical strength (for exposed trees (Fisher 1992)), with slight randomisation, showing the optimisation process of evolution.

The growth rules needed to drive these models can be generated by measurement of relatively few plants, then tweaked to match local conditions. This technique has been employed to generate large scenes for remote sensing simulations (Disney *et al.* 2006) with some software available commercially (Onyx Computing Inc 2009).

An exciting recent development is the use of laser scanning to generate complete plant models. Laser scanners generate dense point clouds of targets rapidly (less than 10 minutes for a hemisphere). However, unlike a human interpreter in 3-D digitisation, the scanner does not know which points connect to which, much less what plant organs they represent. The conversion of a point cloud into a plant model is not trivial (Omasa *et al.* 2007) and explains the much slower pace of development compared to the comparatively simple building modelling. It has recently been shown that it is possible to use knowledge of plant structure (ie. a leaf must be connected to a branch which must be connected to trunk which must be connected to the ground) can be used to generate a plant model from a point cloud (Côte *et al.* 2009) that looks the same and (through Monte Carlo ray tracing) produces similar remote sensing signals based in the computer graphics method of Xu *et al.* (2007). This still requires some manual input to help connect the dots but it is a promising line of research.

Abstractions Completely explicit models with accurate element BRDFs do not rely any effective parameters to simulate accurate signals (Widlowski *et al.* 2005), however such detail comes at a heavy computational price and requires an enormous amount of data to set up. In addition to the efficiency techniques given in section 2.2.3, some abstractions have been used to reduce the

computational burden and data requirements.

Having unique bidirectional reflectance and transmittance spectra for each element would require either a set of look up tables or separate functions. These would most likely be wavelength dependent (for a leaf NIR reflectance is more specular than in the visible (Grant *et al.* 1993)) and so separate ray paths would be needed for each wavelength. If it is assumed that the bidirectional reflectance and transmittance are the same shape for all wavelengths (but not the same magnitude) then a single ray tree can be used for all wavelengths (Lewis 1999). This greatly increases speed of multi-spectral simulations and the difference caused by brdf shapes has been shown to average out at the stand scale (Disney *et al.* 2006), although a comprehensive validation has not been performed at finer scales (such as lidar's often centimetre scale). Typically reflection and transmission are assumed to be perfectly Lambertian, removing the need for look up tables or more complex functions.

In coniferous forests the vast majority of elements, and so intersection tests and computational expense, are made up of needles. Therefore abstracting a needle shoot to a single simple geometric primitive will make an enormous saving. It has been shown that such a model can reproduce stand and shoot scale brdfs (Rochdi *et al.* 2006) but care must be taken. Smolander and Stenberg (2003) showed that whilst using primitives with the same average projected area as needle shoots can recreate the single scattering reflectance accurately, it does not deal with internal multiple scattering and so to correct for this the parameters become effective rather than physical (Widlowski *et al.* 2005). This suggests that the results of such models cannot be taken as entirely physically accurate and so explicit models should be used were physical realism is important. There are moves towards faster methods that take scattering into account physically but these have not yet reached maturity (Smolander and Stenberg 2005, Rautiainen *et al.* 2009).

For complete realism all structures larger than the radiation's wavelength should be explicitly modelled, including surface texture. For tree bark this would require many small facets, making ray tracing more computationally expensive. Using fewer large, smooth objects (such as cylinders) to represent these surfaces will miss this detail but be far faster to trace and requires far less memory to store. Various processes have been created in computer graphics to modify a simple geometric

primitive's surface to emulate this small scale surface texture (Koenderink and van Doorn 1996). These work by a process of "bump mapping", rotating local surface normals whenever a ray strikes to make the brdf more like that of a textured surface. This slightly increases the computational expense compared to geometric primitives alone (requiring a surface normal jitter value to be generated with each interaction) but this is more than made up for by the reduced number of objects to test for intersection. There are methods to deal various levels of detail, some simply rotating surface normals, others calculating how such rotations would shadow adjacent surfaces (Cabrel *et al.* 1987), but most remote sensing simulators do not go down to this level of detail, trusting that any such effects will average out on the scales of interest (pictures tend to be far higher resolution than remote sensing detectors). These techniques have been shown to produce realistic images of bark (Oppenheimer 1986) but, as far as the author is aware, the effect has not been quantified except for relatively simple scenes (Ulbricht *et al.* (2006) presents some results, mainly from architecture).

A method to reduce the memory requirements of objects is to use cloning. Rather then representing many similar objects (such as leaves, pine shoots), each can be defined once, then copied to locations as required. These clones can be nested (clone leaves into shoots, shoots into whorls, whorls into trees, trees into stands, stands into forests) to make the scene model even more compact. This has no effect upon the computer processing requirements.

Some modern ray tracing models use turbid medium forests for computational speed (North 1996), whilst these are many hundreds of times faster than fully explicit models their reliance on effective parameters to explain clumping, multiple scattering and the hotspot limits their physical realism.

2.3.2 Spectra

With the accurate geometry described in the previous section along with the assumption of identical brdf shapes with wavelength, a ray tree can be generated. To convert this to an intensity signal the elements need to be "coloured in" with accurate reflectance and transmittance spectra.

There have been many campaigns to collect element reflectance and transmittance spectra (for example BORREAS (Sellers *et al.* 1997) and OTTER (Peterson and Waring 1994)) and libraries

of different species are readily available (Hosgood *et al.* 1994). These tend to be hemispherically averaged values, ignoring any directional effects, leaving the user no choice but to assume Lambertian behaviour. Whilst there have been some studies of directional reflectance (Grant *et al.* 1993) there are no libraries readily available and so they are not widely used.

The measurement of reflectance and transmittance is typically carried out with an integrating sphere such as the Licor LI-1800 (LI-COR 1988). These have a sphere with a reflective coating to collect hemispherically reflected light, containing a source illuminating an area (of about $1cm^2$) with a detector placed either behind the target to measure transmittance or in the wall of the sphere to measure hemispherical reflectance. This calculation assumes that all light is incident upon the target material, requiring a sample that fills the $1cm^2$ window; easy enough for broad leaves and bark but not for needle leaves. Some investigators cram enough needles into the window, ensuring there are no gaps by using multiple layers. This will increase measured reflectance through multiple scattering and drastically decrease apparent transmittance. Otherwise a single layer is carefully laid out, correcting for any gaps by repeating the transmission measurement with all needles painted matte black (Daughtry *et al.* 1989).

There have been few attempts to model element optical properties compared to the number of canopy models (Liang 2004), perhaps due to the relative ease of collecting real element reflectance data. However, models are required to invert element biophysical properties from remote sensing signals.

Leaves The earliest attempts to model leaf optical properties treated them as a semi-infinite parallel plate of cells bounded by air above and below (Allen *et al.* 1969). Light undergoes multiple scattering between the plate's bounds so that the reflectance and transmittance could take more into account than pigments alone. This was extended to multiple layers of leaf cells with air gaps between to better represent real leaf structure (Allen *et al.* 1970a); reflectance and transmittance depend upon pigment concentration, the number of cell layers and their refractive index.

The idea was extended by Jacquemoud and Baret (1990) to take illumination angle into account to produce the popular PROSPECT model. This has been modified over the years to allow

modelling of leaves in all states of health (Jacquemoud *et al.* 1995) and is seen as the state of the art, being by far the most widely used (Liang 2004). The modified version is driven by five parameters; the number of layers, chlorophyll concentration, water content, protein content and a "lignin and cellulose" parameter. These parameters can be adjusted to represent the reflectance and transmittance of many types of leaves and attempts have been made to invert leaf biochemistry from spectral canopy reflectance (Zarco-Tejada *et al.* 2004), although the accuracy has been low except for a limited set of conditions (Liang 2004).

Figure 6 shows an example of a spectrum created from PROSPECT compared to a measured spectrum of white fir collected in the Sierra Nevada mountains (July 2008). The model has captured the main features, although PROSPECT is optimised for broad leaves which have slightly different reflectance values from the needle leaves shown here.

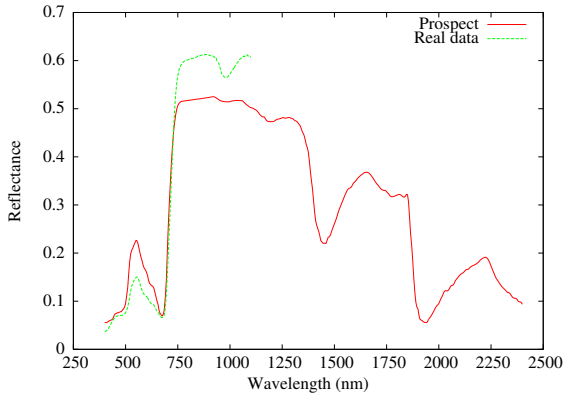

Figure 6: Comparison of real white fir needle leaf spectra and a two layered PROSPECT leaf

The parallel plate model's assumption of semi-infinite layers is fine for broad leaves (where the width is much greater than thickness) but does not hold for needle leaves. In addition the cellular structure of needles is slightly different than for broad leaves (spherical cells (Dawson *et al.* 1998) as opposed to rhomboids (Govaerts *et al.* 1996)). The LIBERTY model (Dawson *et al.* 1998) was created to try to address some of these issues. It used a modified parallel plate where the upper boundary is replaced by a set of Lambertian spheres (representing cells) with multiple scattering between these spheres and a plane below. The finite horizontal extent of a needle (compared to its thickness) was not taken into account. It has been suggested that this can be used to invert leaf biochemistry in the same way as PROSPECT (Dawson *et al.* 1999).

Other methods for modelling have been proposed, including Markov chain (Maier *et al.* 1999), turbid medium (Richter and Fukshansky 1996) and Monte Carlo ray tracing (Govaerts *et al.* 1996). As they are harder to parametrise or far more computationally expensive they have not achieved the same popularity as parallel plate models (Liang 2004). They do have the advantage of being able to take cell level heterogeneity into account, a feature the parallel plate model cannot. These models may then be better for examining the angular dependence of leaf spectra, particularly Monte Carlo ray tracing (if an explicit cell model can be generated) although the author is not aware of any angular comparisons with parallel plate models.

Bark There has been far less interest in understanding the reflectance of bark; leaves being the main energy and chemical exchange organs of a plant. As far as the author is aware there have been no attempts to create predictive bark reflectance models, other than psycho-physical attempts for purely artistic use (Dana *et al.* 1999). The field data libraries mentioned in the previous section also contain spectra for wood and bark and these will have to suffice.

It is unclear how the reflectance will change with viewer and illumination angle, or whether coherent backscatter will be make a noticeable contribution.

Soil Soil reflectance is of interest for ecology, agriculture and hydrology where the type, grain size, moisture level and organic content are needed by models (Liang 2004). Models have been created in order to determine soil properties from remotely sensed data. A comprehensive review is available in (Liang 2004), chapter 4 and as such an inversion will not be attempted in this thesis, the review will be kept brief, covering only those issues relevant to forests (for which they form the lower bounding layer) and lidar.

One popular approach is the solution of Chandrasekhar's (Chandrasekhar 1960) radiative transfer equations (Hapke 1981). This treats the soil as a turbid medium of small particles and, just like canopy models, various modifications are needed to take into account all effects, particularly self shadowing (Jacquemoud *et al.* 1992). For these models, soil grain size, refractive index, water content and organic concentration are the driving parameters. Unlike vegetation canopies, coherent backscatter is not negligible (Hapke *et al.* 1996) and so the hotspot reflectance (such as measured

by a lidar) may be higher than predicted from the hemispherical average.

More geometrically explicit models have been developed to account for self shadowing in a physical way. These use much the same techniques as geometric canopy models (Ni *et al.* 1999) with the proportions of shadow and direct sunlit material controlling brdf (Ciernewski 1999). Unlike canopy models the geometric primitives (typically spheres or ellipsoids) are not filled with turbid media but are either opaque or characterised by a refractive index; in addition grains are generally evenly spaced on grids. These models are harder to invert but show promise for representing observed soil brdfs.

Like vegetation there are libraries of soil reflectance values (Stoner *et al.* 1980). It has been found that these spectra cluster into groups and can be explained as a mixture of five generic examples or "soil vectors" (Price 1990). Any deviations from these were assumed to be due to measurement error and detector noise (these vectors could account for 99.6% of observed variance). These vectors have been used to "colour in" soil in computer models (Disney *et al.* 2006).

2.4 Validation

Any model, however detailed, is only a representation of reality and all make assumptions at some level (even if it is only that the scene model is accurate). For us to have confidence in the results the model must be validated. There have been attempts to compare radiative transfer models with real data, but this requires a perfectly accurate (both optically and geometrically) model of the target.

Direct validations have been performed for simple (not vegetation) test pieces (Govaerts and Verstraete 1998) and shown to agree, although the limit to a Monte Carlo ray tracer's accuracy is most likely the forest model and so a test with perfect Lambertian cubes will not assess the radiative accuracy for forests. Attempts have been made to compare most radiative transfer models with data over real vegetation (Kimes and Kirchner 1982, Pinty *et al.* 1990, North 1996, Kuusk 1996, Ni *et al.* 1999, Qin and Gerstl 2000, Disney *et al.* 2006) but the complexity of forests means that the scene model can never be a perfect representation of reality and so it is not certain if any disagreements are caused by the radiative transfer or the scene models.

For this reason the modelling community decided that the only way to validate their models over vegetation was to compare them against each other. From an "informal cook off" in the late 1980s the RAdiation transfer Model Intercomparison (RAMI) exercise was formed (Pinty *et al.* 2001).

Instead of trying to compare radiative models against real data and have uncertainty in the scene model, RAMI sets out a group of vegetation models and illumination conditions so that the radiative transfer predicted by different models can be tested under near identical situations. It does this through comparison of absorption by the canopy, transmittance through the canopy and bidirectional reflectance. To date there have been three phases (RAMI I to III).

In the first phase (Pinty *et al.* 2001) scene models were either 1-D models (turbid media slabs or layers of evenly distributed leaves depending on the radiation model) or spheres of leaves with a range of canopy covers. This showed some worrying differences between certain models' predictions. RAMI II (Pinty *et al.* 2004) introduced more heterogeneity, with mixed crown shapes and sizes spread over different topographies and again some models showed worrying deviations. These results were taken on-board by modellers who acted to improve them (such as DART improving its multiple scattering (Gastellu-Etchegorry *et al.* 2004)) leading to much better agreement in RAMI III (Widlowski *et al.* 2007). There was one notable outlier in RAMI III, the radiosity method of (Qin and Gerstl 2000) but the authors were not sure if this was due to a bug in the model's code or something more serious.

In RAMI III the five Monte Carlo ray tracers tested showed "striking" agreement, so much so that it has been suggested that these should form a "surrogate truth" to benchmark all other radiative transfer models against. A similar conclusion was reached independently in computer graphics, where "naïve Monte Carlo ray tracers" (those that use no non-physical acceleration methods) are seen as the only way to test the physical realism of graphics programs (Ulbricht *et al.* 2006).

RAMI has also shown the varying computational requirements and limitations of the different models, the geometrically explicit ray tracers being many many times slower than all other methods whilst some methods requiring large matrices (such as the discrete ordinate method (Gastellu-

Etchegorry *et al.* 1996)) struggle with large, heterogeneous scenes within computer memory limits (Pinty *et al.* 2004). The next phase of RAMI is due for completion within the next year. This has extended the comparison to range resolved, lidar like, measurements. In the meantime a RAMI On-line Model Checker (ROMC) has been made available to for users to test their models against the surrogate truth (Widlowski *et al.* 2008).

It was originally intended to validate biophysical parameter inversion models within the RAMI exercises, but this has been taken up by the community (Pinty *et al.* 2001), possibly due to the far greater complexity. No mention of inverse models has been made in subsequent phases (Pinty *et al.* 2004, Widlowski *et al.* 2007).

Chapter 3: Measurement of forests

Chapter explained that in order to fully understand ecological processes, their impact on and response to global change, accurate biophysical parameters are needed on a global scale. Two of the most important parameters for such models are biomass and leaf area index (LAI). This chapter will outline methods for providing the biophysical parameters needed, making use of the mathematical relations given in the previous chapter.

3.1 Ground based methods

Whilst satellites are needed to provide regular global data and fully characterise surface heterogeneity, they do not make direct measurements of biophysical parameters. Normally some form of reflectance is measured from which vegetation parameters are inverted using the models described in the previous chapter. In order to have any confidence in these inverted values they must be compared to a known "truth" (or as close as possible); therefore ground based measurements are needed as validation. Care must be taken when using a measurement as truth because even direct, ground based measurements have limitations (Pinty *et al.* 2001).

3.1.1 Direct measurement

It is possible to directly measure the full structure of vegetation by ruler (or digital equivalent (Raab *et al.* 1979)) or by non contact methods (such as photogrammetry (Innes and Koch 1998)). This can give complete structural measurements such as leaf area, orientation and wood volume. Biomass is not directly measured and has to be converted from volume with an estimate of density. However this is very time consuming (and so expensive) and is not always practical in complex or tall canopies, where occlusions and difficulty in reaching all parts make the procedure very tedious, fraught with difficulty and unlikely to be accurate (Bréda 2003) (particularly with non-contact methods where occlusions will be a real issue).

The difficulties of tall and complex canopies can be partially overcome by cutting down the vegetation and chopping it up, known as destructive sampling. This allows tall plants to be measured, bit by bit, at ground level, giving access to all parts in dense canopies. This also allows

the various parts to be weighed, giving a direct biomass rather than a volume. To speed the process, rather than measuring the area of every leaf, only a few samples are measured and a relationship between surface area and mass derived. This allows the surface area of the rest to be estimated by weighing.

Destructive sampling can measure as accurately as the slightly more tedious direct digitisation but it is not sensible to use it over the large areas required to fully characterise heterogeneous scenes and does not allow the repeat readings needed to monitor seasonal change (Bréda 2003).

Such time consuming methods are impractical for routinely characterising foliage but have been used for small scale structure characterisation experiments. These experiments have not been for ecological models and so were discussed in section 2.3.

3.1.2 Allometric relationships

There are certain characteristics of trees that are easy to measure, such as diameter at breast height and total height and these (or combinations of them) can be indicative of other biophysical parameters. By relating biophysical parameters to easily measurable quantities with "allometric equations" the involved direct measurements described in the previous section can be upscaled to bigger sites. The most common quantity is *dbh*, that is the diameter of a trunk 1.3m above the ground, as it is very easy to measure. There are tables linking *dbh* to total biomass for many species and locations, for example (Ter-Mikaelian and Korzhukin 1997). The accuracy of biomass estimates can be improved by including extra factors such as tree height and even stem taper (the way the trunk narrows with height) (Hofton *et al.* 2002).

These hold better for simple trees such as white fir, where the majority of the biomass is held in a long straight trunk. For more complex trees, such as oaks with their twisting, bifurcating trunks and thick branches, the biomass is not as cleanly related to *dbh* and height.

Foresters and ecologists are often interested in stand scale statistics rather than individual tree properties. There have been many stand scale allometrics proposed such as Lorey's height (mean height weighted by basal area), top height (mean height of the hundred tallest trees in one hectare) and layer height (mean height within a vertical slice) (Jupp and Lovell 2007).

Due to their structural simplicity it is quite straightforward to characterise a tree trunk by direct

measurements of height, *dbh* and some estimate of taper (obviously this is easier for a nice straight conifer trunk than a twisty, gnarled oak) and allometric relationships have been well developed by foresters. Whilst attempts have been made to speed the process up with laser scanners (Jupp *et al.* 2009, Bienert *et al.* 2007). This method is conceptually little different from measuring it by hand and so for the rest of this review the focus will be on the more complex LAI measurements.

Attempts have been made to link LAI to easily measurable biophysical parameters such as *dbh* (Gower and Norman 1991) (reporting r^2 of over 0.9 against destructive sampling, for simple trees), though these have not been as widely used as for biomass, possibly due to the relative ease of other methods compared to the destructive sampling needed for calibration and the lower accuracy (Turner *et al.* 2000).

A method suggested by Grier and Waring (1974) (cited in Waring (1983)) is to relate the area of sapwood in a tree trunk to the amount of foliage. This is based on the earlier pipe model for describing branching diameters (Shinozaki *et al.* 1964), first proposed by da Vinci (Xu *et al.* 2007). The sapwood is the material that conducts water from the roots to the foliage, so should control how much foliage can be supported. This method has found popularity and seems to give better results than *dbh* based allometrics (Turner *et al.* 2000).

Another rapid way to estimate leaf area is to collect and measure dropped foliage, known as the leaf litter method (McShane *et al.* 1983) (cited in Jonckheere *et al.* (2004)). For deciduous trees it would be possible to collect all the leaves at senescence, allowing accurate leaf area to be determined but at other times of the year, and for evergreen species, the rate of litter fall is not directly related to total foliage but to environmental conditions and tree health (Bréda 2003) and so complex allometric relations are needed.

None of these methods of deriving LAI from allometric relationships give any information on the leaf angle distribution, so whilst they may be suitable for parametrising ecological models, other sources of data would be needed to estimate the canopy reflectance.

When creating allometric relations it is only possible to sample a finite number of trees with a finite range of biophysical parameters. These will not necessarily hold for trees outside of this range, for example using *dbh* allometrics on trees larger than the largest used to derive the relations

leads to dramatic overestimates of LAI (Thomas and Winner 2000a). Even the physically based sapwood method will not hold for all tree ages (Yoder *et al.* 1994). Care must be taken to use allometrics that cover the full range of observed biophysical parameters and never extrapolate beyond these bounds. Measuring older, larger trees are much more time consuming and expensive to thoroughly measure, which is why some studies generate allometrics from smaller trees.

Whilst these allometric relationships have found great popularity amongst the community they are all species and site specific (Gower *et al.* 1999, Jupp and Lovell 2007). This is not an issue for foresters, who are primarily interested in a limited number of species on the land that they own, but will be very difficult to implement for the whole world, particularly complex tropical forests. Therefore their applicability to the large scale measurement of LAI is questionable.

3.1.3 Point quadrats

Directly measuring leaf area is very time consuming, whichever method is used. Levy and Madden (1933) (cited in (Wilson 1959)) proposed measuring leaf area by sampling contact frequency. A thin needle, known as a point quadrat, is inserted into a canopy and the number of contacts with vegetation recorded. The number of contacts gives the fraction of projected leaf area in the sample site, and so LAI. The early attempts only inserted needles vertically and so ignored the effect of LAD. If the canopy were anything but planophile the method would underestimate LAI. Other authors suggested inserting the needles at other angles (Tinney *et al.* 1937). These reported improved accuracy, probably due to increased path length and so sampling (Wilson 1959), but still at only a single angle and so the estimate of LAI would depend upon LAD. This "hinge point" has become a useful tool for decoupling LAI from LAD (Jupp *et al.* 2009).

In order to measure true LAI, independent of LAD, (Wilson 1959) suggested using vertical and horizontal needles, which would give vertically and horizontally projected LAI, similar to the model of (Suits 1972) (explained in section 2.1.1). As shown by (Verhoef 1984) such an LAD will not capture many real situations, particularly leaves oriented at 45^o. In a further refinement it was proposed to incline the needle at an angle (Wilson 1960), although still only a single angle. By solving analytically for constant angle LADs it was determined that at a zenith angle of 57.5^o the impact of the LAD on measured LAI would be at a minimum (less than 5%).

With this method contacts must be measured manually, an extremely time consuming and tedious process, even for the simple grass and crop canopies it was designed for (many thousands are needed to accurately characterise LAI (Jonckheere *et al.* 2004). It is obviously impractical to stick a needle though a forest canopy and count contacts (MacArthur and Horn 1969) (or indeed any canopy over 1m tall (Wilson 1959)) and so the method has not been used routinely in forests. One attempt was made in order to assess the accuracy of LAI estimates by allometric relationships, using a wire suspended from a crane and binoculars (Thomas and Winner 2000a). As the method makes no assumptions about canopy structure it will give completely accurate LAI. This study concluded that allometric relationships were overestimating LAI of larger trees.

A non-contact version was suggested, using a telephoto lens with a very shallow depth of focus and a calibration between focal length and range (MacArthur and Horn 1969). The range to an object can be be found by focusing it and reading the focal length. A grid is etched into the lens and the number of leaf contacts at each height is recorded (or fraction of sky if individual leaves cannot be resolved). From these contact frequencies the LAI can be calculated with height. Unlike the point quadrat method, a contact obscures further potential contacts, so that the true LAI cannot be directly calculated (Weiss *et al.* 2004). Instead the differential equations of (Kubelka and Munk 1931) are solved to get true LAI (explained in section 2.1, equivalent to equation 14 in section 2.1.4). Whilst this method is slightly more practical for tall canopies it is no less tedious and so has not found popularity.

3.1.4 Optical transmission

The methods described above will give accurate biophysical parameters and for simple parameters such as biomass are sufficient, but for LAI and other foliage characteristics they are prohibitively time consuming, particularly for forests. Much more rapid methods are needed if foliage properties are to be collected over large areas at an acceptable cost (Gower and Norman 1991).

Rather than manually inserting a probe through a canopy, the sun's light can be used as a probe, relating the transmission of light through the canopy to the gap fraction (and so canopy properties through equation 14). A number of different instruments and techniques have been developed to measure gap fraction from transmission, the simplest of which is a camera fitted with

a hemispherical or "fisheye" lens ((Bonhomme and Chartier 1972) cited in (Dufrêne and Bréda 1995)).

A hemispherical camera has a field of view of 180^o, so that a photograph taken vertically upwards will stretch from horizon to horizon. The pixels containing sky should be lighter than those containing plant elements so that all pixels with a brightness above a certain threshold can be classified as sky and the rest as plant canopy. The proportion of sky pixels is the gap fraction, allowing inversion of LAI through equation 1. Care must be taken to ensure that dark sky pixels (due to uneven sky conditions) are not mistaken for canopy and bright canopy elements (due to sun flecks) are not mistaken for sky. For this reason it is recommended that the method is only used when the sky is uniform and the sun is out of the field of view (whether obscured by cloud or beneath the horizon) (Jonckheere *et al.* 2004). Note that the element reflectances do not appear in equation 1 so that no knowledge of them is needed for accurate inversion (Doughty and Goulden 2008).

The choice of threshold for classification is vital, small variations can cause large differences in predicted gap fraction. Some investigators allow a human operator to manually set a threshold, based upon their interpretation of the image. This has the benefit of using a human's knowledge of what is sky and canopy but can be biased by an individual's choice (Jonckheere *et al.* 2004). Some studies have attempted to remove any manual bias by having a number of users process the same images and taking an average. A more objective method is to use an algorithm to automatically set a threshold. There have been a number of algorithms proposed ranging from simple brightness histogram analysis to complex spatial methods (Jonckheere *et al.* 2005). All have their own strengths and weaknesses, none performing flawlessly, particularly in the presence of the brightness variations described above, but it is possible to get a reasonable estimate of gap fraction without relying on an individual's interpretation.

Early wet film hemispherical cameras were very expensive and tedious to process which limited their application (Dufrêne and Bréda 1995). The method had a surge in popularity once high quality consumer digital cameras became available at affordable prices; around the turn of the century (Bréda 2003). Some doubts were raised over the accuracy of results from such low cost instruments

(Frazer *et al.* 2001), particularly their ability to properly focus all wavelengths. Failure to focus spreads the influence of canopy elements across many pixels, reducing the brightness contrast with the sky and potentially affecting gap fraction estimates. The effects of chromatic aberration can be lessened by using a single wavelength that suffers less from aberration (most cameras recording red green and blue light, red being the least abhorrent). Digital cameras offer much larger dynamic ranges than wet film, helping to separate the dark sky and bright canopy (Jonckheere *et al.* 2005). These days investigators have no worries about using digital hemispherical cameras.

There are many software packages available for processing hemispherical photographs (comprehensive lists are given in Jonckheere *et al.* (2004) and Jonckheere *et al.* (2005)). They all perform the same basic operations and so they will not be explained in any detail.

Rather than measuring the fraction of gaps and canopy, with all the potential for errors during processing described above, the fraction of sunlight transmitted through the canopy will also give an idea of the gap fraction. The canopy's transmission can be measured by comparing the brightness recorded by radiometers positioned above and below the canopy. One of the most popular instruments to use this technique is Licor's LAI-2000 (LI-COR 1992). This measures the light with wavelengths between 320nm and 490nm (where absorption by vegetation and atmospheric scattering are at a maximum, giving dark canopy and bright sky) within 70^o of the vertical. The zenith range of 70^o to 90^o is left out to avoid obstructions such as the ground and operator, particularly for the above canopy instrument where an unobstructed view of the sky is essential. Other instruments are available for making these measurements, such as the Sunscan ceptometer, but these are primarily for crops and thought of as unsuitable for forests (Dufrêne and Bréda 1995).

The gap fraction does not depend on LAI alone (as explained is section 2.1) and so so additional structural parameters must be accounted for to get accurate LAI.

Leaf angle distribution The angular distribution of scattering elements will alter the surface area projected in a given direction, as introduced in section 2.1.1. Beer-Lambert's law is modified to the form given in equation 11. Both hemispherical cameras and the LAI-2000 make measurements of gap fraction across a range of zenith angles (the LAI-2000's detector is split into five annuli), so if the LAD and LAI are assumed to be constant throughout the canopy it is possible to solve

equation 11 at a range of zeniths with an assumption of one of the LAD models (in section 2.1.1) (Baret *et al.* 1993). The models are needed to help constrain the data as high angular resolution across the full range of orientations is rarely available (Lang *et al.* 1985).

The assumption of uniform LAD throughout the canopy is not shared by all (Wilson 1959) and so the accuracy of these methods is not assured. However the assumption is necessary to estimate LAD from a single transmission measurement.

Clumping The non-randomness of canopies, explained in section 2.1.3, causes the relationship between gap fraction and LAI to deviate from a Poisson distribution. Some report that it is the largest source of error in LAI from transmission (Jonckheere *et al.* 2004). Clumping factors to account for this non-randomness have been introduced (equations 12 and 13). Some authors believe this to be an insignificant effect (Lang and Xiang 1986), stating that Beer-Lambert's law alone gave accurate LAIs when compared against those derived from allometric relations to *dbh*. This view seems to have fallen out of fashion, with many authors reporting underestimates of LAI without clumping correction (Bréda 2003, Chen *et al.* 1997, Gower and Norman 1991, Law *et al.* 2001) (the study of Lang and Xiang (1986) may have been an instance of two wrong assumptions arriving at the right answer, the clumping perhaps being subsumes into the angular distribution).

Larger scale clumping Whilst many canopies are distinctly non-random, it is possible to get a measure of this non-randomness and so correct for it. Typically when calculating gap fraction a large area is used (either the whole image or an annulus at constant zenith). The canopy is unlikely to be random over this whole area, so rather than calculating the fraction of gaps across the whole area, the gap fraction can be calculated in sections (Lang and Xiang 1986). The LAI can then be inverted by taking natural logarithms of Beer-Lambert's law (equation 11) of each segment and the average LAI determined. This does not assume that the elements are randomly distributed throughout the whole canopy, only within each segment. The ratio of the LAI determined this way to that found by assuming completely random distribution gives the clumping factor and is known as the "log average" method (Chen and Cihlar 1995).

$$LAI_{rand} = \frac{\ln(\frac{1}{P_{total}})}{G(\theta)} \tag{15}$$

$$LAI_{clumped} = \frac{1}{n_{seg}} \sum_{i}^{n_{seg}} \frac{\ln(\frac{1}{P_i})}{G(\theta)} \tag{16}$$

$$\Omega_e = \frac{LAI_{rand}}{LAI_{clumped}} \tag{17}$$

Where P_{total} is the gap fraction for the whole scene, P_i is the gap fraction for the i^{th} segment for a scene with n_{seg} segments and $G(\theta)$ is the LAD.

The clumping factor, Ω_e, can then be used to correct for clumping using equation 12 from any gap fraction measurement. There are a number of instruments used to calculate this factor, the most simple of which is a hemispherical camera. Annuli of constant zenith are further divided into segments and the above equations solved (van Gardingen *et al.* 1999), this has the same issues as standard hemispherical photography, requiring uniform sky without direct sunlight. Another method is to use direct sun beams as point quadrats. A radiometer can be used to measure the size and number of gaps by recording the instances of direct sunlight along a transect. This was the instrument the log average method was initially developed for (Lang and Xiang 1986) and version are available commercially (such as DEMON (Lang *et al.* 1985, Sommer and Lang 1994)). Vast improvements in LAI accuracy are reported using this method (Fassnacht *et al.* 1994).

These sunbeam transmission methods can be used to measure LAD but as they rely on direct sunlight measurements have to be taken across half a day in cloud free conditions to measure the full range of zeniths. For this reason it is recommended to use them in conjunction with more rapid angular detectors such a the LAI-2000 or hemispherical cameras (Bréda 2003), despite the reported superiority of the DEMON over the LAI-2000 (Dufrêne and Bréda 1995, Sommer and Lang 1994) (no one wants to sit at a single plot for six hours).

The choice of segment size (or sample length) is vital (van Gardingen *et al.* 1999). Segments should not be left empty, as the logarithm of zero is undefined, also Poisson's law is strictly only true for an infinite (or very large) number of scattering elements and so the segment needs to be large enough for that to be appropriate. Through comparison of transmission results to direct

measurements a sample size of ten times the leaf (or shoot for conifers) size is suggested (Lang and Xiang 1986), although it is not practical to make segments large enough to be statistically certain of none zero contact frequencies in all (Lang and Xiang 1986). Studies suggest that the clumping factor (and so predicted LAI) determined from hemispherical photographs can vary dramatically as segment size is decreased, eventually reaching a plateau at around 100 to 200 segments depending on homogeneity (van Gardingen *et al.* 1999). Therefore segments should not be left too large either. It has been suggested that multiple scales of clumping and so segmentation would improve results (van Gardingen *et al.* 1999) although this does not seem to have been tested yet.

The LAI-2000 does not measure any spatial information and so cannot estimate the clumping factor in the same was as hemispherical photographs. One option is to restrict the azimuthal field of view (to 45^o or less) and use a set of measurements at different locations in the plot, forming up the segments of a hemispherical photographs over multiple measurements.

An alternative method to determine the clumping parameter is to look at the distribution of gap sizes. Miller and Norman (1971) (cited in Chen (1996)) proposed a function relating the total area of gaps at a given size to the apparent LAI, ($L = \frac{LAI.G(\theta)}{\cos(\theta)}$), gap size λ, and a characteristic scatterer dimension, W, (average leaf or shoot width) for a completely random canopy.

$$F(\lambda) = (1 + L_p \frac{\lambda}{W}) e^{-L_p(1+\frac{\lambda}{W})} \tag{18}$$

Gap sizes can be measured by walking along a transect with a radiometer, comparing the instances of direct and indirect sunlight by the variations in the ratios of directional and hemispherical intensity (Chen 1996). These measured gap sizes (which will be lengths along the transect rather than areas) can be plotted against the total area at each size to give a version of the function in equation 18. Miller's idealised case can be plotted alongside; if the two are identical then scattering elements are randomly arranged. If the canopy is not completely random there will be more gaps with larger sizes than for the random case. According to (Chen 1996) the point at which the two distributions starts to deviate is related to clumping by the following equation.

$$\Omega_e = (1 + \Delta g) \frac{\ln(F_m)}{\ln(F_{mr})} \tag{19}$$

Where Δg is the total fraction, F_m is the measured total gap fraction and F_{mr} is the gap fraction after removing all gaps that deviate from the random case (the large gaps). As L and Ω_e are unknown in equation 18 it must be solved iteratively. This method requires an accurate representation of the gap size distribution so the transect needs to be long enough to ensure this. Success with this method has been reported (Chen 1996, Leblanc *et al.* 2002).

Like DEMON, TRAC (Tracing Radiation and Architecture of Canopies) can be used to measure the angular distribution, but would need to measure over half the daylight hours to sample enough angles.

Shoot scale clumping Individual needles cannot be resolved in transmission measurements due to their size and penumbral effects, therefore the methods described above cannot be used to create a shoot scale clumping factor (Chen and Cihlar 1996). A separate clumping factor (γ_e in equation 13, also known as $\overline{STAR}$) is needed, measured externally to the transmission method. This can easily be found by measuring the shoot's projected area, by photographing it over a background of known area (such as a piece of paper) and thresholding (giving A_{shoot}), then pulling off all the needles, laying them flat and measuring their projected area (giving $A_{needles}$) (Gower and Norman 1991). The clumping factor is then the ratio of these two areas. The projected area should be measured for all angles and averaged (Stenberg 1996) for the reasons given in section 2.1.3.

$$\gamma_e = \overline{STAR} = \frac{\overline{A_{shoot}}}{A_{needles}} \tag{20}$$

Wood The measurements above will give the area of canopy elements, corrected for clumping and angular distribution. This will include both leaf and wood and so is actually PAI rather than LAI. It is possible to convert between these two area indices with a woody correction factor α, as shown in equation 14 in section 2.1.4.

There is disagreement as to how important the woody correction factor is, some claim it to be a negligible fraction of PAI (Gower and Norman 1991) whilst others say it is significant (Deblonde *et al.* (1994) cited in Kucharik *et al.* (1998b)). This obviously depends strongly on species.

Destructive sampling can be used to determine the true wood area (Chen 1996), this can be

compared to the true LAI to get an allometric relationship between *dbh* and α. Others have suggested that LAI is the difference between the plant area index (PAI) and the wood area index (WAI) (Fassnacht *et al.* 1994). This is much easier to collect than destructive sampling, the WAI being found from the gap fraction in leaf-off conditions (eg. winter for deciduous trees). LAI is not necessarily the difference of these as wood and foliage are not randomly arranged with respect to each other; leaves are always clustered around branches and so tend to hide them. A simple difference will underestimate LAI (Dufrêne and Bréda 1995) and in addition, for evergreen species it requires all leaves to be stripped (Omasa *et al.* 2007).

An alternative to the wood area index is the bole area index (BAI), that is the projected area of tree trunks visible in a measurement per unit ground area (Barclay *et al.* 2000). It is reported that the bole area is far more significant than branch area for the woody correction, at least for coniferous species. The BAI can be calculated from a map of tree locations relative to the measurement, *dbh* and height to live crown. Collecting these data is quite time consuming though nowhere near as laborious as destructive sampling, however it only gives the projected area of trunks, not the woody correction factor. It is not clear how to convert one from the other (Barclay *et al.* 2000), for this reason the method has not gained popularity.

To take account of the tendency of leaves to clump around branches these methods require allometrics to convert between the wood (or bole) area index and the woody correction factor which will again be site and species specific. A method of directly measuring the fraction of leaf and bark area was proposed by (Kucharik *et al.* 1998b). They created the Multiband Vegetation Imager (MVI) to take an image at 400nm to 620nm (visible) and another at 720nm to 950nm (NIR) with high dynamic range (16bit) vertically with a field of view of 20^o. The high reflectance of vegetation in the NIR and low in the visible should allow the classification of leaf, bark and sky returns, thereby giving the actual LAI and WAI with no need for any additional woody correction. The instrument struggles with variable lighting conditions with brightly lit bark being mistaken as leaf and heavily shaded leaf as bark. The same issues prevent the classification of colour hemispherical photographs. A subsequent study suggested that despite the small range of zenith angles sampled it would be possible to measure LAD by looking at the proportion of

directly sunlit leaves (Kucharik *et al.* 1998a). This is a complex process and requires comparison with Monte-Carlo ray tracing results of explicit canopy models (clouds of disks contained within ellipsoids), greatly limiting its practicality (Gower *et al.* 1999).

3.1.5 Transmission conclusion

With these various correction factors Beer-Lambert's law gives accurate LAI estimates when compared to more direct methods (Eriksson *et al.* 2005). The estimation of wood appears to be the only measure that cannot easily be obtained; heterogeneous illumination conditions preventing reliable spectral classification and non-randomness preventing simple wood and plant area difference. Fortunately the wood fraction appears to be a small source of error compared to canopy scale clumping, which is well accounted for by log averaging.

These methods rely on gap fraction and it has been shown that this saturates at LAIs of 3 to 4 (Jupp and Lovell 2007), therefore transmission methods cannot reliably extract LAIs above this. In these cases, the time consuming destructive and point quadrat methods appear to be the only reliable option.

3.2 Remote sensing

Ground based methods can provide accurate measurements of biophysical parameters, however they require people to visit sites. This is a slow process, even for transmission measurements and so can only be done over a small proportion of the Earth's land surface. The results must be "upscaled" from a limited set of plots to whole landscapes, a process which requires an assumption of homogeneity. This would not be an appropriate assumption for vegetation (Hurtt *et al.* 2004). Remote sensing from satellites and aircraft is capable of making global measurements and, very importantly, regularly throughout the year. This allows explicit measurement of surface heterogeneity (Omasa *et al.* 2003) and provides the temporal resolution vital for monitoring dynamic processes. Without temporal measurements it must be assumed that a system is in equilibrium, greatly limiting the realism (Hurtt *et al.* 2004).

A frequent problem with using ground based data for studying global effects is a lack of consistency in methodology and even definitions (is a land type forest or Savannah?) (Defries *et al.*

2000). Global satellite measurements will all be made by exactly the same instrument with the same assumptions and so give much more consistent, controlled results. Measurements from aircraft are generally not global due to the enormous expense of flying an instrument around the world and so the emphasis of the thesis will be on satellites. The same principles are true for airborne sensors but with less atmospheric attenuation.

There has been a huge effort to provide remote sensing satellites, from Landsat the first true earth observation (EO) satellite in 1972 through to NASA's EOS drive at the end of the 20^{th} century (Knyazikhin *et al.* 1998) and ESA's current Earth explorer missions (ESA 2010). These provide a variety of different measurements at different scales specifically tailored to the study of natural processes.

3.3 Passive optical

The first and most common remote sensing instruments make passive optical measurements. They use radiometers measuring a variety of wavelengths (typically between 400nm and 2μm with some thermal channels around 8μm), with some spatial resolution (from 50cm up to 8km) and occasionally have angular resolution. Liang (2004) classed these sensors as "multi-spectral" or "hyperspectral". Multi-spectral instruments typically measure three to seven bands with band widths of around 20nm whilst hyperspectral instruments can measure hundreds of bands with widths down to a few nanometres. This review will focus on some common satellites, mainly NASA's Moderate Resolution Imaging Spectrometer (MODIS) (Barnes *et al.* 1998) and MultI-angle SpectroRadiometer (MISR) (Diner *et al.* 1998).

MODIS was built to acquire fine spectral and temporal resolution data at the expense of spatial resolution. This makes it an ideal instrument to monitor dynamic systems such as vegetation. It has a spatial resolution of between 250m and 1km depending on the wavelength, with a 3,000km swath allowing it to cover the whole Earth's surface in a day and a half. There are two MODIS instruments, one on board the Terra satellite and the other on board Aqua so that every spot on the Earth's surface is overflown by a MODIS instrument at least once a day. It records seven spectral bands from the visible to infrared (see figure 8).

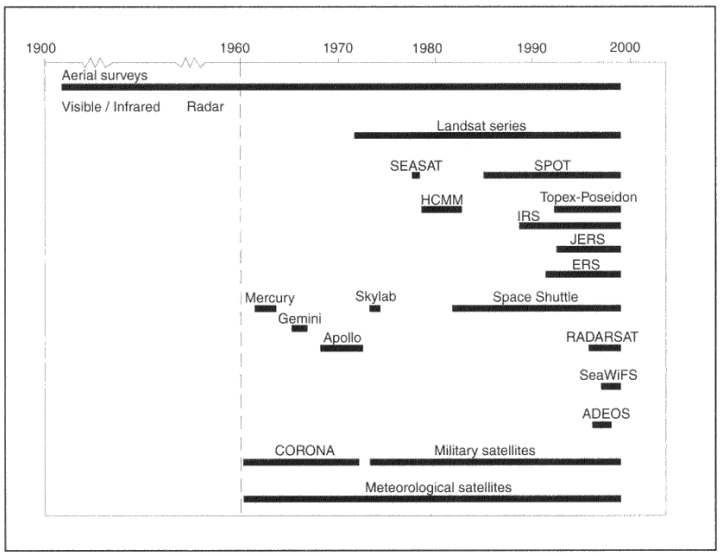

Figure 7: A time line of popular satellites, from Liang (2004)

MISR was built specifically to make multi-angular measurements. It has between 250m and 1.1km spatial resolution (again wavelength dependent) and a swath width of 360km with a repeat time of nine days. It records in four bands (three visible, one infrared) and over nine view angles between $+70.5^o$ and -70.5^o zenith allowing multi-angular measurement. There is only one spaceborne MISR, also on board the Terra satellite, NASA's EOS flagship.

Both of these instruments are quite coarse spatial resolution. There are much higher available (Landsat at 30m down to GeoEye at 50cm) but for monitoring vegetation higher resolution offers little advantage. Forests become very heterogeneous at these scales and are too irregular to be easily processed and interpreted. The stand scale measurements of MISR and MODIS are seen as suitable for most ecological needs, although they struggle for areas where the land cover changes within 1km (such as most of Britain).

Hyperspectral measurements tend to only be an advantage when looking for subtle biochemical effects. The addition of more wavebands adds information for inversion, but there is a lot of redundancy in the data, so most users believe multi-spectral sensors are the most suitable for making structural measurements of vegetation. Of course hyperspectral wavebands can be aggregated to the same spectral resolution as multi-spectral sensors, but for the rest of this review only multi-spectral techniques (typically two to seven bands) will be discussed (Liang 2004).

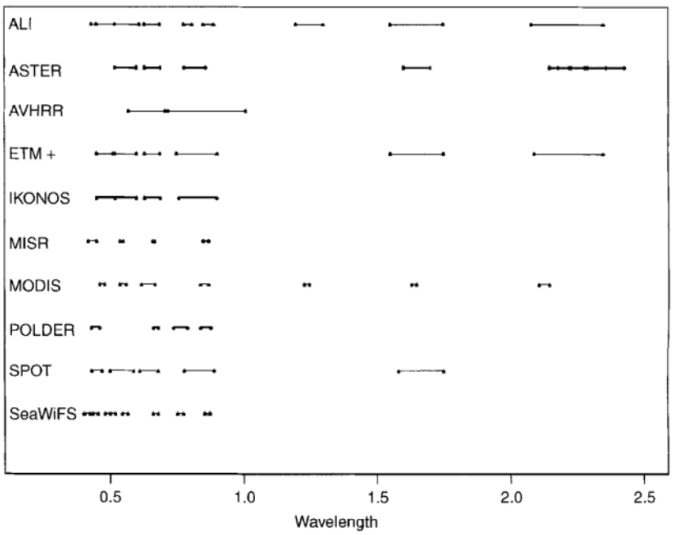

Figure 8: Wavebands of some popular remote sensing instruments, from Liang (2004)

Satellite radiometers do not directly measure any biophysical properties but radiative flux in a certain waveband from a given direction. This must be inverted to get to the biophysical parameters that caused this signal. Vegetation has a unique spectra (an example is shown in figure 6). The most striking feature is the sharp rise from low reflectance in the visible (from 400nm to 650nm) to high reflectance in the near infra-red (NIR, from 750nm to around 1,200nm). This feature is unique to vegetation and so looking at the ratio of radiative flux in NIR to that in the visible should allow satellites to distinguish it from bare earth. There have been a number of these ratios, or "vegetation indices" proposed, one of the most common being the Normalised Difference Vegetation Index or NDVI (Justice 1986).

$$NDVI = \frac{\rho_{NIR} - \rho_{red}}{\rho_{NIR} + \rho_{red}} \tag{21}$$

Where ρ_{NIR} is near infra-red reflectance and ρ_{red} is red reflectance. Red reflectance from vegetation is very low (typically around 10%), as is atmospheric transmission (due to increased Rayleigh scattering at shorter wavelengths), so a straight ratio of these bands would be very sensitive to noise. In addition changing illumination, such as those caused by topographic effects, will affect the ratio of bands. The NDVI was created to reduce this sensitivity to noise and illumination conditions.

This can be empirically related to biophysical parameters by matching remote sensing data to ground based measurements (Huete *et al.* 2002). This approach makes no attempt to account for the physical processes involved (described in chapter 1.3) and so can lead to inaccurate results. In particular for any canopy with less than complete cover the soil will contribute to the signal. Vegetation is much more reflective in the NIR than the visible, so far more NIR light will reach the ground through multiple scattering than visible. This adds a non-linear dependence on canopy cover to the soil contribution to NDVI, preventing simple a ratio correction. NIR light also has much higher atmospheric transmission than visible so that variations in atmospheric conditions will affect ρ_{red} more than ρ_{NIR} and so change the NDVI.

To account for the soil and atmosphere's effect on predicted LAI, more tolerant indices were proposed such as the Enhanced Vegetation Index (EVI, previously known as SARVI2). This was developed from the earlier soil resistant index of Huete (1988) and the atmospherically resistant index of Kaufman and Tanré (1992).

$$EVI = G\frac{\rho_{NIR} - \rho_{red}}{\rho_{NIR} + C_1.\rho_{red} - C_2.\rho_{blue} + L} \tag{22}$$

Where G is a gain factor, ρ_{blue} is the blue reflectance, L is the canopy cover and C_1 and C_2 are coefficients of the aerosol resistance term (Huete *et al.* 2002). These variables have fixed values based upon how the data has been pre-processed (Huete *et al.* 1997).

Studies have reports that EVI is more robust to saturation than NDVI, displaying none in the test sites used (Huete *et al.* 1997), but the LAIs of these sites were not given so it is unclear whether EVI will suffer from saturation at higher densities. All vegetation indices require the red and near-infra red reflectance to be sensitive to changing LAI. Canopies can become so dense that nearly all light interacts with foliage, so increasing LAI will not affect reflectance (Gobron *et al.* 1997). They showed that for a horizontally homogeneous canopy (a SAIL type model (Verhoef 1984)) the signal's variation with LAI will drop below measurement accuracy by an LAI of 3 to 4. Figure 9 shows the saturation of NDVI. A real canopy will include some levels of clumping, increasing the gap fraction for a given density and so the LAI at which the ground stops contributing to the signal. But these changes in LAI may not be detectable by vegetation indices. LAI derived from EVI has

been declared to be operational (Gao *et al.* 2000, Huete *et al.* 2002) and has been embraced by the modelling community.

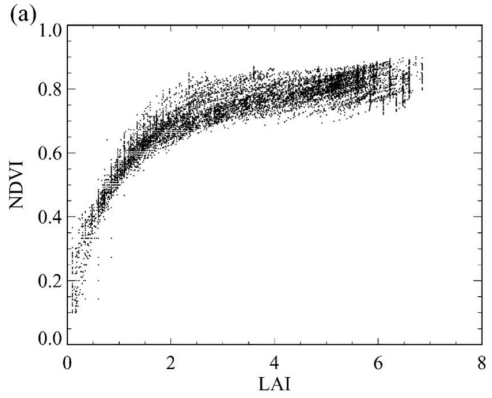

Figure 9: LAI against NDVI, clearly showing saturation, taken from Myneni et al. (2002)

The literature provides overwhelming evidence for the saturation of vegetation indices at LAIs of between 3 and 4 (Gobron *et al.* 1997, Myneni *et al.* 2002, Lefsky *et al.* 2002, Boudreau *et al.* 2008) whilst ground based studies have shown that LAIs over 6 are not uncommon (Thomas and Winner 2000a) and existing global products derived from vegetation indices acknowledge that they cannot determine forest properties above a certain canopy cover (80% in the case of Defries *et al.* (2000)). The link between vegetation indices and LAI is not clear (Gao *et al.* 2000) with many other forest properties affecting indices, such as leaf angle distribution and clumping (Huete *et al.* 1997, Gao *et al.* 2000, Huete *et al.* 2002) and so care should be taken when using them. Better inversion accuracy should be achieved by taking contributing factors into account in a more physically based way.

In chapter 1.3 methods for relating radiometric signals to vegetation properties were introduced. These can be used to perform a more physically based inversion, where attempts are made to take all properties into account. It was not until the end of the 1990s that the theory and computer resources had developed sufficiently to allow inversion of these canopy models (Myneni *et al.* 1995). All radiative transfer models capable of capturing canopy structure are non-linear (Liang 2004) and so analytic solutions are not possible, they must instead be inverted by iterative numerical regression (such as Powell's method (Press *et al.* 1994)). These methods will not be described in detail in this thesis; comprehensive discussions are available in Press *et al.* (1994) and Liang

(2004) for the interested reader.

Vegetation canopies are complex and the models can include many parameters, so a range of data are needed to constrain the results. The more complex the model the greater the amount of data needed. For this reason fully explicit geometric forest models are not used for inversion, the principle of Occam's razor should be applied (Widlowski *et al.* 2005); an inversion should not be attempted with a model with more unknown parameters than available measurements.

Certain parameters cannot be reliably constrained by passive optical remote sensing data, such as element (leaf and bark) optical properties and so these must generally be supplied by ground based measurements (Myneni *et al.* 2002). For the simplest models the element reflectances and remote sensing data may be sufficient for inversion (such as SAIL (Verhoef 1984)). For more explicit models, such as GORT (Ni *et al.* 1999) and DART (Gastellu-Etchegorry *et al.* 1996) other parameters, such as LAI, tree density and crown size, couple together so that only a product can be extracted. To get to parameters of interest (say LAI) values of the other variables must be fixed, or else their ratios fixed. Sources of data other than passive remote sensing have to be used to set these parameters. Most attempts have used a limited number of land cover classes (eg. grassland, crops, broad leaf forest or needle leaf forest) to select a set of suitable parameters (Knyazikhin *et al.* 1998) or else intensive site specific measurements.

This approach has been declared operational using both MODIS and MISR data (Myneni *et al.* 2002, Hu *et al.* 2003) using the same generic 3D radiative transfer approach for both and using six different land cover classes to parametrise the model (Knyazikhin *et al.* 1998). This is a global product and so the structural parameters used in the model have been chosen to try to be applicable to all the Earth's surface of that class. This will obviously not be entirely true due to heterogeneity and even changes with time (leaf reflectance changes with age (Doughty and Goulden 2008)) but is currently the best global estimate available.

Even one of the most complex models has been successfully inverted (DART, (Kimes *et al.* 2002)) although this required heavy pre-parametrisation with an intensive ground based campaign at a small site. This pre-parametrisation allows inversion from reduced sets of data, for example purely nadir measurements.

Even though models allow inversion from single view data, multi-angular data greatly improves accuracy, delaying saturation and should be used when available (Kimes *et al.* 2002, Zhang *et al.* 2000). It has been suggested that model inversion is still possible with MISR data if the underlying land classification is incorrect, albeit with a lower accuracy (Hu *et al.* 2003). This highlights the importance of multi-angular data and the benefit of redundancy in driving data.

Iterative numeric solutions are computationally expensive and would be unsuitable for processing regular (monthly) global data. To speed inversions a look up table (LUT) of expected reflectance angular and spectral signals can be created for a range of vegetation properties (Myneni *et al.* 2002). Measured signals can be compared to the LUT to find the most likely set of vegetation properties far quicker than an iterative numerical solution. The complexity of models means that even with pre-parametrisation, radiance measurements can be non-unique, particularly the coupling of LAI and crown scale clumping (Knyazikhin *et al.* 1998). In these cases it would be difficult to decide what set of structural parameters are the truth. For the MODIS/MISR product it has been suggested to use an extra set of weighting factors to further constrain the results.

These methods will not always succeed in finding an answer and so the MODIS/MISR inversion uses a back up empirical NDVI to LAI relationship (Myneni *et al.* 2002). This will suffer saturation at an LAI of 3-4 as already stated. Even if an inversion is successfully performed the models still rely on changes in LAI altering the measured signal and so will saturate (Gobron *et al.* 1997). The MODIS LAI product states a value of 7 as the highest it can reliably extract (Myneni *et al.* 2002) and higher values will be truncated to this.

Biomass So far this section has concentrated on LAI, which is the biophysical parameter most directly linked to optical reflectance, and even then inversion is non-trivial. Other parameters, such as biomass and tree height, are even less connected to measurements, being relating only tangentially if at all (Dubayah and Drake 2000) and so successful estimation of these parameters is far less reliable. Attempts have been made to track changes in biomass by using estimates of LAI and amounts of photosynthetically active radiation in forest growth models (Saatchi *et al.* 2007), but the initial amount of biomass cannot be retrieved.

Attempts have been made to extract tree structure from photogrammetry. Bacher and Mayer

(2000) showed that it is possible to extract 2D vertical cross sections of structure from shadows cast by leaf off trees onto flat surfaces using only aerial photographs and knowledge of the sun angle. This method is obviously unsuitable for use in forests and would not work in the presence of leaves. Stereo photogrammetry is widely used for calculating surface elevation but over forests only the top of the canopy can be reliably measured. The chance of enough recognisable objects being visible on the ground from two view directions is low (Tanaka *et al.* 1998) and so an alternative topographic model would be needed. There is currently no global ground height map that performs reliably over forests (Dowman 2004) and so tree height cannot be determined with any accuracy.

3.3.1 Passive optical conclusions

Passive optical instruments can provide regular global coverage, particularly the wide swath sensors such as MODIS. This makes them ideal for producing regular global estimates for use in ecological models. However some biophysical parameters cannot be measured, such as biomass (except through tenuous allometrics), and others saturate, such as LAI at 3-4 if vegetation indices are used or 6-7 if modelling is employed. The literature shows that LAI certainly reaches 9 (Thomas and Winner 2000a) and some authors report values as high as 22 (Waring *et al.* 1978) cited in (Marshall and Waring 1986), although this may be an artifact from using allometric relationships on trees beyond the development batch's bounds (described in section 3.1.2). Therefore passive optical instruments cannot capture the full range of the Earth's vegetation and reliance on this data will introduce bias.

Even the most detailed models rely upon some form of abstraction as that is the only way to allow inversion (Knyazikhin *et al.* 1998). Therefore any inverted parameters are likely to be effective parameters and may not directly relate to reality (Widlowski *et al.* 2005). Another danger is that many validation campaigns use ground based optical transmission techniques to provide "truths" in order to acquire data over enough plots in a sensible timescale (Myneni *et al.* 2002). These instruments also require models to invert biophysical parameters and so estimates will also be effective. Thus the data used to validate remote sensing estimates may use the same assumptions and so be inaccurate for the same reasons (Eriksson *et al.* 2005). The two datasets might appear to agree whilst not matching reality, obscuring physical effects such as saturation.

Of the methods described so far only destructive sampling and point quadrats can provide actual truths, but these are too time consuming to be used on anything but limited special experiments (Thomas and Winner 2000a). An alternative, rapid, non-saturating method is needed to give confidence in global data.

3.4 Radar

Radar is an active form of remote sensing. Active systems provide their own energy source rather than relying on the sun, giving them much greater control over illumination than possible with passive instruments. This greatly simplifies some model inversions and, uniquely, allows range resolved measurements. For these, a very short burst of radiation is emitted and the time taken for reflected energy to return recorded. With knowledge of the speed of electro-magnetic radiation this time can be converted into a range.

3.4.1 Synthetic aperture

Radars operate in the microwave domain, between 1cm and 1m, far longer than optical instruments. Due to the relationship between the diffraction limit of resolution (the smallest angular separation that can be resolved before diffraction causes objects to merge) and wavelength, much larger apertures are required to get usable ground resolutions from space (Tipler 1999, page 1128). Rather than use long antennae (which may flex, causing artifacts (Brooks 2008)), returns are collected as the satellite moves through its orbit, giving the effect of a larger aperture and so increasing resolution. This process is known as synthetic aperture radar (SAR) and was first developed as part of project "wolverine" during the 1950s, on behalf of the American military (Cutrona *et al.* 1961).

Whilst the long wavelength means that the illumination beam cannot be focused by reasonable sized antennae, various properties can be used to split the returns up into sections, using the synthetic aperture to create an "imaging radar".

All electromagnetic (EM) radiation incident on a surface with a component of motion normal to the beam's direction will suffer from a Doppler shift (Tipler 1999, page 463). In addition, for a moving radar platform (such as a satellite or aircraft) the reflected frequency will be higher

for surfaces coming towards the detector and lower for those moving away, much like the pitch change of a passing siren. As the beam has a finite width, the surfaces within different parts of the footprint will be travelling at different velocities and so result in Doppler shifts of different sizes. For a radar beam at an angle to the ground, the range to a return is related to the distance along the ground of its origin.

Therefore if a radar beam is pointed to the side so that no part of the beam crosses the platform's velocity vector it is possible to slice the footprint up along the direction of motion using the Doppler shift, known as "along track" or "azimuthal" resolution. If the beam is not pointing straight downward, it is possible to split the footprint up along the beam's axis using the ranging information, known as "across track" or "range" resolution. This then splits the footprint up into a two dimensional image, giving the effect of many, much higher resolution, radar footprints. This requires the full EM waves to be recorded, which at radar frequencies is possible. Unfortunately current electronics cannot respond to frequencies higher than a few tens of giga-Hertz, so the same techniques cannot be used at optical or thermal wavelengths.

To maximise the difference in Doppler shifts the beam points at right angles to the platform's motion, then at some zenith angle to trade off between the distance to the surface (and so energy required) and angle of incidence (and so across track resolution).

Generally the range resolution of an active sensor is limited by the width of the outgoing pulse, as all returns will be convolved with this (Zebker and Goldstein 1986). The across track resolution can be further improved by using a range of frequencies in the outgoing pulse by starting off at a high frequency and returning to low during emission. This is known as a "chirp pulse" (Davidson *et al.* 1996). In addition more power can be transmitted in total without needing a higher peak power (which could damage the system's circuits).

Interactions with vegetation For optical instruments, where the wavelength is much smaller than canopy elements, it is assumed that all interactions are in the geometric domain and can be described by structure and BRDFs. Due to the longer wavelength this is not true for radar. For objects and gaps smaller than the wavelength the Rayleigh domain is entered (Tipler 1999, page 1031) and energy will be scattered from gaps that shorter wavelength energy could pass through

unhindered. In the Rayleigh domain the strength of scattering is related to the ratio of the scattering object size to the wavelength. This means that for shorter wavelength radars (<50cm) little energy reaches the canopy floor and so signals suffer from saturation at only moderate LAI values (typically 3-4 (Waring *et al.* 1995b)). For this reason the reflected intensity of shorter wavelength SARs suffers exactly the same problems of saturation and bias as passive optical sensors over forests (Lovell *et al.* 2003).

The range information can still be used to measure forest properties. Balzter (2001) used returns from bare ground to estimate nearby tree heights. This first study used the edge of a sharply bounded forest in Britain, however such features are not common around the globe and nor are clear gaps within forests, limiting the usefulness of such a direct approach.

Kellndorfer *et al.* (2004) proposed using the range resolution of SAR data to produce a height map of the top of forest canopies, then subtracting an existing ground height dataset (in this case from the USGS) to give tree height. However, the weak interaction of radar with vegetation means that the height predicted by SAR would not be to the tree tops but at a point somewhere within the crowns and so height was underestimated. Comparison with more reliable data sources (lidar and ground surveys) have confirmed this (Kenyi *et al.* 2009).

Longer wavelength SAR penetrates further into the canopy, so it may be possible to use it to measure the ground position and a shorter wavelength SAR to measure the tree top position (Hyde *et al.* 2007). However, the high frequency signal will always penetrate someway into the canopy whilst the longer wavelength will interact with tree trunks and larger branches (unless it is very long wavelength, unsuitable for satellites due to antennae size and atmospheric effects (Hyde *et al.* 2007)), leading to an underestimate of tree height (Balzter *et al.* 2007). This can be accounted for by site specific empirical relationships, but this would limit their global usefulness (Sexton *et al.* 2009).

ESA's proposed Biomass Earth explorer mission plans to make use of a 60cm radar (ESA 2010), which will pass through foliage virtually unhindered but react strongly with tree trunks (which are around the same size as the wavelength). Whilst tree height measurements would not be trivial (requiring canopy models to predict attenuation) and it would have very little sensitivity to LAI,

the strength of the return should be related to trunk size and density and so biomass (Drinkwater *et al.* 2008).

This is an exciting prospect in the early stages of development and may be launched around 2015. However long wavelengths radars suffer from increased interactions with the ionosphere (Freeman and Saatchi 2004).

3.4.2 Interferometry

Even with the various methods for improving range accuracy described above, the range resolution from an echo return of EM wave cannot be shorter than the carrier wavelength; which can be up to a few tens of centimetres. The resolution can be improved beyond this using interferometric SAR (InSAR). The signal reflected from a target at two different antennae locations will be out of phase, the phase difference depending on the difference in path length.

Combining these two measured signals results in interference and if the path difference is known, the phase difference can be used to give a more accurate estimate of range. This was first used to measure the topography of Venus from the Earth (Rogers and Ingalls 1969) (cited in Zebker and Goldstein (1986)) and first used in an airborne platform by Graham (1974).

Whilst the range resolution can be dramatically improved, it can only be determined as an integer multiple of the wavelength. If the range difference between the target and the two antennas is more than a wavelength, the interference wraps around. Therefore the phase information must be "unwrapped" to remove all ambiguities. Reliable methods have been developed to achieve this (Goldstein *et al.* 1988).

The two antennae need not collect data at the same time, to date there has only been one single pass InSAR in space, the SRTM mission of 1999 (Werner 2000). All other satellite InSAR attempts have used separate passes, either from two overflights by the same satellite or from two satellites on different orbits. Using measurements from two different times introduces complications. Any change in the target surface between the two passes will confuse the interferometry, an effect known as "temporal decoherence". Over forests, where light breezes can move branches, this effect can be significant (Wagner *et al.* 2003), preventing accurate range estimates. Changes in weather conditions between passes, particularly rain, can have the same effect (Santoro *et al.* 2002).

Interactions with vegetation Interferometry has been shown to give accurate results over hard targets (Elhuset *et al.* 2003). However over diffuse targets, such as forests, the two antennae will travel along slightly different paths and so be affected by different scattering elements. This effect is known as "volume decoherence" and prevents accurate height estimation using the method described for non-interferometric SAR in the previous section with InSAR. However the volume decoherence itself contains information about the diffuse nature of the surface.

Sarabandi (1997) showed that, in theory, tree height can be physically related to the magnitude of volume decoherence. Studies have attempted to extract tree height from InSAR, however they found that the effect saturated at only moderate tree heights, 5-10m (Santoro *et al.* 2002, Wagner *et al.* 2003). This may be because temporal decoherence tends to dominate over volume decoherence, limiting the accuracy possible (Wagner *et al.* 2003) and partly due to the saturation of signals at moderate canopy covers (Waring *et al.* 1995a). Santoro *et al.* (2002) states that "tree height retrieval from InSAR has severe limitations".

3.4.3 Radar conclusions

An important advantage of radar is that it is in the Rayleigh domain in clouds, and so can see through with only weak attenuation. This is a huge advantage in frequently cloud covered regions, such as tropical rain forests (which also happen to contain the majority of the Earth's above ground biomass), where, despite regular passes, successful optical measurements can be rare (Waring *et al.* 1995b).

Studies have used radar derived metrics (such as the decorrelation of repeat measurements) to classify ground cover, but quantitative studies seem to be less common (Wegmüller and Werner 1997). When attempting physically based inversions, due to its weak interaction with canopies it tends to underestimate canopy height (Santoro *et al.* 2002, Balzter *et al.* 2007) and due to the long wavelength saturates at only moderate canopy densities (Waring *et al.* 1995a). Direct comparisons of inverted biophysical parameter accuracy against other active remote sensing techniques have shown radar to be inferior (Sexton *et al.* 2009).

Despite its limitations, the accuracy possible with radar is still greater than the uncertainty that would result from extrapolating between infrequent (once every 40 year) ground surveys (Wagner

et al. 2003). Combined with radar's all weather capability and spatial coverage it can still provide valuable information for monitoring the environment (Sexton *et al.* 2009) . However due to the lack of available long wavelength SAR data and the saturation of shorter wavelengths the rest of this thesis will concentrate on optical wavelengths. Of course the fusion of radar and optical data presents many exciting possibilities for constraining inversions and there seems to be much interest in this direction (Hyde *et al.* 2006) but this is beyond the scope of the thesis.

3.5 Lidar

Lidar is a one of the newest forms of remote sensing, first used in the 1960s for bathymetry (Omasa *et al.* 2007) and first sent to space on Apollo 15 (Hofton *et al.* 2000). The principle is much the same as radar except that a laser is used to illuminate the target instead of a radio antennae, emitting wavelengths between 532nm and 1.5μm. This small wavelength ensures that lidar energy is in the geometric domain when interacting with vegetation. This means that unlike radar, light can penetrate through small gaps in the canopy, allowing measurement of much denser canopies (Hofton *et al.* 2002). In addition, reflected light will be strongly related to foliage structure and properties, allowing direct measurement of biophysical parameters impossible with other instruments. These inversions are greatly aided by the fact that lidars always measure in the hotspot direction, simplifying the radiative transfer equations (Knyazikhin *et al.* 1998).

As lidars provide their own energy they can operate at day or night and can use wavelengths not provided by the sun. This requires a lot of energy, something in short supply on solar powered satellites. For this reason only limited areas can be illuminated (currently single footprints no bigger than 100m in diameter (Harding and Carabajal 2005)) at a time and the broad swaths and rapid repeats enjoyed by passive optical sensors are unlikely in the foreseeable future. The laser technology is nowhere near as mature as passive optical detectors, combined with the greater energy requirements this makes lidar satellites a much greater risk than optical sensors. This was demonstrated by the partial failure of ICESat's lasers (Schutz *et al.* 2005) and cautious cancellation of ESA's A-scope lidar mission pending more robust laser technology (Drinkwater *et al.* 2008).

Care must be taken not to blind anyone; lasers must be eye-safe (Kovalev and Eichinger 2004).

This means making sure that the intensity at a given wavelength is not so high as to cause damage. This limits the laser power that can be used, particularly in the visible region where the eye is especially sensitive.

There are a number of different ways to measure range with lidar, the simplest conceptually is pulsed lidar. These emit a very short pulse of radiation (typically a few nanoseconds corresponding to a range of a few metres) and the time taken between emission and detection after reflection gives the time of light which can be converted to range by dividing by twice the speed of light (use twice the speed because the light has had to travel to the target and back). For pulsed lidars the returning energy can be recorded in a number of different ways. These are;

First return, where the range to the first point at which the signal intensity rises above some threshold is recorded.

Last return, where the range to the last point before the signal drops below some threshold is recorded.

First-last return, where both of the last two ranges are recorded.

Discrete return, where a number (typically between five and twenty (Lim *et al.* 2003)) of ranges to thresholds are recorded.

Full waveform, where all energy reflected from a target is recorded against time.

First return, last return, first-last return and discrete return are all referred to as "discrete return" systems since they are only capable of recording ranges to a finite number of targets; first and last returns can be thought of as special cases of discrete return systems where only a single range is measured. Some discrete return systems also measure intensity, giving information on the properties of an object as well as its location. Full waveform systems (hereafter referred to as "waveform") record all light reflected from a target. As a finite amount of energy is needed for recording, reflected energy is gathered into bins by range. The length of these bins depend upon the speed the detector can digitise the signal and this sets the instrument's range resolution. The range resolution is the digitisation rate multiplied by half the speed of light, so that LVIS's 2ns

(see table 1) corresponds to a range bin 30cm long. The finer the range resolution the more bins the signal will be spread over, diluting the energy and so decreasing the signal to noise ratio.

The other form of lidar is know as "continuous wave". This constantly emits light, modulating the intensity with a known frequency. The phase shift between transmitted and reflected light gives range as long as the surface reflectance is reasonably constant and the range is less than the modulation wavelength. This allows much more rapid data collection, as the system does not have to wait for the previous pulse to return before sending out another, but only a single range can be measured. Over forests, the reflection is from a diffuse surface (the canopy) and heterogeneous reflectance means that the exact location within the canopy for which the range is measured is not obvious and so this type of lidar is thought of as unsuitable for measuring vegetation (Jupp and Lovell 2007) and no further mention will be made of it.

The measurement method depends very much on where it is being taken from, the relative merits of discrete and waveform lidar will now be discussed, depending on whether they are being used for above or below canopy measurements.

3.5.1 Above canopy lidar

It has already been stated that satellite measurements are needed to collect regular, consistent data (section 3.2). For lidar this means emitting a laser pulse downwards from above the canopy. An example of a full waveform return from above a forest is shown in figure 10. From this it can be seen that certain structural parameters can be directly measured, the most obvious being tree height (Dubayah and Drake 2000), which is not directly measurable by any other remote sensing method. Other variables can be measured more directly than with other methods, such as canopy cover, which needs only an estimate of ratio of canopy to ground reflectance to scale the ratio of energy returns from these elements; a far simpler method than the radiative transfer models needed for passive optical measurements. Figure 11 gives a list of biophysical parameters and how they relate to lidar measurements.

The first step for the physically based measurement of all biophysical parameters from lidar is the separation of canopy from ground returns. This gives the relative energies returned from canopy and ground, tree height, the shape of the canopy return (related to foliage distribution)

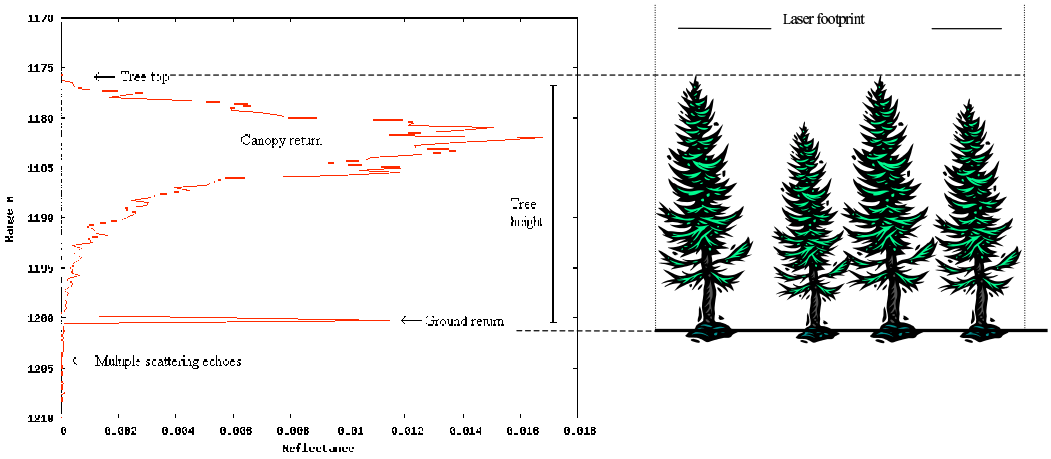

Figure 10: Lidar waveform over forest with features marked

Forest Characteristic	Lidar Derivation
Canopy Height	Direct retrieval
Subcanopy Topography	Direct retrieval
Vertical distribution of intercepted Surfaces	Direct retrieval
Aboveground Biomass	Modeled
Basal Area	Modeled
Mean Stem Diameter	Modeled
Vertical Foliar Profiles	Modeled
Canopy Volume	Modeled
Large Tree Density	Inferred
Canopy Cover, LAI	Fusion with other sensors
Life Form Diversity	Fusion with other sensors

Figure 11: How biophysical parameters can be derived from lidar data, from Dubayah and Drake (2000)

and the shape of the ground return (related to ground slope). Without this separation, parameters must be related to lidar metrics by site specific relationships (for example Lefsky *et al.* (2007)), removing the benefit of direct measurement. This separation requires the identification of the start and end of the canopy and ground returns.

For any forest on flat ground (as shown in figure 10) this needs returns from both the tree top and ground. This is obviously impossible with first return systems, where only tree tops will be measured unless there are large gaps in the canopy. Even for discrete return systems, all of the signal may come from the canopy in dense forests (Næsset and Økland 2002). Much processing is needed to get an idea of the ground with discrete lidars, extrapolating between adjacent footprints (Clark *et al.* 2004) and even then errors are in the order of 2m. Returns from the canopy "blind" the lidar to later targets and this is the main limitation of discrete sensors, we have no idea what is not being measured. For tree height, as long as some signal reaches the ground this is not an issue and the technique has been used successfully (Innes and Koch 1998, Omasa *et al.* 2003, Patenaude *et al.* 2004, Donoghue and Watt 2006) but for parameters that depend on the relative energies (canopy cover and foliage profile) accurate inversions are not possible with discrete return systems. Full waveform suffers no such problem, returns from all surfaces being recorded, although binned into discrete range intervals. Energy is conserved, allowing inversion of far more parameters.

Attempts have been made to use a canopy top map from first return lidar to get tree height by subtracting an external digital elevation model (DEM) (Boudreau *et al.* 2008). This gave usable results but global DEMs are not available with sufficient accuracy over forests to make this a practical solution (Rosette *et al.* 2007) and even the proponents of this method cite the need for a specific biomass measuring mission (Boudreau *et al.* 2008).

Another issue with discrete return is that the exact way a recording is triggered is not always known and so how a range relates to a target is uncertain. These triggering mechanisms are proprietary and not generally released by lidar manufacturers (Lefsky *et al.* 2002) so it is not clear whether the range is to the point at which the signal first rises above a threshold, the maximum intensity after the threshold or a more complex algorithm. What is fairly certain is that some signal will be lost due to the thresholding (Baltsavias 1999) and so the range to tree tops will be

overestimated, leading to an underestimate in tree height. As waveform lidars record all reflected signal this truncation is avoided and steps can be taken to extract the true tree tops (more on this in chapter 4.3).

For these reasons all authors agree that full waveform lidar is preferable for measuring vegetation and discrete return should only be used as a stop-gap until waveform datasets are more widely available. This is gradually happening with a number of waveform lidars commercially available (Wagner *et al.* 2006), in some cases replacing discrete lidars for every day use (such as the Riegl VZ-400 terrestrial scanner). Table 1 shows a list of waveform lidars used for measuring vegetation with their characteristics and primary references.

One key consideration when using lidar for forestry is footprint size and coverage. In order to measure tree height accurately there need to be returns from the tree top and so the area of constant coverage needs to be big enough to ensure this. Figure 12 illustrates a set of small widely spaced footprints missing tree tops and so underestimating tree height. It is generally accepted that to be sure of measuring the top the area of coverage needs to be around the size of a crown, between a 10m and 30m diameter footprint (Zimble *et al.* 2003, Hyde *et al.* 2005). This can be achieved with either a single footprint (Hyde *et al.* 2005) or by aggregating arrays of smaller footprints (Reitberger *et al.* 2008).

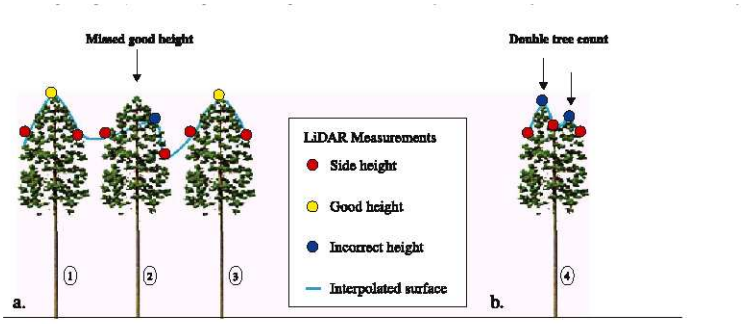

Fig. 5. Tree height variance can be inflated due to misperceived tree heights (from large post spacing) within the tree height-finding model. (a) Height of trees 1 and 3 is measured correctly because LiDAR returns intercept tree peaks (yellow). Height of tree 2 is incorrectly measured because the LiDAR return is from the side of the crown (blue). (b) Tree 4 is counted as two stems (and heights) due to a forked or irregular tree crown.

Figure 12: Small footprint missing tree tops leading to underestimate of stand characteristics, taken from Zimble et al. (2003)

Arrays of small footprints (around 10cm-20cm) provide spatial data, allowing some interesting

Instrument	Pulse width	Altitude	Swath	Footprint	Spacing	Repetition	Digitiser	Wavelength	Reference
ICESat	11.9ns	600km	NA	52m-90m	1km	40Hz	1ns	1064nm	(Harding and Carabajal 2005)
1981 lidar		450m	NA	10m			2.5ns		(Nelson *et al.* 1984)
SLICER		up to 8km	56m	10m		20Hz	0.7ns		(Harding *et al.* 1994)
LVIS	16.9ns	up to 8km	1km	10-30m	10m	400Hz	2ns	1064nm	(Hofton *et al.* 2000)
ALTM 3100	13.6ns	$<$ 2.5km		0.3m-0.8m		$<$100kHz	1ns		(Wagner *et al.* 2006)
LMS-Q560	6.8ns	1.5km		0.5m		$<$100kHz	1ns		(Wagner *et al.* 2006)
TopEye II	6.8ns	$<$ 1km		1m		$<$50kHz	1ns		(Wagner *et al.* 2006)

Table 1: Table of lidar systems with pulse lengths

analysis. Some have tried to identify individual tree crowns using image analysis techniques. This would be a great advantage to biomass estimates, where stem density is as important as tree height (Patenaude *et al.* 2004). One study coarsened the vertical range of a first return surface map (the same technique could be applied to the first return of a waveform lidar) until local maxima were some expected separation (Friedlander and Koch 2000). This required a lot of supervision to guide the process but demonstrates that crowns could be found. A more recent effort used wavelet analysis (Kaiser 1994) to find crowns of known shape but unknown size from a crown surface map (Falkowski *et al.* 2006). This worked very well for regular shaped trees such as conifers, requiring little supervision once the tree shape had been decided, but may struggle with deciduous species with their less regular crowns (as would any method) (Omasa *et al.* 2007).

The footprint size will affect the amount of energy that can be emitted whilst being eye-safe. The broader the footprint the lower the intensity will be for a given energy and so more can be used (Nelson *et al.* 1984). This is a great bonus for waveform lidar, where returns are spread over many bins, each requiring sufficient energy for detection. Many authors believe that waveform lidars need large footprints (Næsset and Økland 2002); certainly all current discrete return systems are small footprint. Some of the newer commercial waveform lidars have small footprints (Wagner *et al.* 2006), perhaps aided by improved detector efficiencies, but these are airborne instruments. The energy requirements for spaceborne systems are much greater and so it seems that despite the advantages of small footprints, spaceborne lidar will remain large footprint for the foreseeable future (Lefsky *et al.* 2002, Dubayah *et al.* 2008). In addition the scanning needed to get constant coverage may not be possible at the speed of a satellite (Omasa *et al.* 2003).

As this thesis is concerned with global measurements, ideally regularly and consistently, the rest of the above canopy sections of this thesis will focus on large footprint lidar.

3.5.2 Large footprint lidars

Waveform lidar is a relatively new technology, first developed by Saab in the early 1980s for bathymetry (the Hawkeye system). Because of its obvious advantages this was soon applied to measuring forests (Nelson *et al.* 1984), though the first instrument (referred to as the "1981 instrument") was very limited, only working up to an altitude of 450m; not an ideal height to fly

an aircraft at through mountains. This was developed into the far more capable "scanning lidar imager of canopies by echo recovery" (SLICER) by NASA in the early 1990s (Blair *et al.* 1994) which has been further improved into the "laser vegetation imaging sensor" (LVIS) (Blair *et al.* 1999).

Spaceborne waveform lidar is still in its infancy and as yet only two instruments have been launched on satellites, both by NASA. The Mars orbiter laser altimeter (MOLA) on board the Mars global surveyor satellite in 1996 (Smith *et al.* 2001) and the geoscience laser altimeter (GLAS) aboard ICESat in 2003 (Schutz *et al.* 2005). SLICER and LVIS were intended as prototypes for the vegetation canopy lidar (VCL) satellite mission (Dubayah *et al.* 1997); unfortunately this seems unlikely to be launched.

There is increasing interest in lidar and several missions have been proposed (NASA's DesDyni (Dubayah *et al.* 2008), ICESat II (Abdalati *et al.* 2007) and SIMPL (Harding *et al.* 2008) and CSIRO's VSIS (Jupp and Lovell 2007)) whilst others have been shelved until the technology is made more robust (ESA's A-scope (Drinkwater *et al.* 2008)), so space lidars can only become more common in the future.

3.5.3 Above canopy data processing

The early studies manually interpreted lidar waveforms to identify ground and canopy returns (Hyde *et al.* 2005). Whilst more robust than automatic methods this is obviously not practical for global studies and so more recent studies have concentrated on developing automatic methods.

The first, and easiest step, is to find the tree top. This is taken as the first point at which the signal rises above a noise threshold. To prevent abnormally large noise spikes causing premature triggering a cumulative energy threshold rather than an intensity threshold is used (Hofton *et al.* 2000). The total energy above a noise threshold is calculated, then the point at which the cumulative energy above noise rises to 1% of the total is taken as the signal start. Determining the ground position and the separation between ground and canopy returns is more complex. First features must be identified then classified as ground or canopy. The traditional technique is to fit Gaussians to the waveform by non-linear iterative algorithms (Hofton *et al.* 2002, Wagner *et al.* 2006) such as the Levenberg-Marquardt method (Press *et al.* 1994). This is an unstable process

and previous studies found that around 4% of waveforms could not be fit to (Hofton *et al.* 2002). It is also a mathematically ill-posed problem (Hofton *et al.* 2000) and so even if a waveform is successfully fit, the features may not be an accurate representation of reality.

It is difficult to reliably identify the ground, especially in dense forests were returns may be very weak (Hofton *et al.* 2002). A simple approach is generally taken, labelling the brightest of the last two features as the ground (Hofton *et al.* 2000) and this is reported to work well, even in very dense tropical forests (Hofton *et al.* 2002). Some have used the number and arrangement of identified features to perform qualitative land cover classifications (Reitberger *et al.* 2008), reporting success when used on well defined and separated vegetation types (herbaceous borders, coniferous forests and fields of grass).

Another feature that lidar directly measures is the fraction of energy returned from the canopy and ground. This can be used to calculate canopy cover if the ratio of canopy to ground reflectance is known (Lefsky *et al.* 1999) by the following equation;

$$Cover = \frac{\rho_g}{\rho_c} \frac{1}{\frac{E_g}{E_c} + \frac{\rho_c}{\rho_g}} \tag{23}$$

Where E_g is the energy returned from the ground, E_c is the energy returned from the canopy, ρ_g is the ground reflectance and ρ_c is the canopy reflectance (which will depend upon leaf and bark reflectance and canopy structure as described in section 1.3). So far studies have assumed values for the ratio of ρ_c to ρ_g from ground data. For example (Lefsky *et al.* 1999) used a factor of 2.

When using a 10m to 30m diameter footprint it is not entirely clear how many trees are being measured and so the relationship between height and forest biomass is not clear. Some have suggested using stand scale metrics (described in section 3.1.2) to relate lidar signals to biomass (Rosette *et al.* 2008). Lidar's direct measurement of vertical structure allows new metrics to be developed which can be empirically related to biophysical parameters with ground based data (Lefsky *et al.* 1999).

It is still early days for relating lidars measurements to forest parameters and so there is currently a profusion of metrics as investigators try to find robust and accurate inversion techniques. There is little agreement on the best metrics as yet. One of the most popular metrics is the height

of median energy (HOME) (Drake *et al.* 2002). The cumulative, energy from the top down, is calculated and the median value found. The height that this median value is reached above the ground is the HOME. This will depend on both tree height and canopy density with height. Tall, old canopies with the majority of foliage at the top, will have high HOME and also high biomass, whilst shorter or less dense canopies will have much smaller HOME and also low biomass. This way tree height and stand density, the two most important factors in biomass, are taken into account. HOME was linked to biomass through empirical relationships and found not to saturate, even in dense, structurally complex tropical forests (Drake *et al.* 2002).

Tree height can be converted to biomass through allometric relationships and some authors believe that these relationships are similar for many species, meaning that global allometrics could be used.

Topography presents a big problem for large footprint lidar. The ground return will be spread out by the height variation across the footprint, as will canopy returns depending on its heterogeneity, reducing their separation. If the ground height variation is greater than the separation between the bottom of canopy and ground the two signals will not be distinguishable and a physically based inversion will not be possible. Figure 103 illustrates this for a 30m footprint over a 30^o slope, the ground return is completely indistinguishable from the canopy.

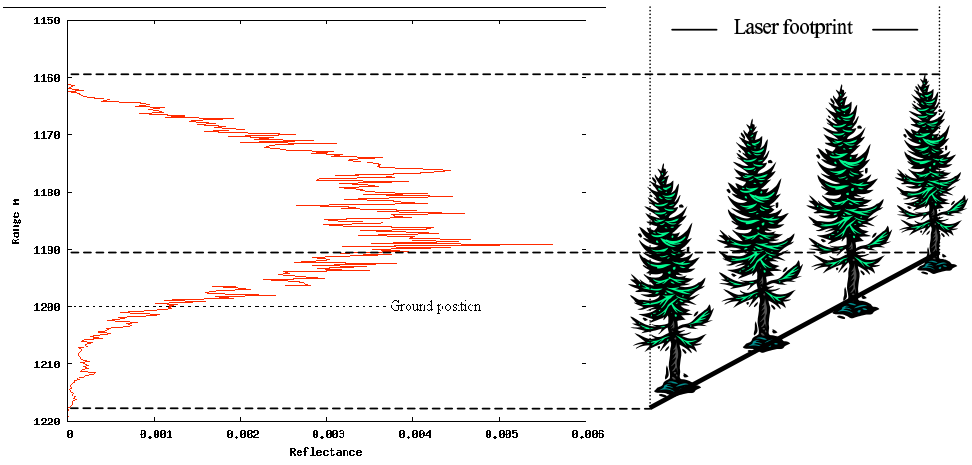

Figure 13: Illustration of topographic blurring of a 30m footprint on a 30^o slope

It is the variation in ground height across the footprint that causes the blurring, so the smaller the footprint the less the blurring. In fact, small discrete return systems report little difficulty

over steep terrain (Takahashi *et al.* 2005). Any off nadir pointing will cause blurring so large footprint lidar cannot make multi-angular measurements. There have been attempts to use external topographic maps to determine the ground slope within each footprint, this gives an idea of the extent of the ground return which can be overlaid on the waveform, allowing the fraction of energy from the ground to be determined (Harding and Carabajal 2005, Rosette *et al.* 2008), illustrated in figure 14. The absolute elevations of the two datasets do not have to match, as the end of the lidar waveform must correspond to the end of the ground, but the horizontal location and resolution of the DEM are vital.

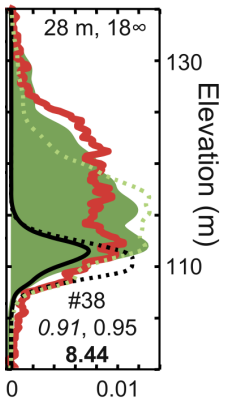

Figure 14: ICESat waveform(red) matched up to a DEM (black dotted) to predict the ground return (black), from Harding and Carabjal (2005)

This method has only been used in areas with very accurate DEMs (Britain's Ordnance Survey and America's USGS) but such accurate maps are not available for the whole world (Rosette *et al.* 2007). There are remotely derived near global DEMs (such as the shuttle radar topography mission, SRTM (Werner 2000) and ASTER (Yamaguchi *et al.* 1998)) but their reliability over forests is questionable (Dowman 2004) and are coarse resolution compared to lidar footprints (90m for SRTM outside North America) so that local topographic variations will be missed.

An attempt has been made to use SRTM (30m resolution within North America) to calculate slope for correcting ICESat (90m footprint) waveforms (Boudreau *et al.* 2008). They hoped that the radar scattering centre (somewhere within the canopy) would mirror the ground, so that it did not matter that the SRTM DEM was not true ground when calculating slope. This should be

the case in homogeneous canopies but the assumption may not hold for more heterogeneous cases. They reported an r^2 of 0.65 when comparing ICESat/SRTM derived heights to those from small footprint lidar. This is an encouraging result but far from perfect.

Lefsky *et al.* (2007) proposed a method to extract the mean tree height within a footprint (a useful metric for evaluating biomass) from a topographically blurred waveform alone. They calculated three metrics from ICESat waveforms, total extent (distance from first to last return above noise threshold), leading edge extent and trailing edge extent (both defined later in section 5.9.3, their exact meaning is not important right now) into empirical correction factors by comparison with intensive ground data. Even for an empirical relationship, the proposed equations lack elegance (equation 24 shows the equation for the trailing edge correction factor as an example). These factors were subtracted from total waveform extent to get mean tree height.

$$tf = \sqrt{te} + 0.92 * te - 88.5 * \frac{te}{we} + 2049.5 + \frac{te}{we^2} - 14171.4 * \frac{te}{we^3} \tag{24}$$

Where tf is the trailing edge correction factor

te is the trailing edge extent

we is the total waveform extent

This approach reduced the tree height errors on slopes to an average of 5m, which they claim to be "consistent with the requirements of a global dataset", though without further qualification of those requirements. Interestingly they found that the signs of the correction factors were the opposite of what would be expected; highlighting the non-physical nature of the approach. They admit that this is only a first step on the path to measuring sloped forests, however, such a non-physical method will always be species and site specific and a more physically based method would be preferable.

Conclusion The abilities of large footprint waveform lidar to remotely collect forest structural data have been well demonstrated, most importantly the measurements do not saturate until much higher densities than passive optical and radar signals, allowing measurements of previous blind

spots on the Earth's surface. The link between measured signals and certain biophysical parameters is far more direct than with other techniques, particularly tree height and canopy cover. It is no surprise that the remote sensing community has such an interest in new lidar missions.

There is still some confusion about how best to go about relating lidar data to forest parameters, but this should dissipate as validation campaigns continue and data becomes more widely available. Lidar footprints are smaller than many other remote sensing instrument's pixels (30m as opposed to 1km for MODIS). At these scales forests are very heterogeneous and so a geolocation error of a few tens of metres of the lidar footprint might mean that ground measurements are made of completely different trees, weakening allometric relationships and frustrating validation attempts (Drake *et al.* 2002). This is cited as one of the primary causes of uncertainty in lidar inversion (Næsset and Økland 2002, Hyde *et al.* 2005, Drake *et al.* 2002) and it is difficult to advance our understanding of the processes involved without reliable validation data. Here radiative transfer modelling offers the potential to aid understanding (North *et al.* 2008, Ni-Meister *et al.* 2001), as long as the model can be trusted to capture effects at the scale of a lidar footprint.

3.5.4 Ground based lidar

Lidars can also be used for making ground based measurements. The range resolved measurements allow lidars to collect structural data that would only be possible with destructive sampling or point quadrats, but much more rapidly (Jupp and Lovell 2007, Clawges *et al.* 2007). In addition they can provide the data required to validate above canopy range resolved measurements (Ni-Meister *et al.* 2008); something current rapid ground based measurements are unable to do.

The modes of operation are exactly the same as for above canopy measurements, with both discrete and waveform lidar available. The first attempts were made in the 1980s, not long after airborne methods had been tried (Vanderbilt 1985). This attempt used a primitive terrestrial lidar, since then the use of hemispherical scanning first return lidar for surveying buildings has been well developed and they are used routinely. Buildings are much "harder" targets than forests so first return lidar can capture all the data needed for modelling work. The large, hard surfaces of buildings are not so different from tree trunks so it it little surprise that this was where much of the early effort has been directed. The trunks are also the most profitable part of a tree, forestry

companies are willing to spend money on developing instruments for rapid measurements and so this area has been well funded.

An alternative laser system known as "laser plane range finding" has been proposed for forestry (Tanaka *et al.* 1998). This uses a laser pointing at a known angle to illuminate the target, the 3D location of this spot is then determined by triangulation from a camera at a fixed distance from the laser. Whilst this allows range resolved measurements of structure it will suffer from the same problems of occlusion as traditional stereo photogrammetry. It is unclear why these authors decided not to use the standard lidar range finding methods, with its simpler hotspot measurements, and no comparison has been made to prove that it can perform as accurately.

Several studies have used first return hemispherical ground based lidars to examine the diameter and height of trunks as a way to rapidly assess the growth rate and amount of merchantable wood (Watt and Donoghue 2005, Pfeifer *et al.* 2004). For hard targets, such as trunks, the beams are totally obscured so there are no later targets for discrete systems to be blinded to and they will suffice. These typically have beam divergences of a few tenths of a milliradian, corresponding to a spot size of a few millimetres at a range of ten metres. The returns form a dense "point cloud" from which the objects have to be identified through image processing techniques. The problem is slightly harder for trees because unlike buildings these have no sharp corners and hard edges that can be used to tie scans from different locations together (Pfeifer *et al.* 2004). Multiple views are essential to overcome occlusions and so artificial targets must be used. Some report that it can take around four scans and up to an hour to fully characterise a single tree (Clawges *et al.* 2007). One study went a step further and once trunks had been identified by point cloud analysis, draped high resolution photography over, using the texture to identify tree species (Reulke and Haala 2004).

The point clouds are unlikely to be dense enough to allow the reliable extraction of leaves by image interpretation, particularly in coniferous forests (Omasa *et al.* 2007) and so an explanation of point cloud methods will not be given here. There have been successful attempts to extract complete tree models, including leaves from point clouds (Xu *et al.* 2007, Côte *et al.* 2009). These required extensive sets of prior information and models for the shape and distributions of

branches and leaves to fill in the gaps from occlusions and between points. It has been found that even for simple structures (compared to needle shoots) like primary branches, small deviations from assumed shapes can cause inaccuracies (Pfeifer *et al.* 2004). The successful authors partially overcame this issues by supervising the process (Côte *et al.* 2009).

Of far more interest to ecologists and climate modellers are the canopies and accurately deriving LAI. The range resolution and small beam size of a laser makes the analogies with a point quadrat (Wilson 1960) obvious. An instrument for making point quadrat type measurements was created by mounting a lidar on a tea tray pointing vertically (Parker *et al.* 2004). As an operator walks through a forest the range to the first foliage element above the sensor (or a gap) are recorded. As the laser beam will suffer from occlusion this is more correctly a version of the telephoto lens method of MacArthur and Horn (1969), but can be collected far more rapidly. Beer-Lambert's law must be used to convert contact frequencies into LAI (equation 14) whilst the range resolution allows the calculation of LAI in layers of constant height, giving foliage profile.

Traditional surveying laser scanners can be used to make the same gap fraction measurements, much like a range resolved hemispherical camera. This allows estimation of the angular distribution and clumping factors in exactly the same way (described in section 3.1.4) with the added detail of range resolution. Lidar scanners take a little longer to set up than hemispherical cameras and the LAI-2000, but the extra detail more than makes up for the extra effort. It has even be suggested that the woody correction factors can be found by comparing leaf-off to leaf-on scans (Clawges *et al.* 2007), although this will suffer from exactly the same issues of non-randomness of the two materials as passive optical, leading to an overestimate of visible wood area in the leaf on case (Kucharik *et al.* 1998b) and will not work for evergreen species.

It has been found that when used this way, terrestrial lidars underestimate gap fraction, and so underestimate LAI, when compared against hemispherical photography (Danson *et al.* 2007). It is hypothesised that this is caused by small gaps (or small obstructions over large gaps) reflecting enough laser light to trigger a return and so being marked as a blocked pixel. These small objects would not bias optical transmission methods (depending on the threshold chosen) but the lidar only marks gaps that are larger than the laser beam, missing all others and so underestimating

gap fraction.

One solution to this triggering by small targets is to use full waveform lidar. Such an instrument has been developed specifically for forest measurement, the Echidna laser scanner (Lovell *et al.* 2003). It currently exists as a prototype, the Echidna validation instrument or EVI. Industry has recently unveiled the first commercially available terrestrial waveform lidar, Reigl's VZ-400, announced in September 2008. This instrument does measure the full waveform but does not yet record it in the same sense as LVIS or Echidna, but processes it (again with proprietary algorithms) to allow any number of discrete returns. The instrument has been tailored for the surveying industry where diffuse targets are rare.

Figure 15: Photograph of the Echidna laser scanner in Northumberland national forest near Sydney. Dr. Darius Culvenor is in the left and Dr. Nicholas Goodwin on the right. Photograph by Professor Jan-Peter Muller.

Echidna's characteristics are given in Jupp *et al.* (2009). It scans a zenith range from -137^o to +130^o and 0^o to 180^o azimuth to give a little over a hemisphere. The outgoing laser pulse is at 1064nm and is a 25.3ns long slightly, skewed Gaussian (Jupp *et al.* (2009) gave the full width half maximum, FWHM, which is 14.9ns whereas the point at which intensity drops to $1/e^2$ of the maximum is used throughout this thesis). The beam starts off 29mm wide and the divergence can be adjusted between 2mrad and 15mrad. The waveform is sampled every $\frac{1}{2}$ nanosecond giving a range resolution of 7.5cm. The pulses are generated at a rate of 2kHz, so it takes around twenty

minutes to record a full hemisphere. This provides a high resolution, multi-angular dataset of the intensity returned from all visible objects; perhaps the richest non-contact dataset available.

Echidna is still a prototype and not all of the possibilities of such a dataset have yet been explored. So far studies have concentrated on extracting stem dimensions for foresters (Yang *et al.* 2008), as this is the most commercially viable use for such an instrument, and LAI (Jupp *et al.* 2009). The stem dimensions are extracted using exactly the same methods as for discrete return lidars (for hard targets there is no difference between waveform and discrete measurements) and these will not be explained here.

The initial attempts to extract LAI from Echidna have tried to show that it can be found as reliably as with traditional passive transmission techniques (outlined in section 3.1.4). These have used gap fraction based techniques, relating to LAI with the Beer-Lambert law but with the advantage of being range resolved (so giving an idea of the vertical heterogeneity) and providing its own illumination. This means the measurements are insensitive to natural lighting and so can be taken no matter what the conditions are rather than having to wait until the clouds, sun and moon are in the right positions.

Echidna scans at a coarser resolution than typical hemispherical cameras, the spot size being between 5cm and 18cm at a range of 10m, and so small gaps will be missed unless the fraction of gap and canopy within a beam can be calculated. Measurements by Echidna are not quite like transmission techniques, where the recorded intensity depends only on the projected area of elements. Returned light is reflected from elements and so measured intensity depends on the projected area, reflectance and orientation of objects. For example a small bright leaf will return exactly the same intensity as a leaf twice as big but half as reflective; these cases have different gap probabilities and LAIs. This coupling complicates the problem somewhat. Mathematical models are needed to link measured intensity to gap fraction.

The instrument measures returned intensity with range and this needs inverting to get to the canopy's properties. The apparent reflectance, η, can be calculated by correcting measured intensity, I, for range, R, detector efficiency K and outgoing intensity I_0,

$$\eta = \frac{I.R^2}{K.I_0} \tag{25}$$

The range and outgoing intensity are measured for each beam and the detector efficiency can be measured in a laboratory with targets of known optical properties.

This apparent reflectance is related to the target's actual reflectance, ρ_c, projected area as a fraction of the field of view (equal to one minus the gap probability, P_{gap}), and the phase function, $\Gamma(\theta)$ which describes the directional reflectance of a surface illuminated and viewed at an angle θ relative to the reflectance if all an object's surfaces were at right angles to the illumination and viewing vectors.

$$\eta = \rho_c.\Gamma(\theta).(1 - P_{gap}) \tag{26}$$

Of course these equations are for a single range bin at a time. The complete signal will be the sum of these as far as the lidar can see. Equation 26 can be solved to get gap fraction which can be used to find LAI with Beer-Lambert's law, equation 14.

The properties for bark and leaf may be slightly different, requiring a separate apparent reflectance for each material, but for the first attempts it has been assumed that they are similar (Jupp *et al.* 2009) and so the equations above can be applied to the whole canopy and a PAI calculated. A woody correction would then be needed to convert between PAI and LAI.

It has been suggested that the phase function is the square of the angular distribution function, $G(\theta)$, so $\Gamma(\theta) = G^2(\theta)$ (Ni-Meister *et al.* 2008), from empirical observations. If it is assumed that the LAD and LAI are constant throughout the canopy the LAD can be calculated in the same way as with hemispherical photography. This can be done by either by fitting to models such as an ellipsoid (Campbell 1986) or beta distribution (Goel and Strebel 1984), or by recording the gap fraction in bins of constant zenith (Goudriaan 1988). The assumption of homogeneity may not be entirely true (Wilson 1959) but is the only way to estimate LAD from a single scan. The model can be used to predict the fraction of total surface are projected in a given direction. A linear model has been proposed as a simple approximation to an ellipsoid (Jupp *et al.* 2009), giving good agreement during inversion.

Clumping can be found with the same log averaging method used for hemispherical photographs (see section 3.1.4 (van Gardingen *et al.* 1999)), except that the signal can also be split into range-wise segments. The current prototype emits only a single wavelength so it is not possible to spectrally separate leaf from bark. It is possible to use the shape of a return to tell something about a target. Solid objects that completely fill the field of view will return a strong signal with roughly the same shape as the outgoing pulse whilst diffuse targets will cause weaker, more spread out returns. In forests the only solid elements are trunks and the ground, so all strong, outgoing pulse shaped signals above the ground can be classified as bark. Some estimate of branch area to leaf area is required to get to LAI rather than PAI. Branches are generally smaller than the field of view and so will give diffuse returns, preventing the separation from leaves by the same method.

This only leaves the element reflectance as an unknown. This can be measured in the field and some believe it to be quite constant at 1064nm for different species and even for leaf and bark (Jupp *et al.* 2009), most of the spectral variation occurring in the visible and water absorption bands. The phase function depends upon the angle between an element's surface and the laser Poynting vector and so depends upon the LAD, $G(\theta)$ and laser direction, θ.

This method has been used successfully, giving LAI values comparable to those found from hemispherical photography but far more consistent over changing solar illumination conditions (Jupp *et al.* 2009). Some issues were found with clumping factors coupling together with LAD, making it hard to calculate either reliably and more work is needed in this direction.

Studies (Ni-Meister *et al.* 2008) have been performed linking the GORT radiative transfer model (described in section 2.1.2) to Echidna measurements. The model was slightly modified to include the effect of tree trunks, generally negligible in above canopy measurements but can have a considerable effect on hemispherical below canopy scans. This would allow LAI inversions to take crown scale clumping into account, greatly improving accuracy. It would also allow above canopy lidar measurements to be predicted from Echidna measurements, an important development for the validation of these new instruments.

As GORT is not spatially explicit only the LAI averaged in slices of constant height could be used, not making use of Echdina's potential for measuring horizontal heterogeneity. Any informa-

tion on stand density derived becomes very indirect and can couple to other factors. The GORT model assumes that trees can be described as ellipsoidal envelopes containing a turbid medium, but it is questionable whether such heterogeneous scenes as forests can be described by such simple geometric primitives (Parker and Brown 2000). In addition the above inversion requires LAI and LAD to be constant throughout the crowns, another assumption which does not fully capture the heterogeneity of a forest. It is not clear whether the assumption of stand scale and within crown homogeneity of GORT type models is appropriate at the scale of Echidna measurements as a comparison has not yet been carried against explicit models.

An alternative method is to use a DART type model (Gastellu-Etchegorry *et al.* 1996) to estimate canopy parameters in an array of voxels. Hosoi and Omasa (2006) performed the first study, using a first return terrestrial lidar, incapable of measuring intensity, contact frequency being used instead. This allowed an explicit description of element locations rather that the statistical distributions of GORT. The radiative transfer equations must be solved for every voxel and so much more data is needed. Fortunately Echidna data is very rich and has the potential to invert such a model without the heavy pre-parametrisation needed for sparser datasets (described in section 3.3, (Kimes *et al.* 2002)). In order to get LAD measurements from a range of angles are needed for each voxel. This necessitates multiple overlapping scans, which will also help overcome occlusion of voxels. The woody correction term was calculated by removing all leaves (simulating winter) and re-measuring, then subtracting the gap fraction with leaves from that without. It has already been shown that this may lead to an underestimate of LAI (Kucharik *et al.* 1998b) and this may have biased their findings.

Unlike the other terrestrial lidar studies, Hosoi and Omasa (2006) performed a rigorous validation of results by destructive sampling. This revealed that whilst the attempt successfully calculated LAI values, it suffered from coupling of LAD, woody correction and clumping factors, indicating that perhaps even richer data is needed to invert a model of this complexity. Of course, using full waveform rather than first return lidar should have greatly helped accuracy, allowing measurement of surfaces that would be obscured behind small objects to a first return system.

These are only first steps and it is hoped that much more can be done with this instrument in

the future, particularly using the beam divergence to extract different scales of clumping (Lovell *et al.* 2003).

Currently there is only a single prototype Echidna, requiring specialist technicians. This has limited the use of this data source. Future instruments will hopefully be more robust and easier to use. There have been suggestions of improvements. Currently two of the biggest limitations are uncertainty in element reflectance and the fraction of leaf and wood. Dual wavelength laser systems have been proposed to ease the problem of the woody correction (Tanaka *et al.* 2004). These would enable all the analysis of passive multi-spectral systems (Kucharik *et al.* 1998b) but with carefully controlled illumination and so not suffering from light bark and dark leaves confusing classification.

3.6 Measurement conclusions

This chapter has described current methods for measuring forests. Satellites are essential for global studies, being the only way to provide frequent and, equally importantly, consistent measurements. The three main remote sensing instruments, passive optical, radar and lidar have their own advantages and disadvantages.

Passive optical sensors are relatively cheap, require minimal power, can provide multi-spectral or hyper-spectral measurements over large areas and have been in continuous use since 1972. They are the only practical way to make multi-angular measurements, so helpful when estimating land surface parameters. Unfortunately their measurements saturate at only moderate canopy densities (LAI of 3-4 for vegetation indices or 6-7 with modelling) and so much of the heterogeneity and dynamics of vegetation will be invisible to them.

Radars offer the unique ability to make measurements through clouds and can provide reasonable spatial and temporal coverage. Shorter wavelength radars also saturate at only moderate canopy covers and so will have the same blind spots as passive optical instruments. Longer wavelength radar signals should not saturate over dense canopies, or even interact at all with foliage, offering the exciting potential to measure standing biomass relatively directly. Such an instrument has not been launched and many complications need to be overcome before it can (atmospheric

interference is especially strong at that wavelength and a very large antennae is needed to get a usable ground resolution). Interferometric radar has the potential to measure forest height, in theory, but is difficult to implement in practice (Sexton *et al.* 2009).

Lidar measurements do not saturate until very high canopy densities, a feature shared only with long wavelength radar. They also offer direct estimates of features that are only tangentially related to passive optical and radar measurements. Therefore they have the potential to open up the blind spots of other instruments and greatly reduce uncertainty in global maps of biophysical parameters.

On the downside the energy requirements and relative immaturity of lasers means that only very narrow swaths will be possible (DesDyni is proposed to have five pixels, each 1km apart whilst ICESat has only a single pixel) and so it will take years to sample all the Earth's surface rather than the two days of MODIS. They are not a complete solution but are the best technique for measuring tree height (and so biomass) and do not saturate as readily as current passive optical and radar sensors. For these reasons the rest of this thesis will concentrate on the measurement of forests by lidar at the global scale. A mixture of all of these data sources would help constrain a model and there is much interest in data fusion techniques (Hyde *et al.* 2006).

Ground based Ground based measurements provide a much more direct estimate than satellites, allowing close up human interpretation of a site and so whilst it is not possible to perform global studies from ground measurements alone, they are a vital tool for validating remote sensing estimates.

Direct measurements of vegetation, whilst accurate, are time consuming, expensive and often require the complete destruction of a plot. These are useful for intense, small scale validation campaigns but are not practical for collecting regular, large scale measurements needed to validate global remote sensing products.

Passive optical transmission methods are fast and do not damage the plants but are only indirectly related to biophysical parameters. Beer-Lambert's law is needed to reach the forest parameters, but this only gives effective parameters which saturate at moderate canopy covers (LAI of 5-6). The limitations and assumptions of ground based transmission methods are very

similar to those used for remote passive optical measurements and so important physical processes, such as saturation, could be hidden if they are relied upon. In addition the transmission methods depend upon illumination condition, limiting measurements to an hour before sunrise and after sunset, or in uniformly overcast conditions.

Though not explicitly stated, some authors' description of the ideal ground based canopy measurement device bears a startling resemblance to a multi-spectral version of the Echidna lidar (Jonckheere *et al.* 2004). The latest hemispherical, waveform terrestrial lidars are capable of rapidly measuring tree trunks, giving good estimates of above ground biomass. They also provide the richest possible dataset (range resolved and multi-angular) and so have the potential to create very complex canopy models, giving spatially explicit estimates of biophysical parameters (so fully characterising heterogeneity) and predict above canopy measurements, including range resolved measurements. It remains to be seen whether their full waveform measurements can overcome the saturation of transmission methods and much more work is needed to fully understand the possibilities and limitations of their measurements.

The thesis will explore the potential of ground based full waveform lidars for providing ground truth measurements.

Chapter 4: The Simulator

Vegetation parameters inverted from remotely sensed data must be validated before it can be used with any confidence. However plant canopies, particularly forests, are very complex so collecting the field data necessary to fully characterise the structure and spectral properties needed to validate a scene is often not possible (Bréda 2003). Even if an area of vegetation were fully characterised it is not easy to geographically match ground based measurements to those from satellites and so direct comparisons are not generally possible (Hu *et al.* 2003). This makes it hard to know the accuracy of remotely sensed parameters and the source of any disagreements.

Simulations using computer models offer an alternative method of validation. In computer models the truth is always known (to whatever detail it is modelled), a situation that is rarely achieved in reality (Pinty *et al.* 2001). Parameters inverted from simulations of remote sensing instruments can be compared against the original scene models (a known truth) without any geolocation issues to give validations in which confidence can be had. A "virtual laboratory" can be created (Lewis 1999) where the scene can be controlled, allowing experiments that would be impossible to perform in reality.

Methods for simulating remote sensing signals from different vegetation canopies were presented in chapter 1.3 and it was concluded that naïve Monte Carlo ray tracing (one that uses no non-physical acceleration techniques) over explicit vegetation models give the most accurate radiometric predictions. All other methods would use non-physical acceleration or effective structural parameters (Widlowski *et al.* 2005). These effective parameters and acceleration methods may hide errors and physical processes when trying to invert biophysical propertied, especially if the inversion algorithms make the same assumptions as the models.

For this reason a Monte Carlo ray tracer and geometrically explicit forest models will be used to simulate data of current and future lidar instruments over a range of forests. This will allow an assessment of error with much better accuracy than is possible with real data as well as allowing an exploration of the potential of instruments for which real data is not readily available. This chapter will describe the design of the ray tracer, forest models and the efforts taken to ensure realism.

4.1 Design of the ray tracer

The ray tracer used was based on the earlier simulators of Lewis (1999), previously known as "ararat", "prat", "drat", "frat" and now converted into a library of C functions, "Rat Lib" (Lewis 2006). The radiometric accuracy over vegetation has been comprehensively tested in the RAMI exercises (Pinty *et al.* 2001, Pinty *et al.* 2004, Widlowski *et al.* 2007) (see section 2.4) and this particular simulator forms part of the surrogate truth. This provides confidence in its prediction of remote sensing signals over vegetation. The validations have not yet included range resolved measurements but these are being carried out for the fourth phase of RAMI (European Commission, JRC 2009). There is no reason to suspect the simulations will not be accurate for lidars but it cannot be said for certain until the fourth phase is complete, sometime at the beginning of 2010.

The basic operation of the intersection tests and scattering of Monte-Carlo ray tracers has been well covered in other sources (Foley *et al.* 1992, North 1996, Lewis 1999) and was not modified as part of this thesis, so no more detail than was given in section 2.2.3 will be provided. It was a tool to simulate remote sensing signals rather than a focus of the research. The scan pattern and information recorded is particular to the instrument being simulated and so that will be described in detail throughout the rest of this chapter. The Rat Lib library was used to create a ray tracer optimised for hemispherical (or part of), multi-spectral waveform lidar simulations, named "*rat" or "starat". This could simulate Echidna signals, or by limiting the angular range and setting appropriate location and footprint, above canopy instruments such as LVIS and ICESat.

The ray tracer library can act in forwards or reverse mode, tracing rays from the illumination source or from the detector respectively. For lidars the field of view will never be smaller than the illuminated footprint and is often slightly larger to ease alignment (Kovalev and Eichinger 2004). In this case, if reverse ray tracing were used, rays traced from the detector to points outside the laser footprint will contain no first order scattered light, only multiple scattered if the ray happens to scatter into the laser footprint. These rays will require as many computations as rays whose first interaction falls within the laser footprint but contribute only a small fraction of the overall signal; obviously this is an inefficient situation. With forwards ray tracing the first interaction of every ray traced from the camera will fall within the field of view and so contribute to the total

signal whilst rays scattered outside the laser footprint that interact within the field of view will still be recorded. Therefore the same result is obtained with far fewer computations and so the ray tracer will be operated in forwards mode. Of course if the field of view is exactly the same size as the laser footprint the two modes will be computationally equivalent and either can be used.

Of the instruments that will be simulated Echidna has by far the most complex scanning pattern. This sends out beams between -137^o and +130^o zenith, stepping by the beam divergence so as to leave no gaps. The sensor then rotates azimuthally by the beam divergence again before scanning another zenith swath. This way a full hemisphere is built up leaving no gaps between beams, except those from trying to build up a square wall with round footprints. For all zeniths except those pointing horizontally there will be overlap between azimuthal neighbours and at nadir all azimuths will be looking at exactly the same point. This gives the data a fair amount of redundancy and may allow some interesting analysis of sub-pixel heterogeneity (Jupp and Lovell 2007).

All other instruments can be approximated as a set of nadir looking scans (their off-nadir pointing being negligible), which is a special case of an Echidna scan with an extremely narrow angular range. Therefore the simulator was set up to mimic Echidna's scan pattern.

The ray tracer is controlled by defining a location within the scene, a beam divergence, a field of view, step angle (generally set as the beam divergence) and a zenith and azimuth range to scan over. For Echidna the angular range used was from -100^o to +100^o zenith (the full range was not used as this thesis is interested in the measurement of the canopy rather than the ground) and 0^o to 180^o azimuth. For above canopy instruments only a single footprint -180^o zenith and 0^o azimuth was scanned.

Figure 16 shows a comparison between a real LVIS footprint (taken from Sun *et al.* (2008)) and a ray traced version over a similar forest. Figure 17 shows a real Echidna scan (from Jupp and Lovell (2007)) and a simulated version. The forest for the simulated scan was much younger than that in the real data.

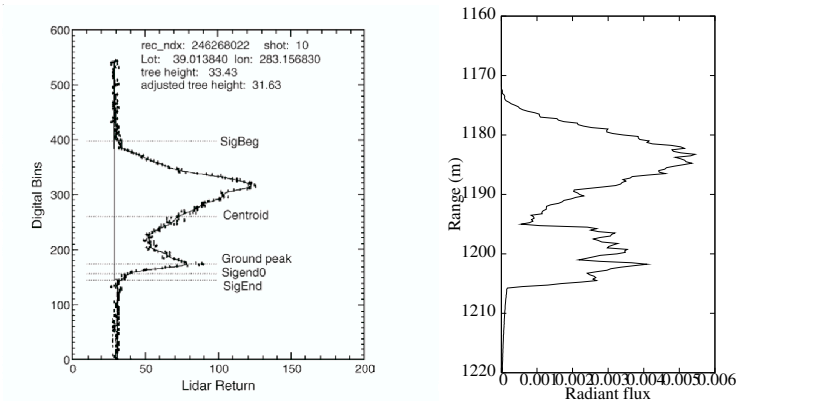

(a) Real data (b) Simulated data

Figure 16: Starat LVIS like waveform compared to a real waveform

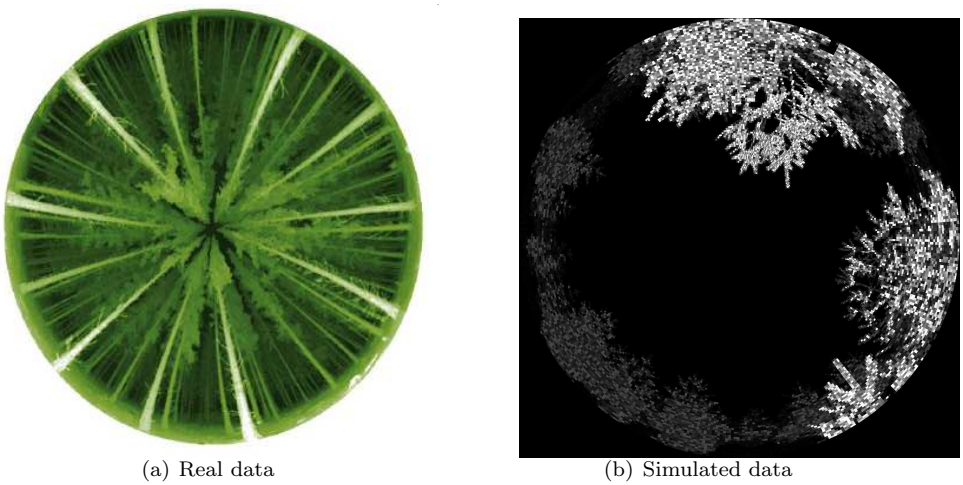

(a) Real data (b) Simulated data

Figure 17: Starat Echidna like scan compared to a real one

4.1.1 Sampling

In Monte Carlo ray tracing the number of rays, and so samples of the scene, are defined independently of the scene's complexity; this is its main advantage over other realistic simulation methods (Disney *et al.* 2000). To ensure that the Monte Carlo results are representative of reality there must be a sufficient number of rays to adequately sample the scene and this number will be related to scene complexity. The number of rays required depends upon the variability of the scene at the scale of the field of view, if the scene is a single plane all rays will see exactly the same surface and return the same reflectance, so a single ray will suffice. For a scene as complex as a conifer forest many hundreds of rays will be needed to sample all the objects and curved surfaces.

In addition to the sampling of surfaces by directly reflected light (rays that have undergone a single interaction) multiple scattered light must also be adequately sampled. The intensity of multiple scattered light will depend upon the element reflectance and the probability of a multiple scattered ray returning to the detector (which in turn will depend upon the field of view, scattering element density and orientation of scatterers relative to each other). For computational efficiency the ray tree is truncated after a certain number of interactions (once the contribution from scattered light has become negligible).

To ensure an even areal sampling and because a single lidar beam's measurement is not spatially explicit within the footprint (unlike a camera), the laser footprint was divided into segments and a set number of rays traced per segment. The segments were made to be of constant solid angle, or as near as possible without leaving gaps. The field of illumination was first divided into zenith annuli of a given angular resolution α_{res}. These were then divided into azimuthal segments, each of as close to the sine of α_{res} as would fit an integer number of times into a full circle. This gives the sampling pattern seen in figure 18. Rays were traced from the lidar scan centre through a random point within a segment. This random jittering allows different scans with the same resolution which may give different results if not enough rays are used. These segments could also be used as pixels to create a two dimensional picture, although the full three dimensional distribution of intensity was not recorded to reduce the memory requirements.

A set of tests were performed to make sure that the scenes were sufficiently sampled without

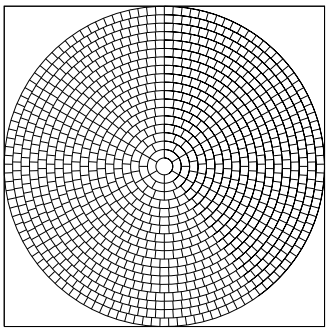

Figure 18: Starat's sampling pattern

using so many rays as to make the simulations impractically slow.

Above canopy lidars The above canopy lidars used in this investigation (in section 4.3) will have 30m footprints, about the size of LVIS (Hofton *et al.* 2000) and the proposed DesDyni (Dubayah *et al.* 2008) instruments. These will be simulated over Sitka spruce and birch forests of different densities, ages and topographies (the creation of which is describes in section 4.2). The denser the forest the greater the scene complexity, also the larger the trees in the forest the greater their complexity. The coniferous trees used contained more elements than the birch and so were more complex. A sparse young Sitka spruce forest was used as an example of a simple forest whilst a dense old Sitka spruce forest was used to find the number of rays needed for the most complex scenes. The dense forest was used to set the number of rays; the sparse forest was tested to see how the required number of rays changed with complexity. Topography should not affect the number of rays needed to sample the scene. It does slightly spread out scattering elements which may have an impact on multiple scattering though this should cause a reduction in the contribution if at all.

Maximum interactions The number of rays needed to characterise a scene cannot be determined until it has been decided how many interactions to limit the ray tree to. Multiple scattered light is attenuated by the element reflectance to the power of the order of scattering, therefore to ensure that the simulation's accuracy is never limited by ray tree truncation the wavelength with the brightest reflectance were used to choose the truncation point. Within the canopy (where the majority of multiple scattering will occur) there is a mixture of leaves and bark, therefore the

spectrum of interest will be a mixture of these two spectra, depending upon the probability of light scattering between the various elements. As leaves are by far the densest scattering elements in conifers (whilst bark can have as large a surface area as leaves this is made up of a few large elements) and so the majority of multiple scattering is likely to come from them. For the particular spectra used in this investigation the maximum leaf reflectance was at a wavelength of 920nm.

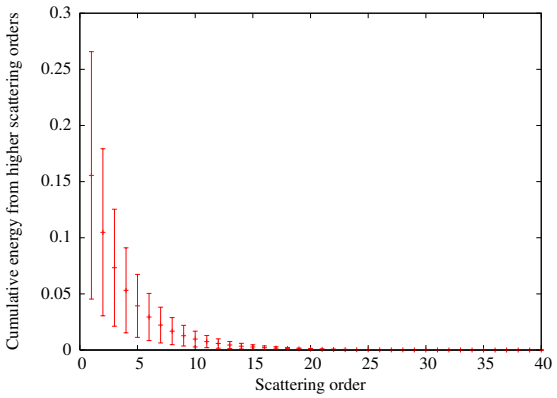

Figure 19: Fraction of energy at higher orders of scattering for a dense (99.9% canopy cover) forest

A set of twenty five simulations were run over different locations in a dense old and a sparse young Sitka spruce forest. Ray trees were allowed to include up to one hundred interactions (by which time there should be no contribution). The fraction of total intensity that would be truncated if the ray tree were limited to a maximum number of interactions (adding up over all ranges) was calculated for each footprint. The mean and standard deviation of the fractional contribution was calculated from these twenty five footprints.

No contributions were recorded above sixty interactions, so limiting to one hundred interactions has not affected the results' realism in any way. From figure 19 it can be seen that for the maximum multiple scattering conditions (dense canopy, high reflectance) around 84% of the signal comes from singly scattered light. Closer examination reveals that limiting the ray tree to 30 interactions would truncate only $6.5 \times 10^{-3}\%$ of the total energy with a standard deviation of $5.3 \times 10^{-3}\%$, a negligible fraction on the edge of a computer's floating point precision. After fifty eight interactions this fraction dropped below the precision of computer doubles and cannot be measured by the ray tracer (and so is effectively zero).

The analysis was repeated for the sparsest canopy (around 20% canopy cover) to see how

it varies. For this case 86% of the signal comes from single scattered light and rays stopped contributing after 42 interactions (after thirty interactions the contribution was 1.5×10^{-3}% with a standard deviation of 5.2×10^{-3}%). This shows that the number of interactions necessary to sample a scene is related to tree density, but the fractional contribution of multiple scattered light is not. The majority of the multiple scattering contribution was from low orders of scattering, possibly within individual tree crowns so that tree density does not affect it.

Therefore limiting the ray tree to thirty interactions should not limit simulation accuracy and will not take too long to compute (a few hours for the most complex scenes on a 2GHz processor).

Number of rays Again the densest, oldest and so most complex forest was used to determine the number of rays required to accurately characterise a 30m diameter footprint. With starat the number of rays was controlled by the number of segments in a footprint and the number of rays per sector. Care must be taken not to make the solid angle of the sectors too small, to avoid any danger of rounding issues in the jittering of rays within segments.

Simulations were run with different numbers of rays, at first with one ray per sector until the solid angle became small, at which point the sector size was limited and the number of rays per segment increased.

The literature reports a range of methods to ensure adequate sampling, however these are mainly for psycho-physical results (Koenderink and van Doorn 1996). Whether an image would look correct to a person is not of interest, only the reflectance with range. The method of (Hofton *et al.* 2000) uses a cumulative threshold of 1% of the total energy to remove noise, therefore it would be sensible to ensure that the measured intensity is correct to this level. For safety the accuracy should be higher than this, if computational expense allows.

From figure 20 it can be seen that the fractional variation was relatively small compared to the overall intensity, even down to a hundred rays. The variance began to flatten off at around five hundred rays reaching a plateau at around two thousand rays, suggesting that there is little point in using more than this many rays. For these forests one thousand rays would seem to be a sensible number. Not as many samples were available for the dense forest due to the extra computational expense but one thousand rays would seem to be sufficient.

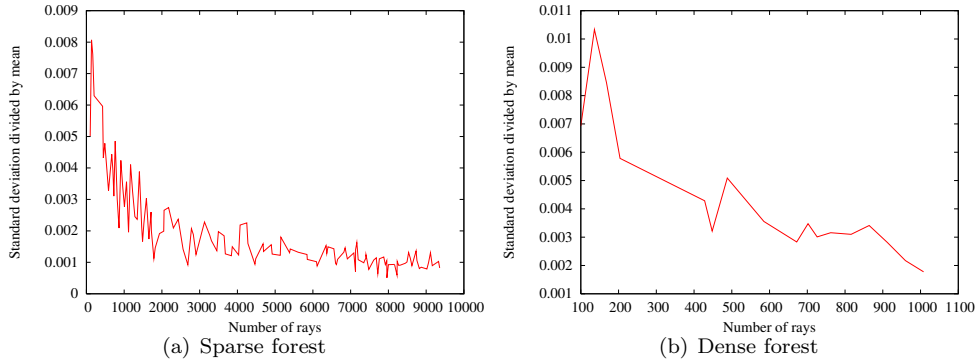

(a) Sparse forest (b) Dense forest

Figure 20: Standard deviation divided by mean against number of rays for a 30m footprint over Sitka spruce forests

Below canopy lidar The thesis will also include simulations with CSIRO's Echidna ® terrestrial lidar (described in section 5.14). This has a much smaller footprint than the above canopy instruments, a beam divergence of between 2mrad and 15mrad from a starting diameter of 29mm (Jupp *et al.* 2009) giving a footprint of between 49mm and 179mm at a range of 5m and between 149mm and 929mm at a range of 30m and so fewer elements will contribute and fewer samples should be needed per beam.

Forests Echidna simulations take a considerable amount of time and computer resources to complete. Even at the coarsest resolution (15mrad beam divergence) a full scan between -100^o and 100^o zenith contains 48,740 individual beams, therefore only segments of the scans will be investigated. The total canopy density is less of an issue than it is for large footprint lidar as the beam footprint will always be completely filled by a single tree and it is unlikely that light will be multiply scattered into an adjacent crown and back into the field of view. For this reason sparse canopies will suffice, using only small sectors covering trees.

The small footprint of Echidna means that some returns may come entirely from hard targets, such as trunks, which are unlikely to have any contribution from multiple scattering so the search for convergence was limited to diffuse targets (targets which have returns in multiple range bins).

Comparing figure 21 to figure 19 it can be seen that the smaller footprint of Echidna leads to much smaller contributions from multiple scattering. In this case light makes no contribution after twenty interactions whilst limiting the ray tree to only five orders of scattering would truncate

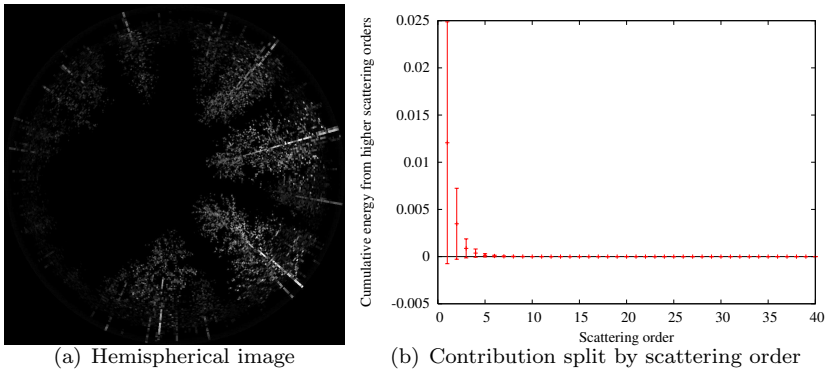

(a) Hemispherical image (b) Contribution split by scattering order

Figure 21: Intensity of contribution against scattering order for Echidna simulations of a sparse birch canopy at 920nm

only $6.4^{-3}\%$ of the energy, around the precision of a floating point.

As footprint size is proportional to range it is reasonable to assume that more distant targets may have more multiple scattering than closer targets. Examining a different sector with more distant trees (at 8.5m rather 7m) gave similar results, with multiple scattering contributions completely disappearing after twenty orders of scattering, although the fraction stayed above $10^{-3}\%$ until seven orders of scattering, adding weight to the argument that that larger footprint sizes include more multiple scattering.

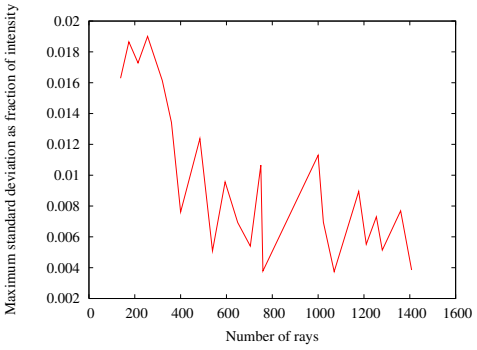

Figure 22: Maximum standard deviation between ten different samples against number of samples for an Echidna simulation of a birch forest

Sitka spruce, with its needle shoots, should suffer much more multiple scattering than birch and on a much smaller scale. To save computations with the more complex scenes only a single sector was examined, containing distant trees.

For Sitka spruce, whilst multiple scattering contributed 7% with a standard deviation of 6% of

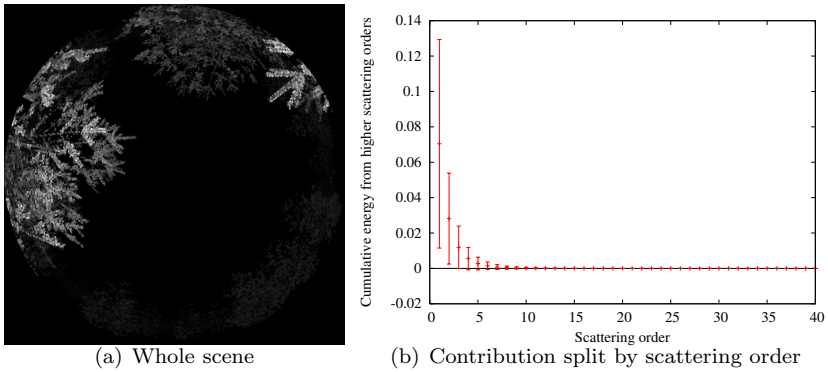

(a) Whole scene (b) Contribution split by scattering order

Figure 23: Intensity of contribution against scattering order for a Sitka spruce canopy at 920nm

the total energy. The contribution dropped below the precision of a double variable after thirty six interactions and down to 4.8×10^{-3}% with a standard deviation of 1.4×10^{-2}% after thirteen interactions. Therefore a limit of thirteen interactions will not affect simulation accuracy. In fact all orders of scattering beyond four contributed only 1% of total energy, so a much lower ray tree limit may be acceptable if computation time becomes an issue.

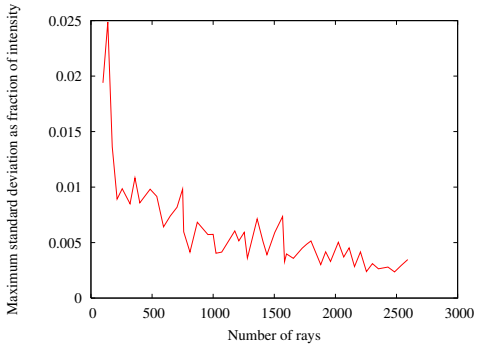

Figure 24: Maximum standard deviation between ten different samples against number of samples for an Echidna simulation of a Sitka spruce forest at 920nm

From figure 24 it can be seen that using one thousand samples would have a maximum error of around 0.5%. For a beam divergence of 15mrad this corresponds to segments of solid angle 4.8×10^{-8}strad and 11 rays per segment. This sampling number will be used for all 15mrad beam divergence simulations with Sitka spruce forests. At this sampling rate each beam took a maximum of 31 minutes and a mean of 8 minutes on a 2GHz processor. This is for the most complex portion of the forest and so it should be possible to complete a number of complete scans within a reasonable

time.

With this level of sampling and the lack of assumptions of ray tracing described in section 2.2.3 the ray traced signals can be taken as accurate representations of reality. Inversion algorithms can be tested as if the signals were real data and compare the results against a known truth, a feat impossible in reality (Pinty *et al.* 2001). Of course more intelligent sampling could be employed, with denser sampling around curved and complex areas than flat planes or empty sky, but this thesis is about understanding the physical processes that make up lidar signals, not about ray tracer development so the extra effort will not be expended, even though it means wasting some computer time.

4.1.2 Variable field of view

The contribution from multiple scattering is likely to increase with beam divergence, as suggested by comparison of the fraction of multiple scattering for 30m footprint above canopy simulations and Echidna (figures 19 and 23). Echidna has a variable beam divergence and so different settings may need different numbers of rays and maximum interactions to adequately sample the scene. The fraction of energy that would be truncated if the number of interactions of a ray were limited was recalculated for a number of different beam divergences, shown in figure 25.

Whilst there was an increase in the contribution from multiple scattering with beam divergence, it was not dramatic. For all cases tested the average contribution falls below 1% of the total energy after four interactions and drops below 10^{-3}% after fifteen interactions; this is not what was expected. To see why the experiment was repeated with a regular array of small spheres (with diameters less than half the laser footprint) and the results, in figure 26, show that in this case the increase in contribution with beam divergence was much more pronounced. This suggests that for Sitka spruce the multiple scattering did not increase as expected because of irregularity of the arrangement of scattering elements.

In the regular array of spheres used in figure 26, as the field of view increases more and more scattering elements were measured within each range bin and so there was an increased chance of scattered rays striking an object within the field of view and contributing whilst the singly scattered contribution was unaffected. In real forests scattering elements are clumped, so increasing the

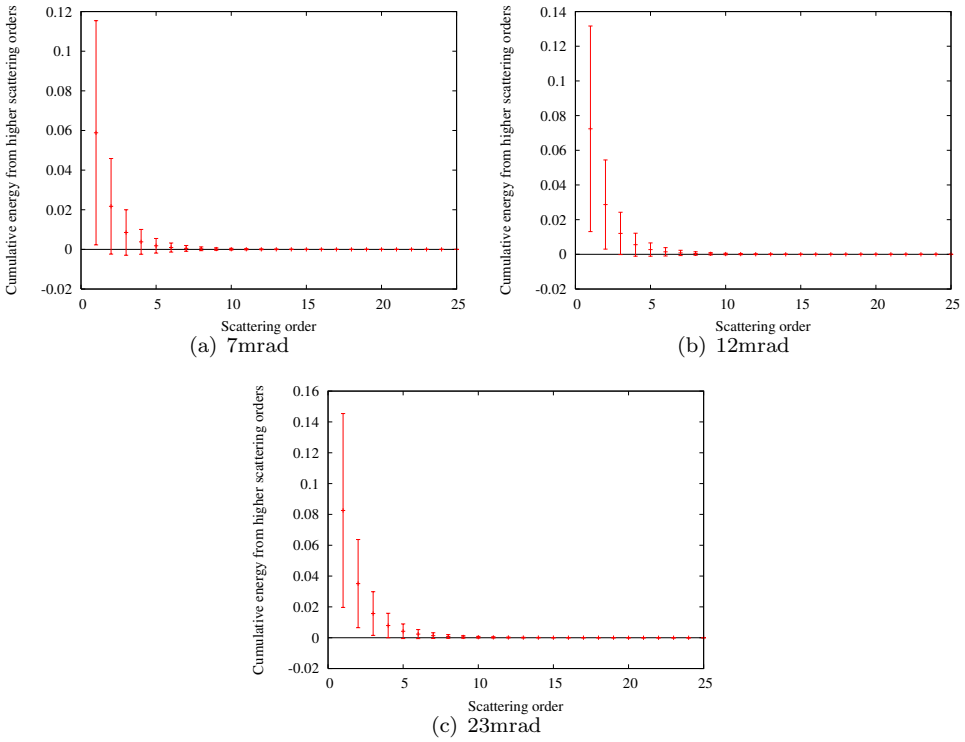

(a) 7mrad (b) 12mrad

(c) 23mrad

Figure 25: Fraction of energy truncated if the ray tree is limited against maximum number of interactions for a range of beam divergences over a Sitka spruce forest

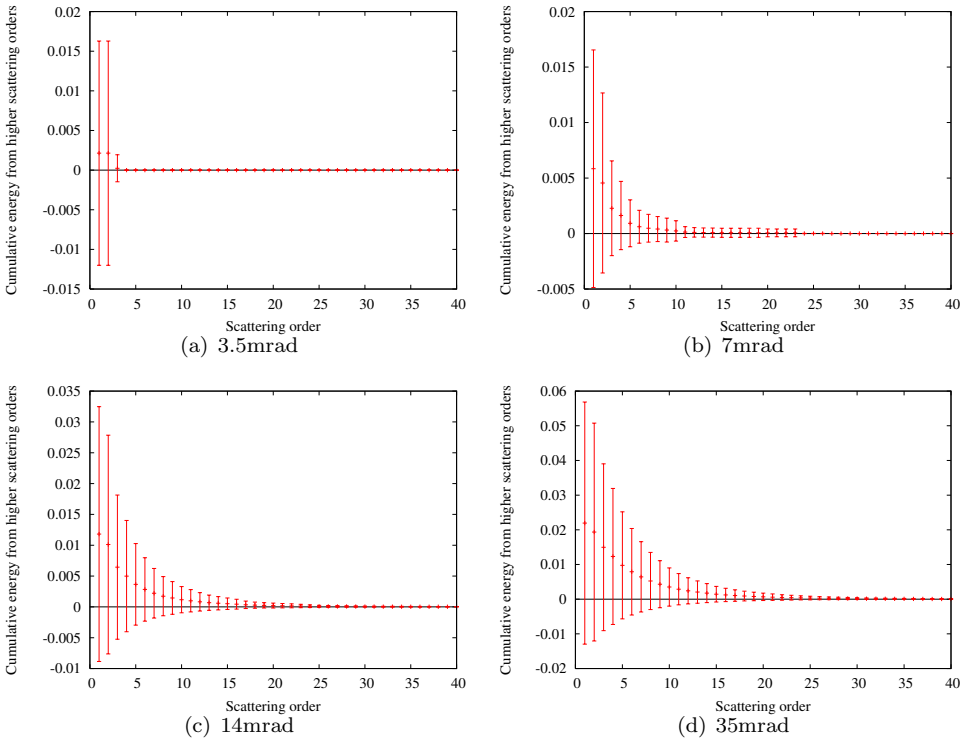

Figure 26: Fraction of energy truncated if the ray tree is limited against maximum number of interactions for a range of beam divergences over an array of small spheres

beam divergence will not necessarily increase the number of scatterers within a range bin and so the contribution from multiple scattering will not increase. Most of the multiple scattering would seem to be within a single shoot.

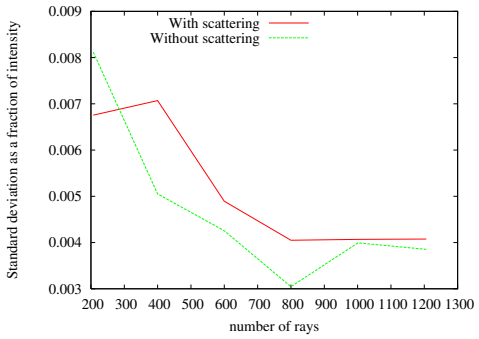

Figure 27: Standard deviation of measured intensity between ten scans with different random number seeds against number of rays for different beam divergences in a Sitka spruce forest

In real instruments the field of view is unlikely to be be exactly equal to the beam divergence. This would need very precise alignment to ensure no laser energy is wasted and so the field of view tends to be greater than the beam divergence. The only Earth orbiting spaceborne lidar, ICESat has a much larger field of view than beam divergence to allow a degree of pointability (Schutz *et al.* 2005). The viewed area outside the illuminated footprint cannot contain any directly reflected radiation but will contain multiple scattered light, therefore this setup will increase the contribution from multiple scattering. Figure 28 shows that the relationship between the contribution from multiple scattering and field of view was very similar to that for beam divergence, with a very slight increase but not so much as to require a higher limit for maximum interactions. Again the effect was a far more pronounced for a regular array of spheres than for Sitka spruce, but as this situation is unlikely to occur in forests the results are not presented.

This section suggests that the number of rays and orders of scattering already chosen (twenty orders of scattering and one thousand rays per beam), will not limit the simulation accuracy for any beam divergence or field of view likely to be used in a real below canopy instrument. It will be possible to use lower limits whilst keeping the error below 1% if computational time becomes an issue, particularly for the narrower fields of views and beam divergences. More regular scattering objects may require increased sampling, but such situations are unlikely to occur in forests.

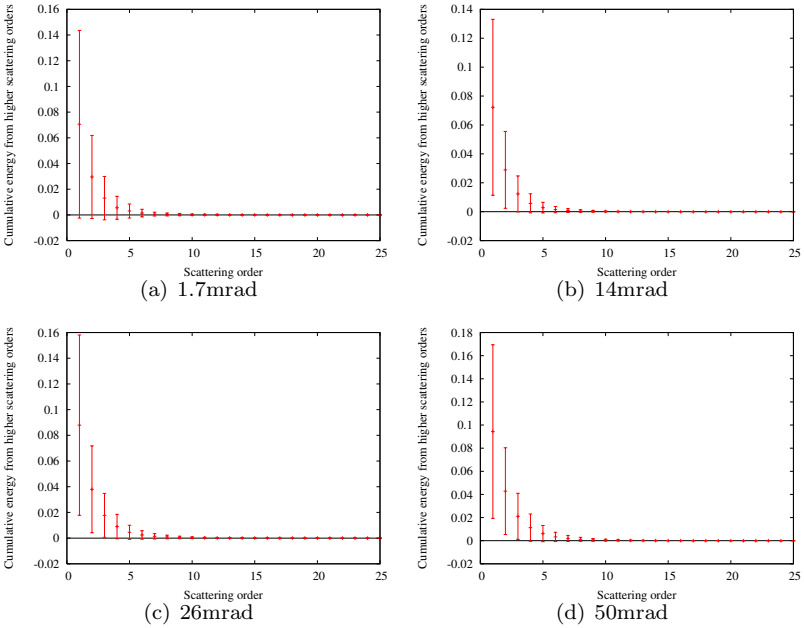

Figure 28: Fraction of energy truncated if the ray tree is limited against maximum number of interactions for a range of fields of view with a fixed beam divergence of 14mrad in a Sitka spruce forest

4.1.3 Noise

All real instruments suffer from unwanted noise and this can cause errors in inverted parameters. Any potential method must be able to cope with noise, even if it reduces their effectiveness in unnoised cases and so noise must be included in the simulated data to see how the inversion algorithms would perform in real life. Using a range of noise levels allows us to determine the system parameters (laser power and detector efficiency) required to collect usable data. The ray tracing process is computationally expensive, taking several hours per simulation, it would take a prohibitive amount of computer resources to run a particular lidar waveform with a range of noise levels applied during tracing. Therefore all simulations were run without noise, it being added just before inversion.

A real lidar suffers from noise caused by photon statistics, background light and detector noise and each of these must be accounted for. Photon statistics, also called "photon noise", n_{photon}, is caused by the random arrival rate of photons to the detector (Kovalev and Eichinger 2004). This can be modelled as Gaussian with an amplitude proportional to the square root of the number of photons arriving in a ranging bin, N_{photon}, the more photons in a given bin the greater the

magnitude of the noise but the smaller the relative error. This is a fundamental physical effect and cannot be reduced.

The ray tracer returns an apparent reflectance value, the reflectance of the scene relative to a white Lambertian surface perpendicular to the laser beam. For noise to be applied this must be converted into an energy, which is done by assuming that a given number of signal photon (without noise) are returned. The simulated reflectance is scaled to contain this many photons, then noise applied. This is rescaled to apparent reflectance for any inversion algorithms. The photon statistics noise is then;

$$n_{photon} = N_{photon}\sqrt{-\ln(k)} \tag{27}$$

Where k is a random number between 0 and 1. This is called from a pseudo-random number list in the C program, every subsequent call gives the next value in the list. The random number can be "seeded" to start at any point in the list so that different sets of noise can be added to the same waveform, giving a more general idea of the effect of noise and avoid skewed conclusions from abnormal spikes.

The detector will record all light incident upon it, whether it comes from the laser, sun or atmospheric scattering. All light from sources other than the laser will cause background noise. The amount can be limited by filtering out all wavelengths other than the laser's and keeping the field of view around the same size as the laser beam divergence (although the closer the two are in size the harder the system is to align), but it can never be completely removed. The energy from background illumination reaching the detector, $P_{background}$, can be found by multiplying the sun's radiant flux at the laser wavelength I_{sun} by the field of view solid angle T_{fov}, the cosine of the solar zenith θ_s, atmospheric transmittance T_{atm}, filter bandwidth Λ_{width} and the length of a range bin L_{bin}.

$$P_{background} = I_{sun}.\frac{T_{fov}^2}{4}.A_t.\cos\theta_s.T_{atm}.\Lambda_{width}.L_{bin} \tag{28}$$

Note that only the one way atmospheric transmission is needed as I_{sun} takes the attenuation from the sun to the ground into account. The number of background photons, $n_{background}$ can

be found by scaling by Planck's law (equation 29). This gives the number of background photons reaching the detector per unit time, not all of which will be recorded.

$$N_{photon} = \frac{P}{h\nu} \tag{29}$$

Where P is the light's power, h is Planck's constant and ν is the frequency of electro-magnetic radiation.

Background photons also arrive at a random rate and so the value is rescaled by a random number and then the detector's quantum efficiency, QE, to get measured photons;

$$N_{background} = \frac{P_{background}}{h\nu}\sqrt{-\ln(k)}QE \tag{30}$$

The detector will suffer from shot noise, thermal noise, amplifier noise and the dark current. For a well made detector (such as would be used in a satellite) these sources of noise should be negligible compared to photon statistics and background light (Kovalev and Eichinger 2004). They were not included in the simulations, slightly conservative overestimates being used for the other sources.

$$n_{detector} \ll n_{background} \tag{31}$$

The total noise is the root of the sum of the squares of the individual noise elements multiplied by the noise excess factor, F.

$$n_{total} = \sqrt{(n_{photon}^2 + n_{background}^2 + n_{detector}^2).F} \tag{32}$$

The values used in the above equations are;

$T_{atm} = 0.8$

$\theta = 0$

$A_t = \pi.0.5^2 m^2$

$T_{fov} = 200\mu radians$

$QE = 0.5$

$\Lambda_{width} = 1nm$

$n_{detector} \approx 0$

$F = 2$

These were all over cautious estimates, erring on the side of increased noise. The solar intensity at ground level is taken from Neckel and Labs (1984) and is shown in figure 29.

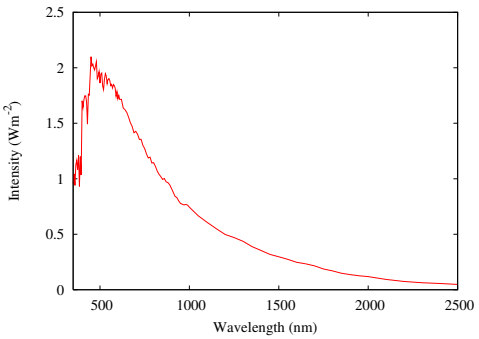

Figure 29: Solar intensity at ground level used to calculate background noise

The noise here is based upon the number of signal photons. To convert this to the required laser power it should be converted into an energy (with Planck's law) then be scaled by the two way atmospheric transmission, telescope size and detector efficiency. In ray tracing the finite number of rays results in incomplete sampling, known as Monte-Carlo noise (Metropolis and Ulam 1949) and is directly analogous to the photon noise described above. However, to use the number of rays traced to control photon noise would require separate simulations for every noise level investigated. Therefore it was decided to carry out a single noiseless (as near as possible) simulation for each experiment, allowing a range of noise levels to be applied afterwards and saving a great deal of computer time.

This thesis is not concerned with building an actual instrument, only in developing an algorithm that can cope with data from a real instrument. Therefore no attempt will be made to suggest necessary laser powers, only the minimum number of signal photons needed to ensure that noise will not limit accuracy. All results will be an over cautious lower limit and it may be possible to reduce this number with more accurate engineering modelling.

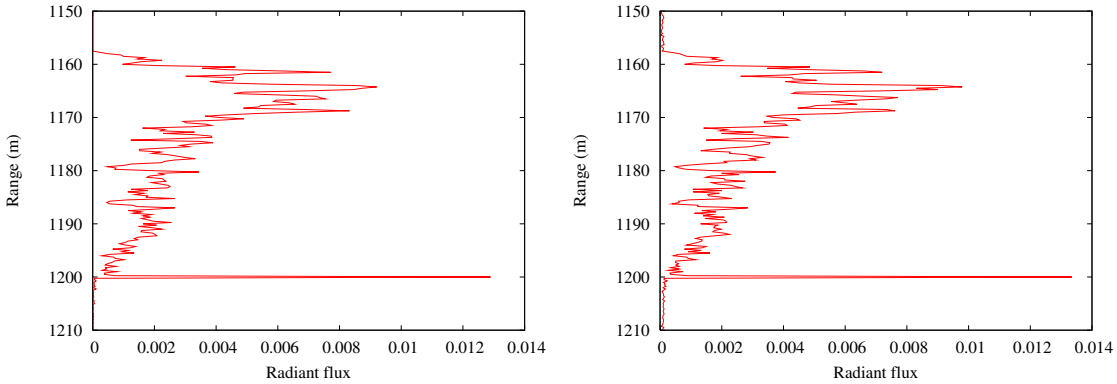

(a) unnoised

(b) 15,000 signal photons

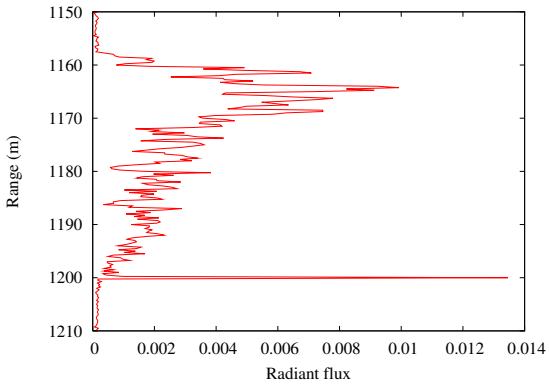

(c) 10,000 signal photons

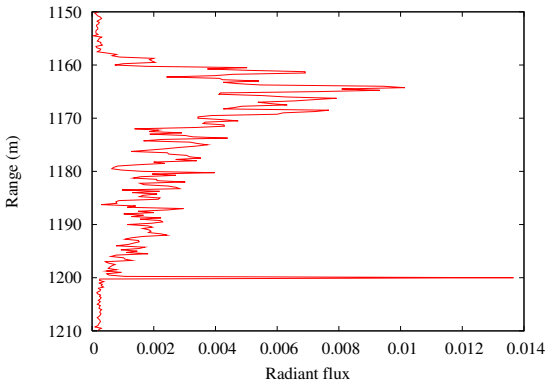

(d) 6000 signal photons

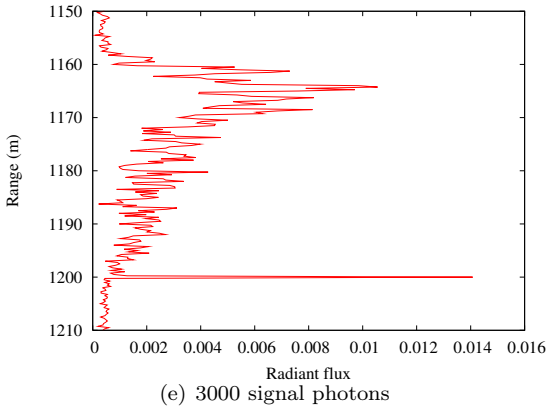

(e) 3000 signal photons

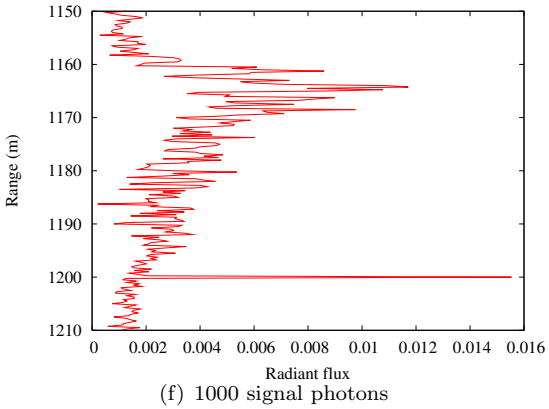

(f) 1000 signal photons

Figure 30: Simulated waveform with different levels of noise applied

4.1.4 Laser pulse

All lasers emit a pulse with a finite length (Baltsavias 1999). An infinitely short pulse would require an infinite intensity to contain any energy, similarly the longer the laser pulse the greater the outgoing energy can be made for a given intensity, allowing very high energy lasers whilst staying eye safe and below component damage thresholds. The recorded waveform will be blurred, or convolved, by the outgoing pulse, complicating inversion. This blurring and subsequent extraction will be discussed in detail in the next chapter but the effect must be included in the ray tracer to allow testing of algorithms on fully realistic data.

The majority of pulses can be modelled as Gaussian (such as ICESat and LVIS (Hofton *et al.* 2000)). For a Gaussian pulse the intensity I at a range r is given by;

$$I(r) = \frac{1}{\sigma\sqrt{2\pi}} e^{\frac{-(r-\mu)^2}{2\sigma^2}} \tag{33}$$

Where σ is the pulse length and μ is the range to the scattering object.

Some instruments have a slight forwards skew, a sharpening of the signal start and extension of the tail (such as Echidna (Jupp *et al.* 2009)). This skew can be modelled as a log normal pulse, the intensity of which is given by;

$$I(r) = \frac{1}{(r-\mu)\sigma\sqrt{2\pi}} e^{\frac{-(\ln(r-\mu))^2}{2\sigma^2}} \tag{34}$$

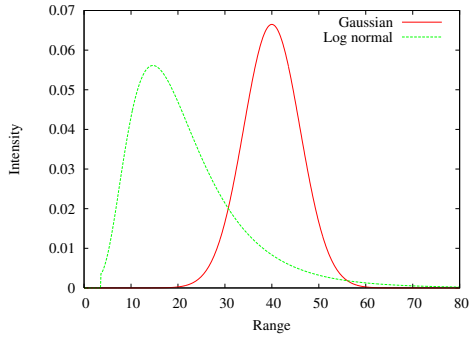

Figure 31: Example of a Gaussian and a log normal pulse

In the ray tracer the pulse shape is stored in an array, taking care to Nyquist sample it with respect to the lidar's range resolution. It can then be convolved with the measurements to produce

a pulsed return.

It would be computationally efficient to make a single trace of a scene then convolve with the pulse just before analysis, in the same way as noise is applied. However this would not capture all the physical processes. During the simulated recording the waveform is digitised into discrete bins, the exact range within a bin that a ray originated from is not recorded. If the waveform were convolved after recording would have to be assumed that, on average, all objects were in the centre of the bin, giving perfect Gaussian returns. This will not always be the case, as illustrated in figure 32. The digitisation of the waveform into discrete bins causes complications to inversion (see section 5.9), particularly if some form of deconvolution is used.

For this reason the pulse shape was convolved with each return before digitisation. Every separate pulse length and shape needed a new simulation, but realism was not compromised. Figure 33 shows different pulse lengths applied to simulated lidar waveforms over the same forest.

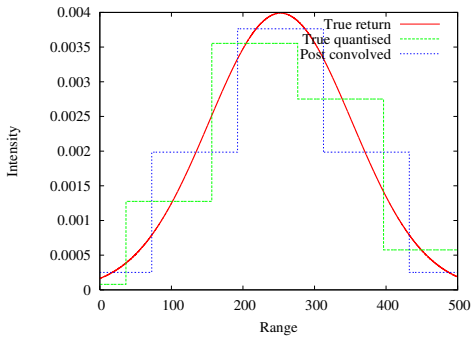

Figure 32: Example of quantisation of an off centre pulse

4.1.5 Wavefront

The energy is rarely constant across a laser beam (Wilson and Hawkes 1987), this distribution of energy is known as the "laser wavefront". Often the laser intensity is greater in the centre of the beam than at the edge and the distribution can be modelled as a Gaussian. Figure 34 shows the energy distribution of a flat and a Gaussian wavefront, both contain the same amount of energy. From this it can be seen that with a Gaussian wavefront, objects in the centre will contribute far more to the signal than objects towards the edge.

Applying this effect after tracing would require the spatial distribution of returns within a

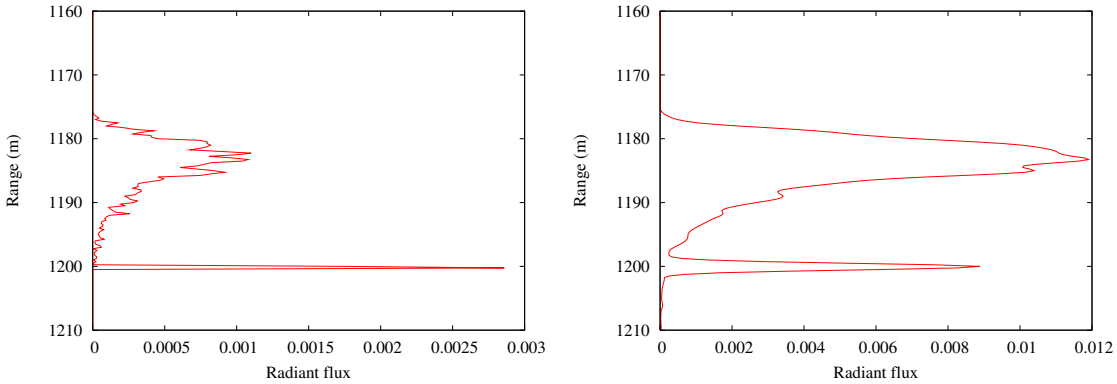

(a) Infinitely short pulse

(b) 7ns pulse, TopEye II

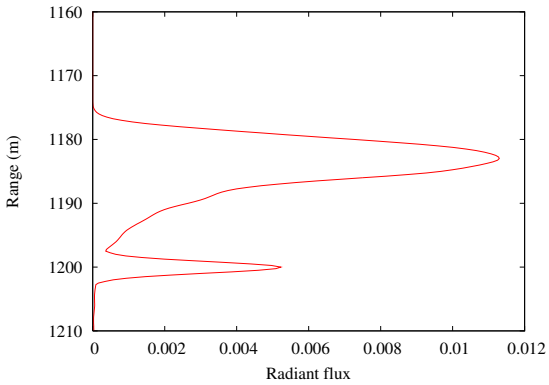

(c) 12ns pulse, ICESat

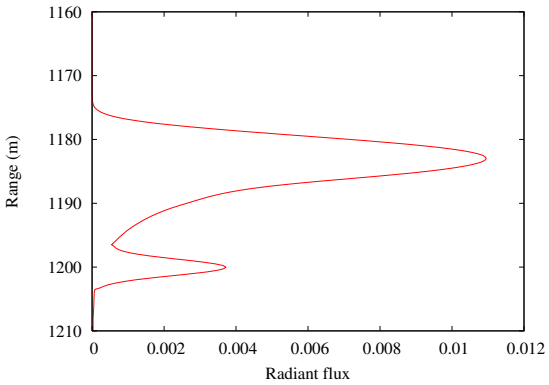

(d) 16.9ns pulse, LVIS

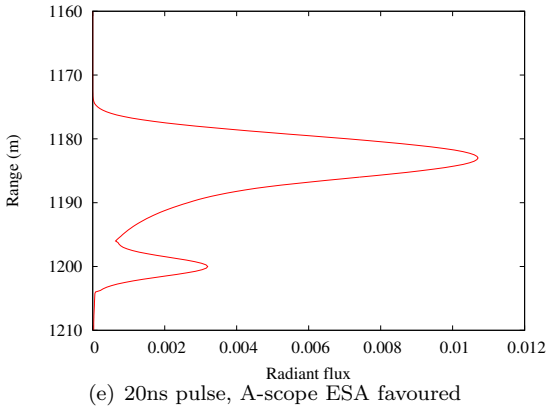

(e) 20ns pulse, A-scope ESA favoured

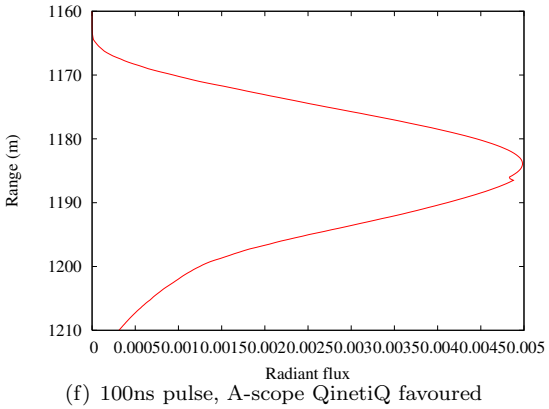

(f) 100ns pulse, A-scope QinetiQ favoured

Figure 33: A waveform blurred by laser pulses of different durations

footprint to be recorded, combined with multiple range bins and the beams of Echidna this would be a prohibitive amount of information and so it must be applied during ray tracing. Like the laser pulse length, this will require a separate trace for every different wavefront, but ensures that the simulations are as realistic as possible.

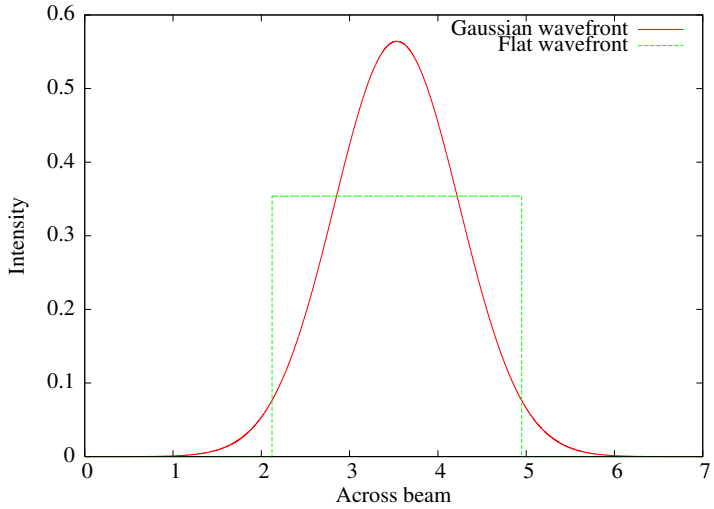

Figure 34: Illustration of laser wavefront

Simply weighting the returned intensity by its position within the laser footprint would mean that rays towards the edge will be contributing less to the final signal than rays in the centre, but require the same number of computations. A more efficient method is to vary the density of rays with laser intensity, a form of importance sampling (Foley *et al.* 1992). Starat achieves this by changing the number of rays per pixel in figure 18 to follow a Gaussian distribution. This will result in a slightly quantised wavefront and so a correction factor was applied to the intensity from each zenith range to give the correct energy distribution. Figure 35 shows the effect of a laser wavefront on the weighting of returns.

4.1.6 Recording mode

It would be advantageous to be able to simulate instruments with different recording modes, such as discrete return lidars (see section 3.5 for a description). The ray tracer records only the full waveform, which is the signal that any detector type would receive (with some range quantisation). This can be modified to a discrete return signal after tracing, so that one simulation can represent

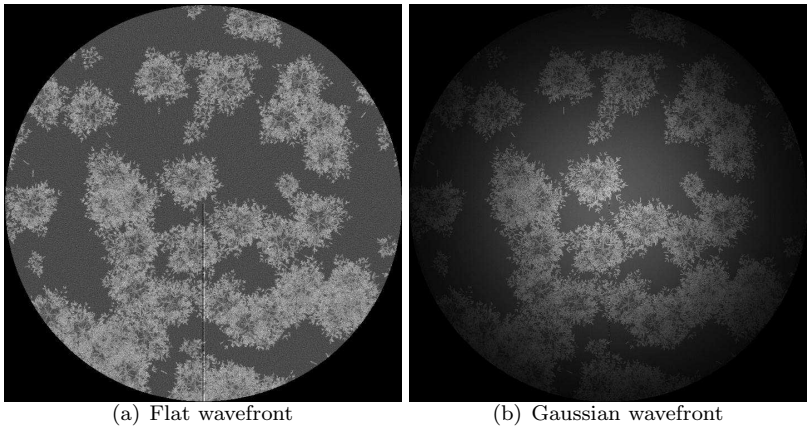

(a) Flat wavefront (b) Gaussian wavefront

Figure 35: Image of a 30m lidar footprint with a flat and Gaussian wavefront

any recording mode.

As this is performed after tracing a description will not be given here but in the analysis chapter.

4.1.7 Additional variables

The ray tracer can record variables that would be impossible with a real instrument. These can be used to explore the different physical processes contributing to the measured signal and help evaluate sources of errors in inversion.

In addition to the intensity with range at different wavelengths, starat recorded the intensity against order of scattering and the fraction of the field of view filled by each material. The fractional area of each material gives the projected area and so the gap fraction, very useful when evaluating Beer-Lambert based methods. Separating returns by scattering order allows us to test inversion algorithms with and without multiple scattering, gradually developing them to cope with more realistic situations. It was also used to perform the tests shown in section 4.1.1 from single simulations.

Other variables could be returned by the ray tracer but unfortunately there was not enough time to implement them. A very interesting metric would have been the mean free path of scattered rays. This should be related to scattering element density and so clumping, it may even have been possible to see different scales of clumping in a histogram plot. Of course a real instrument would not be able to measure mean free path, but as will be shown later, it may be possible to relate it

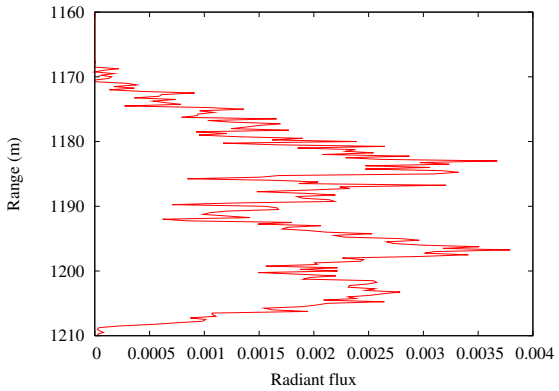

(a) Waveform at 1064nm

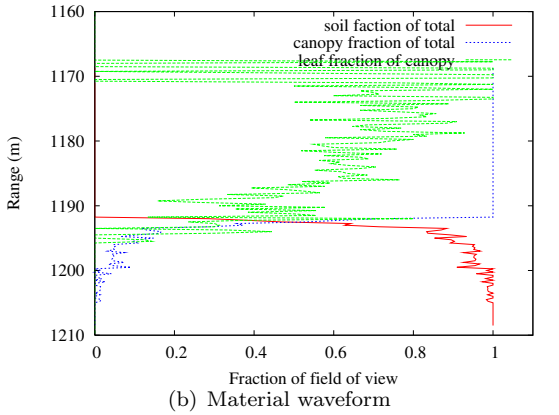

(b) Material waveform

Figure 36: Material waveform from LVIS like starat simulations over a Sitka spruce forest

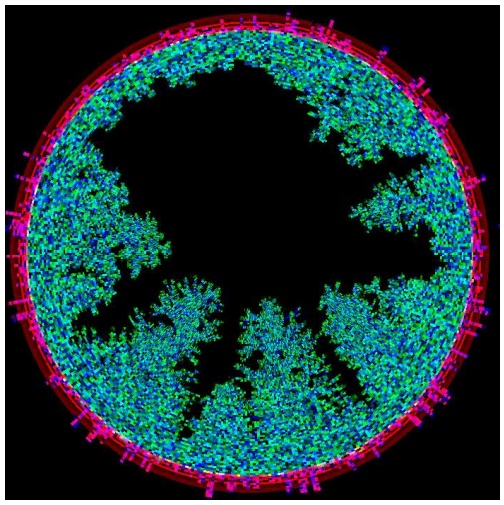

Figure 37: Material map of an Echidna scan

to other metrics.

The angle of incidence of rays on objects (related to LAD) was not explicitly recorded, although it could be determined for each material by combining the material information with known reflectances and multi-spectral intensity and so the phase function and visible surface area could be extracted.

4.2 Creation of the forest models

To minimise assumptions and avoid effective parameters that may hide important physical processes, fully geometric forest models were used. Certain assumptions were made to speed up computation and reduce the data storage required. These were that all surfaces are perfectly Lambertian and that all elements of a certain kind (whether leaf, wood or soil) have a single reflectance and transmittance spectrum. The assumption of Lambertian surfaces greatly speeds ray tracing, without it a separate brdf would be needed for each element type, which would have to be interrogated at each interaction. Such element brdf measurements are not readily available and in the absence of such data Lambertian reflectance must be assumed, hoping that any deviation will average out at the scale of measurements. It was not possible to do a direct assessment of the impact of the assumption of Lambertian surfaces in this investigation due to the lack of element brdf measurements and the time this would have taken to integrate into the ray tracer library.

The assumption of uniform spectra can easily be tested by examining the variance of spectra measured for the same species at a variety of locations and samples. This will be covered in section 4.2.2.

4.2.1 Geometry

The investigation focused on two species, Sitka spruce and birch, based upon measurements of Thetford forest in the UK and Abisko in Sweden respectively. These cover both needle leaf and broad leaf trees and so should give a picture of the broad behaviour of these main classes. Data from other species were available, but due to the computational expense of forest creation and ray tracing there was not enough time to simulate data for all the necessary experiments for more than these two species.

Individual Sitka spruce tree models were created with the Treegrow program (Disney *et al.* 2006). As these were not created specifically for this thesis but taken from earlier studies only very brief details of the program's operation will be given. Tree models are created based upon the age and density of the forest in which they grow. Growth rules are used to describe the formation and death of branches, then needle shoots are cloned to the relevant locations afterwards. This is a stochastic process, so a random number seed can be adjusted to give different trees of the same age class and growth conditions. For this thesis six different aged trees were used, 5, 9, 12, 20, 30 and 40 years old with four or five different trees at each age class.

Figure 38 shows one of each of the six different aged Sitka spruce trees; that they appear convincing gives us confidence in their geometry. A more rigorous evaluation of the precise geometry would be tedious and time consuming (Bréda 2003), so was not attempted. Simulated remote sensing signals were validated against real data and the two found to agree (Disney *et al.* 2006), although this does not rule out an error in either the ray tracer or the forest model, only the combination of the two.

Figure 38: Ray traced images of six different aged Sitka spruce tree models, taken from Disney at el (2006)

Plant growth models such as Treegrow require a lot of effort to create, being based upon detailed structural measurements for plants at a range of ages and growing conditions and so few have been written for academic studies. The computer graphics community is a much bigger user of forest

models and programs are commercially available. One such model is Onyx (Onyx Computing Inc 2009), this is a parametric model, using a small set of parameters to create tree like structures in much the same was as L-systems (Lindenmeyer 1968a). Some manual tweaking is needed to ensure that the trees match those at the field site and Onyx includes a graphical display to allow easy comparison to photographs. The creation of each tree is a little more labour intensive than with Treegrow and requires supervision but the parametric approach is more easily adaptable to a wide range of species than growth rules. For this reason all other trees used in this thesis were created with Onyx, using photographs and some basic measurements from particular field sites as guides.

As part of the Abacus (Disney *et al.* 2009) experiment measurements were made of Arctic birch in Abisko in Sweden. From a set of basic dimensions (*dbh*, tree height, crown extent and photographs) three different birch trees were grown (one is shown in figure 39).

Figure 39: Ray traced images of a single birch tree model created with Onyx compared to a photograph from the field site

These trees were used to create forests of different densities on different ground slopes. The density was set by defining the number of trees per 30m by 30m plot (to ease parametrising from field data); trees were cloned at random locations within a sub box, which formed a bounding box in the ray tracer. Trees were rotated and shifted downwards by a random amount to prevent unnaturally regular forests. A minimum separation was enforced to prevent trees growing on top of one another, although they were allowed to intersect to allow very dense canopies.

For Sitka spruce, combinations of different aged trees were used to represent a range of forest types, illustrated in figure 40. For uniform stands all trees were of the same age (figures 40(a),

40(b) and 40(c)) Bimodal canopies were created by using an equal proportion of the oldest and youngest trees (figure 40(d)) and mixed forests were created with an equal proportion of all age classes (figure 40(e)). In the mixed and bimodal forests the youngest trees are short enough to represent understory shrubs. Only equal proportions were used because at the scale of a lidar measurement, only a few trees will be visible, so samples from different locations in the same forest will give very different results.

The ground was modelled as a flat plane and topography was included by tilting this by a fixed angle (figures 40(f) and 40(g)). This will not model all topographic effects, but at the scale of lidar measurements (no more than 100m diameter) a sloped plane will suffice.

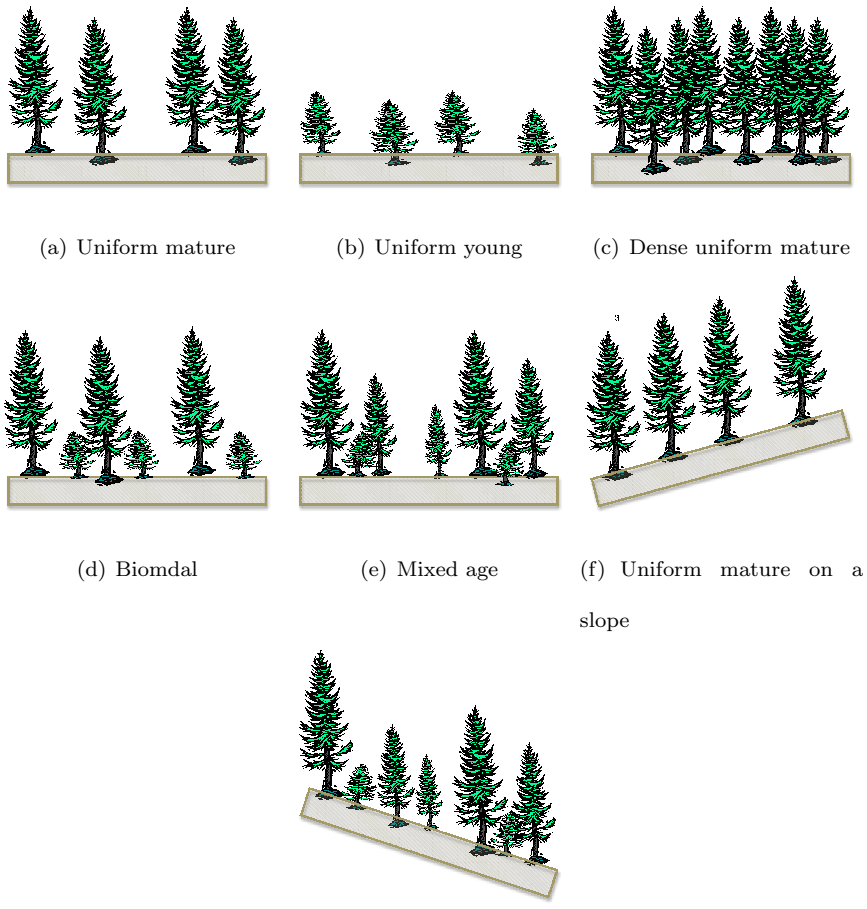

(a) Uniform mature (b) Uniform young (c) Dense uniform mature

(d) Biomdal (e) Mixed age (f) Uniform mature on a slope

(g) Mixed age on a slope

Figure 40: Illustration of the range of forest models used

During July 2009 field data were collected in the Sierra Nevada mountains during a campaign led by A. Strahler and R. Dubayah. This included the principal dimensions and photographs of

trees at a few specific plots and at around the same time measurements were made with both the terrestrial Echidna and airborne LVIS lidars so that simulated lidar signals can be directly compared to real data.

The dimensions measured were total height, height of the start of live crown above ground, crown width along and across slope, *dbh* and position relative to the plot centre; the average branch spacing and angles were also noted. Detailed measurements were made of needle shoots, including needle dimension along three axes, needle angles and spiralling patterns around twigs. This information was used to create a tree's woody architecture in Onyx.

Onyx outputs needles as triangular meshed surfaces, with no cloning or bounding boxes at all. This allows a wide variety of shapes but makes files large (almost 2Gbytes for a typical 30m tall red fir) and makes ray tracing prohibitively slow. As needle shoots were found to be so regular it was decided to replace the triangular meshes with cloned shoots formed from ellipsoids, greatly reducing the size of files and speeding ray tracing.

Growing and filtering trees with Onyx was still not a fast process, requiring several days of computer time (all unsupervised apart from the initial twenty minutes) per tree. For this reason only a small number of trees could be grown, not enough for a full stand.

4.2.2 Spectra

The main focus of this thesis was the measurement of forest structure and so whilst element spectra have an effect upon measured signals, only the relative reflectance of the different materials in a few broad bands are of interest. Separate simulations would be required for each set of spectra, vastly increasing computer time and so a single general spectrum was chosen for each element; leaf, bark and soil.

The Prospect model (Jacquemoud and Baret 1990) was used to create a leaf spectrum between 400nm and 2,500nm. Within Prospect there are a number of parameters that can be adjusted to recreate the spectrum of any species, these include leaf thickness, chlorophyll content and nitrogen content. The LOPEX spectral library (Hosgood *et al.* 1994) was used to choose suitable parameters for Prospect. Figure 41 shows that the resulting spectrum agrees fairly well with the average of the LOPEX database, particularly in the near infra red. The model gives slightly higher results

than the database in the visible, but still within two standard deviations.

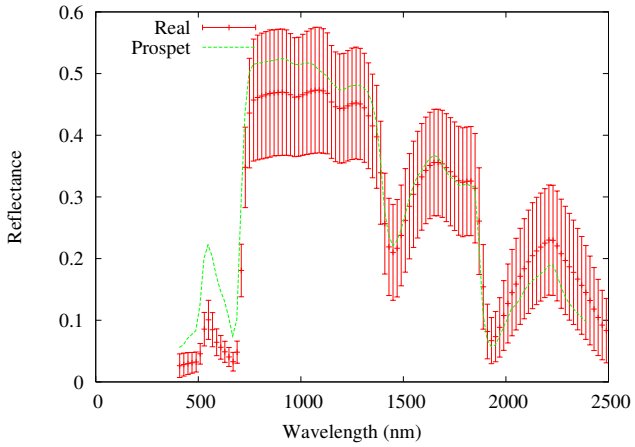

Figure 41: Comparison of Ponderosa pine reflectance spectrum from LOPEX to Prospect spectrum. Error bars show one standard deviation

The soil spectrum came from the model of Price (1990). Figure 42 shows a comparison of this spectrum to elements found on the floor of the Sierra Nevada forests in California. Whilst the field data only extended between 400nm and 1100nm, it can be seen that the Price spectrum roughly matches, though it is a little on the dark side. This should not be an issue as the Sierra Nevada soils are particularly bright. More of a problem would be short vegetation covering the ground, such as moss. This has a very different spectrum from soil and leaf litter and forests with mossy floors may give very different remote sensing signals than those with soil or leaf litter floors.

It was decided to use only soil spectra for the floor, but the methods should be tested over other floor types for generarality.

The bark spectrum came from the LOPEX database (Hosgood *et al.* 1994) and comparison with field data showed it to be slightly brighter but that it followed the same shape.

During the Sierra Nevada field campaign many measurements of element spectra were made for a range of species using an LI-1800 (LI-COR 1988) with repeat measurements for each species. These spectra only extended between 400nm and 1,100nm so could not be used on their own but could be used to assess the variance of spectra within species in this region. Figure 44 shows the spread of leaf reflectance values for the five samples each of the two most measured species during the campaign, red and white fir. The samples were taken from a number of sites and ages of trees.

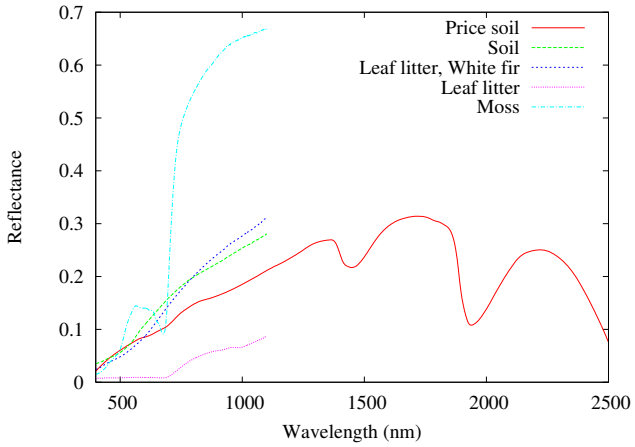

Figure 42: Comparison of soil spectrum from Price (1990) with data collected in the Sierra Nevada

Due to the difficulty in measuring the spectrum of a needle the measurements were made in a variety of ways. Some used many needles pressed together in multiple layers to ensure there were no gaps. This is the standard technique for fir needles (Daughtry *et al.* 1989) and will underestimate transmittance whilst possibly slightly overestimating reflectance. Other samples used a single layer of needles taped together as tightly as possible, trying to prevent any gaps but due to the curved edges this is impossible and transmission may be overestimated whilst reflectance might be underestimated (figure 43 shows sugar pine needles arranged in one layer for spectra measurement). Thus much of the variance shown may be due to the difference in measurement technique rather than the element spectra. There was not sufficient time to collect the many tens of samples needed to explore the exact cause of the variance, there being many other measurements that needed taking in the limited time available.

Even with the variations in measurement technique the variance shown in figure 44 is low (0.03 for white fir at 1,064nm for a mean reflectance of 0.66 and 0.05 for red fir for a mean reflectance of 0.70). Of course in the visible region, with its lower reflectance, the relative variance becomes much more significant and care should be taken when choosing wavelengths for a final instrument. This limited set of measurements suggest that it is fair to assume that leaf reflectance is reasonably constant within a species, certainly in the near infra-red where most lidars operate. The trees were predominantly coniferous and these showed brighter reflectance than the average LOPEX values, around the values of the Prospect spectrum, therefore it was decided that the slightly

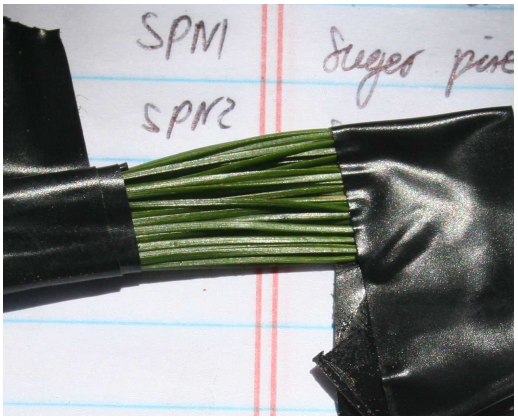

Figure 43: Sugar pine needles prepared for spectra measurement

higher spectrum was acceptable.

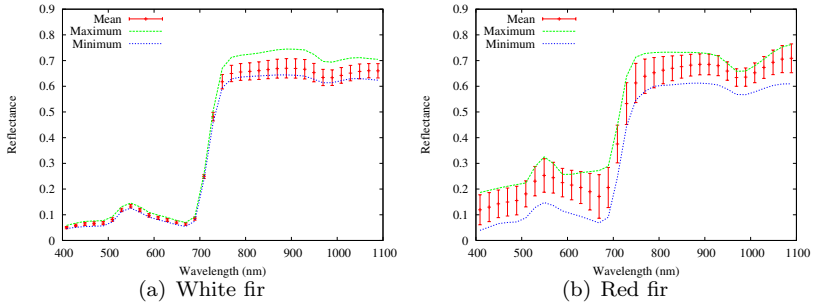

(a) White fir (b) Red fir

Figure 44: Spectra for needles over five samples per species from Sierra Nevada data. Error bars show one standard deviation

The spectra of eight pieces of sequoia bark and wood and five pieces of white fir bark are shown in figure 45. Bark shows much more variation within species than leaves, particularly sequoia which included both healthy and burnt bark. Burning reduced the reflectance to almost zero, causing the enormous variance in figure 45(b). The changes in bark reflectance caused by fire has been cited as a source of error in inversion from terrestrial lidar data (Jupp *et al.* 2009) and there seems to be little that can be done to correct for it other than manually noting burnt areas. The white fir samples in figure 45(a) did not include any burnt bark but still shows significant variance between samples. This variance seems to be mainly between different aged trees. On young trees the bark has a leaf like spectrum with a distinct red edge whereas older bark is much woodier and does not have this. For white fir at 1,064nm, the young trees' bark has a reflectance around 0.7

whilst older bark is around 0.4. Therefore the assumption of constant bark reflectance may not be appropriate, particularly between young and old trees.

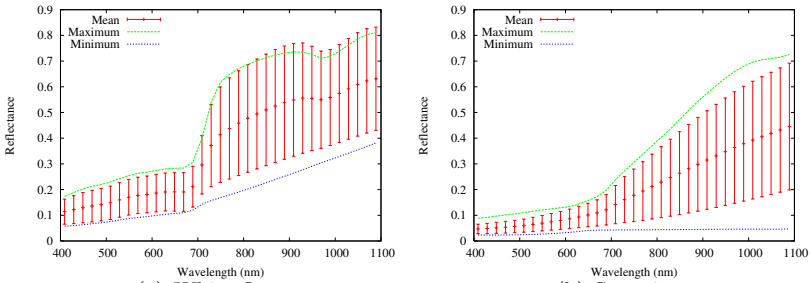

(a) White fir (b) Sequoia

Figure 45: Spectra for bark from Sierra Nevada data. Error bars show one standard deviation

The LOPEX database (Hosgood *et al.* 1994) is far more comprehensive and consistently measured than the data from the Sierra Nevada campaign, although it is not possible to determine the within species variation from it. It does give a good idea of the variation between species and figure 46 shows that this is similar to that found from the Sierra Nevada data within species, having a mean reflectance at 1,064nm of 0.47 with a standard deviation of 0.10 for sixty species.

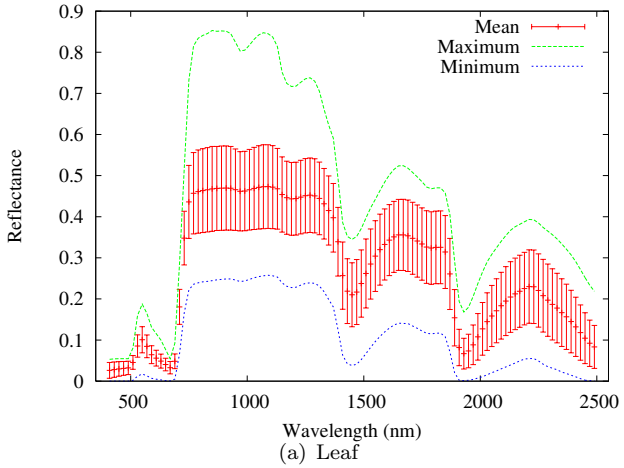

(a) Leaf

Figure 46: Spectra for leaves in the Lopex data. Error bars show one standard deviation.

Simulations were run with a wide range of wavelengths so that whilst the spectra used may not be entirely realistic, different wavelengths could be used that have more realistic reflectances for that element and so the narrow range of spectra used should not limit the accuracy of any results, only the certainty in the choice of particular wavelengths will suffer. There may be an issue with

forests that include a mixture of old and young bark.

The final spectra used for leaf, bark and soil for all forests are shown in figure 47. Figures 48 and 49 show colour ray traced images of the forests using these spectra. Whilst the spectrum used are not comprehensive they are sufficiently realistic to explore and understand lidar measurements. The soft focus and speckle noise in figures 48 and 49 appears to be an artifact introduced during the conversion from hips (the ray tracer's native image format) to an enhanced post script for display in the thesis. The original images (and so simulated data) do not suffer from such noise.

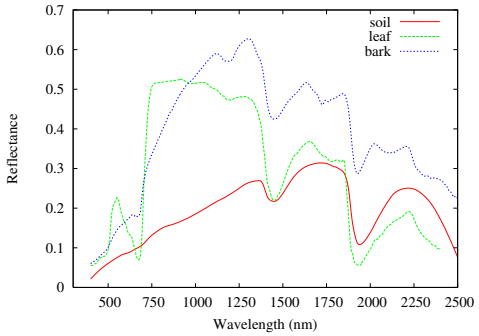

Figure 47: Spectra used for leaf, soil and bark

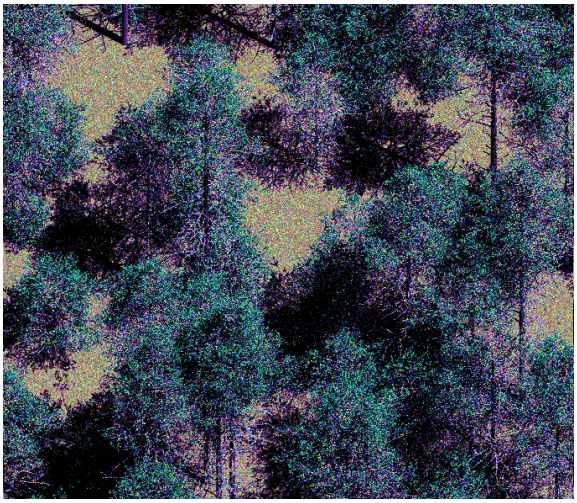

Figure 48: Ray traced true colour image of a Sitka spruce forest model

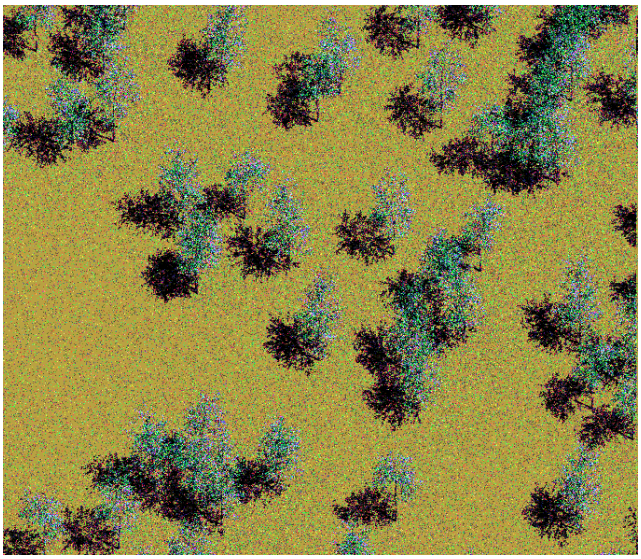

Figure 49: Ray traced true colour image of a birch forest model

4.3 Simulator conclusions

This chapter has introduced the simulation tools and models that will be used to investigate the performance of a range of lidar systems over different forest scenes. The ray tracer developed is capable of simulating all current airborne, spaceborne and terrestrial lidar systems capable of forest measurement as well as those likely to become available over the next few years. Experiments were carried out to determine the most computationally efficient parameters to use without limiting the simulation's accuracy, maximising the number of simulations that can be run within the time available.

The next two chapters will concentrate on developing methods for inverting biophysical parameters from the lidar signals simulated by the tools presented here.

Chapter 5: Above Canopy Lidar

As discussed in chapter 2.4, satellites are needed for frequent and consistent global measurements. Both passive optical (Defries *et al.* 2000, Boudreau *et al.* 2008) and radar signals saturate over moderately dense forests (Waring *et al.* 1995a) or are not robustly related to biophysical parameters (Sexton *et al.* 2009). Spaceborne lidar offers the potential to measure forests with very high canopy covers (Hofton *et al.* 2002) as well as directly measuring parameters impossible with other methods (Dubayah and Drake 2000). Such non-saturating and physically based measurements are a great advantage for global modelling.

An accurate and robust method for determining forest parameters from above canopy lidar over all terrain is needed. This chapter will outline the current methods for extracting tree height from lidar and use the simulator described in the previous chapter to assess the impact of different system parameters and forest characteristics, ultimately suggesting lidar instruments and inversion techniques to improve global coverage, accuracy and precision.

5.1 Forest measurement

To reiterate, to extract any forest biophysical parameters with lidar, the returns of the canopy and ground must be separable and give accurate relative positions of the tree top and ground. Once the ground position and canopy top are known the tree height can be calculated. Further metrics can be derived, such as the canopy cover from the fraction of energy returned from ground and canopy and the height of median energy above the ground (HOME, (Lefsky *et al.* 2007)). These can be related to biomass and LAI through empirical relationships (Lefsky *et al.* 1999) or else used as physical values if the model can cope with them (Hurtt *et al.* 2004). This separation of canopy and ground is illustrated in figure 10. Various factors, such as noise and forest density will complicate the inversion process and must be dealt with by any practical inversion algorithm. In particular previous studies have struggled with topography (section 3.5.3) and this has not yet been dealt with in a physical and globally applicable way.

5.1.1 Tree Top

The tree height extraction method used is based upon that of Hofton *et al.* (2000). For this a threshold is calculated from the statistics of a known empty portion of waveform (all signal over 150m above the ground). This investigation used the mean background level plus four standard deviations. It should be possible to estimate a point over 150m above ground level with a global DEM such as SRTM (Werner 2000) (SAR's saturation in forests will tend to overestimate ground height and so there is little likelihood of any lidar signal being treated as background noise in error), or 150m above the brightest return.

Hofton *et al.* (2000) took the point at which the cumulative energy above the threshold is greater than or equal to one percent of the total energy above that threshold as the signal start. Using the cumulative energy is more robust to extreme noise values than the instantaneous radiance, leading to far fewer premature triggerings and resultant enormous overestimates of tree height. However, the energy threshold must be set high enough to avoid any chance of premature triggering and so will always miss some portion of the signal. This contributes to the "well known underestimate of tree height by lidar", of the order of 1m (Morsdorf *et al.* 2008a) which would bias any global assimilation scheme.

It should be possible to avoid this bias by using the full waveform information. Taking the bin in which the signal rises above the threshold as a starting point (it is certain that the signal has started by that range, but not by how much it has been overshot) tracking back along the raw signal until the instantaneous value is equal to or lower than the mean noise value provides a point that is as equally likely to be an underestimate as an overestimate, giving an unbiased result. This would not be possible with discrete return lidar as the necessary information is not recorded (see section 3.5).

As can be seen from figure 51, the threshold alone gave a roughly normal distribution of errors with a mean bias of 1m. Tracking this back to the mean noise level gave a similar spread of errors but no mean bias and should therefore lead to better tree height estimates for modelling. The higher the background noise level the greater the advantage of tracking back through the noise.

Once the signal start has been determined, the background noise is removed by subtracting the

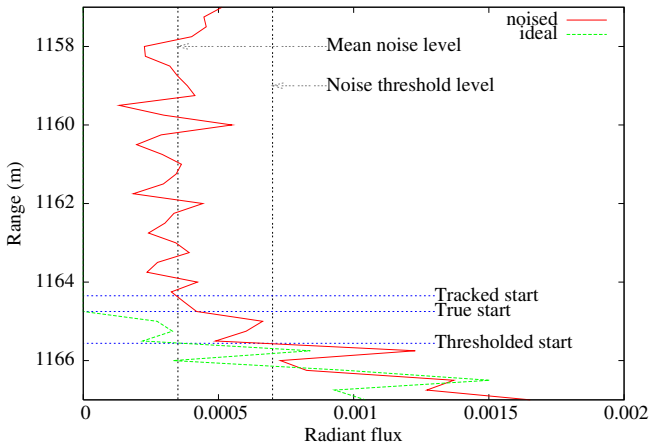

Figure 50: Illustration of noise tracking

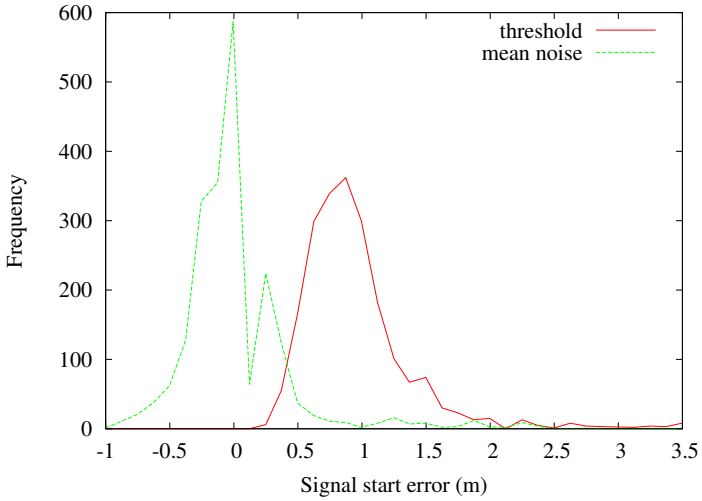

Figure 51: Histogram of signal start errors with and without noise tracking for the waveform shown in 54(d)

threshold or the maximum recorded noise value, whichever is greater.

5.1.2 Ground detection

The traditional method to distinguish ground returns from canopy returns is to fit Gaussians to the measured signal (Hofton *et al.* 2000). These Gaussians can be taken as significant features, allowing information extraction (Wagner *et al.* 2006). Previously the ground was taken as the brightest of the last two feature (Harding and Carabajal 2005) whilst some authors have simply classified land type upon the number of features (Reitberger *et al.* 2008), forgoing quantitative analysis.

Gaussian fitting was implemented, trying both the Levenberg-Marquardt and Powell's methods of non-linear inversion (Press *et al.* 1994). Figure 52 shows a successful fitting. However this was found to be an unstable process, failing for many cases and often for the same waveform with different sets of noise (of the same magnitude with different random number seeds). This may have been a weakness of our implementation, although the literature reports a similar failure rate (Hofton *et al.* 2002). Instead of fitting functions to the signal a simpler method of smoothing and searching for turning points was used.

The signal was smoothed by convolution with a Gaussian (chosen for its smooth derivatives). The width of the Gaussian is determined by sensor range resolution (length scale of noise features) and the separation of ground and canopy bottom. It must be narrow enough to leave a minimum between the ground and canopy whilst eliminating any turning points caused by noise. After examining the simulated waveforms a width of 3m was chosen. This simplified method was found to be as accurate as function fitting whilst being far more robust to noise (shown in figure 53).

Features were defined by the location of a maxima and the energy contained between minima. The ground position was taken as the last feature containing over (an arbitrary) 5% of the total energy.

5.2 Factors affecting inversion

The ability of successful inversions of biophysical parameters and accuracy of those estimates will depend upon the characteristics of the lidar system and the forest being measured. The rest of

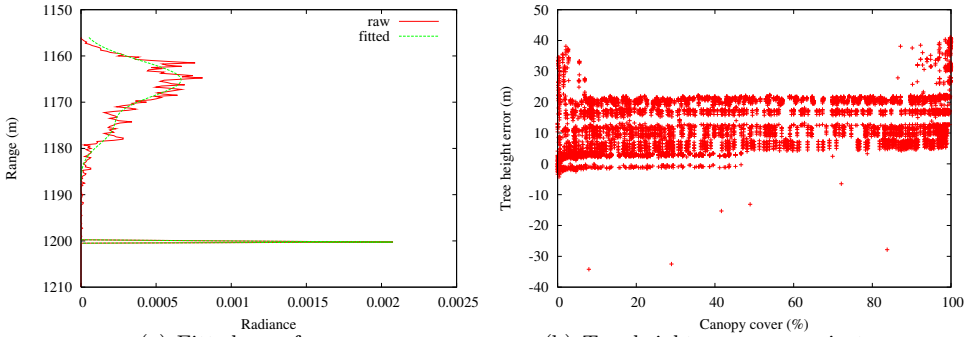

(a) Fitted waveform (b) Tree height accuracy against cover

Figure 52: Original waveform; set of Gaussians fitted by Levenberg-Marquardt and height errors against signal level showing instability

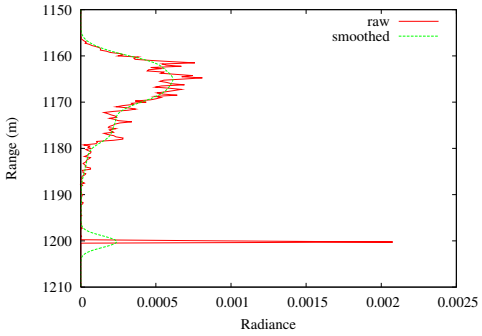

Figure 53: Ground position detection by smoothing

this chapter will explore the dependence of tree height accuracy (and so the ability to distinguish canopy from ground returns) on all lidar system parameters and forest characteristics. They shall be presented in their order of dependence; for example minimum range resolution depends upon the type of detector and the effect of canopy shape cannot be determined until these two system characteristics have been set.

5.2.1 Forest Characteristics

Any method will have to cope with a large range of canopy covers and tree heights (more particularly the separation between the bottom of the canopy and ground). Figure 54 shows the returned waveforms for Sitka spruce and birch forests with a range of canopy covers (tree density), heights (tree age) and foliage profiles (age heterogeneity) to illustrate the information available to algorithms. For all cases the ground is at a range of 1,200m.

The forest properties likely to affect inversion accuracy are;

Canopy cover

Tree height

Vertical distribution

Underlying topography

The hypothesised and observed affect of each of these forest characteristics on inversion accuracy will be presented in the following sections.

5.2.2 System Characteristics

The ability of a lidar system to separate canopy and ground returns depends very much on its characteristics. Parameters of interest are;

Range resolution

Signal to noise (including wavelength)

Footprint size

Pulse duration

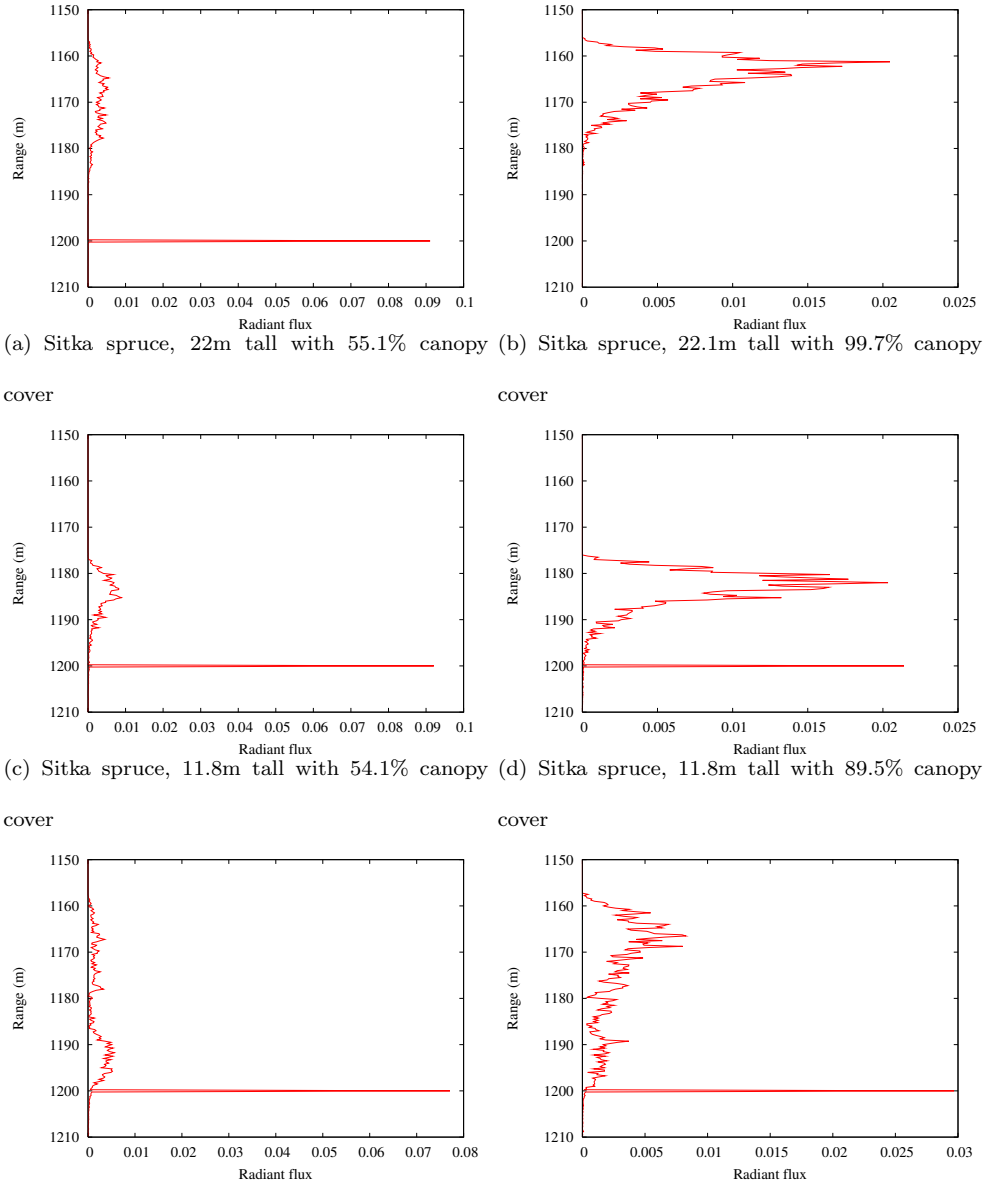

(a) Sitka spruce, 22m tall with 55.1% canopy cover

(b) Sitka spruce, 22.1m tall with 99.7% canopy cover

(c) Sitka spruce, 11.8m tall with 54.1% canopy cover

(d) Sitka spruce, 11.8m tall with 89.5% canopy cover

(e) Sitka spruce, 21.1m tall with 61.3% canopy cover, mixed age

(f) Sitka spruce, 21m tall with 85.2% canopy cover, mixed age

Figure 54: Range of waveforms for Sitka spruce and birch forests with different tree densities and heights at 1,064nm

Laser wavefront

Recording method

Table 1 (in section 3.5.1) shows a list of parameters of recent and current lidar systems used for forest measurement. Inversion accuracy is controlled by the lidar system parameters and forest characteristics. These interact so that certain system characteristics cause inversion accuracy to be more sensitive to some forest parameters.

Simulated data was created using the Monte-Carlo ray tracer and forest models described in chapter 3.6. Unless otherwise stated the characteristics of LVIS (see table 1) were used; other system characteristics were used but these cases will be made clear. These simulated datasets were used to explore the effect of each parameter, both forest and instrument, on inversion accuracy. Tree height was used as a measure of inversion accuracy for each set of characteristics. This requires the ground return to be separated from canopy returns, the first step for any parameter inversion and so should be indicative of the accuracy achievable for other parameters.

5.3 Canopy cover

Canopy cover will have a very direct effect upon inversion. The higher the cover the less of the ground that will be visible and so the smaller the ground signal. This can become lost in background noise and multiple scattering echoes.

From figure 54 it can be seen that increasing canopy cover leads to weaker ground returns. The above inversion method was applied to the full range of Sitka spruce forest models available. Figure 55 shows that for very dense forests ($>$ 98% cover) the ground returns can be lost in background noise, preventing accurate height estimation. Higher noise levels will obviously lower the maximum invertible coverage, which will be covered in section 5.5. The relationship between noise and the "10,000 signal photons" reported in figure 55 was explained in section 4.1.3.

Worryingly, it has been reported that such high canopy covers are not unheard of, particularly in tropical forests (Hofton *et al.* 2002). A measurement is still possible but some saturation and bias must be expected. For forests with between 30% and 70% canopy cover, figure 55 shows

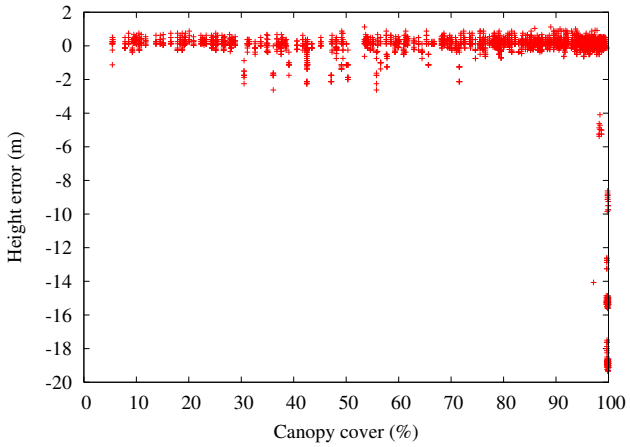

Figure 55: Inverted tree height accuracy against canopy cover for fifteen sets of noise applied to 344 separate waveforms with 10,000 signal photons

some inversions with larger errors than the norm. These are mixed aged forests, such as that in figures 40(e) and 54(e) and will be covered in more detail in section 5.10.7.

5.4 Tree height

Tree height controls the separation between the ground and canopy and so the ease of distinguishing these two features. Figure 56 shows tree height error against tree height separated by canopy cover. It can be seen that the average error increased with tree height, which seems the wrong way around. However that is only because taller, older trees tend to have higher canopy covers (on the scale of a 30m footprint) and that the increased error is entirely due to very high (>95%) canopy cover.

The short forest models used did not have high enough canopy covers to completely obscure the ground. Whilst there was no clear separation between the ground and canopy, the ground return's intensity was always great enough to have a maximum centred on it. Estimates of canopy cover (and so LAI) would be more complicated in this case, but the first step of locating the features is possible. Therefore, at least on flat ground (slopes will be dealt with in section 5.11), canopy cover and foliage heterogeneity can have bigger impacts on inversion accuracy than tree height.

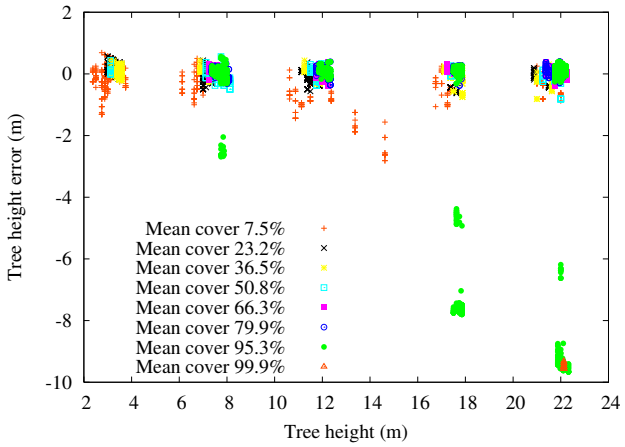

Figure 56: Inverted tree height accuracy against tree height separated by canopy cover, for fifteen sets of noise applied to 344 separate waveforms with 10,000 signal photons

5.5 Noise Level

Noise adds spurious features through background signal and distorts the shape of the waveform. Obviously the greater the noise the less accurate the inversion will be. Weak real signals will be lost in background noise and features can be moved (illustrated in figure 30). The effect of noise level on tree height accuracy was explored by adding different sets of noise (using the method described in section 4.1.3). To get an overall picture of the dependency of accuracy on noise, rather than have some waveforms affected by unusually large background spikes (from random numbers) each simulated waveform had different sets of the same level of noise added by changing the random number seed. This gave fifteen measured waveforms from each simulated waveform.

Each of these measured waveforms with less than 97% canopy cover (as these inversions would fail, even without noise) were inverted with the above simplified method. The mean is plotted in figure 57, the error bars showing one standard deviation.

The larger errors at low signal to noise ratios (SNR) are apparent. Interestingly, as well as increased error, lower SNRs had a negative bias. Closer investigation reveals that this was entirely due to signal start errors, the ground being relatively unaffected by noise. Figure 58 illustrates the signal start being lost in high background noise.

For lower noise levels, this bias disappeared with 68% of the inversions lying within 20cm of the truth. The majority of inversions (99%) were within 60cm of the truth; this compares favourably

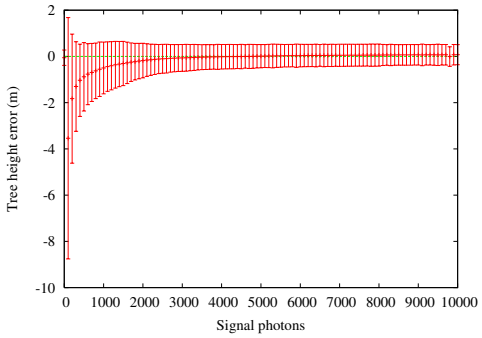

Figure 57: Mean tree height error and standard deviation against noise level for 1,000 inversions of waveforms over Scots pine forests with covers less than 97%

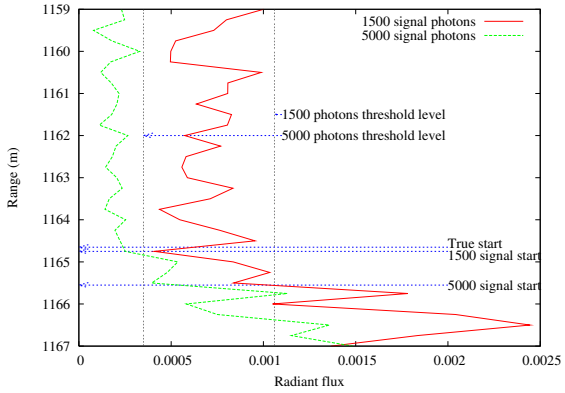

Figure 58: Illustration of signal start being lost in high background noise

with field studies. Means *et al.* (1999) reported an RMSE of 3.8m on flat ground whilst Hyde *et al.* (2005) reported errors of over 8m on sloping terrain, though their RMSEs had the extra complication of matching ground and lidar measurement locations. The improvement of accuracy with noise seems to flatten off at around 5,000 signal photons for the inversion method used, therefore an instrument should record at least that number of photons.

For safety, a signal level of 10,000 signal photons was chosen. The number of photons recorded depends upon the outgoing laser power, atmospheric transmission and surface reflectance at that wavelength, detector telescope, quantum efficiency and flying altitude. It has been stated by industry (Foster 2008) that this is easily achievable from space with a 1m telescope and could be mounted on a relatively small satellite.

5.6 Detector Type

To measure a forest with lidar, the ground and canopy returns must be clearly distinguishable. The detector type could potentially have an impact upon a lidar's capability to do this. As discussed in chapter 2.4, full waveform lidar is preferable for measuring canopy cover, foliage profile and ensure accurate tree heights due to the diffuse nature (in range) of the surface. Discrete return systems have been used in the past with some success (Coops *et al.* 2006). Certain discrete detector systems can be made far more compact and energy efficient than traditional waveform detectors; this has an obvious appeal for satellites and if they could give accurate results would be the preferred instrument. They rely on multiple footprints in a small area to sample both the ground and canopy. This requires scanning and such a system has not been proposed for space yet. For the moment spaceborne lidars look set to be large footprint.

Discrete systems are triggered by a return above an intensity threshold, a range is then recorded (sometimes with the intensity of the triggering return). Discrete return systems can only record a limited number of returns (typically five though some up to twenty (Lim *et al.* 2003)) and in dense canopies these can all come from the upper layers. This greatly limits the range and accuracy of biophysical parameters that can be inverted.

Geiger mode avalanche photo diodes (APDs) have been suggested for canopy lidar (Harding

et al. 2008). These are light sensitive n and p type semi-conductor junctions (Tipler 1999, page 1225) with a large bias applied, above the break down voltage, (Zappa *et al.* 1996). Absorption of a single photon pushes the voltage over the break down point, causing an avalanche of electrons over the junction (measured as a current). There is then a long dead time whilst the bias is restored. Any photons hitting the detector between the initial avalanche and the resetting are lost without record. Currently this dead time is 45ns-50ns (Zappa *et al.* 2002) corresponding to a distance of 6.75m-7.5m; an unacceptable blank space for tree measurement. This figure will be reduced with time and single Geiger mode APD measurement may become feasible in the future but for the moment a single Geiger mode APD element can only measure the first return. They would allow ranging systems with very low power sources of illumination, since only a very few photons need to be returned. Renker (2006) gives a comprehensive history for interested readers.

Such a system is very sensitive to noise, any stray photons will set it off, giving wildly inaccurate ranges (Albota *et al.* 2002). The probability of stray light can be reduced with range gates and averaging repeat readings.

One idea, suggested by Dr. Mike Foster of Lidar Technologies ltd. (Foster, 2007 pers comms), would be to carefully tune the detector sensitivity so that triggerings are caused by returns from a representative cross section of the target; thereby allowing inversion. Too low a threshold will over sample the leading edge (including spurious signals from noise) whilst too high a threshold will miss large parts of the signal. Either of these cases will bias or prevent accurate inversion.

A sample waveform was converted into Geiger mode APD returns by examining the return strength in each bin, from nearest to farthest. The first bin in which the waveform radiance was greater than the sensitivity threshold (set as a fraction of the maximum intensity) multiplied by a random number (between zero and one, a new one generated for each bin) was taken as the trigger point. A count of one photon was added to that bin in the resultant waveform; the signal a single Geiger mode APD would record.

To sample the full waveform and obtain a measure of radiance, repeat readings have to be made. These repeat measurements can either be done with multiple pulses (which would require accurate pointing to keep a satellite looking at exactly the same ground spot), by an array of

elements or by a mixture of the two. For repeat measurements many windows were passed across the same waveform with different random numbers seeds. The results were counted up to create a pseudo-waveform (photon count rather than intensity in each bin).

From figure 59 it can be seen that around four hundred repeat readings would be needed to get a useful pseudo-waveform with realistic noise levels and the ideal threshold. Here a useful waveform is one in which the ground and canopy features are distinguishable with roughly the right cross sections. This is a huge number of APD repeat readings, and that is using the ideal detector sensitivity. Figure 60 shows that the pseudo-waveforms were reasonably tolerant to the trigger threshold and could be expected to work over a wide range of land covers.

5.6.1 Detector conclusions

The required number of repeat readings alone negate any size, weight and power savings gained from using Geiger mode APDs. The sensitivity to the trigger threshold is not too much of an issue, especially if the land class (and predicted reflectances) are known beforehand, though it is a potential extra source of error. Geiger mode avalanche photo-diodes are therefore felt to be unsuitable for structural forest measurements *until* the dead times can be reduced to sub-nanosecond intervals.

For the rest of this work the use of true, full waveform detectors will be assumed. Whether they be photo-multipliers or avalanche photo-diodes in non-Geiger mode is irrelevant (neither have dead times); the measurement will be the same, given the same number of signal photons. It may make a difference when scaling from signal photons to required laser power through the detector efficiency but that is beyond the scope of this work.

5.7 Range resolution

Range resolution is critical for forest measurement. It directly controls the amount of information available for any processing as well as limiting the precision. Without achieving super resolution through complex deconvolution or fitting techniques, the uncertainty in tree height cannot be less than the range resolution: It is not known where within a bin a feature falls, so the ground and tree tops have a half bin uncertainty each. If the bin size is greater than the separation between

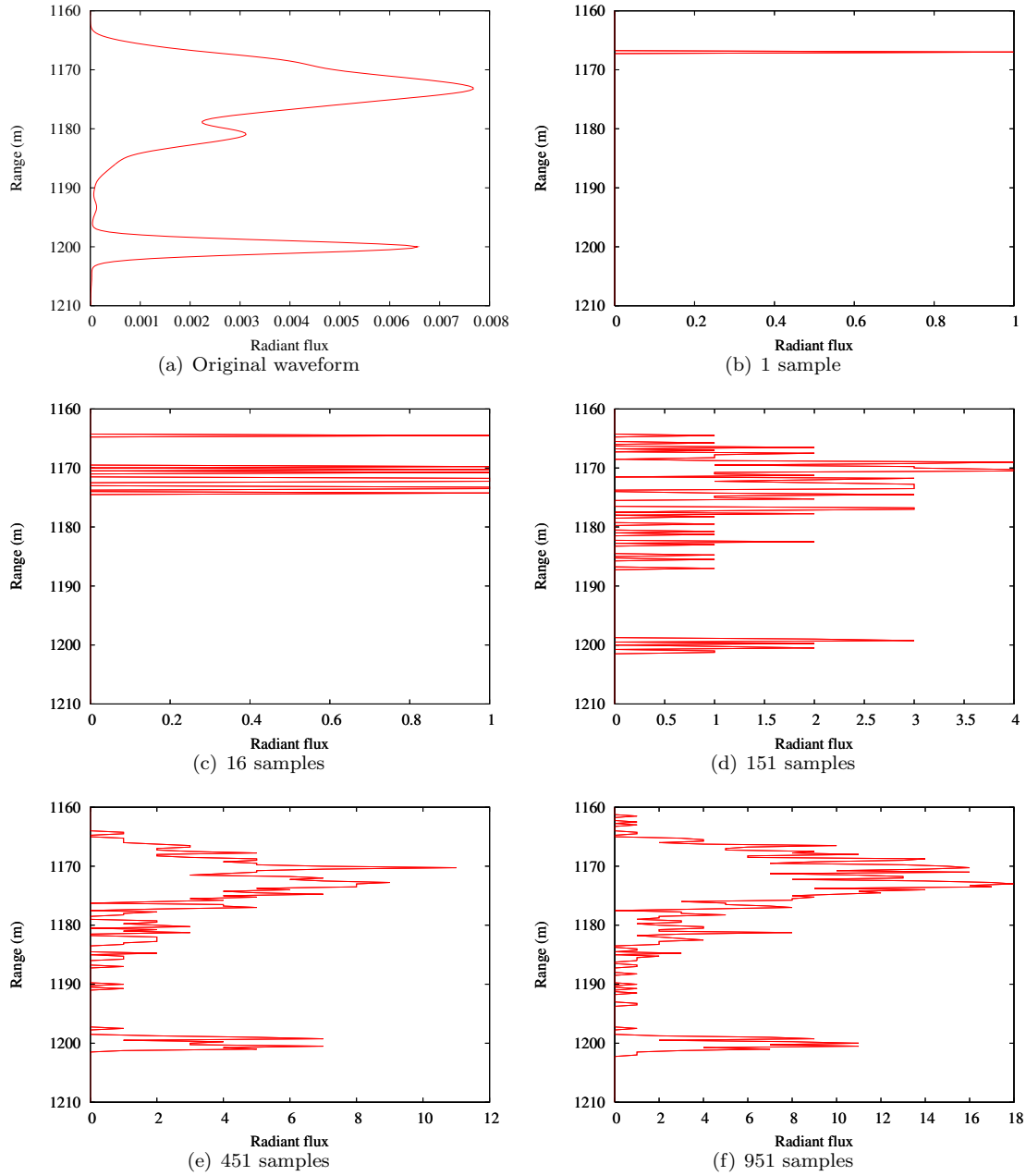

(a) Original waveform

(b) 1 sample

(c) 16 samples

(d) 151 samples

(e) 451 samples

(f) 951 samples

Figure 59: Pseudo-waveforms from aggregating Geiger mode APD samples with a threshold of 0.36 of the maximum intensity

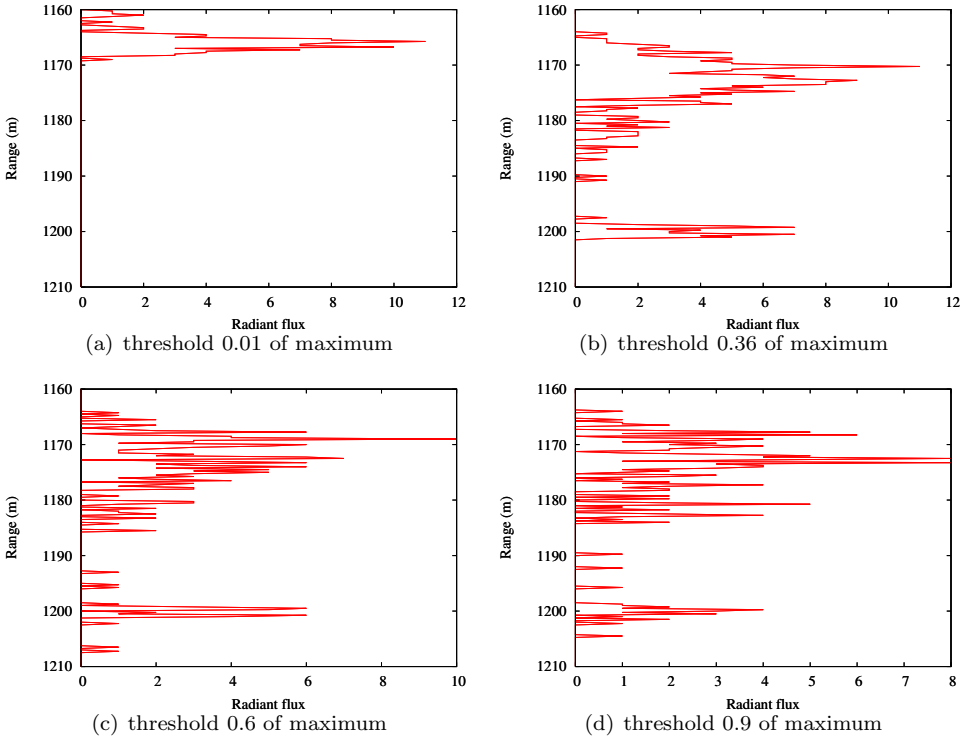

(a) threshold 0.01 of maximum

(b) threshold 0.36 of maximum

(c) threshold 0.6 of maximum

(d) threshold 0.9 of maximum

Figure 60: Aggregated Geiger mode pseudo-waveforms' sensitivity to trigger threshold. 451 samples were made from the original waveform shown in figure 59(a)

the ground and crown, extraction is not possible (except for tree height if the ground return is brighter than the canopy, as in figure 54(e)). To ensure this condition is met the gap should be Nyquist sampled; ie. the bin length should be no more than half the distance between the ground and bottom of canopy. Therefore 1m-2m should be taken as the upper limit of usable resolutions and nothing coarser will be investigated.

Figure 61 shows the mean error against range resolution for all Sitka spruce forests over flat ground, error bars show one standard deviation. Trees had heights of between 3m and 22m (see figure 56). One hundred waveforms were used, each had different sets of noise (10,000 signal photons) added to create twenty measured waveforms per simulation. Only canopies with less than 97% cover were inverted, as these would fail even in the absence of noise.

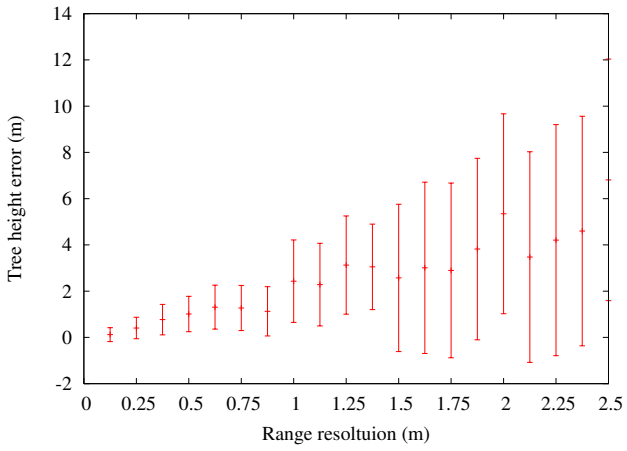

Figure 61: Inverted tree height accuracy against range resolution

The strong dependence of error on range resolution is apparent. For the inversion method used a range resolution of less than 1m is needed. The finer the resolution the better. This corresponds to a digitiser speed of 6.7ns or better. The 0.5ns sampling used by ICESat, corresponding to 15cm resolution (Harding and Carabajal 2005), would be ideal and leave little bias. Simulations will use this digitiser speed for the rest of this chapter.

5.8 Footprint size

The footprint size will have no bearing on the signal processing aspect of canopy measurement; it affects what is measured rather than how accurately it is measured. If only part of a tree is

captured it will be possible to determine the height of that part accurately, whether or not this is the tree top is irrelevant to the extraction algorithm. Of course for ecological models it is preferable to have measurements of whole trees.

The consensus is that the area covered should be sufficiently large to contain at least one tree top. Current NASA studies seem to favour a single footprint of around 10m-30m diameter (Hyde *et al.* 2005, Zimble *et al.* 2003), perhaps to avoid scanning from space. The area covered need not be measured in a single footprint. Several studies have aggregated many small footprints (Reitberger *et al.* 2008), taking the highest returns as tree tops and the lowest as ground returns. As yet there have been no plans for a multiple, small footprint, full waveform spaceborne lidar, although Harding *et al.* (2008) has proposed a pseudo-waveform pushbroom system (using Geiger mode APDs, see section 5.6). An array of small full waveform footprints may be too much of an engineering challenge; requiring either an array of detectors or very accurate laser pointing, but such technological speculation would be outside the scope of this work.

The larger the area of a single footprint the greater the topographic blurring, as shown in figure 104 and covered in more detail in section 5.11. For a 60m footprint (such as ICESat's GLAS (Zwally *et al.* 2002)) the blurring will be twice that of a 30m (a 10^o slope would cause the blurring shown in figure 104(c)), therefore an array of small footprints is attractive.

For the rest of this investigation a single footprint of 30m diameter will be used unless stated otherwise. This raises problems with topographic blurring which will be discussed in detail in section 5.11.

5.8.1 Laser wavefront

With real lasers the energy is not usually uniformly spread across the illuminated spot on the ground (Wilson and Hawkes 1987, page 96). Often it is stronger in the centre than the edges. This brightness distribution is known as the wavefront and is sometimes modelled as a sinc function or (if apodised) a Gaussian, illustrated in figure 34 in section 4.1.5. The return signal will be weighted by this intensity distribution so that if the tallest tree within a footprint is at the edge it will be weakly illuminated and so contribute less to the waveform. This means the signal start is more likely to be lost in noise, leading to larger errors. For a given laser power the converse will be true;

if the tallest tree is in the centre of a footprint it will be strongly illuminated (relatively) and so more likely to be detected above noise.

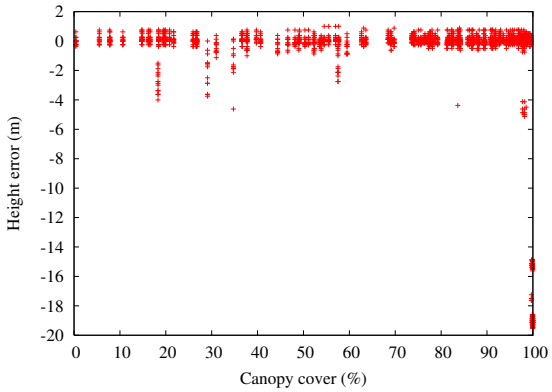

Figure 62: Tree height error for what the lidar could see against canopy cover for a 30m footprint with a Gaussian wavefront

The wavefront can be thought of as reducing the size of the footprint. The effective size and whether trees at the edge are detected depends on the noise level. As illustrated in figure 63, noise truncates the edges of the wavefront and as long as the noise is greater than $\frac{1}{e^2}$ of the maximum returned intensity, the effective footprint of a Gaussian wavefront will be less than that of a flat wavefront. The flatter the wavefront, the sharper the edges and so the smaller the noise dependence of the footprint size.

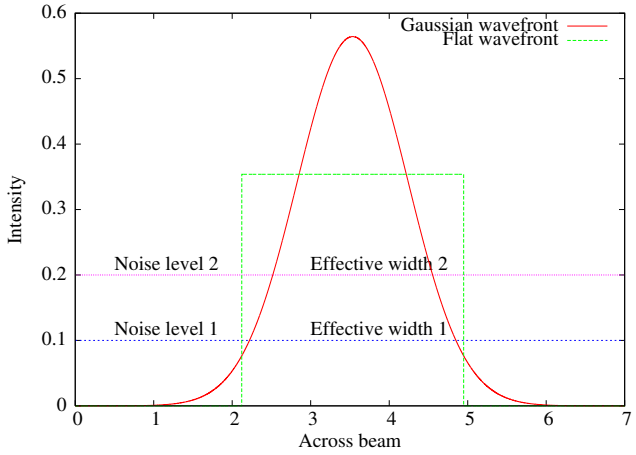

Figure 63: Illustration of the noise dependence of the effective footprint size

The inversions were repeated for all Sitka spruce forests using a Gaussian wavefront. Figure 62

shows that from a signal processing point of view the inversion was not complicated by having a Gaussian wavefront; the errors being similar to the flat wavefront case in figure 55. For these two graphs the tree height error was calculated as the difference between the inverted tree height and the distance from the first recorded interaction and the mean ground return from the ray tracer's material waveform. This is the "apparent true tree height"; the best that could be inverted from the recorded data and takes no account of what was within the footprint but not recorded due to weak illumination.

Figure 64(a) shows the difference between the inverted tree height and the height of the tallest tree whose base fell within the footprint ("absolute error"). The tallest tree's top will not necessarily have been recorded in the waveform and so the error goes some way to taking into account the difficulty in relating real data to ground measurements (Hyde *et al.* 2005). The errors are different to those in figure 62, however they are not noticeably different to the errors in the flat beam wavefront case (figure 64(b)) and so the difference is more likely to be due to the mismatch of measured tree tops and trees whose bases lie within the footprint rather than the wavefront shape. Therefore from a signal processing point of view the beam wavefront makes little difference.

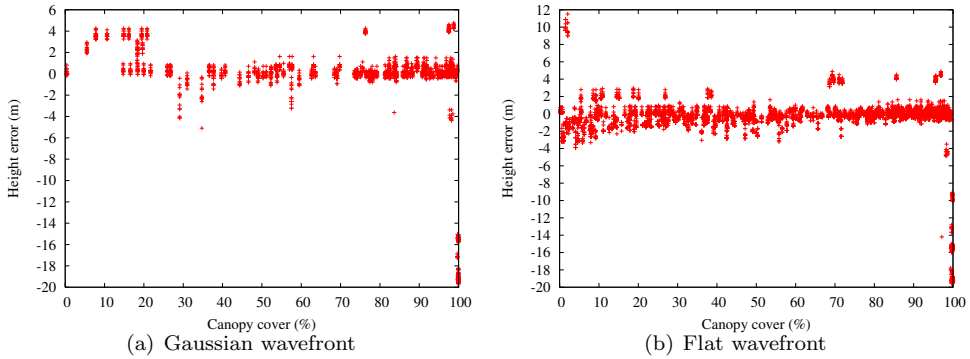

(a) Gaussian wavefront (b) Flat wavefront

Figure 64: Tree height error calculated from what was within the laser footprint against canopy cover for a 30m footprint with a Gaussian wavefront

A method for estimating the footprint size above noise is beyond the scope of this thesis, other than to suggest that an instrument have as flat, well defined a laser footprint as possible. A perfectly flat wavefront will be used for the rest of the investigation, noting that the effective footprint size may vary if a non-flat wavefront is used.

5.9 Pulse length

All laser pulses have a finite duration (Baltsavias 1999) otherwise an infinite amount of power (albeit for an infinitely short period) would be required to transmit any energy. The longer the pulse the more energy (integral of the pulse) can be carried with a smaller peak intensity (illustrated in figure 65). This allows high energies whilst maintaining eye safety and staying below damage thresholds of optical components (Kovalev and Eichinger 2004, page 99). If the pulse duration is longer than the waveform digitisation speed some blurring will occur. If this blurring exceeds the separation between the ground and canopy, parameter inversion can be prevented. Table 1 (in section 3.5.1) shows that all canopy lidar instruments suffer from some blurring.

It is sometimes claimed that the pulse length is the limiting factor of range resolution (Baltsavias 1999). This is not necessarily the case; deconvolution has been used successfully in many fields to remove blurring effects, whether they be optical defects in telescopes (White 1994), to increase the spectral resolution of radiometers (Kauppinen and Partanen 2001, page 205) and to increase the resolution of lidar systems (Gurdev *et al.* 1993) and should, ideally, allow waveforms to be resolved down to the bin length, regardless of the laser pulse.

All detectors also have an impulse response function (Hofton *et al.* 2000) which describes how quickly the detector can respond to incoming light. This will act to blur the measured waveform, therefore the blurring function is the convolution of the pulse shape with the impulse response function. For this investigation only the laser pulse duration will be referred to, though it can be thought of as the total blurring function from the laser and detector.

For a typical waveform lidar such as ICESat the pulse is described by a Gaussian (sometimes slightly skewed forwards) with a width of 11.8ns (full width half maximum of 7ns (Harding and Carabajal 2005)). Here pulse width is defined as the point at which the intensity falls to $1/e^2$ of the peak intensity rather than the half width full maximum normally presented. This contains 93.9% of the total pulse energy as opposed to 65.4% within the full width half maximum.

11.8ns corresponds to a blurring of 1.78m. This hides much of the heterogeneity of the return signal but is not so extreme as to prevent inversion, except for very short canopies. The proposed A-scope instrument, optimised for measurement of atmospheric CO_2 by differential absorption,

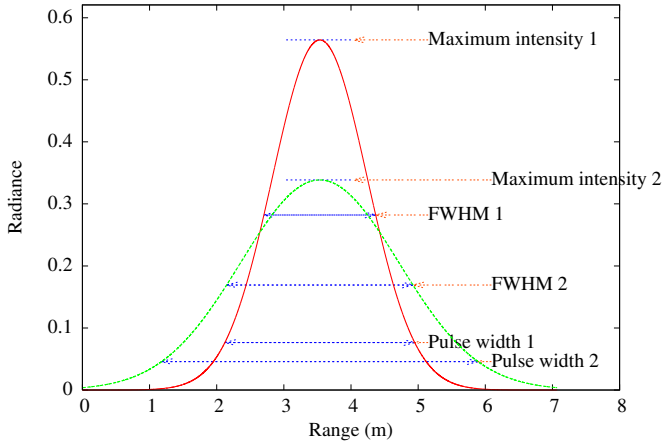

Figure 65: Illustration of the relationship between pulse length, energy and peak intensity for two pulses with the same total energies but different durations.

will have a pulse length of between 20ns and 100ns, corresponding to a blurring of between 3m and 15m. The 100ns pulse, as provided by a fibre laser, is favoured by Davies *et al.* (2008) as it eases coupling to their hollow waveguide technology (Jenkins *et al.* 1992). Such a pulse length will all but obliterate forest details from a waveform.

Figure 66 shows effect of different pulse lengths on a measured waveform. Note the total loss of detail caused by the 100ns pulse. The signal is still made up of a number of Gaussians so function fitting should be able to locate the ground, however often there is not enough deviation from a single Gaussian feature to separate out the ground, as shown in figure 67. For any information to be extracted from such a signal some form of deconvolution is required. The simplest form is described by equation 35.

$$\mathcal{F}(o) = \frac{\mathcal{F}(i)}{\mathcal{F}(s)} \tag{35}$$

Where $F(o)$ is the Fourier transform of the deconvolved waveform

i is the measured waveform

s is the blurring function

Deconvolution is a mathematically ill posed method, with many possible solutions for a given

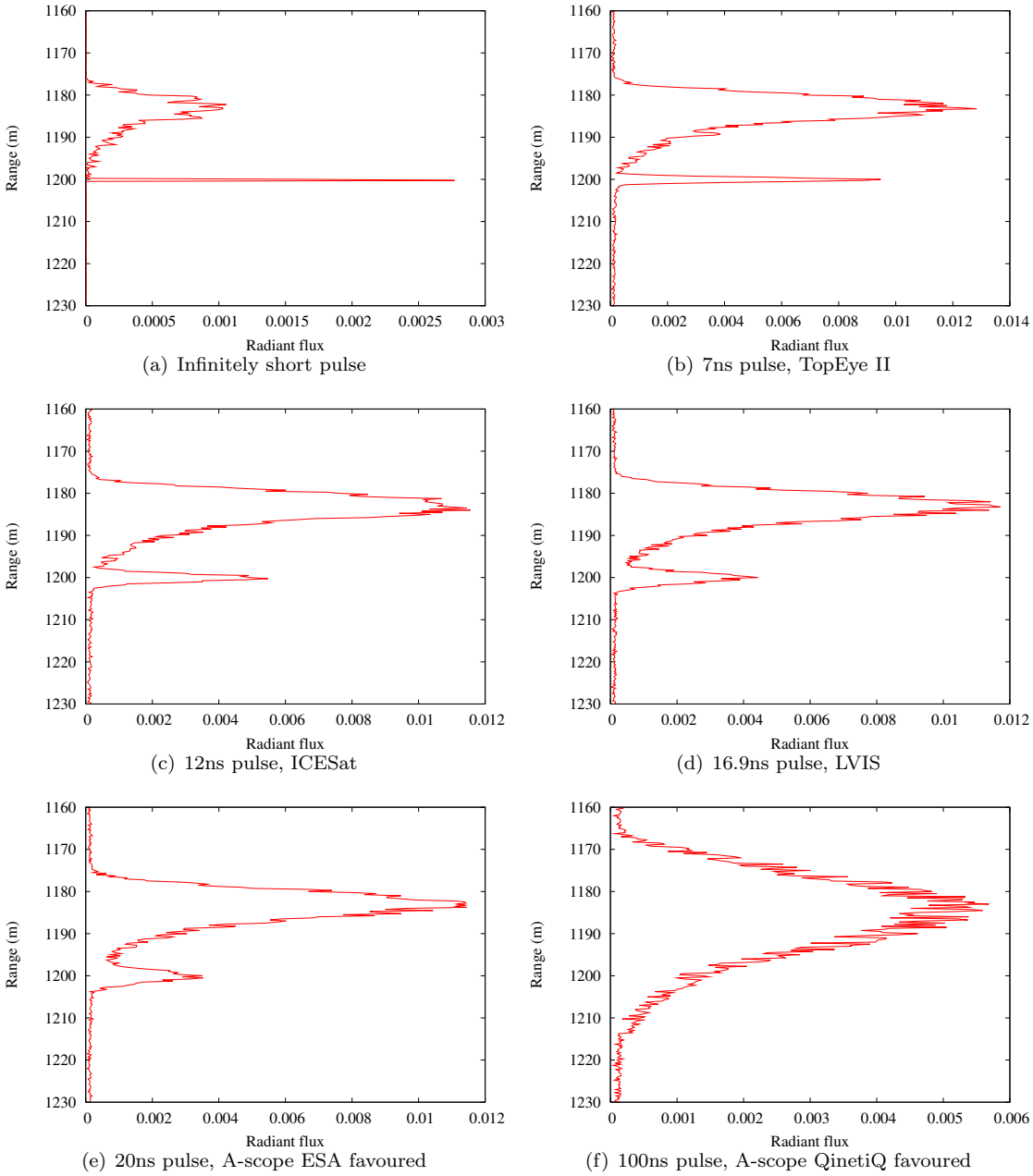

(a) Infinitely short pulse

(b) 7ns pulse, TopEye II

(c) 12ns pulse, ICESat

(d) 16.9ns pulse, LVIS

(e) 20ns pulse, A-scope ESA favoured

(f) 100ns pulse, A-scope QinetiQ favoured

Figure 66: Effect of different pulse lengths on measured waveform over a Sitka spruce forest of height 12.1m and 78.0% canopy cover with 10,000 signal photons

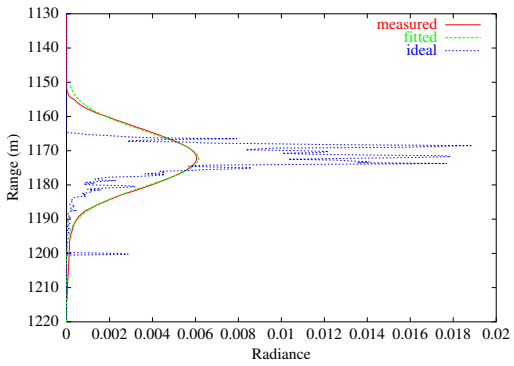

Figure 67: Function fitting to waveform over a forest of height 17.8m, 97% canopy cover with a 100ns pulse

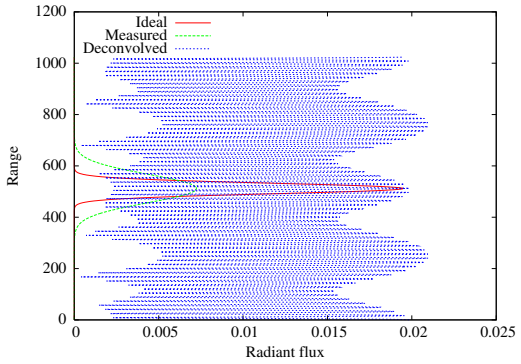

Figure 68: Result of deconvolution using equation 35 on synthetic data

problem (Jansson 1997). It is only too easy to arrive at physically impossible solutions such as negative intensities (for example figure 68, using equation 35). There has been much work on constraining deconvolution methods to ensure realistic results and increase robustness to noise. Gold's method of iterative re-blurring (Gold 1964) was selected for this investigation as being the most robust with the available information. This has been phrased by Jansson (1997, page 115) as;

$$o^{(k+1)} = o^{(k)} \frac{i}{s \otimes o^{(k)}} \tag{36}$$

Where; i is the original waveform

s is the blurring function

$o^{(k)}$ is the k^{th} estimate of the original waveform

and $o^{(0)} = i$

This re-blurs the current estimate of the deconvolved waveform with the original pulse before using it to divide the product of the current estimate of the deconvolved waveform with the measured waveform. Effectively the waveform is gathered up a little more after each iteration until the original, undistorted waveform is reached. As this only takes ratios in the spatial rather than frequency domain negatives values are not possible and multiplying by the measured waveform ensures no features outside its bounds (which would be physically impossible).

To implement this the waveform and pulse must be sampled at the same rate. An instrument must measure the outgoing pulse in great detail (higher sampling rate than the waveform) for convolution to be possible. For aliasing to be prevented this should be at least Nyquist sampled (the programs used sampled the pulse at four times the waveform sampling rate). The waveform was resampled to the pulse sampling rate (permitting super resolution), putting all the energy in each waveform bin into only the central bin (as shown in figure 69). This may increase the quantisation noise but, as will be shown, accurate results were reached. Figure 70 shows this working to allow complete, accurate and precise inversion.

Deconvolution is notoriously sensitive to noise. Background noise is gathered up into spurious

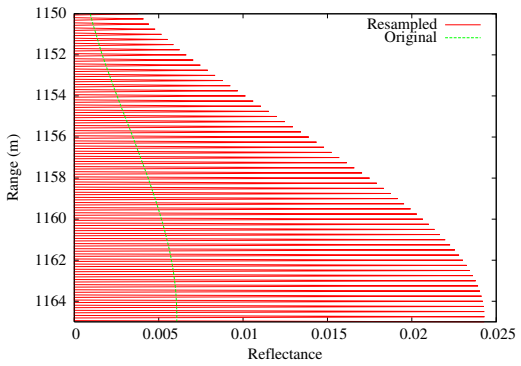

Figure 69: Illustration of resampling waveform to pulse resolution

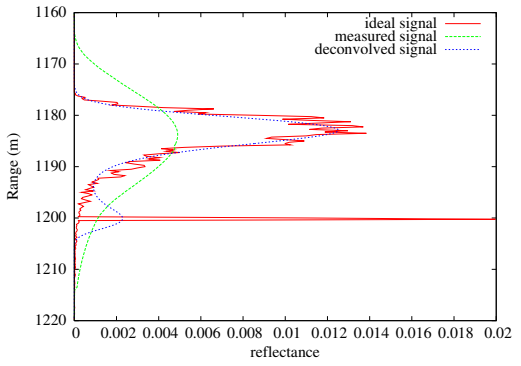

Figure 70: Gold's method successfully deconvolving a waveform with a 100ns pulse after 6,000 iterations. No noise was added

features and distortions from instrument noise are enhanced, destroying any information content (figure 71). The pulse and object features will be heterogeneous down to very fine scales; all of which is summed up into range bins. During deconvolution none of this heterogeneity is taken into account. This quantisation noise alone leads to poor recreations, as seen in figure 71(b).

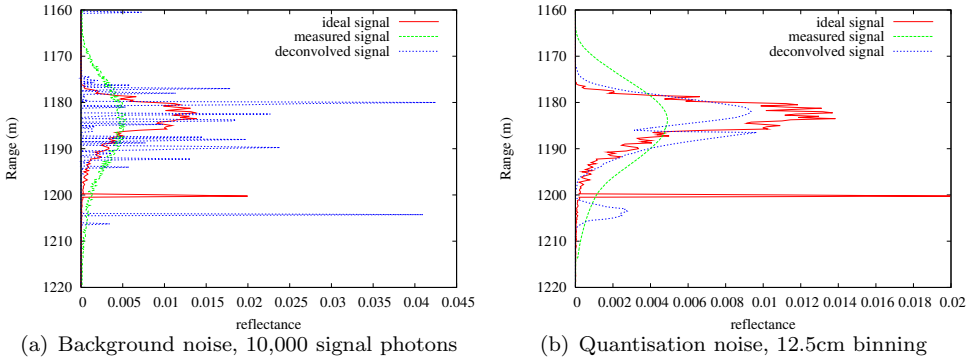

(a) Background noise, 10,000 signal photons

(b) Quantisation noise, 12.5cm binning

Figure 71: Effect of noise on deconvolution

A measured waveform cannot contain any real features with a higher spatial frequency than is contained in the outgoing pulse. Any such features must be due to noise and should be removed. High spatial frequencies can be filtered out by convolving the measured signal with the original pulse. The blurring function, s in Gold's method must also be convolved with itself to get the filtered signal back to the truth. This is expressed mathematically in equation 37. Blurring a waveform to later sharpen it seems counter intuitive; however it should be kept in mind that the frequency domain is being filtered rather than smoothing the spatial domain. Background noise should be removed by subtracting the DC bias. For computational efficiency the extra smoothing would be performed only once rather than every iteration.

$$o^{(k+1)} = o^{(k)} \frac{(i - DCbias) \otimes s}{(s \otimes s) \otimes o^{(k)}} \tag{37}$$

Where; i is the original waveform

s is the blurring function

$DCbias$ is the background noise level

$o^{(k)}$ is the k^{th} estimate of the original waveform

and $o^{(0)} = i \otimes s$

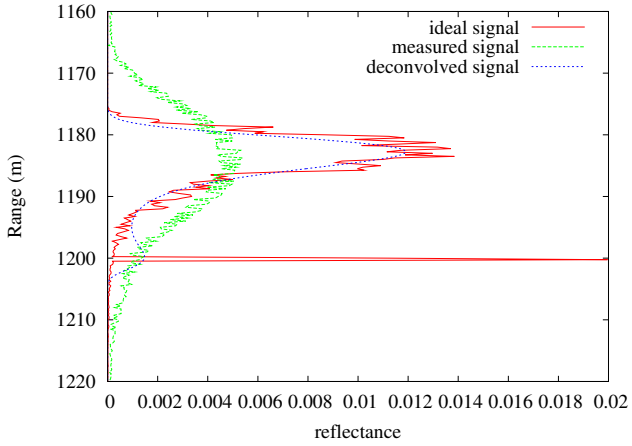

Figure 72: Effect of noise removal on deconvolution by filtering of spatial frequency

Due to the smoothing required to denoise the deconvolved waveform will never be as sharp as the ideal case. However sufficient detail will be revealed to allow accurate measurement of forest height and canopy cover, as shown in figure 72.

5.9.1 Convergence

As Gold's method is iterative, care must be taken to ensure the right number of iterations are performed to achieve the correct result. Unlike some iterative methods such as the Newton-Raphson method, Gold's method will never converge to a solution of its own accord. The estimate will change with each new iteration, passing through the truth to non-physical solutions. If the wrong number of iterations are used the inverted parameters will bear little resemblance to reality (figure 73(d)). In the case of figure 73, which is unnoised, any number of iterations between 6,000 and 10,000 gave an acceptable inversion. Noise, understandably complicates the issue. A convergence criterion is needed to decide when to stop.

For figure 75(a), a Sitka spruce forest 7.5m tall with 76% canopy cover, any number of iterations between 915 and 1,092 would give the correct signal start position. Note the stepped line caused by the quantisation into bins (the error can only be a whole number of bins). In the absence of a reliable convergence criterion the optimum number of iterations for each simulated waveform were

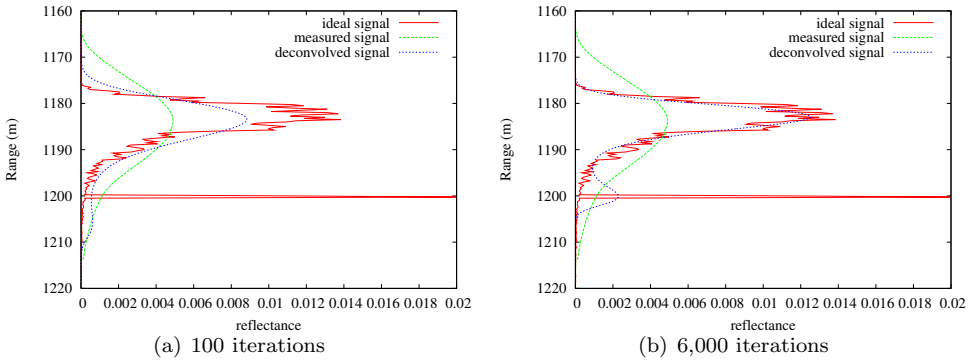

(a) 100 iterations (b) 6,000 iterations

(c) 10,000 iterations (d) 60,000 iterations

Figure 73: Effect of different numbers of iterations of Gold's method on a 100ns pulse

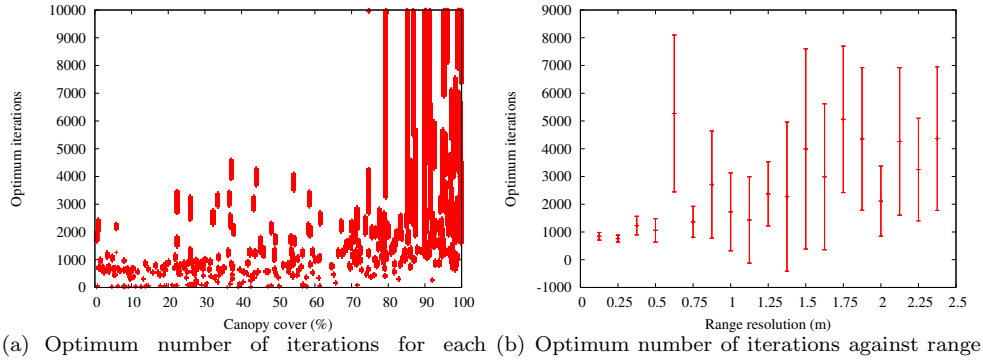

(a) Optimum number of iterations for each canopy cover

(b) Optimum number of iterations against range resolutions with 20%-30% canopy cover

Figure 74: Dependence of number of iterations on system parameters

found separately. Figure 74(a) shows the optimum number of iteration's dependence on canopy cover. Figure 75(b) shows what root mean square error and bias would result from using a fixed value over all forests.

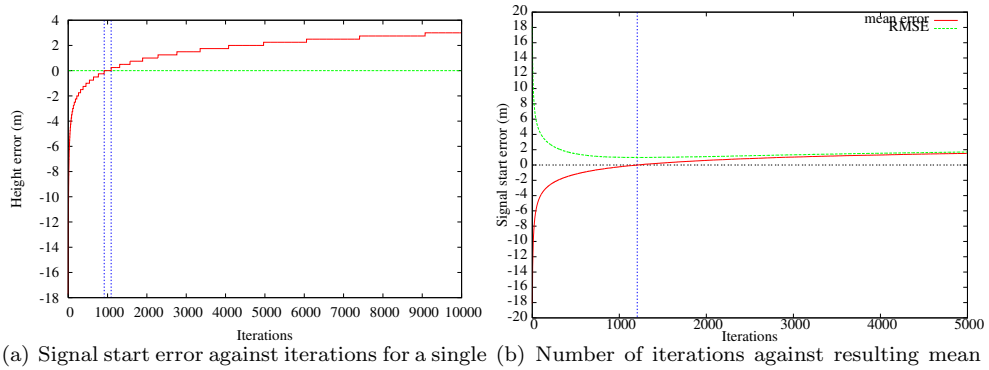

(a) Signal start error against iterations for a single waveform

(b) Number of iterations against resulting mean error and root mean square error for all waveforms

Figure 75: Optimum number of iterations

The number of iterations required depends upon pulse length, noise level and range resolution (figure 74(b)). The reason for the relationship between number of iterations and pulse length and range resolution is fairly obvious whilst that due to noise level is less so. This is due to the truncation of the leading and trailing edges, shifting the start and ends, so causing a large change in inverted tree height. The higher the background noise, the fewer iterations are needed to get the correct tree height.

Figure 75(b) shows that for this data set 1,206 iterations provided the smallest error over all, with a root mean square error of 1m and a mean bias of 1mm for the 328 waveforms tested. This accuracy is comparable to the results from any short pulse lidars currently available, although all forests were on flat ground.

Several different methods for determining convergence were explored. Some showed promise but none were robust enough for reliable use.

The magnitude of the deconvolved signal shift from iteration to iteration was investigated, hoping that it would settle down at the true signal start. As shown in figure 73 the start will not settle down at the true signal start. Instead it shifts backwards from the "gathering up" of the signal until a spurious signal splits off and drifts forwards. This changing of direction of the signal

start would be taken as a settling down when the deconvolved waveform is not close to the ideal, unblurred signal.

The maximum intensity of the deconvolved waveforms cannot be greater than the energy contained within the largest intensity pulse that can be fitted completely within the data. This maximum possible energy was calculated (by sliding the pulse function along the measured signal and finding the largest amplitude that could be contained by the measured waveform) and deconvolution halted when the maximum amplitude of the deconvolved signal reached this energy.

The failure of this method is illustrated in figure 76. This is not unsurprising given that the canopy returns are not dissimilar from Gaussians themselves. Therefore the canopy and pulse will combine to produce a large Gaussian with a greater amplitude than would be contained in any one bin of the ideal signal, leading to too many iterations and the spurious features.

A more sophisticated method would have been to use this value in an iterative method with an upper and lower constraint such as Jansson's method (Jansson 1997). However the added benefit relative to effort is questionable. A fixed number of iterations that minimised the inverted errors was chosen for the rest of the investigation.

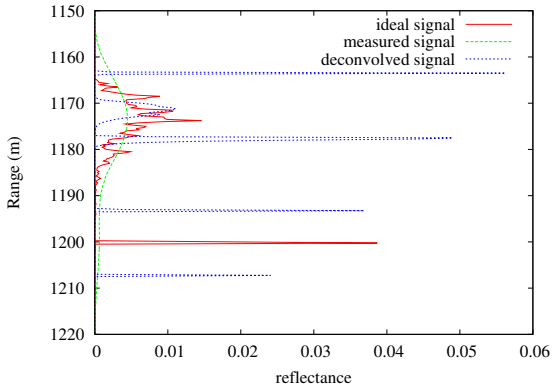

Figure 76: Attempt to use maximum possible amplitude as a convergence criterion. Failed to accurately deconvolve.

5.9.2 Accuracy with deconvolution

The success of deconvolution depends very much on the system parameters. Therefore the parameters that gave suitable accuracies for short pulsed waveforms may not be sufficient for inversion

from long pulse waveforms requiring deconvolution. To this end the dependency of inversion accuracy on canopy cover, noise level and range resolution were re-calculated with a 100ns pulse.

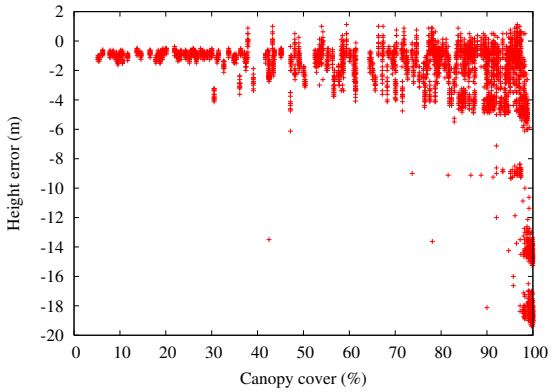

Figure 77: Mean tree height error against canopy cover for waveforms deconvolved from a 100ns pulse. A signal level of 10,000 photons and range resolution of 12.5cm were used

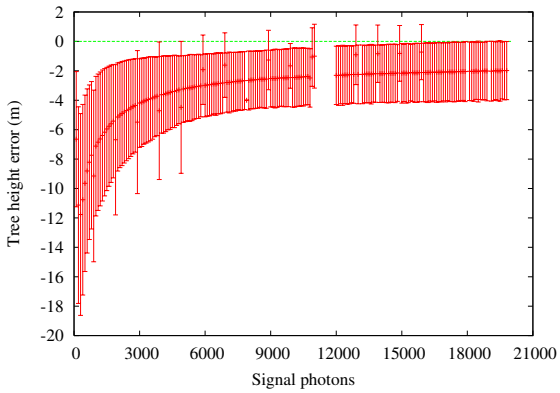

Figure 78: Mean tree height error against noise level for waveforms deconvolved from a 100ns pulse, for a resolution of 12.5cm

Figure 77 shows that the tree height accuracy was not as good as for the short pulsed samples for forests with over 40% canopy cover. A 1m bias was introduced for all canopy covers from using an incorrect number of iterations. No canopies above 97% cover were correctly inverted; for these dense canopies the ground return is very weak and completely lost in all the smoothing operations and background noise removal required for deconvolution. Figure 79 shows deconvolution's greater sensitivity to range resolution than with short pulse waveforms. Again a bias has been added from an incorrect number of iterations giving the appearance that 1.125m range resolution gave a smaller

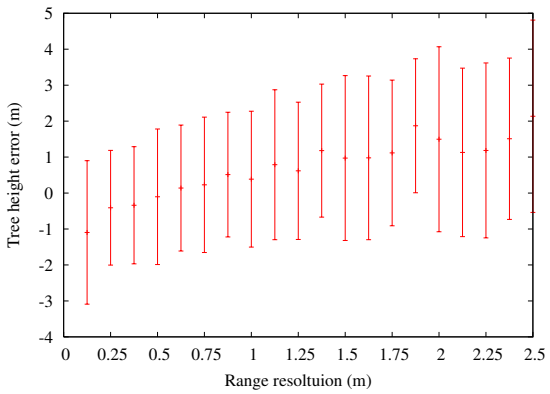

Figure 79: Mean tree height error against range resolution for waveforms deconvolved from a 100ns pulse, for a signal of 10,000 photons

error than 12.5cm.

These graphs show that useful results can still be obtained from long pulse lidar (and the 100ns pulse used is an extreme example). However this will not be as accurate over as wide a range of conditions as short pulse lidar. They also highlight the method's sensitivity to the number of iterations in the absence of a reliable convergence criterion.

5.9.3 Short pulses

The blurring caused by most waveform lidar systems is small compared to the separation of ground and canopy returns, as in figure 66. For all the examples shown, except the QinetiQ vision of A-scope which is optimised for atmospheric rather than land surface measurement, the ground and canopy returns are clearly distinguishable. This allows accurate ground position measurement. The pulse length will shift the signal start upwards, potentially adding an overestimate to tree height and the blurring will limit our ability to resolve the foliage profile.

To date users of lidar for forestry have accounted for the affect of laser pulse length on tree height estimate by either subtracting a constant from the inverted height (Wagner *et al.* 2006) or else empirically relating lidar metrics to ground observations (Lefsky *et al.* 1999, Lefsky *et al.* 2007, Boudreau *et al.* 2008) and not necessarily directly measuring tree height (linking to biomass for example). When deriving actual tree height the magnitude of signal start shift needs to be accounted for. This should depend upon pulse width, signal start gradient and noise level. The

lidar simulator was used to investigate the effect of these parameters.

Section 5.1.1 introduced a method for extracting unbiased estimates of signal start position from background and instrument noise. It is hypothesised that tracking back through the noise should remove the bias of signal truncation caused by de-noising, allowing a constant to be subtracted to account for laser pulse duration. To achieve unbiased estimates of tree top positions in the presence of laser pulses it needs to be seen whether the bias caused by truncating the signal during noise removal is significant compared to the bias added by pulse length. Also, whether a shot to shot gain adjusting system, (such as ICESat, (Harding and Carabajal 2005)) which has the effect of constantly altering the magnitude of background noise, alters the amount of signal start shift and if it is possible to theoretically derive its magnitude from the outgoing pulse shape and signal level to avoid site specific calibration.

Obviously the laser pulse duration will affect the magnitude of the signal start extension. Simulations were run with a range of different pulse lengths and the mean signal shifts and error bars showing one standard deviation are shown in figure 80.

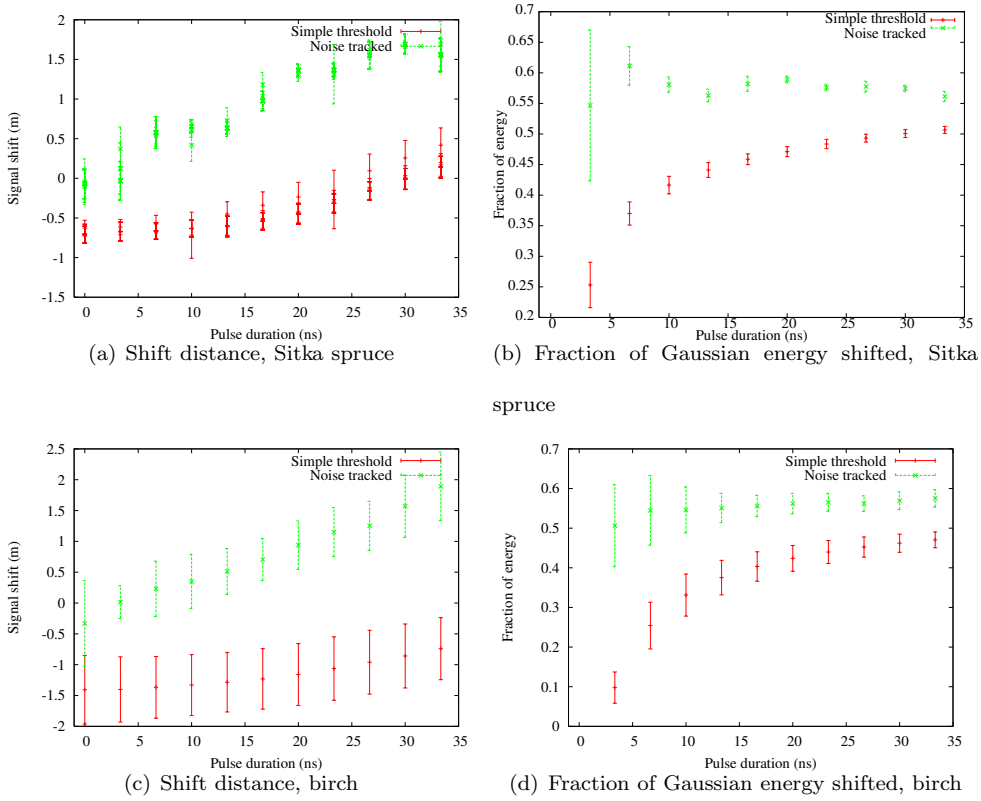

(a) Shift distance, Sitka spruce

(b) Fraction of Gaussian energy shifted, Sitka spruce

(c) Shift distance, birch

(d) Fraction of Gaussian energy shifted, birch

Figure 80: Signal shift against pulse duration for a Sitka spruce forest for 10,000 signal photons

Noise tracking's removal of bias is clearly demonstrated by figure 80(a), with no bias for an infinitely short pulse, whilst finite pulse durations have only that caused by the pulse. A laser pulse duration will not necessarily be constant throughout the laser's life or operation (Schutz *et al.* 2005, Harding and Carabajal 2005), therefore it would be advantageous if the signal start shift could be related to pulse duration. Figure 80(b) shows the signal shift in terms of the fraction of the first return's laser pulse energy after the signal start (ie. one minus the fraction of first return's energy lost through truncation). It can be seen that this was more consistent for different pulse durations with the noise tracking method than for simple thresholding.

That the fraction of pulse energy after signal start for simple thresholding was consistently below 50% shows that the maximum intensity of the pulse reflected from the first element was always lower than the noise threshold. Tracking back ensured that the bias became positive. Therefore the pulsed return from the first element was always above the mean noise level. Figures 80(c) and 80(d) show the same signal shift for birch as Sitka spruce, showing that it is not a species specific effect.

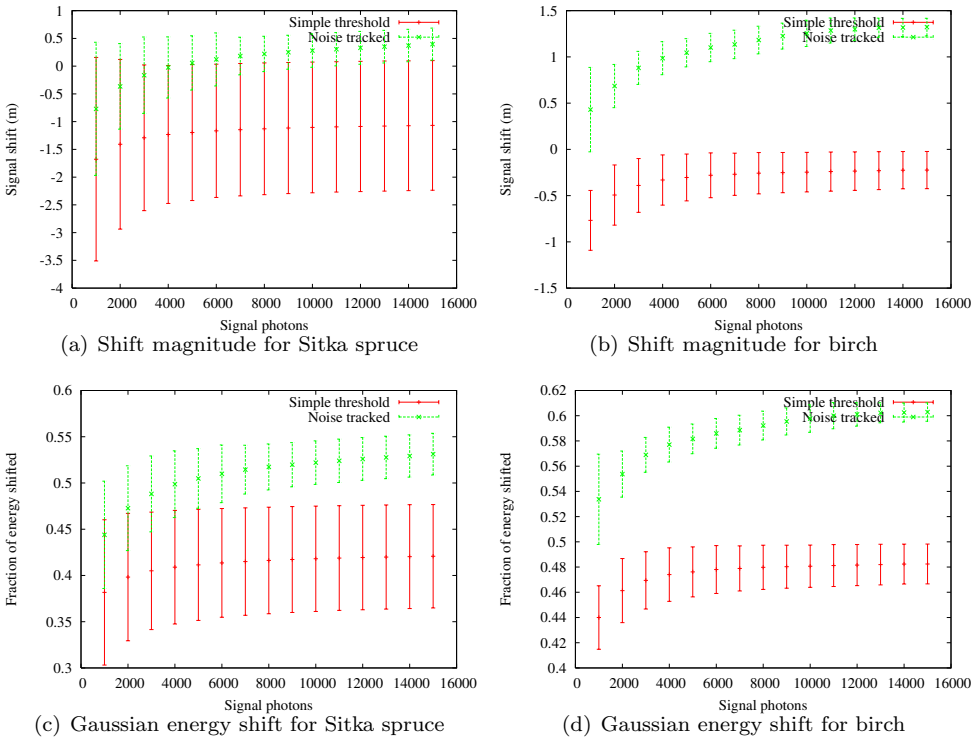

(a) Shift magnitude for Sitka spruce

(b) Shift magnitude for birch

(c) Gaussian energy shift for Sitka spruce

(d) Gaussian energy shift for birch

Figure 81: Signal start shift against noise level for simple thresholded and noise tracked signals

The signal start shift was calculated with and without noise tracking for a 16.9ns Gaussian pulse (LVIS like instrument) for a range of noise levels. Figure 81 shows the mean signal shift for each noise level with error bars showing one standard deviation calculated from waveforms over a range of forest heights, canopy covers and species. Returns from low canopy covers were more likely to be lost in noise than for dense canopies, so had larger errors at a given noise level, particularly for simple thresholding. Tracking back through the noise removed the truncation bias, giving a smaller spread of signal shifts than simple thresholding at all noise levels. Birch and Sitka spruce trees behave similarly, although the smaller range of heights and canopy covers of the birch gave a smaller standard deviation than for Sitka spruce (figure 81(d)). There was no noticeable difference between the shift's relationship with noise in terms of shift distance and fraction of the first return's energy after the detected signal start. This was probably because the relationship between distance and energy underneath a Gaussian is roughly linear in the range the signal shift varies over.

The error levelled off at around 8,000 signal photons, so the accuracy of measurements by an instrument that records 10,000 signal photons will not be limited by noise. Both methods appear to be equally noise dependant, though for a given noise level noise tracking gave a more consistent signal start shift. As long as the shot to shot gain variation does not cause there to be the equivalent of less than 8,000 signal photons and the outgoing pulse shape is recorded it should not affect the consistency of the results. At 10,000 signal photons the mean signal was 58% of the pulse energy, ±4.8% (two standard deviations) which is 1m for a 16.9ns pulse (LVIS). Subtraction of this distance should remove signal start shift caused by pulse duration.

The relationship between shift distance and Gaussian energy is illustrated in figure 82. Here the true start was at a range of 0. The pulse smears this, extending signal beyond (to the left of) the true start, some of which is truncated by background noise removal. 58% of the pulse energy is contained to the right of the solid black line, which for a 16.9ns laser pulse is 1m to the left of the pulse centre.

This adds weight to the argument for tracking back through the noise to determine signal start proposed in section 5.1.1; ensuring that systematic biases are not introduced over different forest

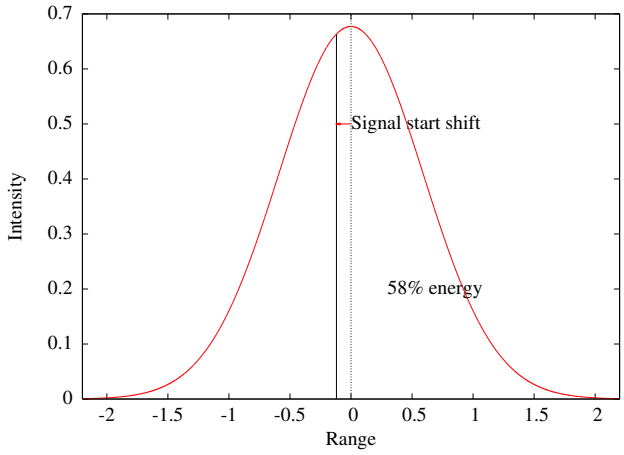

Figure 82: Signal start shift as a fraction of pulse energy

canopies.

5.9.4 Canopy start suddenness and start shift

It is expected that an initially dense (sudden) canopy will have a more intense first return so the leading edge tail caused by pulse duration will extend further above noise than for a canopy whose density builds up gradually. Therefore an initially dense canopy should have a larger signal start shift.

The suddenness of the canopy start has been described by Boudreau *et al.* (2008) with a lidar metric called "front slope". That is the angle made between the line joining the signal start above the noise threshold to the first maximum (in their case of the fitted Gaussians) and the range axis. Lefsky *et al.* (2007) proposed a similar metric called "leading edge extent", that is the distance between the signal start and the point at which the signal first rises above the mean radiance level.

Using front slope and leading edge extent as measures of canopy start suddenness, it was investigated whether it had an impact on the signal start shift. From figure 83 it can be seen that there seems to be some relationship between front slope and signal shift for small front slopes. This may be because these canopies had very low cover, whilst not necessarily being short, so that only a few leaves are caught in the footprint rather than whole crowns. For larger front slope values the shift magnitude settled to a constant. Sitka spruce and birch showed similar shapes (figures 83(a) and 83(b)), although birch had fewer high front slope values due to the smaller range of forests

available. The results were re-run in the absence of noise to see if that was masking a relationship; it was not.

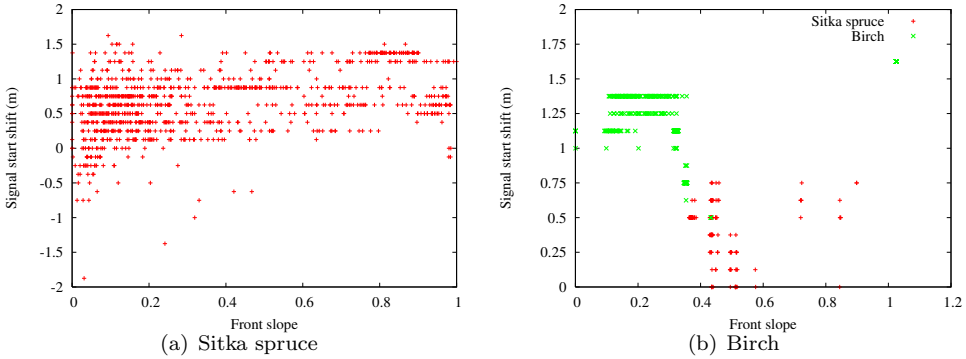

(a) Sitka spruce (b) Birch

Figure 83: Start shift magnitude caused by a 16.9ns pulse against front slope of the ideal canopy with 10,000 signal photons

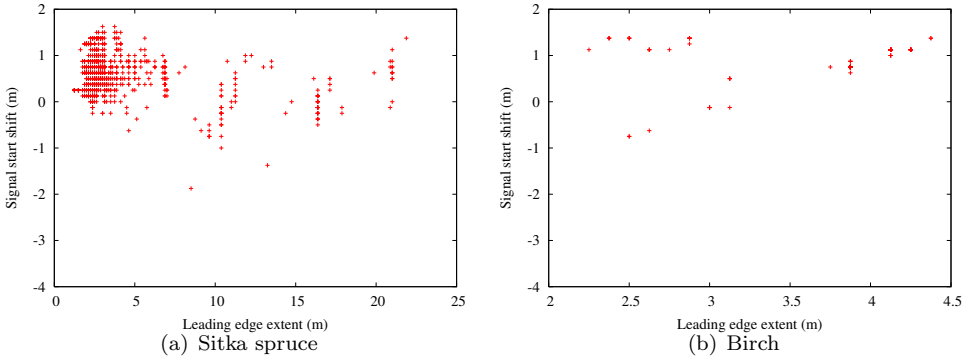

(a) Sitka spruce (b) Birch

Figure 84: Start shift magnitude caused by a 16.9ns pulse against leading edge extent of the ideal canopy with 10,000 signal photons, included only to show the better behaviour of front slope, shown in figure 83.

The results for birch (figure 84(b)) and Sitka spruce (figure 84(a)) suggest that there is no useful relationship between shift magnitude and front slope. This may be because both front slope and leading edge extent are measured over longer scales than the pulse lengthening of the signal start. Maybe another, shorter range metric would show a relationship. Such a metric has not yet been proposed and such a short scale measure would be more sensitive to noise than the existing longer scale metrics.

A shorter range metric was calculated to see if it were better related to signal start shift. This metric was found by drawing the steepest possible line from the signal start to a later point in the

signal and the calculating the angle between this and the range axis. This is analogous to laying a plank against the signal with its foot at the signal start, so it will be called "plank angle". The results are shown in figure 85. Again, no reliable relationship was apparent.

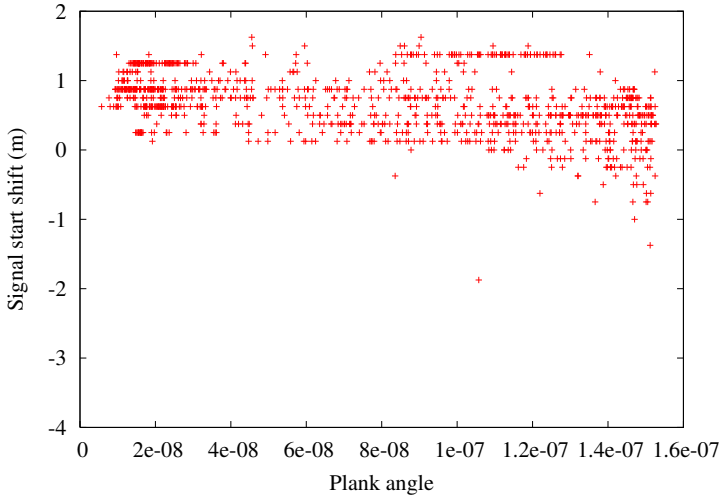

Figure 85: Start shift magnitude caused by a 16.9ns pulse against plank angle of the ideal canopy with 10,000 signal photon

This suggests that the suddenness of canopy start was not significant to the pulse shift, possibly because it did not vary over a large enough range to make a difference.

5.9.5 Short pulse deconvolution

Some authors believe that very high resolution canopy maps, both horizontally and vertically, are needed to manage forests in a natural manner (Zimble *et al.* 2003), to monitor bird habitats (Ross *et al.* 2004) and to predict timber growth (Comas *et al.* 2009).

To this end the possibility of deconvolution of short pulses was investigated by trying to solve a "difficult" forest. That is a relatively dense (85.3%), short (8m) Sitka spruce canopy. This had a weak ground return without a large gap between it and the canopy. The ground signal could be easily blurred into the canopy by a pulse, preventing inversion. Figure 86(a) shows the result of deconvolution of a 10ns pulse by sixty iterations of Gold's method after denoising. The ground return was clearly distinguishable in the measured signal though the signal start has been shifted a little but this can be corrected without having to resort to deconvolution.

For a 20ns pulse, which is longer than any lidar currently used for canopy measurement, (figure 86(b)) there is no longer a turning point in the ground signal, preventing separation and so inversion. Denoising by convolution with the out going pulse and performing sixty iterations of Gold's method reveals the ground return. Therefore deconvolution can aid inversion from shorter (20ns) laser pulses, but the lack of a convergence criterion means it should be a last resort and the simple subtraction of the previous section should be used if possible.

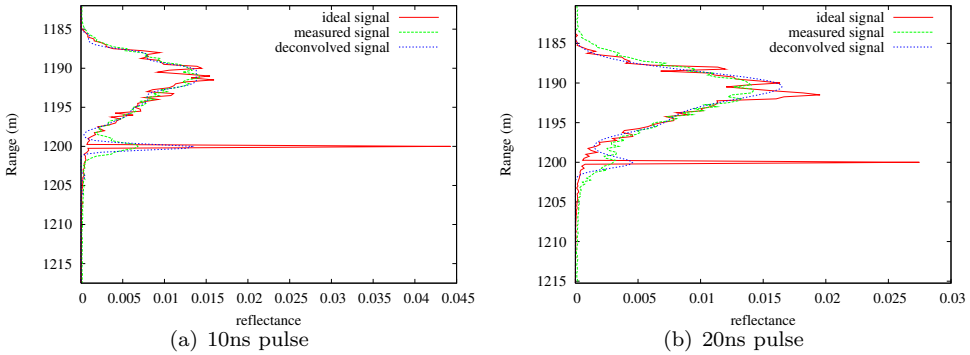

(a) 10ns pulse

(b) 20ns pulse

Figure 86: Deconvolution over a 7.6m tall forest with 85.3% canopy cover and 10,000 signal photons after 60 iterations (optimum).

This short, dense forest is a worse case scenario. Taller or less dense forests could be more easily extracted from a 20ns pulse. However determining whether the ground return has been blurred into the canopy is not easy in the presence of noise and heterogeneity (more on this is section 5.12).

5.9.6 Short pulse conclusions

A short pulse prevents the determination of ground position for only very short ($< 5m$) forests on flat ground. Its main effect is to add a bias to the signal start position. Tracking back through the noise to find signal start ensures that there is no truncation of the signal by noise (provided there are at least 8,000 signal photons) leaving only the extension from the pulse length. The extension caused is reasonably well related to pulse duration whilst being fairly tolerant to canopy cover and "signal suddenness". Therefore it is reasonable to correct by subtraction of a constant distance, containing 58% of the pulse energy ($\pm 4.8\%$). The fraction of pulse energy cut off is somewhat related to noise level, but ensuring a signal level of more than 8,000 signal photons will limit the

change in signal shift to only a few centimetres, a small error compared to other sources. Most importantly this is a physically based method to directly measure tree height without the need for site specific calibration.

Figure 87 shows tree height error against canopy cover for a 16.9ns pulse. Pulse duration has been corrected by subtraction of a constant from the signal start (1m, corresponding to 58% of the Gaussian pulse's energy). It shows that the tree heights found from a 16.9ns pulsed lidar after subtraction of the constant agree very closely with those from an unpulsed lidar, with sub-meter errors. No dependency on canopy cover is apparent; although heterogeneous aged stands, which were left out of the earlier analysis, show greater errors, but no more so for pulsed lidars than the infinitely short case.

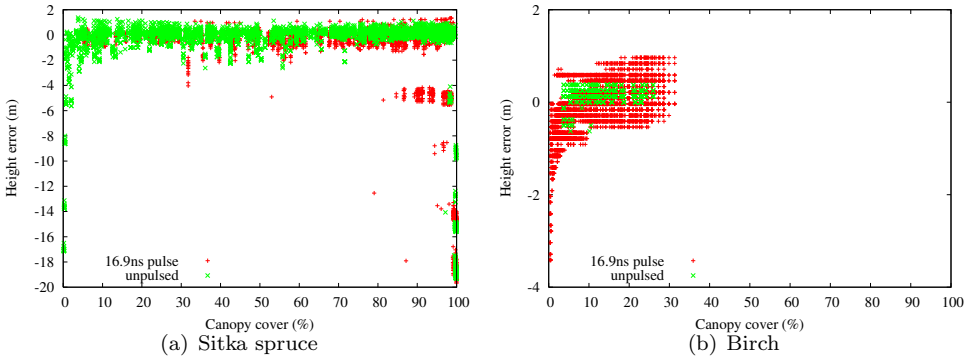

(a) Sitka spruce (b) Birch

Figure 87: Tree height accuracy against canopy cover for a 16.9ns and infinitely short pulses

To test the correction factor of 58% of the energy (1m for a 16.9ns pulse) from the signal start it was applied to the birch dataset, which was not used to derive the shift magnitude. Figure 87(b) shows that, whilst the variance is increased there is no bias.

For the rest of the investigation it will be assumed that a finite pulse duration can be accounted for by subtracting a constant (corresponding to 58% of the pulse energy if Gaussian) from the signal start position. This holds as long as the pulse duration does not blur the canopy and ground returns together, which is a safe assumption for pulses less than 16.9ns on flat ground (the longest pulse for a current vegetation canopy lidar).

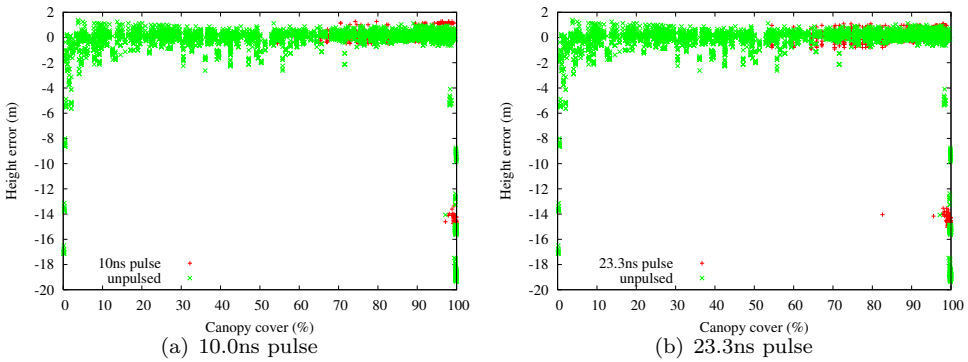

(a) 10.0ns pulse (b) 23.3ns pulse

Figure 88: Tree height accuracy against canopy cover different pulse durations subtracting a distance containing 58% of the pulse energy

5.9.7 Pulse length conclusions

This section has shown the effect of long laser pulses requiring deconvolution on tree height accuracy (and so our ability to distinguish ground from canopy required for all parameters). Accurate, unbiased estimates of tree height can be extracted by deconvolution with Gold's method, although a convergence criterion would be needed to ensure robustness.

Any deconvolution method will always be an extra source of error and it would be preferable to not have to resort to it. The ground returns over flat terrain are distinguishable for reasonably long pulses (20ns, longer than any current system being used for vegetation). In that case the ground position can be found accurately and the signal start determined with a fairly constant offset that can be corrected. Therefore it can be concluded that pulse lengths should not exceed 20ns, though instruments that have to (such as A-scope) still allow some forest measurement. This section focused on tree height, however once the information necessary for tree height has been extracted it should be reasonably easy to extract other parameters such as canopy cover and height of median energy.

The 100ns pulse system was only investigated as it has been proposed for A-scope This is currently the only spaceborne lidar with any chance of measuring forest canopies in the pipeline for ESA. Were it not for this uniqueness, effort would not have been expended trying to get usable tree data from such an instrument.

For the rest of the investigation a pulse shorter than 20ns will be assumed, avoiding the need

for deconvolution. The bias of the signal start for this can be corrected by subtracting a distance containing 58% of the pulse energy (if Gaussian) and so it should have no affect on final accuracy. An infinitesimally short pulse will be used for the majority of the analysis for clarity. All methods proposed will be tested on realistic pulse durations.

5.10 Waveform shape

The success of information extraction obviously depends entirely on the shape of the returned waveform. As well as tree height and canopy cover and pulse length mentioned previously, other structural and optical effects have the potential to change the waveform's shape. The next few sections will assess the impact of each of these features on inversion accuracy as well as investigating some metrics that have been proposed to account for them.

Topography will also have a dramatic effect on the waveform shape, but this will be covered in detail in section 5.11. The rest of this section will deal with flat ground only.

5.10.1 Multiple scattering

As light interacts with a canopy it can be multipley scattered (Ross 1981). This increases the apparent reflectance of a surface above its single scattering albedo and will add extra path length, potentially distorting the waveform shape and confusing range resolved measurements.

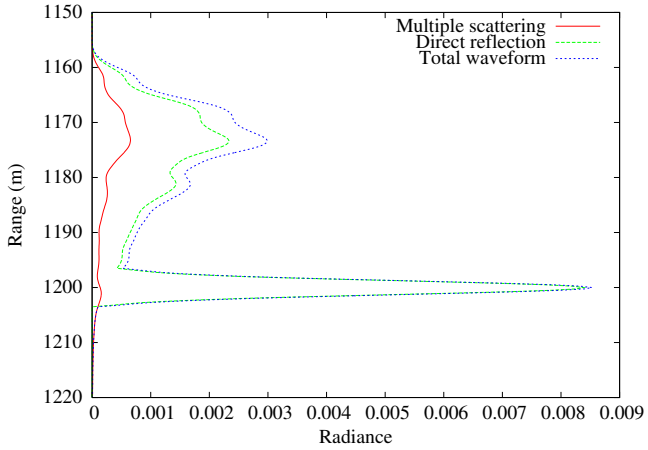

Figure 89: Contribution of multiple scattered light to an LVIS simulation over a 21m tall Sitka spruce forest with 48% canopy cover

Figure 89 shows that whilst it had an effect upon the apparent reflectance, the overall shape of the waveform is largely unaffected. This implies that the majority of multiple scattering is short range (no more than a few range bins), potentially within a single shoot. A small amount of multiple scattering contribution appears to come from beneath the ground and this must come from longer range scattering, however the magnitude is small compared to the short range scattering. Therefore the main effect of multiple scattering is to enhance the reflectance rather than distort the waveform. For very dense canopies the ground return is weakened to such an extent as to be potentially lost in the echoes, however background noise tended to dominate even at these canopy covers. It was not thought necessary to take the echoes into account when calculating tree height (nor have any other authors taken it into account).

5.10.2 Tree shape

The shape of the canopy, specifically its distribution with range, should have an influence on the signal start magnitude and so the ease with which it can be found above noise. It is expected that for an initially dense canopy, which will have a more intense first return, the position of the tree top should be easier to determine. Two metrics have been developed to describe the abruptness of the start of a canopy, "front slope" (Boudreau *et al.* 2008) and "leading edge extent" Lefsky *et al.* (2007), both of which were defined in section 5.9.4. The relationship between both of these metrics and a forest's biophysical parameters will be briefly explored in order to asses their suitability for a physically based inversion method.

5.10.3 Canopy suddenness metrics; front slope

Here front slope has been calculated from the line joining the signal start above noise (tracking back to mean noise) and the first maximum point of the waveform after smoothing by a 3m Gaussian. Smoothing avoids within crown heterogeneity being taken as a maximum rather than the strongest canopy return. Figure 90 shows a comparison between front slope's canopy cover dependence for birch and Sitka spruce forests of similar height. For both species there seems to be no relationship for sparse canopies ($< 5\%$ canopy cover). It is likely that these footprints included only parts of trees rather than whole crowns (leaves from trees outside the footprint being

clipped), giving rise to unusual waveform shapes. For canopies above 5% cover the two species show different relationships which is most likely due to the very different foliage profiles of broadleaf and coniferous trees. Coniferous trees have roughly conical crowns which will have initially low densities for all canopy covers, even very dense. Broadleaf canopies have much flatter tops and so the initial canopy density is much more related to total canopy cover.

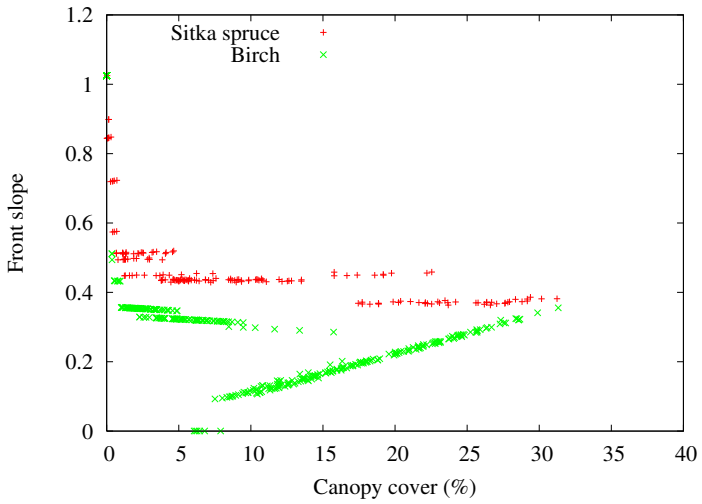

Figure 90: Front slope against canopy cover for birch forests and similar sized Sitka spruce forests

Due to the small range of birch forest heights and canopy covers available the rest of this section will concentrate on Sitka spruce; accepting that any relationships may have a further species dependence. It will be seen whether such a dependence is an issue later.

Figure 91 shows front slope against canopy cover, separated out by tree height for different noise levels. Mixed aged forests have been left out for clarity (figure 92 shows that they display little pattern due to the large variation in waveform extents and shape). This is because mixed aged forests have their canopy returns spread over a larger range than uniform aged canopies, therefore the intensity was lower in each bin for the same canopy density and signal start error was more affected by noise than for uniform aged stands.

The unnoised case in figure 91(a) showed clear relationships between front slope and canopy cover for each tree height class. As it would be expected, denser forests had stronger canopy returns and so larger front slopes than sparser canopies for a given tree height. For a given canopy cover, the maximum return will be further from the signal start for a taller tree than for a shorter

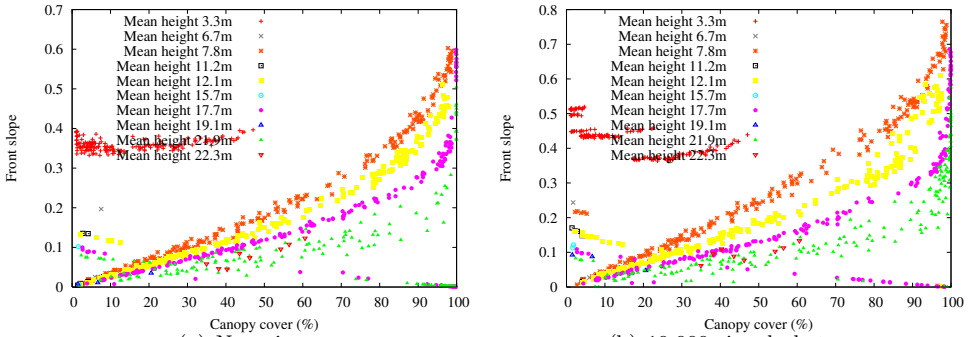

(a) No noise (b) 10,000 signal photons

(c) 3,000 signal photons (d) 1,000 signal photons

Figure 91: Front slope against canopy cover for Sitka spruce forests at different noise levels, separated by tree height for an infinitely short laser pulse

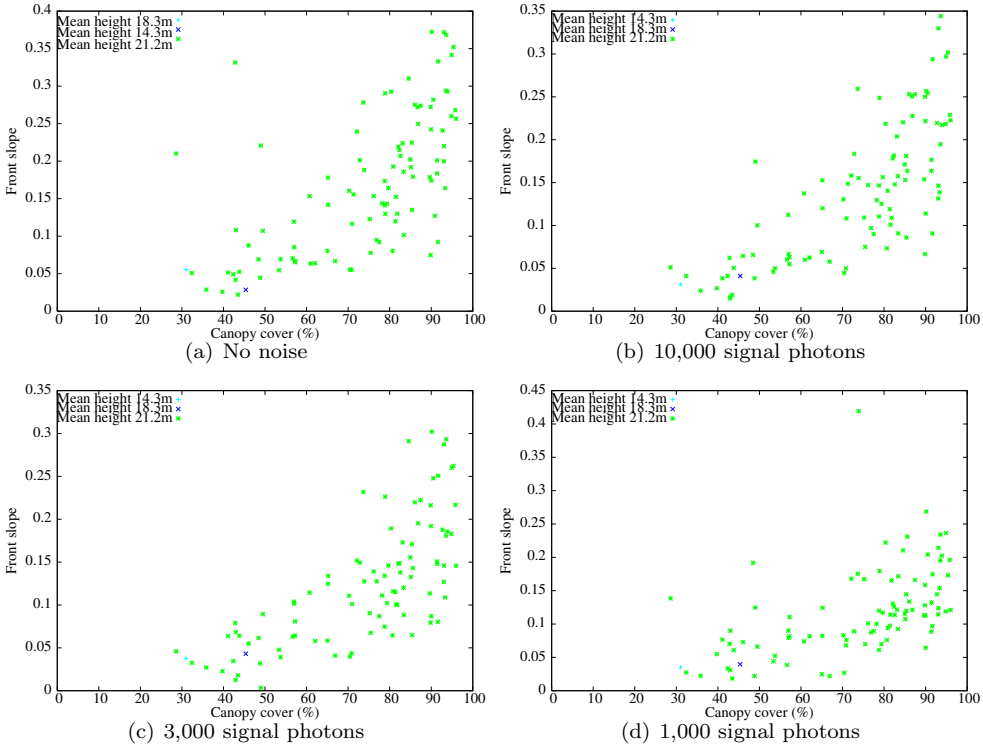

Figure 92: Front slope against canopy cover for mixed aged Sitka spruce forests at different noise levels, separated by tree height for an infinitely short laser pulse with noise tracking

tree, giving a smaller front slope. Therefore front slope is a function of both canopy cover and tree height.

There appeared to be an exponential relationship between front slope and canopy cover for forests over 5m tall and 60% canopy cover. This fits in well with the standard Beer-Lambert law models used to describe the probability of interaction within a canopy. For denser canopies, light is less likely to penetrate far and so the maximum return was nearer the canopy top than for a less dense forest of the same height, thereby giving a greater front slope value than the increased intensity of the return would on its own. This upward shift of the maximum return is visible in figure 54.

Short trees, below 5m, were an exception to this. This is because for short canopies, convolving with a 3m Gaussian blurs the canopy and ground returns together. Therefore the first maximum's peak was influenced by the ground position, not just the canopy signal (illustrated in figure 93). The only maximum corresponded to the ground position and so front slope was far higher than it would be for a taller canopy. For denser short canopies the canopy return may be strong enough to have a maximum separate from the ground return and so have a much lower front slope. Relating the smoothing Gaussian's width to the maximum extent of the waveform may help the relationship for shorter canopies. It must be wide enough to smooth out noise and canopy heterogeneity but narrow enough to prevent the ground returns affecting the position of the first maximum. However, for our purpose such extra complications would only be beneficial if front slope were related to signal shift. For this reason such a method was not pursued further here.

Figure 91(d) had some large values of front slope for low ($< 3\%$) canopy covers, and some even larger values (around 25) for covers less than 0.5%. These were left off the graph for clarity. These extreme outliers were caused by weak canopy returns being completely lost in noise, so that the signal start was taken as the beginning of the ground return, giving a very steep line connecting that to the maximum.

5.10.4 Tolerance of front slope to noise

Convolving with a 3m Gaussian (far larger than the 12.5cm sampling interval) ensured that noise did not affect the position of the maximum and tracking back through the noise negated any

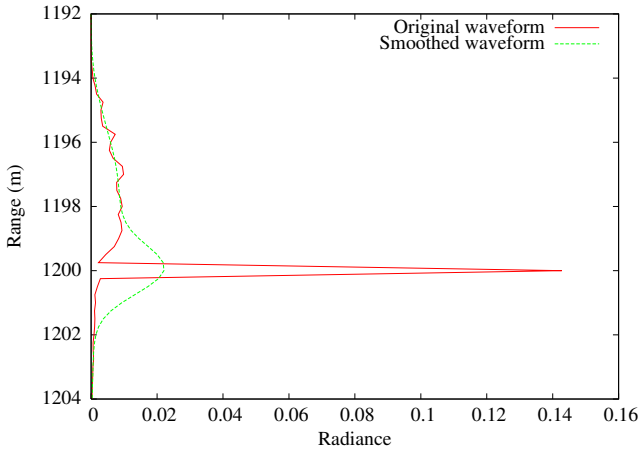

Figure 93: Original waveform and waveform convolved with a 3m Gaussian for a 3.3m tall Sitka spruce canopy with 30.7% cover

truncation, ensuring that the front slope calculations were robust to noise, as illustrated by the similarity in front slope values shown by figures 91(b), 91(c) and 91(d).

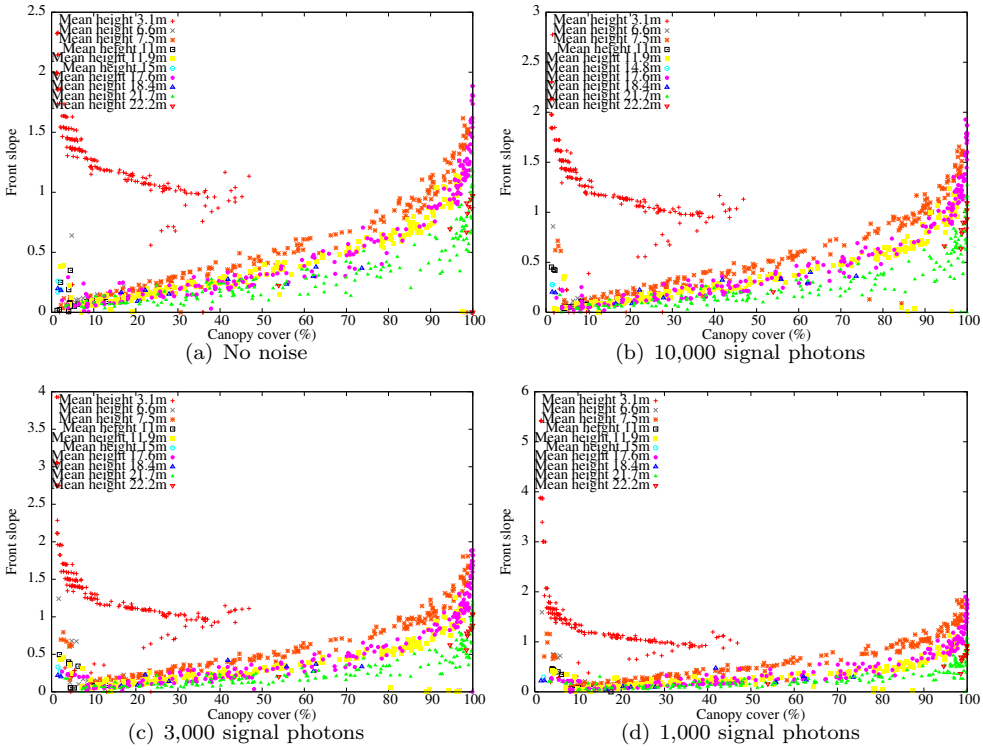

(a) No noise (b) 10,000 signal photons

(c) 3,000 signal photons (d) 1,000 signal photons

Figure 94: Canopy cover against front slope without noise tracking

It was hypothesised that the truncation of the signal start without noise tracking would cause an increase in front slope with noise. Figure 94 shows front slope against canopy cover, split by tree

height and noise level using the simple threshold rather than noise tracking; no difference between that and the noise tracked case (figure 91) was apparent. Therefore either the truncation of the signal start was insignificant compared to distance to the first maximum or the overall decrease in intensity caused by noise removal counteracted the truncation. Figure 80(a) shows that the signal truncation is of the order 75cm without a pulse length whilst figure 54 shows that the distance from the signal start to first peak is about 5m, much longer than the signal start extension. Either way front slope seemed to be robust to noise whether noise tracking was employed or not.

5.10.5 Canopy suddenness metrics; leading edge extent

The leading edge extent, proposed in Lefsky *et al.* (2007), is an alternative to front slope. Here leading edge is taken as the distance between the first return above the cumulative threshold (with noise tracking) and the point at which the signal rises above the median intensity. As it relies on the mean energy level rather than the position of the first maximum is should be even less sensitive to noise, requiring no smoothing and so retaining the full resolution.

Figure 95 shows plots of leading edge extent against canopy cover, separated by height for a range of noise levels. As with front slope, low canopy covers ($< 15\%$ cover in this case, a higher threshold than for front slope) showed much larger values than high covers for the same tree height. This was due to the strength of the ground return skewing the mean energy downwards. Unlike front slope, which only showed this affect for short trees, tall trees are equally affected as the ground return strength always influences the mean energy whereas it will not affect the position of the first maximum for suitably tall trees. For denser ($> 15\%$) canopies there was a slight reduction in leading edge extent with increasing cover (denser canopies have stronger returns near the top), whilst taller trees had slightly larger leading edge extents for the same covers (due to the ground return being further from the signal start).

Both of these dependencies were weak compared to the variation of leading edge extent within a set of covers and heights, especially when noise was introduced. Noise tracking ensured that no overall change in leading edge extent was introduced by noise, although the variance increased. Figure 96 shows that like front slope, mixed aged forests had a much weaker relationship between leading edge extent and canopy cover. Smoothing waveforms before calculating edge extent,

removing any chance of noise affecting the value, had no effect; proving edge extent's inherent robustness to noise.

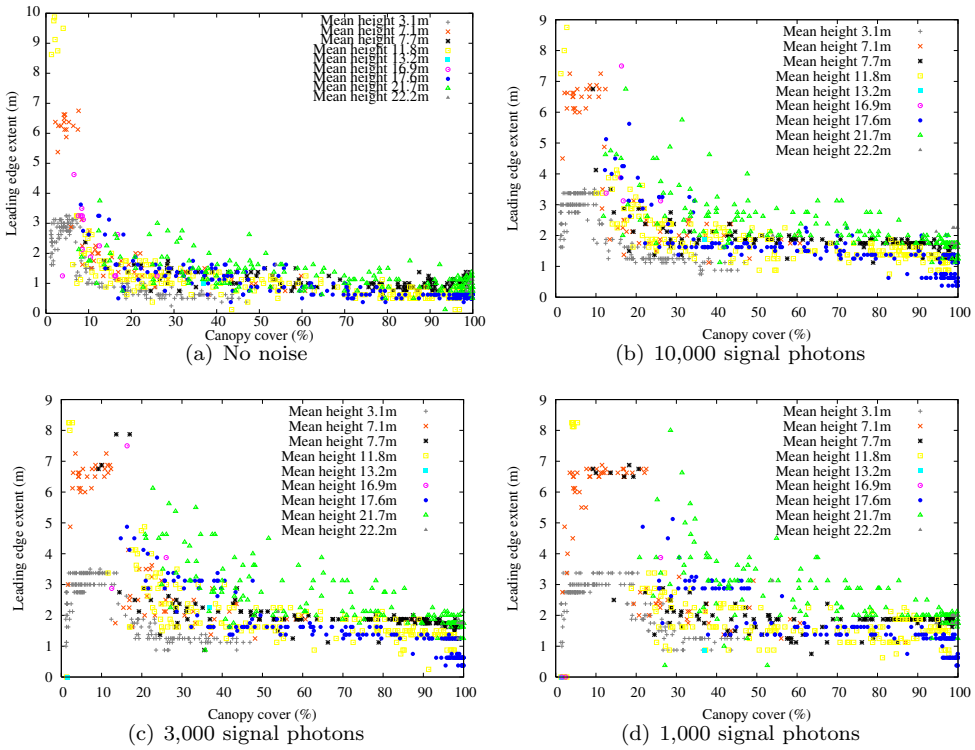

(a) No noise (b) 10,000 signal photons (c) 3,000 signal photons (d) 1,000 signal photons

Figure 95: Leading edge extent against canopy cover for uniform aged Sitka spruce forests at different noise levels, separated by tree height for an infinitely short laser pulse

These results suggest that leading edge extent is not directly related to tree height or canopy cover, certainly less so than front slope. For the rest of the investigation only front slope will be examined in detail.

5.10.6 Canopy suddenness conclusions

Tree height errors against front slope are shown in figure 97. The majority of front slope values showed similar tree height errors. Extreme front slope values showed high errors and from figure 91 it can be seen that these high and low front slope values correspond to extreme canopy covers (<10% or >98%), for which inversions are are known to fail. There were some large errors for moderate front slope values (around 1.5×10^{-6}). Closer examination reveals that they were due to dense, medium height (>95% cover, 6m< height <13m) and short, fairly dense (<8m tall, >85% cover) canopies. These are hard cases to invert accurately, the combinations of height and canopy

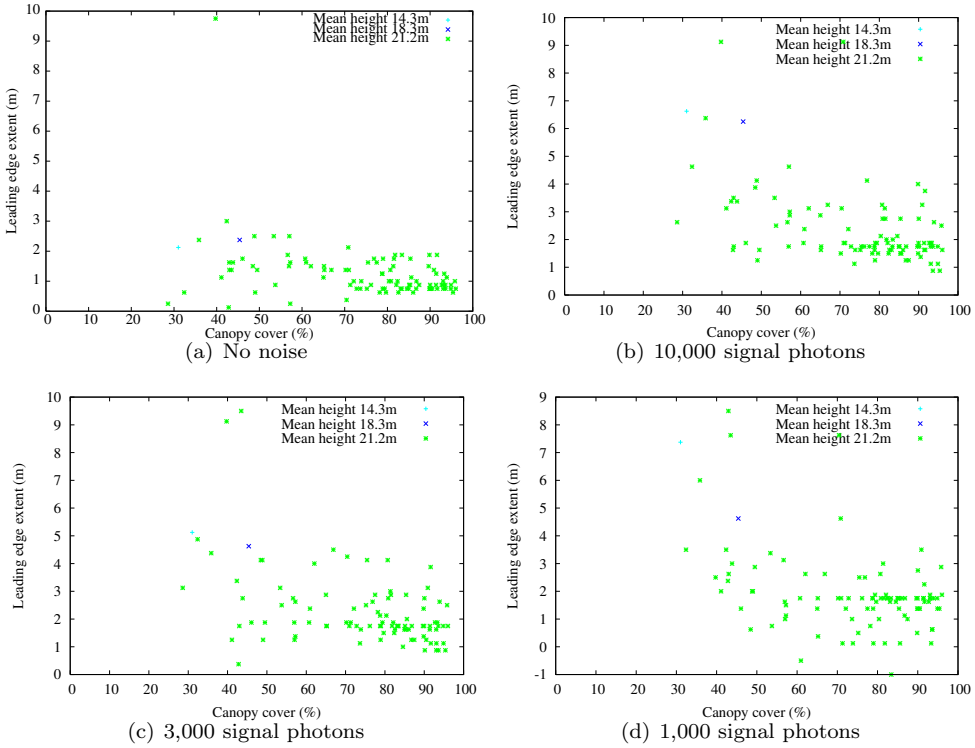

(a) No noise

(b) 10,000 signal photons

(c) 3,000 signal photons

(d) 1,000 signal photons

Figure 96: Leading edge extent against canopy cover for mixed aged Sitka spruce forests at different noise levels, separated by tree height for an infinitely short laser pulse

cover give them only moderate front slope values, giving no indication of the difficulty.

Birch forests showed a similar relationship between front slope and tree height error as Sitka spruce and interestingly showed similar front slope values.

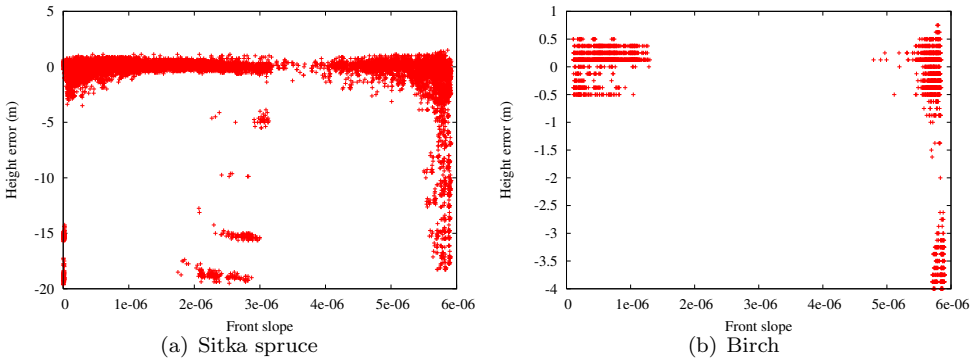

(a) Sitka spruce (b) Birch

Figure 97: Range errors against front slope for Sitka spruce and birch

It seems that whilst front slope is related to inversion error, these dependencies can be better described by tree height and canopy cover. For uniform aged stands front slope is quite directly related to canopy cover and height (figure 91), however this relationship does not hold for mixed aged forests (figure 92). Even for uniform aged stands, front slope's relationship to biomass is complex. Increasing canopy cover (and so biomass) increases front slope, whilst increasing tree height (also increasing biomass) acts to decrease front slope. It is also sensitive to species through crown shape. As worded in Boudreau *et al.* (2008), front slope depends upon the absolute intensity of the maximum canopy return. This will vary with element spectra (and so species) and the shot to shot instrument gain. Inversion processes using similar lidar metrics need to take this into account, or else use site specific relationships, greatly limiting their application. A more physically based method would be preferable.

For the rest of this investigation only more direct forest structure measures such as tree height and canopy cover will be used. Metrics such as front slope may be useful for relating to parameters that are not directly measurable (biomass and LAI), through allometric relationships and principal component analysis. Here they have the advantage of being direct metrics from lidar waveforms rather than needing to be inverted (as tree height is), potentially introducing errors.

5.10.7 Understorey

Understorey spreads out the signal, reducing the instantaneous intensity and causes a loss of distinction between canopy and ground returns, both complicating tree height estimation. Figure 98 shows a waveform returned from a mixed age Sitka spruce forest on flat ground. The forest was made up of Sitka spruce trees of 5, 9, 20, 30 and 40 years old. The 40 year old trees were around 25m tall with large gaps between the ground and canopy, the 5 year old trees were around 3m tall with foliage all the way to the ground. These short trees have the same effect on the waveform as non-arboreal vegetation that makes up more traditional understory, such as ferns and shrubs.

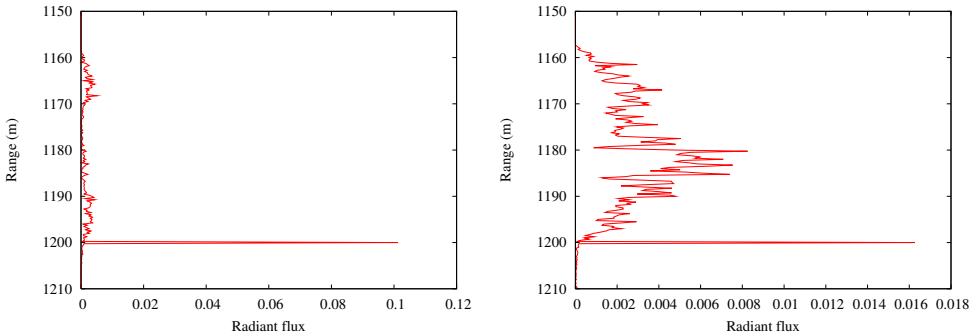

(a) 20.6m tall, 50% canopy cover

(b) 21.5m tall, 91.7% canopy cover

Figure 98: Waveforms of mixed age forest

For this example there was no gap between canopy and ground returns, but due to the extent of the canopy return, even for high canopy covers ($> 90\%$, such as figure 98(b)) the ground return was more intense than the canopy return. There was still a turning point between the ground and canopy, allowing separation and so accurate inversion. The laser pulse duration (covered in detail in section 5.9) will reduce this contrast in intensities somewhat, but as figure 99 shows, there is still a turning point with a 10ns pulse (a typical canopy lidar pulse duration.

Figure 100 shows the tree height error against canopy cover for uniform aged canopies (no understory) and mixed age forests (understory). Not such a broad range of canopy covers was available for the mixed age forests as for the uniform aged forests due to the larger crowns of mature trees (here low cover, uniform forests tend to be made from younger trees). If the canopy and ground returns were not distinguishable tree height would be underestimated and this underestimation would increase with canopy cover. This was not the case and in fact denser canopies

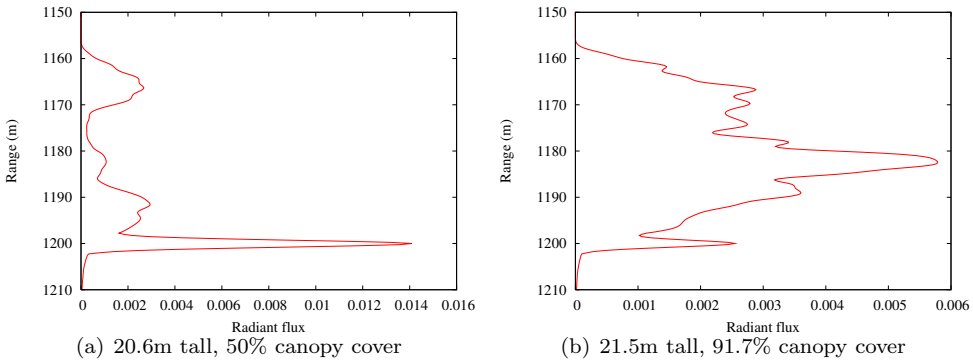

(a) 20.6m tall, 50% canopy cover (b) 21.5m tall, 91.7% canopy cover

Figure 99: Waveforms of mixed age forests with a 10ns pulse. The same forests as figure 98 were used. The ground is at a range of 1,200m

showed more accurate inversions than sparser canopies. This must be due to the more spread out foliage elements giving lower canopy intensity signals whose starts are more likely to be lost in noise. Figure 100(b) confirms that the error in tree height for mixed age stands was almost entirely due to the difficulty in finding the signal start. The ground position errors being identical to the uniform aged crop inversions.

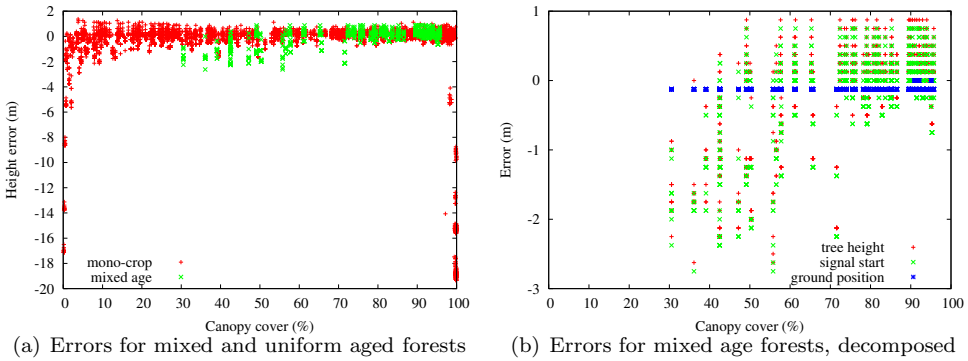

(a) Errors for mixed and uniform aged forests (b) Errors for mixed age forests, decomposed

Figure 100: Tree height errors for forests with and without understory. 10,000 signal photons were used and no pulse length. Each waveform was inverted 15 separate times with different sets of noise.

The experiments were repeated with a 10ns laser pulse (typical canopy lidar) to see if that ever hides the turning point between ground and canopy on flat ground. Figure 101(b) shows that the ground position errors were negligible up to 92% canopy cover. At 93% cover there was one 5m over prediction of ground position but other than that all other ground errors were sub metre (including the other fourteen noise cases of this same waveform).

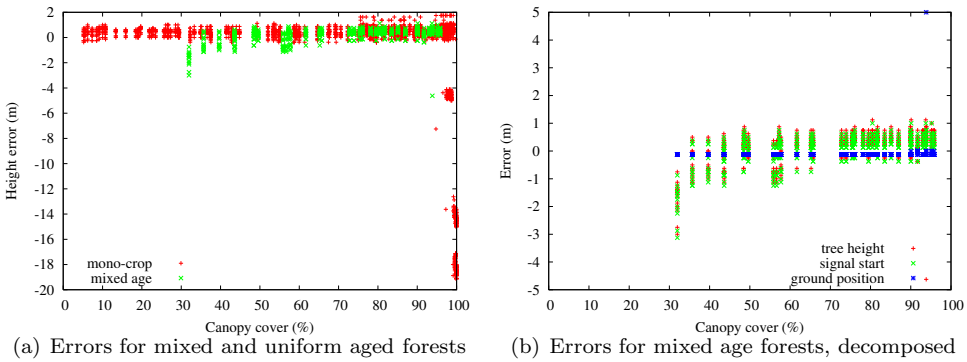

(a) Errors for mixed and uniform aged forests (b) Errors for mixed age forests, decomposed

Figure 101: Tree height errors for forests with and without understory. 10,000 signal photons were used with a 10ns pulse. Each waveform was inverted 15 separate times with different sets of noise.

An occasional failure of ground position is perhaps unavoidable and is only very occasional (0.04% of mixed forests tested). Therefore it would appear that heterogeneous forests (and so understory) do not complicate the ground finding on flat ground. The largest effect is to lower the intensity of the canopy return for a given cover, making it more likely to be lost in noise, particularly with the extra spreading of a laser pulse length. This loss is unavoidable.

This section has dealt exclusively with forests on flat ground. Topography causes extra blurring which may prevent inversion. Figure 102 shows a waveform for a bimodal canopy on a slight slope. In this case the shorter trees are blurred in with the ground but the taller trees are separate and so the algorithm would correctly determine the tallest tree height but would underestimate the total canopy cover and so LAI. There is no way to correct this error with single wavelength lidar, the signal is indistinguishable from a lower canopy cover forest without understory. For a mixed aged forest (such as that in figure 98) there would not be a clear gap between the tall and short canopies and so the height would not be correctly determined. This will be covered in detail in section 5.11.

5.11 Topography

Topography acts to reduce the separation between ground and canopy returns. If the ground height variation across the lidar footprint is greater than the separation between the canopy and ground, returns will be blurred together, as shown in figure 103. This can prevent determination

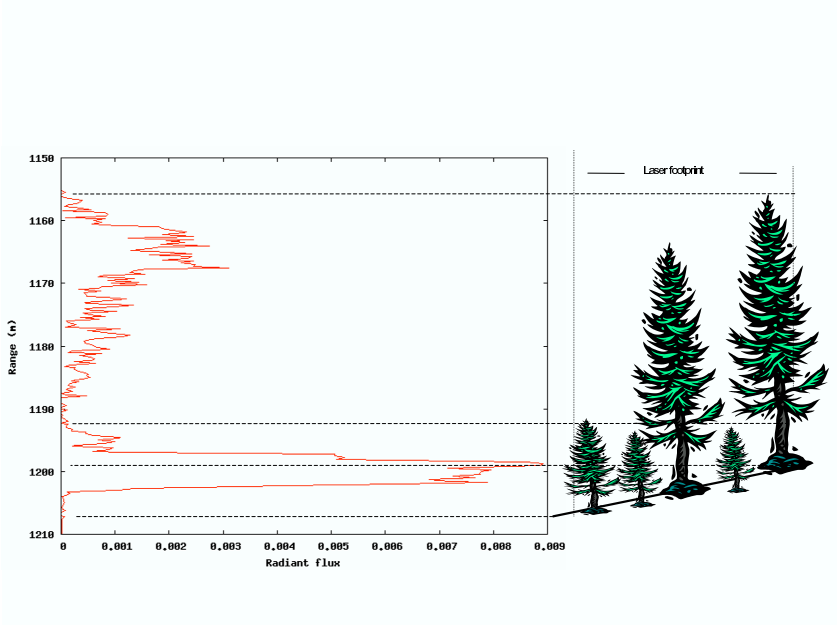

Figure 102: Effect of understory on a simulated waveform over a bimodal forest on a 12^o slope

of any characteristics, other than an upper limit of tree height (from the distance between first and last returns).

As it is the variation of ground height across the footprint that causes blurring, the smaller the lidar footprint the smaller the blurring. However small footprint lidar can miss tree tops if coverage is not continuous (ie. gaps between adjacent footprints), thereby introducing a negative bias ((Zimble *et al.* 2003), illustrated in figure 12). The engineering challenges of achieving continuous coverage with many small footprints over crown sized areas from space has not yet been discussed and is beyond the scope of this thesis. If it were possible it would be the best solution.

Figure 104 shows how a 30m footprint waveform is affected by different slope angles. For this forest a slope of more than 30^o would prevent parameter inversion, even before the extra blurring of the laser pulse duration is included whilst a slope of 20^o would greatly complicate the process.

There are no plans to launch scanning or imaging small footprint waveform lidars into space. Therefore a method of overcoming topographic blurring of large footprint lidar is required. Due to the lack of accurate, high resolution global DEMs and other extra information over forests (Rosette *et al.* 2007, Dowman 2004) a method using only the lidar information (or perhaps other global

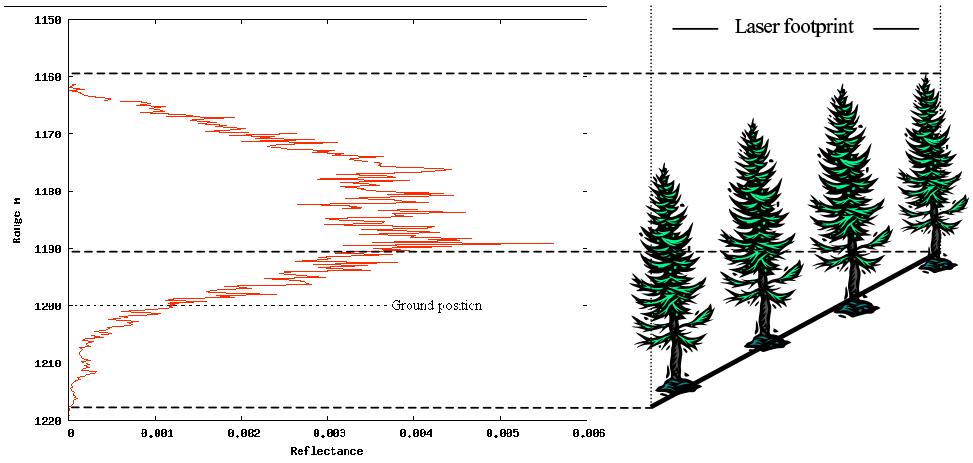

Figure 103: Illustration of topographic blurring of a 30m footprint on a 30^o slope

EO products) for inversion is needed.

5.12 Multi-spectral lidar

There have been recent advances towards multi-spectral and even hyperspectral waveform lidar (Kaasalainen 2007, Morsdorf *et al.* 2008b). This offers many exciting new possibilities.

If two wavelengths with different reflectances for canopy and ground are used, the changing proportions of canopy and ground with height should be visible in the spectral information. This should allow a physically based method to account for slope, requiring little or no empirical calibration. The literature suggests that steeply sloped forests are not uncommon (Lefsky *et al.* 2007, Rosette *et al.* 2008, Goodwin 2006). Indeed, forests commonly grow on steep ($> 20^o$) terrain (Takahashi *et al.* 2005), although their proportion and impact at the global scale have not been quantified.

Figure 105 shows the reflectance of a forest's components against wavelength (from spectra described in section 4.2.2). A real forest canopy is composed of leaf and bark. Assuming that leaves and branches have similar phase functions, the resultant canopy spectrum will be the average reflectance weighted by the visible projected areas of each. For the Sitka spruce models, the average projected proportion of leaf and wood in the canopy was 58% and 42% respectively with a standard deviation of 15% (from the material information recorded by the ray tracer). This proportion was used to make the canopy spectrum.

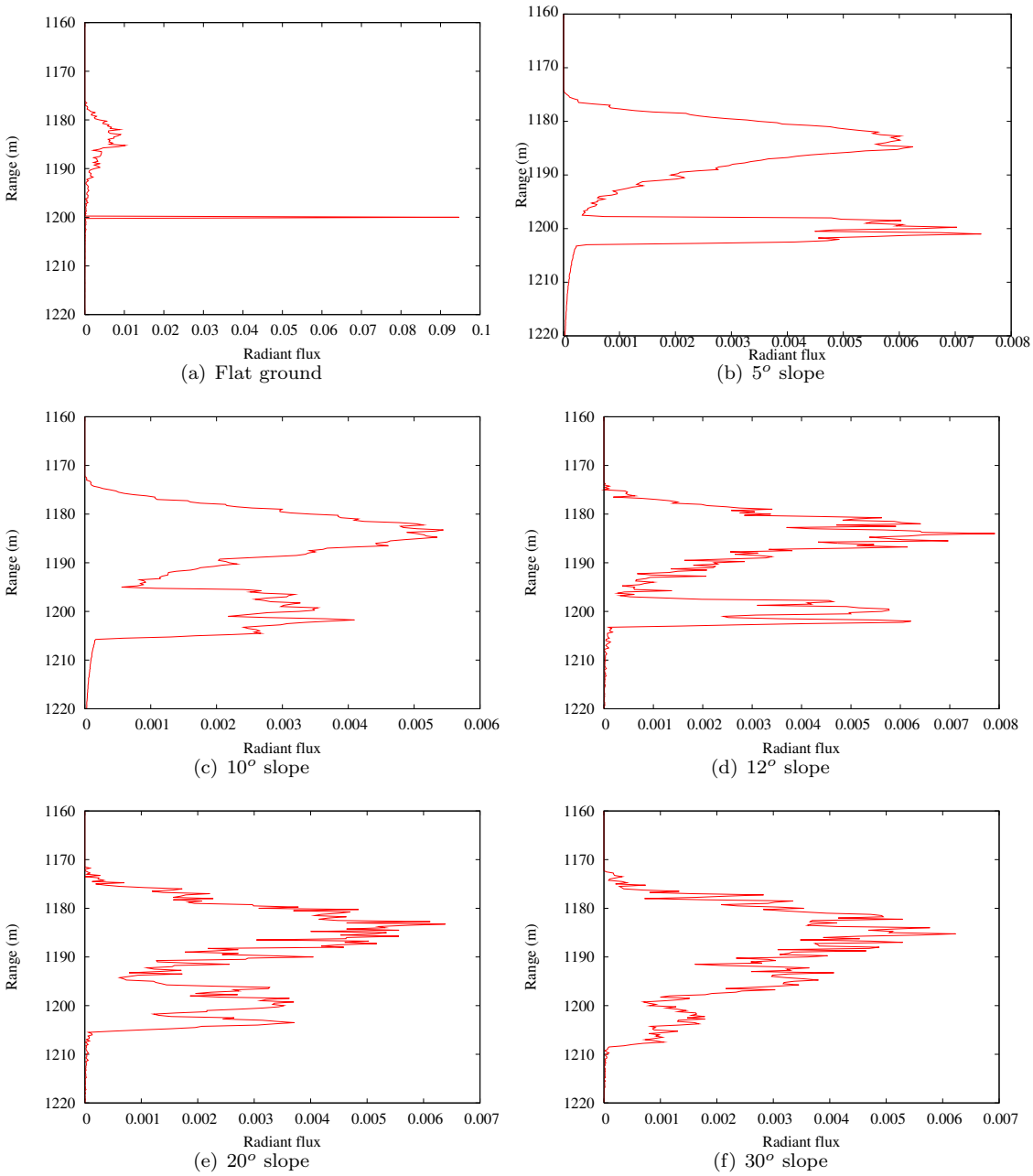

(a) Flat ground (b) 5^o slope (c) 10^o slope (d) 12^o slope (e) 20^o slope (f) 30^o slope

Figure 104: Effect of different surface slopes on 30m footprint waveform over a Sitka spruce forest, 17.5m tall with 83.7% canopy cover. An infinitely short laser pulse was used.

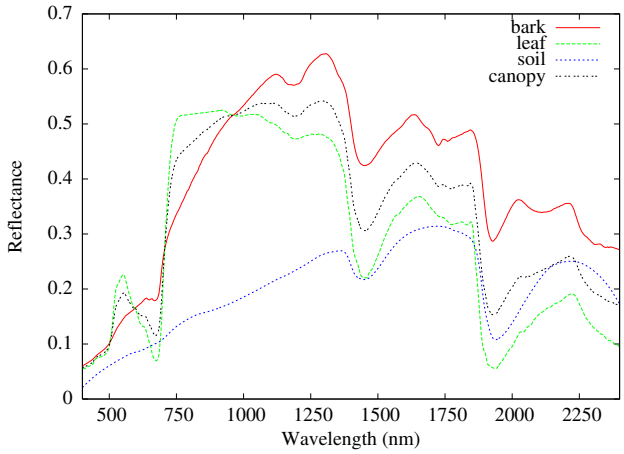

Figure 105: Modelled spectra for leaf, soil, bark and canopy (58% leaf, 42% bark)

Figure 106 shows the ratios of the canopy reflectance (58% leaf) over soil and pure leaf over soil. Two wavebands with vastly different ratios would be preferable. However, regions with low reflectance will give low signal to noise ratios from spaceborne instruments and therefore poor results. These regions (around 650nm) tend to give stronger spectral contrast and have been suggested for airborne platforms (Morsdorf *et al.* 2008b) which, because of their lower altitude, give stronger signal to noise ratios. The mixture of leaf and bark has reduced the spectral contrast between canopy and soil relative to a pure leaf canopy. That is because the bark spectrum has a similar shape to soil, without the pronounced features of a leaf spectrum.

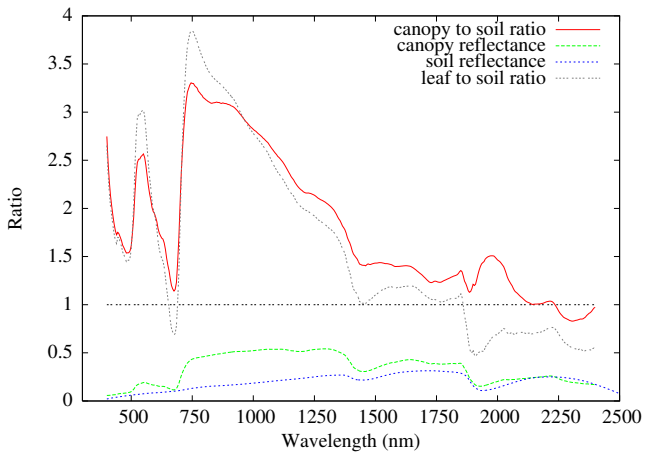

Figure 106: Ratio of canopy to soil reflectance and pure leaf to soil, from modelled spectra

A simple engineering solution would be to use a Nd:YaG laser with a frequency doubler

(Paschotta *et al.* 1994) to produce 1064nm and 532nm beams. The spectral separation is not the best at these wavelengths, however the benefit of needing only a single laser source (though necessarily more powerful than if it produced a single wavelength) in terms of weight and space savings onboard a satellite are considerable.

5.12.1 Multi-spectral information

The spectral nature of the waveform will be directly related to the amount of leaf, bark and ground intersecting the lidar beam (and the angular distribution). The spectral distinction between these elements is too small to allow a standard classification based upon the spectral reflectance of each bin (figure 107(b)), further complicated by the small number of bins containing ground returns. Low intensities on the forest floor and mixture of materials in range bins act to further reduce the separability. However different areas of the waveform should have different spectra so that whilst the spectral separation is small it should be possible to detect a change from one to the other by combining the spectral with the range information.

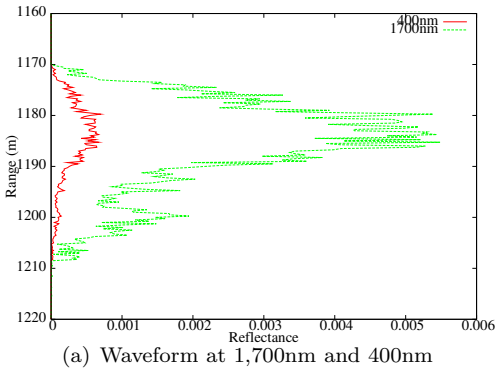

(a) Waveform at 1,700nm and 400nm

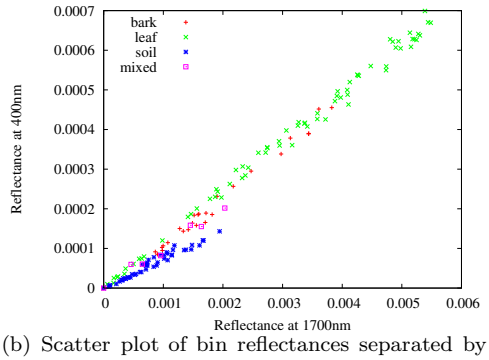

(b) Scatter plot of bin reflectances separated by dominance

Figure 107: Multi-spectral results for a 19.8m tall Sitka spruce forest with 81% canopy cover on a 30^o slope. Dominance was defined as a material that contributes over 50% of the signal, otherwise a bin was classed as mixed.

5.12.2 Information extraction

The traditional method for information extraction from waveform lidar is function fitting (Hofton *et al.* 2000, Wagner *et al.* 2006). The extra information available to a multi-spectral instrument

should allow greater accuracy than the single waveband case. The returns in both wavebands will originate from the same objects, therefore the positions and shapes of the features must be the same at both wavelengths, with only the intensity changing. The number of unknowns will increase by less than the data available for inversion and so a better fit should be achieved.

Separating the canopy from ground with function fitting requires an analytical description of the expected canopy and ground return shapes. Typically they are taken as Gaussian, a shape aided by convolution with the laser pulse. However, forests are heterogeneous and this can cause waveforms to deviate from the ideal case. Figure 108 shows that the clumping of canopy elements into discrete crowns can cause shadows at certain positions on the ground, reducing the ground return intensity in those places. This has taken "bites" out of the ideal Gaussian ground return, so that fitting an analytical function will fail.

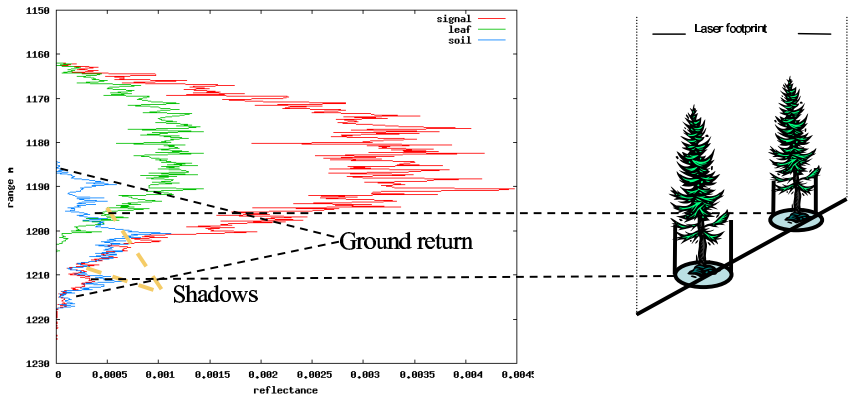

Figure 108: Heterogeneity of a forest causing shadows and the subsequent deviation of features from simple analytical models

Given the unpredictability of the shapes of the canopy and ground returns a method that does not rely on initial estimates of them would be preferable.

5.12.3 Spectral ratio

The easiest measure to calculate is the spectral ratio; the waveform at one wavelength divided by that at another. The spectral ratio is not affected by the absolute intensity and so is robust to heterogeneity, such as that caused by shadowing. Figure 109(b) shows the spectral ratio of 550nm over 850nm (bands with low and high canopy reflectance respectively), clearly showing

the onset of the ground at a range of 1,192.5m. The shape of the spectral ratio is controlled by the proportion of each material visible in a bin, the relative phase functions of each material and multiple scattering.

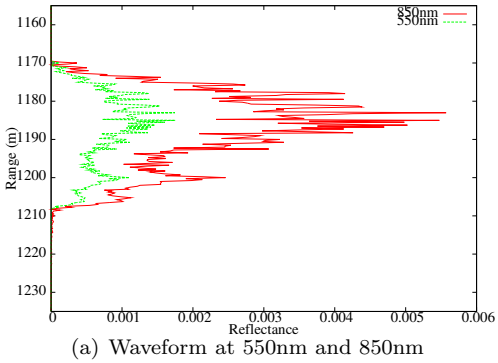

(a) Waveform at 550nm and 850nm

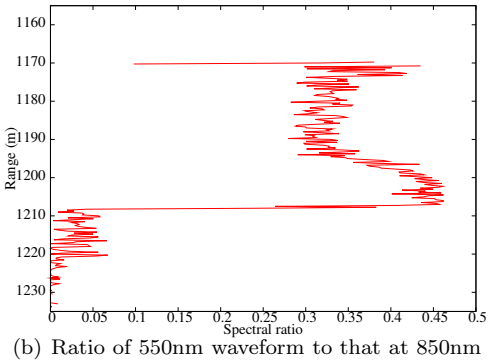

(b) Ratio of 550nm waveform to that at 850nm

Figure 109: Multi-spectral waveform and resulting ratio of reflectance at 550nm to that at 850nm. The canopy was 30m tall with a cover of 75.8% on a 30^o slope.

A typical canopy will be composed of leaves, bark and soil (or leaf litter). The proportions of these will change throughout the canopy, as seen in figure 110(c) and so the overall spectral ratio will be a linear combination of the spectral ratios of the pure materials.

The spectral ratio depends upon the reflectance scaled by the phase function, so if the materials have vastly different phase functions or they are not constant through the canopy, the spectral ratio's shape will be altered. Figure 110(e) suggests that whilst the phase functions do vary through the canopy due to heterogeneity there is no overall trend and so variations could be treated as noise. Also leaves and bark appear to have very similar values.

The magnitude of the multiple scattered signal is especially affected by element reflectance; the light is attenuated by the reflectance to the power of the order of scattering. Therefore, two wavelengths for which the target has different reflectances will have different amounts of multiple scattering, leading to a greater increase in apparent reflectance for the higher reflectance waveband than the lower reflectance. The amount of multiple scattering will change through the canopy as the density of scattering elements changes and because scattering adds a range delay, although small (figure 110(d)). This alters the apparent reflectance at the two wavelengths and so the spectral ratio.

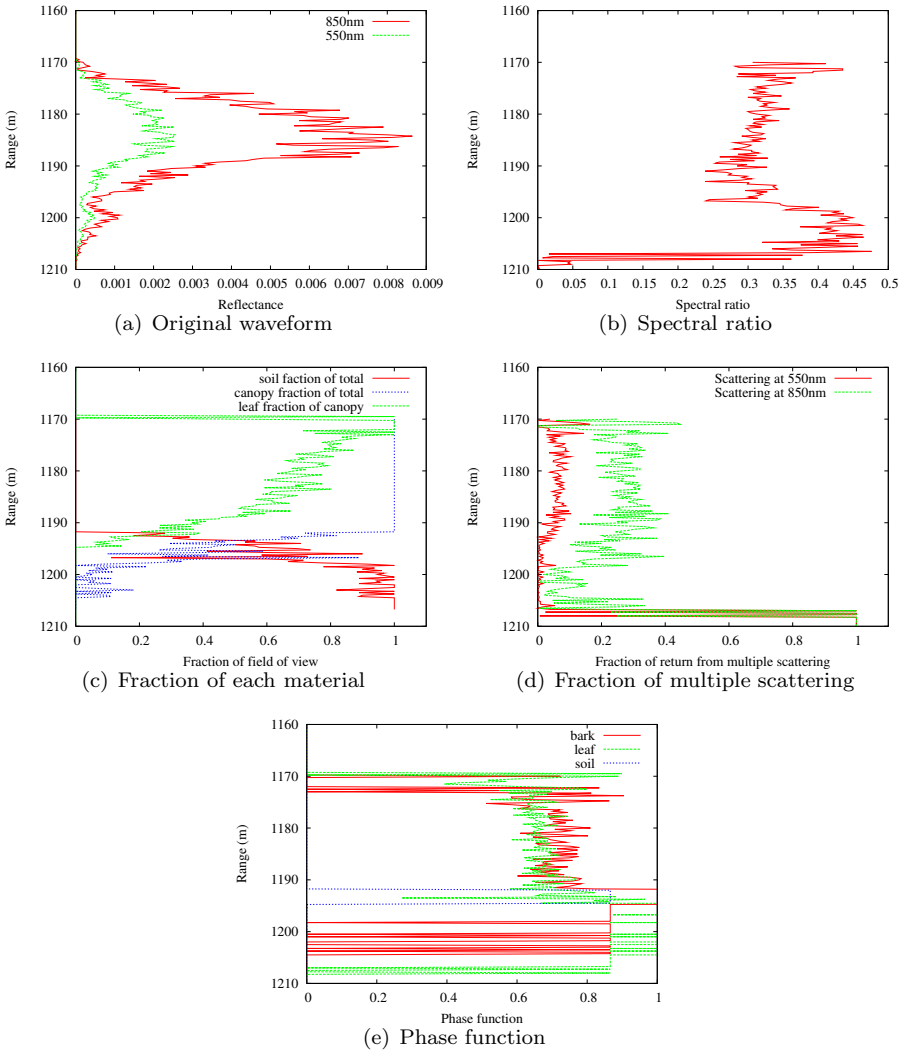

(a) Original waveform

(b) Spectral ratio

(c) Fraction of each material

(d) Fraction of multiple scattering

(e) Phase function

Figure 110: Factors effecting the spectral ratio for a 20m tall, 85% canopy cover Sitka spruce forest on a 30^o slope.

The ratio of the reflectances used at 550nm and 850nm is lower for wood than for leaves, therefore the initial dominance of leaf would cause a higher spectral ratio than the later, woodier canopy. At these wavelengths the ratio for soil is higher than that for both leaf and wood.

The spectral ratio waveform can be separated into five distinct sections, shown in figure 111. The initial peak in spectral ratio with a sharp drop off could be due to the initial dominance of leaf in the canopy or because multiple scattering has not set in. The ratio decreases through the canopy as it gets woodier and multiple scattering increases. It then increases as the ground starts to contribute. The gradient of the increase will depend upon the density of the foliage at the point at which the beam starts to intercept the ground. Once the foliage stops contributing the ratio flattens off to the pure ground value. The length of this section is controlled by the height of the crown above the ground. Finally, the spectral ratio drops down as only multiple scattering echoes are left as the low reflectance waveform almost disappears (if the low reflectance waveform were the denominator this would be almost infinity).

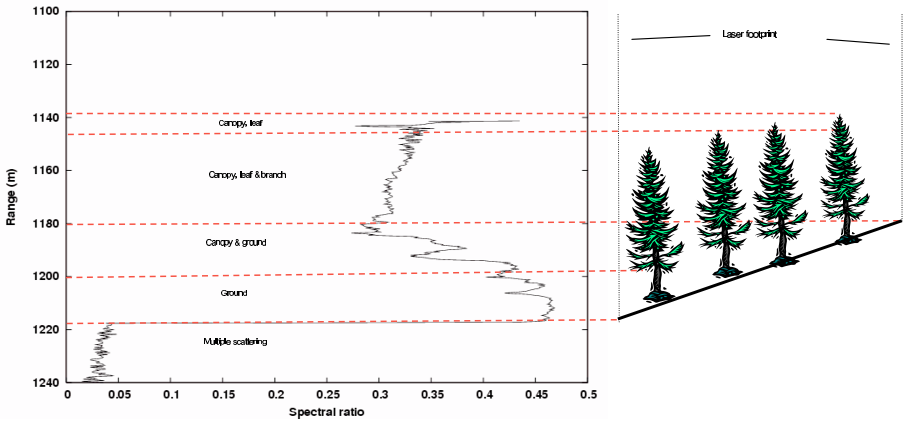

Figure 111: Multi-spectral waveform features.

To investigate the relative significance of changing amounts of multiple scattering and proportions of leaf to wood the spectral ratio was calculated with and without multiple scattering. Figure 112 shows that even without multiple scattering the spectral ratio decreased through the canopy. This can only be due to changing fractions of leaf and wood. Including multiple scattering caused a further reduction in spectral ratio with range. The initial sharp spike was not as apparent in the waveform without multiple scattering. This feature must be because multiple scattering

adds a range delay (in this case about four range bins), so the initial returns contain less multiple scattered light, giving them a lower apparent reflectance in the stronger waveband than the lower. Therefore the initial peak is due to both multiple scattering and increased leafiness. Perhaps the length of this feature, which is related to the range delay and so mean free path, can be used to look at scattering element density. The proof of this is beyond the scope of the thesis.

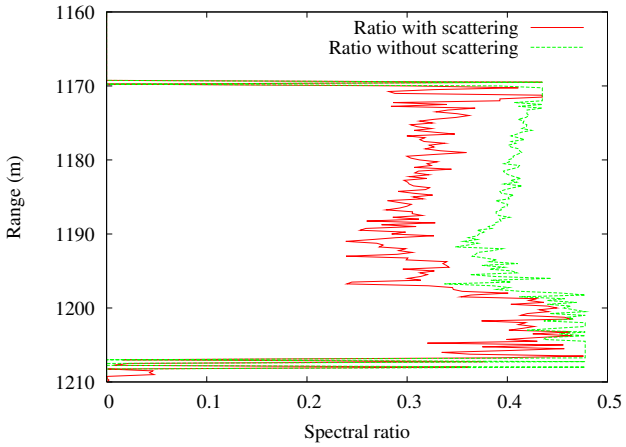

Figure 112: Ratio of waveform at 550nm and 850nm with and without multiple scattering.

Figure 113 shows that birch shows the same trends as Sitka spruce, albeit with more leaves lower in the canopy and less multiple scattering (for Sitka spruce it is probably mainly within shoot scattering due to the higher density of scattering elements). Interestingly, although the ground in figure 113(c) is centred at a range of 1,200m, spreading up and down 7.5m, there are canopy returns deep into the soil returns (predominantly bark). This is due to the small separation between the ground and bottom of canopy. Comparing figures 113(e) and 110(e) shows that the two species have very different phase functions for leaves. The needle leaf Sitka spruce shows an average value of 0.65 whilst the broad leaved birch has a value of 0.85. This is not unexpected given the difference in the arrangement of needle and broad leaves. This will give birch a higher apparent single scattering leaf reflectance than Sitka spruce. The increased multiple scattering within a needle shoot may even this out.

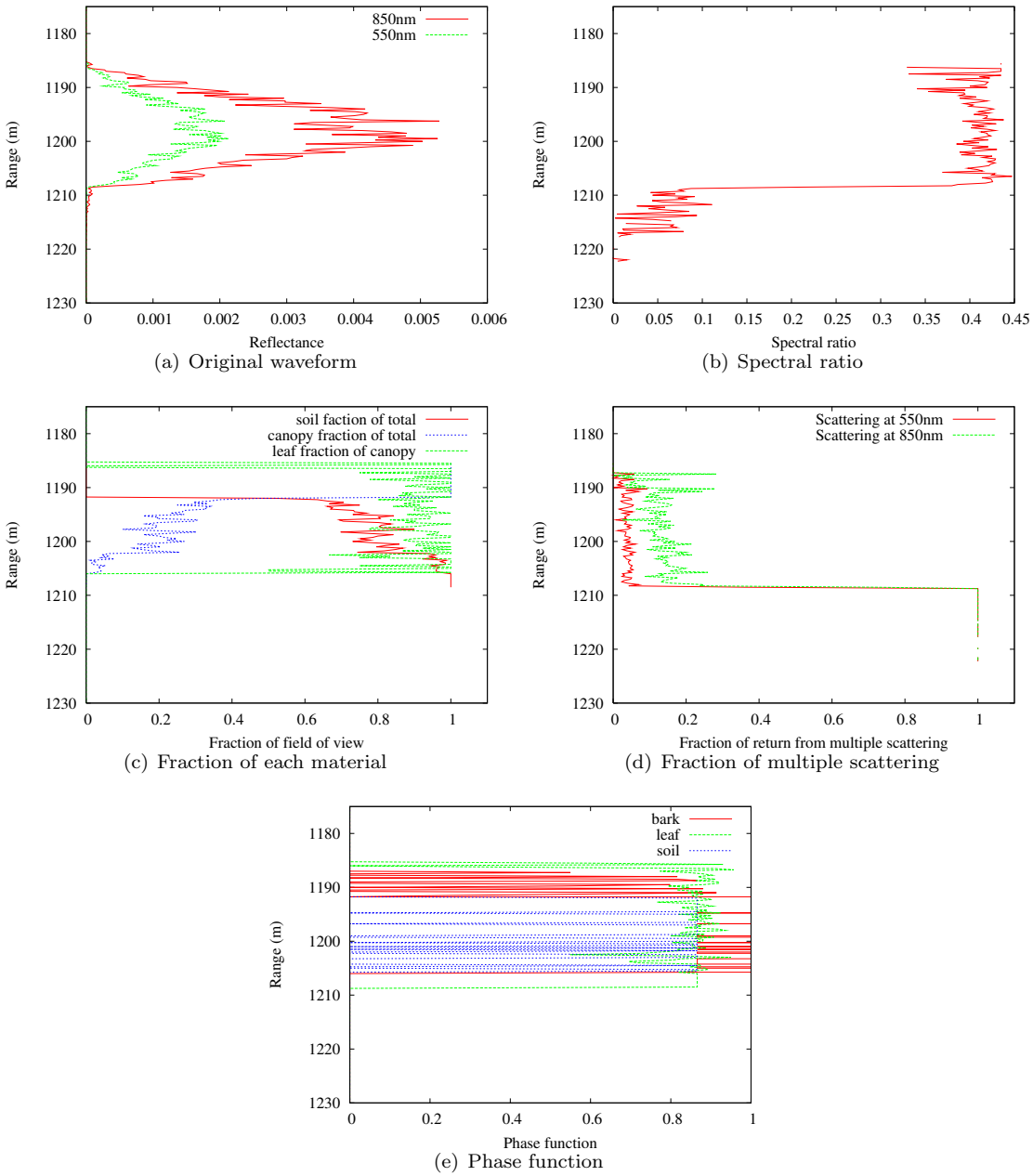

(a) Original waveform

(b) Spectral ratio

(c) Fraction of each material

(d) Fraction of multiple scattering

(e) Phase function

Figure 113: Factors affecting the spectral ratio for birch, 21% canopy cover on a 30^o slope.

5.12.4 Optimum wavelength for spectral ratios

The optimum wavelength combination depends upon the method of information extraction. Different combinations of bands may accentuate features of interest whilst not necessarily having the greatest spectral contrast. Figure 114 shows the spectral ratio for the same forest with a range of wavelength combinations.

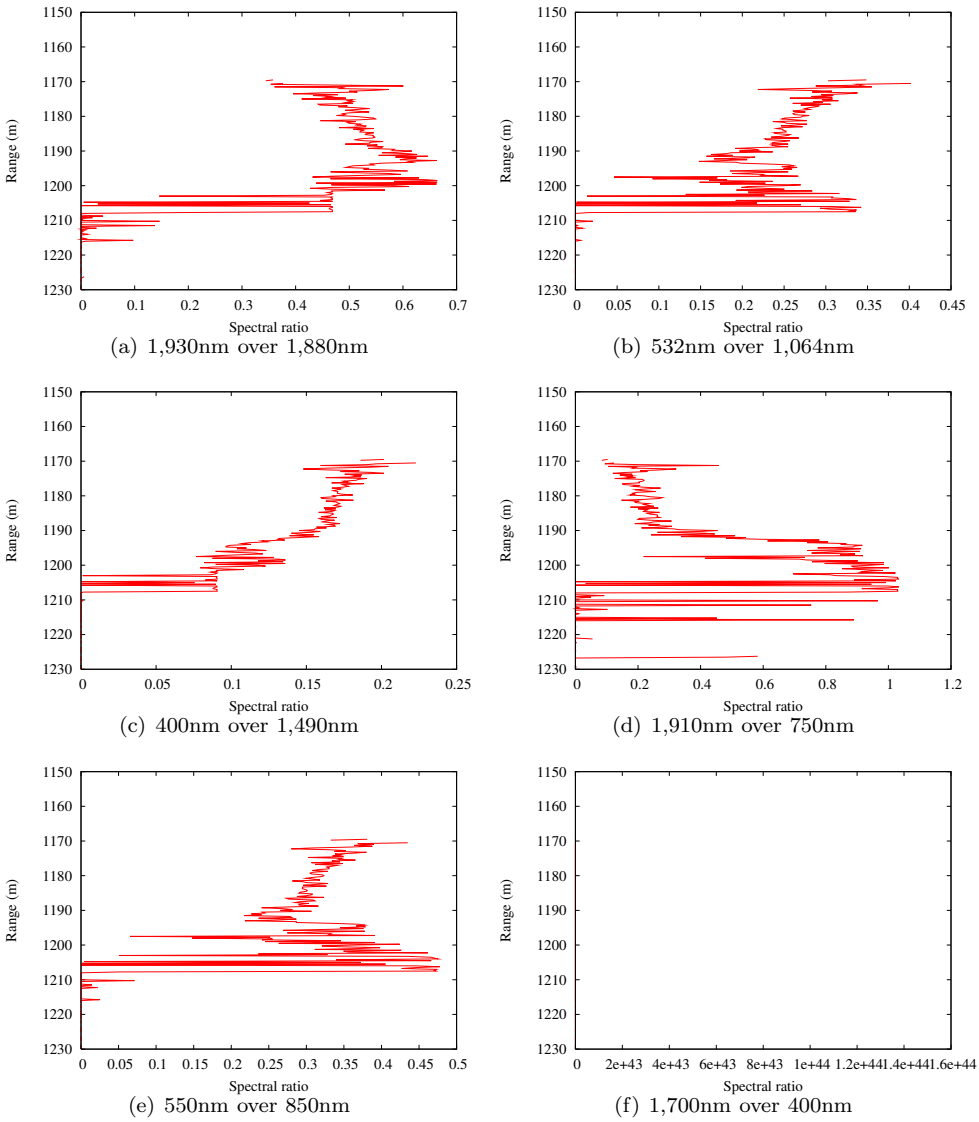

(a) 1,930nm over 1,880nm (b) 532nm over 1,064nm

(c) 400nm over 1,490nm (d) 1,910nm over 750nm

(e) 550nm over 850nm (f) 1,700nm over 400nm

Figure 114: Spectral ratios for different band combinations without noise for an 18m tall Sitka spruce forest with 95% canopy cover

The choice of wavelengths will be critical for multi-spectral lidar. To determine the best pair the contrast between each material was calculated for every wavelength combination using equation 38.

$$Contrast = \left| \frac{\rho_{\lambda,canopy}}{\rho_{\omega,canopy}} - \frac{\rho_{\lambda,soil}}{\rho_{\omega,soil}} \right| \tag{38}$$

Where $\rho_{\lambda,i}$ is the reflectance of material i (which can be canopy, soil, leaf or wood) at wavelength λ.

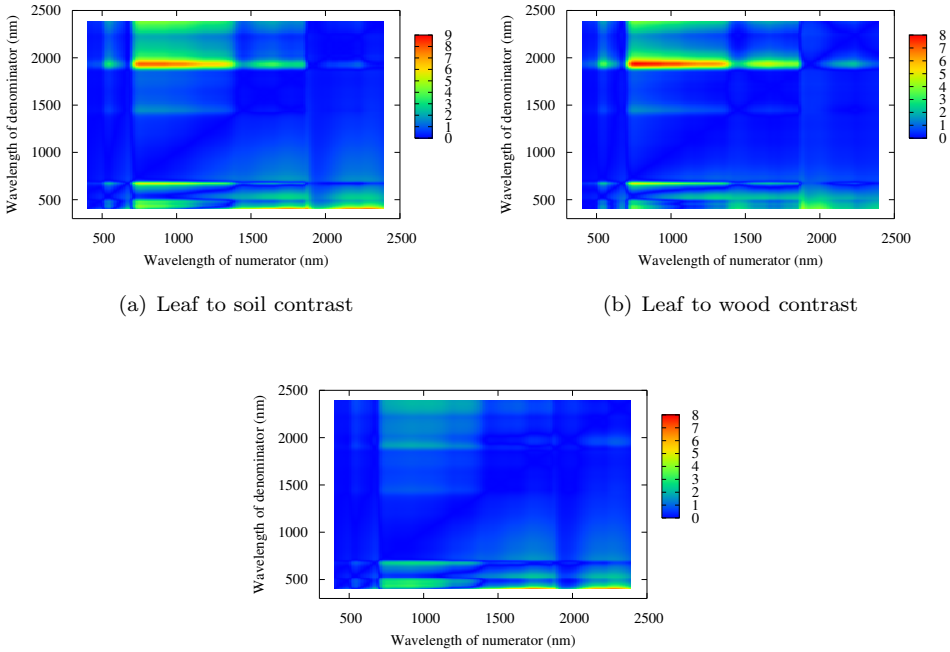

(a) Leaf to soil contrast

(b) Leaf to wood contrast

(c) Canopy, composed of a mixture of leaf and wood, to soil contrast

Figure 115: Spectral contrast between pure materials.

The contrasts for all wavelength combinations for which reflectance data were available are shown in figure 115. Here canopy is taken as 58% leaf, 42% bark (the average value for the mature Sitka spruce forest models). From these plots it can be seen that the best combination of wavelengths would be to use waveforms from lasers at 1,720nm over 400nm to give a contrast of 7.49. It would be unwise to use a 400nm laser in a remote sensing device, particularly from space because of poor atmospheric transmittance, low surface reflectance and high photon energy. The greatest spectral contrast outside of the visible (over 750nm) is achieved with a wavelength of 930nm as the denominator and 2,380nm as the numerator, giving a spectral contrast of 2.04.

For the spectral ratio, a small number on the denominator (a low reflectance value), will cause

large spikes in the spectral ratio waveform, as shown in figure 114(f); potentially reaching infinity, obscuring the features of interest. Noise only exacerbates the problem. Therefore it would be more robust to have the stronger signal as the denominator. This excludes many of the band combinations that showed strong spectral contrast but will cope better with noise.

$$\rho_{\omega,canopy} > \rho_{\lambda,canopy}, \rho_{\omega,soil} > \rho_{\lambda,soil} \tag{39}$$

Figures 110(c) and 110(d) show that both multiple scattering and the proportion of wood in the canopy increased with range (the same trends were observed for all forest models used in this investigation). To get a clearer transition from canopy to soil it would be better to have a combination of wavebands that gives the same trend in spectral ratio with range from increasing wood and multiple scattering. As the stronger signal must be the denominator (to avoid large spikes), the canopy signal will be decreasing with range due to increasing multiple scattering. Therefore a greater contrast will be seen if the spectral ratio is larger for pure leaf than for pure bark, and that the ratio for canopy is lower than for soil. These conditions are given by equations 40 and 41.

$$\frac{\rho_{\lambda,leaf}}{\rho_{\omega,leaf}} > \frac{\rho_{\lambda,bark}}{\rho_{\omega,bark}} \tag{40}$$

$$\frac{\rho_{\lambda,canopy}}{\rho_{\omega,canopy}} < \frac{\rho_{\lambda,soil}}{\rho_{\omega,soil}} \tag{41}$$

The optimum wavelength will depend on the fraction of leaf and bark in the canopy. Any device must be robust to different canopy compositions and species.

The contrast was recalculated enforcing the conditions given in equations 39, 40 and 41 for all possible canopy mixtures using equation 38. Figure 116 shows the greatly reduced contrast produced by forcing the denominator to be larger than the numerator, but the allowed combinations should be much more robust. Here the best result was achieved by dividing the waveform at 2,300nm by that at 1,870nm, giving a mean contrast of 0.28. The spectral contrast for every canopy composition for 2,300nm over 1,870nm and the simple engineering solution of 532nm over 1,064nm are shown in figure 117.

It can be seen that for 2,300nm over 1,870nm the spectral contrast is strong for all possible

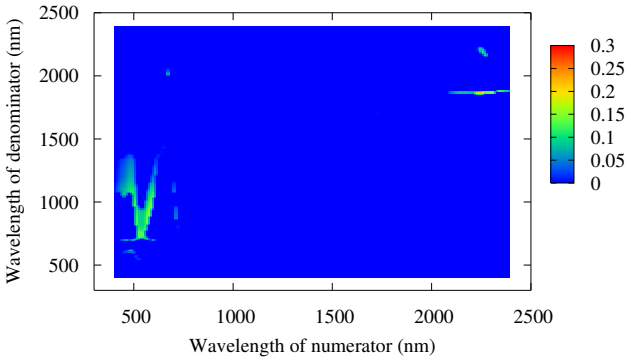

Figure 116: Mean spectral contrast between canopy and soil for all canopy compositions, limited to combinations with higher reflectance on the denominator than the numerator and a greater ratio for soil than canopy.

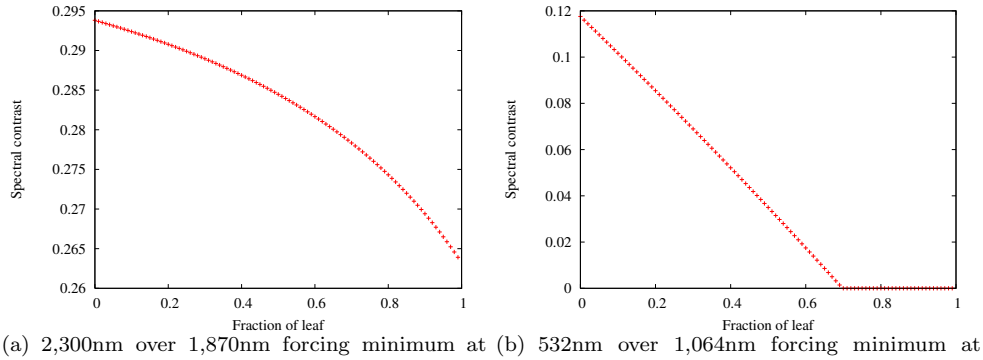

(a) 2,300nm over 1,870nm forcing minimum at transition

(b) 532nm over 1,064nm forcing minimum at transition

Figure 117: Spectral contrast between canopy and soil for all proportions of leaf and bark and a range of wavelengths

Material	Reflectance at 2,300nm	Reflectance at 1,870nm
leaf	0.13	0.22
bark	0.28	0.46
soil	0.23	0.26

Table 2: Reflectance values for the optimum above canopy multi-spectral wavelengths

canopy compositions and that 532nm over 1,064nm is usable until leaves make up more than 50% of the canopy, at which point the spectral contrast for canopy and ground become the same. Therefore, whilst a system using lasers at 2,300nm and 1,870nm may not have the best spectral contrast for every forest, it will have an identifiable point (a minimum) at the transition between ground and canopy for all possible canopies.

Table 2 shows that, for the spectra used, the reflectance at the optimum wavelengths does not drop below 13%, ensuring a reasonably strong signal to noise ratio. Whether there are suitable laser sources at these wavelengths is a question for an engineer. Alternative wavelength combinations can be investigated if suitable laser sources are not available at 2,300nm and 1,870nm. The spectra used here are realistic but not representative of all possible situations. A more comprehensive study using a broad range of data would be needed before the optimum wavelength combination for a global system can be chosen.

5.12.5 Multi-spectral information extraction

Figure 118 shows the spectral ratio of 2,300nm over 1,870nm for a range of forest covers and heights. For all waveforms the ground was centred at range of 1,200m, spreading up and down by 7.5m for a 30m footprint (from 1,192.5m to 1,207.5m). Noise, which is independent for the two wavelengths, can cause large spikes in spectral ratio (sometimes moving the ratio above unity). Convolving the original waveforms with a Gaussian before dividing removes the spikes, revealing the underlying shape (see appendix B).

For shorter canopies (figures 118(a) and 118(d)) there was a very small separation between the canopy and the ground immediately below so the spectral ratio does not settle down to a pure

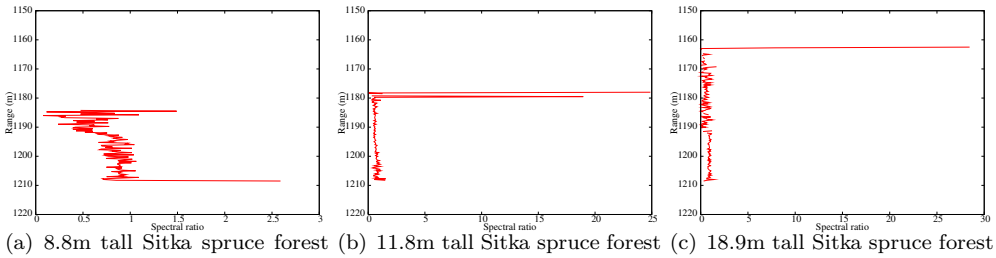

(a) 8.8m tall Sitka spruce forest with 21% canopy cover

(b) 11.8m tall Sitka spruce forest with 87% canopy cover

(c) 18.9m tall Sitka spruce forest with 12% canopy cover

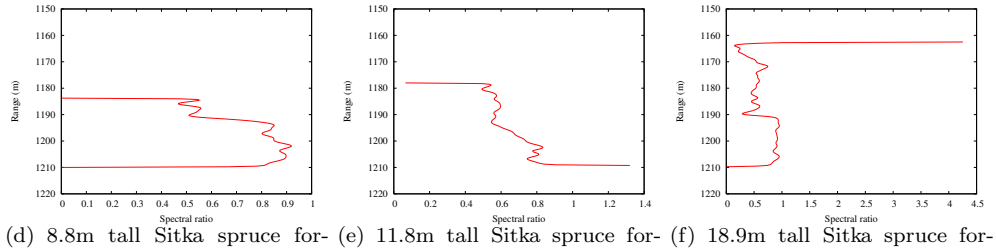

(d) 8.8m tall Sitka spruce forest with 21% canopy cover, smoothed

(e) 11.8m tall Sitka spruce forest with 87% canopy cover, smoothed

(f) 18.9m tall Sitka spruce forest with 12% canopy cover, smoothed

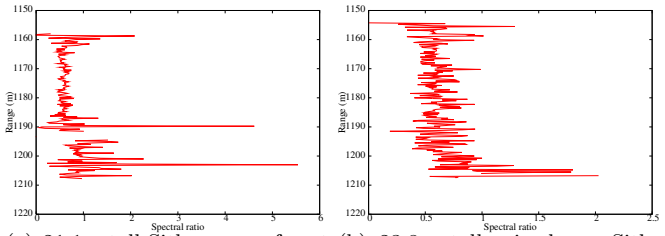

(g) 21.1m tall Sitka spruce forest with 91% canopy cover

(h) 23.8m tall mixed age Sitka spruce forest with 90% canopy cover

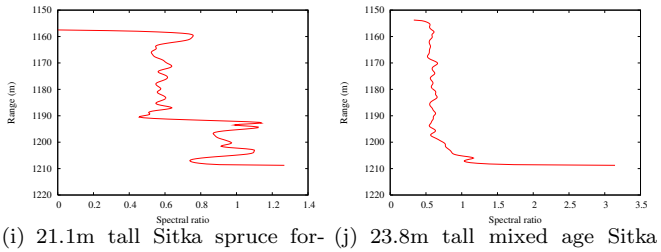

(i) 21.1m tall Sitka spruce forest with 91% canopy cover, smoothed

(j) 23.8m tall mixed age Sitka spruce forest with 90% canopy cover, smoothed

Figure 118: Examples of spectral ratios of 2,300nm over 1,870nm for a range of forests on 30^o slopes for 10,000 signal photons. Smoothing was by convolution with a 3m Gaussian.

ground signal, there being canopy in every range bin. However, there was still a minimum of the spectral ratio around a range of 1,192.5m for all waveforms which will allow separation of it from the canopy.

Examples of 532nm over 1,064nm are shown in figure 119. Older (taller) Sitka spruce forests have a high proportion of wood and there was a clear minimum at the transition (figures 119(c) and 119(g)). Younger (shorter) trees are leafier than mature trees so that there was no minimum of the spectral ratio at the canopy to ground transition. Understory will also increase the leafiness at the interface (here young trees are equivalent to shrub-like understory). 2,300nm over 1,870nm showed a feature at the start of the ground for all canopies, even short dense stands (figure 118(e)). For mixed age forests the minimum was quite subtle and detection may prove problematic (figure 118(h)).

Therefore 532nm over 1,064nm does not seem like a sensible choice of wavelengths. Only 2,300nm over 1,870nm will be used for the rest of the investigation.

5.12.6 Feature detection

A robust method to identify the extent of the ground return is needed to separate it from the canopy. This is the first step towards measuring any biophysical parameters of forests.

Due to the similarity in spectral ratio for pure leaf and pure wood at 2,300nm over 1,870nm (for the datasets used both were 0.61 to two significant figures), there will not necessarily be a minimum at the transition between the ground and canopy. Therefore other features at that point must be relied upon. At the transition the spectral ratio will rapidly increase, levelling off as the signal becomes pure ground. The second derivative should reach a maximum as the ratio changes from pure canopy to a mixture of canopy and ground; this can correspond either to a minimum in the spectral ratio or a sudden increase. There will be a maximum of the first differential somewhere in this transition. The levelling off from a mixture of canopy and ground (with increasing proportion of ground) to the pure ground value will correspond to a minimum of the second derivative. The drop off from the ground return to pure multiple scattering will have a minimum in the second derivative. Therefore a sensible approach would be to look for crossing points of the third derivative.

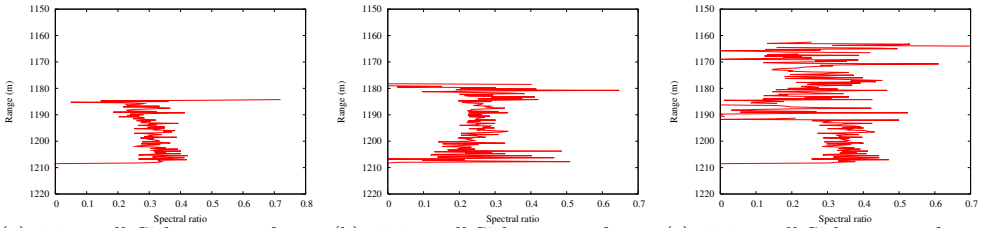

(a) 8.8m tall Sitka spruce forest with 21% canopy cover

(b) 11.8m tall Sitka spruce forest with 87% canopy cover

(c) 18.9m tall Sitka spruce forest with 12% canopy cover

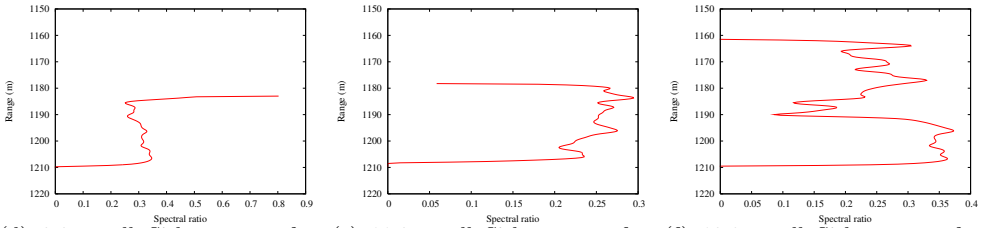

(d) 8.8m tall Sitka spruce forest with 21% canopy cover, smoothed

(e) 11.8m tall Sitka spruce forest with 87% canopy cover, smoothed

(f) 18.9m tall Sitka spruce forest with 12% canopy cover, smoothed

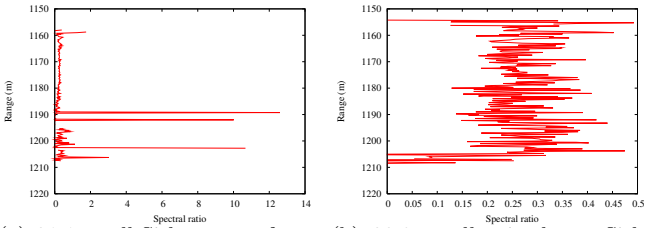

(g) 21.1m tall Sitka spruce forest with 91% canopy cover

(h) 23.8m tall mixed age Sitka spruce forest with 90% canopy cover

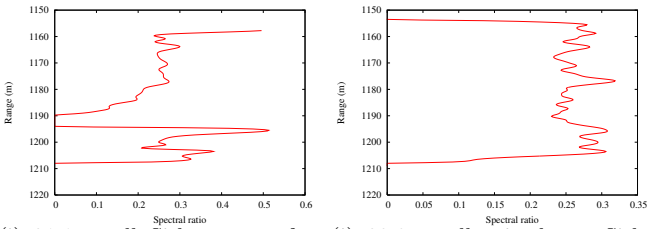

(i) 21.1m tall Sitka spruce forest with 91% canopy cover, smoothed

(j) 23.8m tall mixed age Sitka spruce forest with 90% canopy cover, smoothed

Figure 119: Examples of spectral ratios of 532nm over 1,064nm for a range of forests on 30^o slopes for 10,000 signal photons

Noise and heterogeneity will cause spikes, particularly in the higher order derivatives. Any method will have to robustly see the features of interest through such noise and so smoothing is required. Smoothing each waveform before calculating the ratio will lead to a better behaved result than smoothing the ratio of the noised waveforms; the proof for this is given is appendix B.

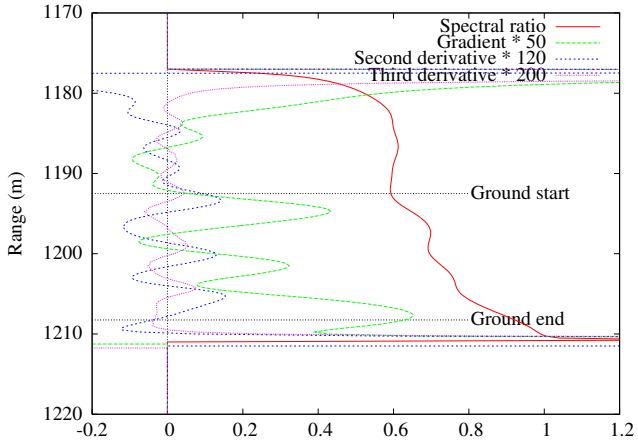

Figure 120: The spectral ratio and derivative waveforms for a Sitka spruce forest

5.12.7 Sufficient smoothing

Noise and heterogeneity can confuse feature detection. Figure 121 shows that, for this particular waveform, smoothing with anything narrower than a 9m Gaussian would leave multiple minima. It would not be easy to reliably decide which of these corresponds to the ground. A robust algorithm should aim to smooth out all features except the one of interest; leaving no doubt as to which is the ground. The narrowest possible smoothing required to achieve this should be applied to minimise the spreading out of the signal and loss of resolution.

The ground will be identified by a sudden increase in the spectral ratio, so a maximum of its second derivative. The smoothing function can be selected by iteratively changing the width until the finest function that leaves a single maximum of the second derivative is found.

Smoothing the signal with a Gaussian will leave long tails in areas of previously empty signal. This will extend the spectral ratio, particularly upwards where the value will be similar to the pure canopy value, complicating feature detection (greater multiple scattering of the denominator wavelength reduces this affect below the canopy). The same cumulative energy threshold used

to find the tree tops (described in section 5.1.1) can be used to find the bounds of the signal of interest, preventing this. The spreading out by smoothing should prevent too much signal being truncated and as the canopy to ground transition is the chief interest, somewhere in the midst of the waveform, this should not be an issue. Here the background is from the tails of the Gaussian rather than random noise, so tracking back to the mean level will not remove the bias. Noise tracking can still be used to find an unbiased estimate of signal start before ratios are taken.

At the beginning and end of the signal there are rapid changes in spectral ratio from no signal to canopy and from ground to multiple scattering values. These "wings" will have large derivatives and should be avoided when searching for features. Only the signal between the first minimum of the second differential (leading wing) and the last minimum (trailing wing) within the useful signal bounds should be examined.

5.12.8 Weighting the smoothing function

A side affect of removing noise by smoothing is the spreading out of features, shown in figure 121. It can be seen that if the signal is smoothed sufficiently to remove all minima except that at the ground to canopy transition, then the smoothing causes the foot of the slope to shift upwards whilst the end of the waveform is shifted downwards, increasing the apparent slope of the ground. Constrained smoothing, as described by DaSheng (1993), varies the smoothing function through the signal. A narrower function can be used on areas of interest, preserving their position and leading to more accurate estimates of ground position than with uniform smoothing. A smoothing function weighted by the gradient of the spectral ratio should preserve the position of edges whilst removing noise from flatter areas.

If the weighting were based on the gradient of the spectral ratio of the measured waveforms noise would cause large spikes, potentially leading to large errors. Therefore the gradient of the spectral ratio of smoothed waveforms should be used. The weighting function will be somewhat blurred by this process, but it should act to spread out the areas of high weighting (reducing all the gradient values so that the relative values are higher) so that areas of interest will not be overly smoothed. A function is then needed to relate the weighting to the smoothing to be applied.

As the gradient of the spectral ratio is likely to include large spikes at the start and end which

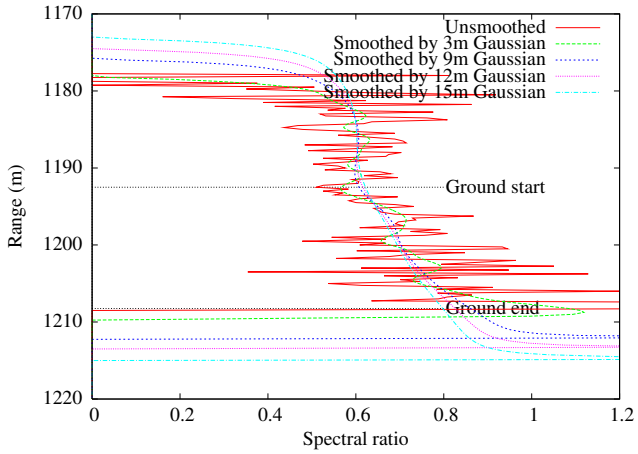

Figure 121: Illustration of the spreading of the spectral ratio features through smoothing

might skew the weighting values (illustrated in figure 122), a function with an asymptote would be preferable to avoid over smoothing areas of interest. A density weighted function would be another alternative, but there may be problems with how well it copes with different distributions of gradients.

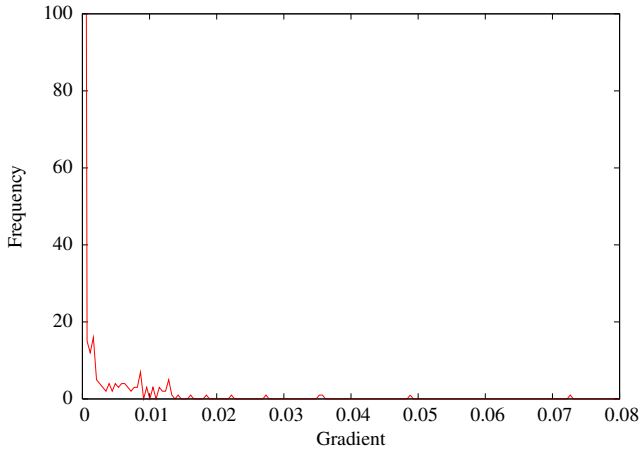

Figure 122: Histogram for gradients of the spectral ratio of a waveform, the axes have been truncated from 1.6 and 350 for clarity

For this reason a function of the form given in equation 42 was chosen to relate the smoothing function's weighting, *weight*, to the gradient of the ratio, *grad*. Here the magnitude of the gradients, irrespective of sign, are used; as steep negative gradients may be of interest.

$$weight = \frac{1}{k(|grad| - a)} + c \tag{42}$$

The constants a, k and c were set by fitting the function through two points. One, the minimum smoothing at the maximum observed gradient ($weight = smooth_{min}, |grad| = |grad_{max}|$), the other the maximum smoothing at the minimum observed gradient ($weight = smooth_{max}, |grad| = |grad_{min}|$). Then, to ensure that the function reaches a noticeable asymptote and provide a third equation, the gradient of the weighting at $|grad_{max}|$ function was forced to flatten off to (an arbitrary) one hundredth of its value at $|grad_{min}|$. The relationship between these constants and the maximum gradient, $|grad_{max}|$, minimum gradient, $|grad_{min}|$, minimum smoothing, $smooth_{min}$ and maximum smoothing, $smooth_{max}$ are given in equations 43, 44 and 45, derived by putting the initial conditions into equation 42.

$$a = \frac{\sqrt{100}\,|grad_{min}| - |grad_{max}|}{\sqrt{100} - 1} \tag{43}$$

$$c = \frac{smooth_{min}(|grad_{max}| - a) - smooth_{max}(|grad_{min}| - a)}{|grad_{max}| - |grad_{min}|} \tag{44}$$

$$k = \frac{1}{(|grad_{max}| - a)(smooth_{min} - c)} \tag{45}$$

Using $\sqrt{100} = -10$ would give the correct value to the left of the vertical asymptote, therefore $\sqrt{100} = +10$ will be used to give the right hand side of the vertical asymptote. Figure 123 shows the weighting function.

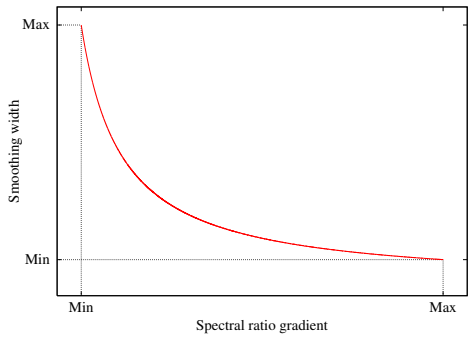

Figure 123: Smoothing weight function

As a first attempt the minimum smoothing was set as 2m and the maximum as the width of the smoothing function found in the iterative method described in section 5.12.7. These are somewhat arbitrary values and should be refined in future studies, without making the function site or species specific.

5.12.9 Multi-spectral inversion algorithm

The steps described above have been combined into an iterative algorithm for determining the ground position and extent from multi-spectral lidar. First a starting point which is known to be on the transition from canopy to ground was calculated using the sufficient smoothing described in section 5.12.7. Half the the smoothing function's width was added to the found position to make sure the point has not been spread beyond the ground signal.

A smoothing weight function was determined using the method and equations described in section 5.12.8. This was applied to the original waveforms and a new ratio and derivatives calculated. The bounds of interesting signal (using the cumulative energy) and the wings (using the minima of the second differential) were determined. The first maximum of the second derivative before the initial ground position estimate was taken as the start of the ground return. The last minimum of the second derivative (the trailing wing) was taken as the end of the ground return. This method is shown schematically in figure 124.

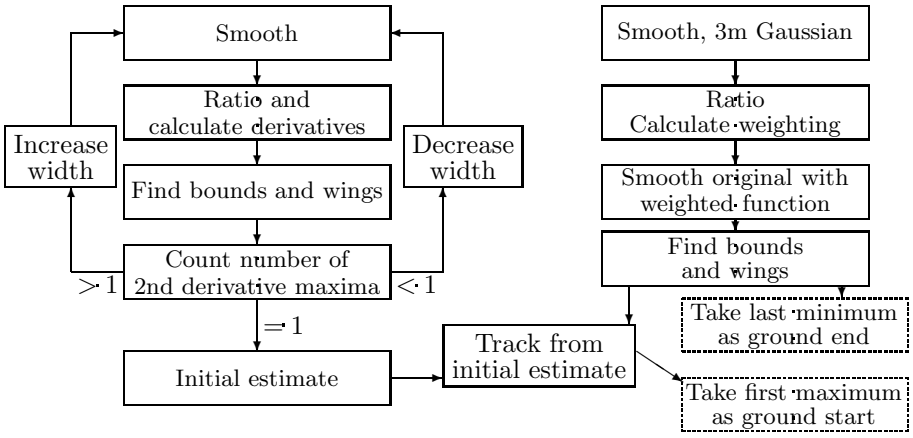

Figure 124: Schematic of the multi-spectral ground finding method

5.12.10 Multi-spectral results

The scatter plot of ground position error against canopy cover (figure 125) shows that the method performed reasonably well. The error is the estimated range to ground minus the true range; so a positive value is an overestimate, a negative an underestimate. The end of the ground return was found almost perfectly until high canopy covers ($> 95\%$). This is the simpler position to find as there is a clear drop off in spectral ratio from the pure ground to the multiple scattering value. At higher canopy covers the ground return is weak and may become lost in noise and multiple scattering, being truncated by the noise and Gaussian tail removal processes.

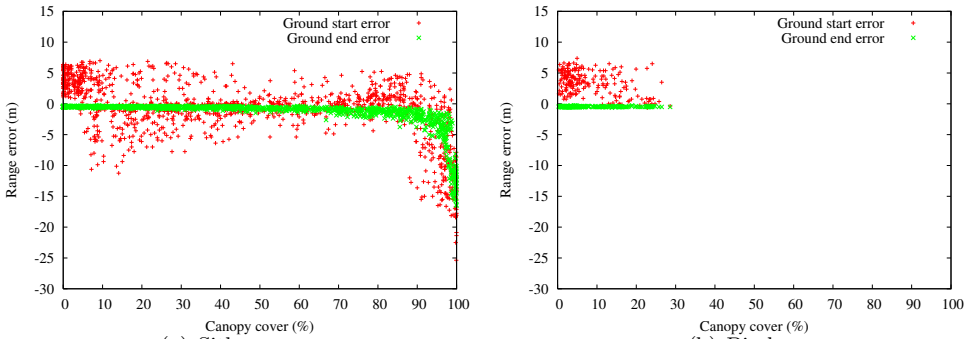

(a) Sitka spruce (b) Birch

Figure 125: Ground position error against canopy cover using the spectral ratio with 10,000 signal photons and no pulse duration for forests on a 30^o slope

The start of the ground proved harder to find, though the errors for all but extreme canopy covers ($< 8\%$ or $> 95\%$) were less than 7m. Figure 126 shows this error broken down by tree height. This reveals that shorter trees ($< 10m$) had larger errors. This is not surprising since these have smaller separation between the canopy and ground and so most of the ground returns include some leaf. This gives the spectral ratio a more gradual slope at first, so the algorithm is likely to overestimate the range to the ground. A similar effect occurred at trees between 10m and 20m tall at higher canopy covers ($> 80\%$), giving rise to greater errors.

At lower canopy covers ($< 30\%$), taller trees ($> 20m$) showed larger errors than moderately tall forests ($10m < height < 20m$). This is due to gaps between the ground and canopy (as shown in figure 118(c)) confusing the algorithm. Instead of the ground, the algorithm finds a point within the canopy. This could be avoided by more careful filtering; such filtering will be a necessity for

the method to work over both flat ground and topography.

The method performed equally well for mixed aged forests as for uniform, suggesting that the method is robust to understory. The method completely failed for forests with greater than 99.8% canopy cover due to the weakness of the ground return. There seems little chance of reliably extracting information from such high covers in the presence of background noise and multiple scattering by whichever method.

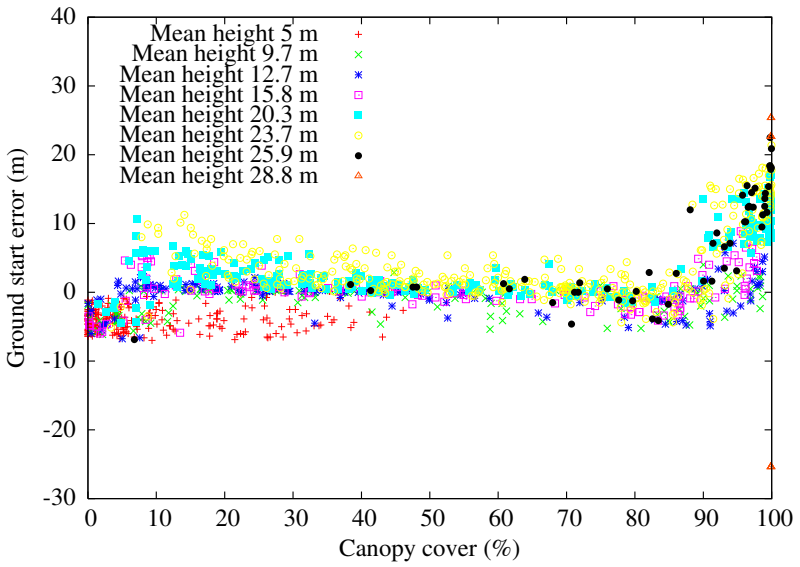

Figure 126: Ground start error against canopy cover broken down by tree height with 10,000 signal photons and no pulse duration for forests on a 30^o slope

The method was developed using the Sitka spruce forests, the birch forests were then used as an independent test. Figure 125 shows that the method performs equally well for both species (though only a small range of birch forest models were available) and is therefore likely to be robust.

5.12.11 Discussion of multi-spectral errors

To determine whether the weighted smoothing is worth the extra computational expense the ground positions were calculated again using the same method as shown in figure 124 but using the smoothing function that left a single maximum in the second differential before determining the ground position rather than the weighted function. The results in figure 127 show that using a

constant smoothing function lead to a consistent underestimate of range to the canopy; due to the upwards shift of the features. Weighted smoothing gave less biased estimates of ground position but interestingly showed larger errors for short ($< 10m$), sparse ($< 20\%$ cover) canopies.

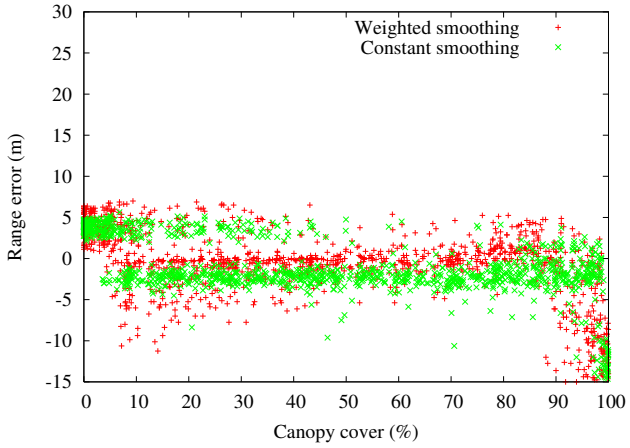

Figure 127: Ground start error against canopy cover using constant and weighted smoothing

Figure 128 shows the waveforms and resulting spectral ratios for one of these short, sparse canopies for which the method failed. There is very little separation between the bottom of the crowns and the ground directly beneath it, meaning there is only a very short region of pure canopy whilst there is some canopy in every ground bin, leaving no pure ground. This region of pure canopy is visible in the ideal, unnoised case but not in either of the two noised cases (figure 128(b)). Due to the low cover the canopy has little influence on the shape of the spectral ratio in the region of mixed canopy and ground, leaving no features to identify. For this forest the constant smoothing method estimated that the ground started at a range of 1,200.75m and the weighted smoothing a range of 1,204m. Both of these are overestimates of the true range (1,192m) and as the pure canopy region has been lost in the background noise the constant smoothing method's lower error is more due to luck than any other reason. To accurately invert such short, dense canopies a better method for determining the bounds of the waveform before calculating the ratio is needed; perhaps in this case the noise tracking method describes in section 5.1.1 would improve the results.

Therefore the extra computational expense (which is not prohibitive on a modern computer) is worthwhile; certainly there is no disadvantage to it.

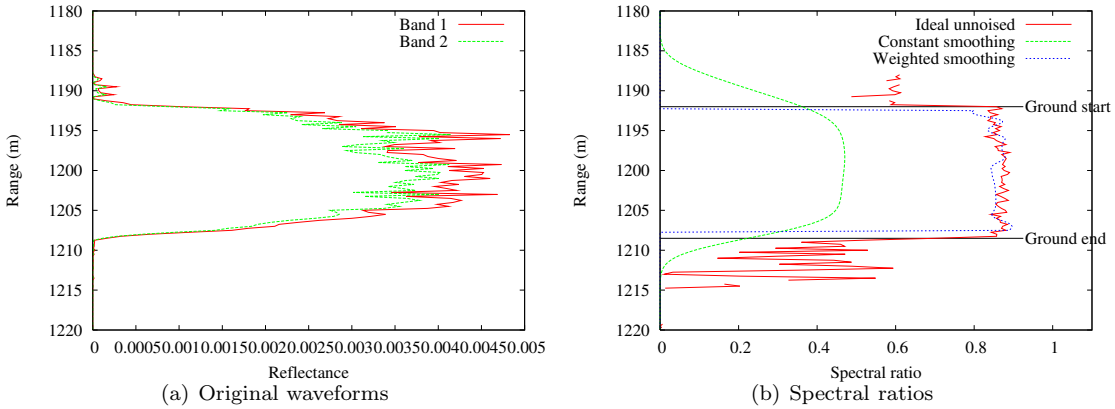

(a) Original waveforms (b) Spectral ratios

Figure 128: Spectral ratio for a 6m tall Sitka spruce forest with 10% canopy cover. The ideal unnoised case and noised waveforms (10,000 signal photons) with constant and weighted smoothing are shown. The original waveforms are shown for comparison.

5.12.12 Multi-spectral pulsed lasers

Including a pulse duration will increase the blurring together of ground and canopy returns, potentially leading to high errors. Figure 129 shows that the ground finding algorithm coped well, with little noticeable difference in accuracy when compared to the infinitely short pulse duration (figure 129(b)).

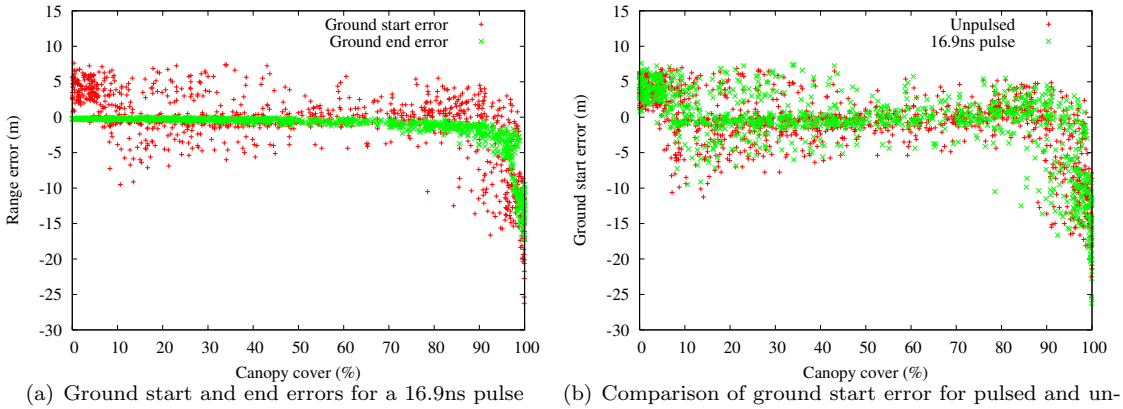

(a) Ground start and end errors for a 16.9ns pulse (b) Comparison of ground start error for pulsed and unpulsed lidar

Figure 129: Ground position error against canopy cover using the spectral ratio with 10,000 signal photons and a 16.9ns pulse duration for forests on a 30^o slope

Pulse duration is therefore not an issue to finding the ground with multi-spectral lidar.

5.12.13 Notes on the final multi-spectral method

Of course the absolute value of the spectral ratio will depend on all sorts of factors, such as the atmosphere, tree species and relative health of the laser sources and detectors. Therefore an inversion method that does not depend upon absolute but relative values would be preferable.

A real instrument will have to cope with returns from forests on a range of topographies, from flat ground to steep slopes therefore a method must be able to cope with, or distinguish between, signals with clearly separated canopy and ground returns and topographically blurred waveforms. An obvious method would be to look for an area of zero or very low signal between two features, indicating a gap between the ground and canopy, as shown in figure 10. However, as figure 108 shows, sometimes other features such as shadow and bimodal canopies can cause similar drops in waveform intensity. Confusing such a feature with the separation between ground and canopy will lead to wildly inaccurate estimates of forest height, canopy cover and surface slope.

The nature of a section of low intensity (whether it is due to a shadow or a gap between the canopy and ground) can be determined by examining the spectral ratio on either side. If the ground and canopy returns are separated the two spectral ratios will be different. If the low intensity is due to a shadow or gap in the canopy the spectral ratio will be the same (noise permitting, hopefully dealt with by smoothing) and it will show a change at another point in the canopy.

Figure 130(a) and 130(b) show the waveforms and spectral ratio for a 17.8m tall Sitka spruce forest with 78% canopy cover on flat ground (at a range of 1,200m); it was smoothed with a 3m Gaussian for clarity. The difference in spectral ratio before and after the gap is apparent. Figure 130(c) shows the waveform for a 22m tall Sitka spruce canopy with 30% cover on a 12^o slope. This canopy is made up of young and old trees, making it bimodal. From the individual waveforms it would seem that the canopy and ground were clearly distinguishable, but from figure 130(d) it can be seen that the shorter trees' canopies were mixed in with the ground return. So taking the obvious break in the signal as the transition would lead to an underestimate of canopy cover. The change in spectral ratio still corresponds to the start of the true ground, so if the period of low intensity could be coped with, should allow a more accurate estimate of canopy cover. Due to the low canopy cover at this point the ground immediately dominates the ratio.

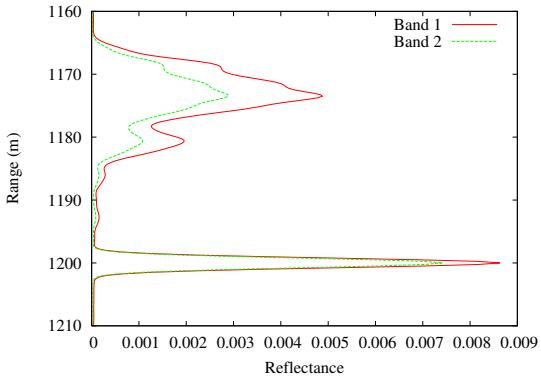

(a) Waveforms for a 17.8m tall, 78% cover Sitka spruce forest on flat ground

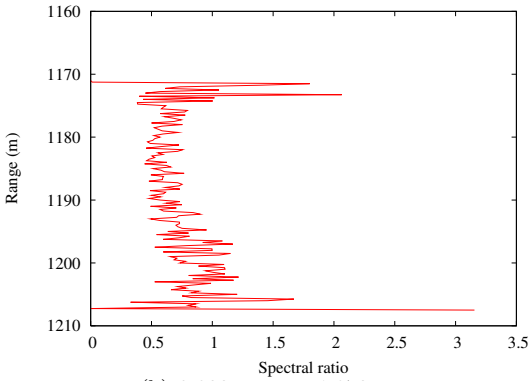

(b) 2,300nm over 1,870nm

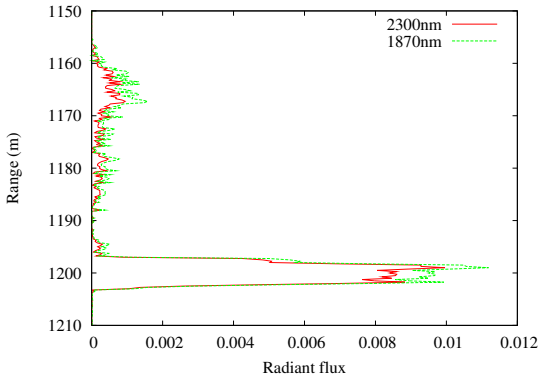

(c) Waveforms for a bimodal Sitka spruce canopy on a 12^o slope

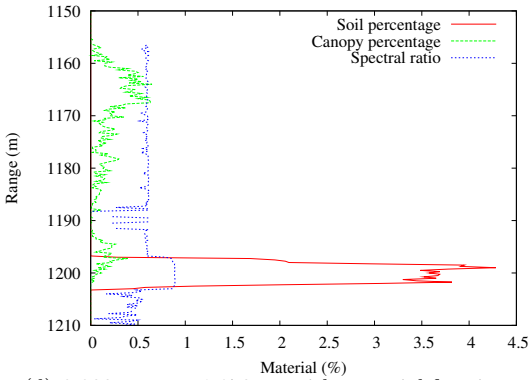

(d) 2,300nm over 1,870nm with material fractions

Figure 130: Gappy spectral ratios for Sitka spruce forests

With more work along these lines a robust method for separating canopy and ground can be developed, allowing determination of tree height, canopy cover and topography. There was not time to carry this out within the thesis.

5.12.14 Multi-spectral conclusions

A physically based method for determining the ground position through topographic blurring and understorey has been presented. Whilst it is not perfect, showing errors of up to 7m (greater for for very high, $> 97\%$ and very low, $< 8\%$ canopy covers) it is a large improvement over single wavelength methods where either prior data on the ground topography is needed (which is not available on a global scale for forests (Rosette *et al.* 2007)), site specific metrics (Lefsky *et al.* 2007) or else accept a higher error on slopes (Hofton *et al.* 2002), none of which would be suitable for a global product. Hyde *et al.* (2005) reported mean errors of 8m using ICESat over a range of slope types. The multi-spectral method presented here performs better than this on 30^o slopes (close to a worse case) and has the added advantage of not needing any separation between the ground and canopy; therefore even the shortest (within a bin length) understory can be characterised.

The Kyoto protocol defines forests as having over 10%-30% canopy cover (Rosenqvist *et al.* 2003). Therefore it is not too much of a worry that the method fails for covers below 8% as these are not classed as forest. The forest models used here had a flat plane for the ground, however this method should work over any topography. Different shaped surfaces would simply have different projected areas of ground within each range bin, the signal processing aspect would be unaffected.

Identifying the ground is the first step to measuring biophysical parameters on a slope, but there needs to be some further processing to extract biomass and even tree height on a slope from such data.

The wavelengths (2,300nm and 1,870nm) were selected to fit the specific spectra used in these models. A more comprehensive look at different spectra, particularly of the ground (which may include grass and moss), would be needed to choose the wavelengths for a global instrument. Hopefully it will not be too long before such an instrument is available.

5.13 Small footprints over topography

Section 5.12.9 described a method for large footprint lidar to cope when the ground's height variation is greater than the separation between it and the canopy and across a footprint. As alluded to in section 5.8, the blurring caused by topography is directly proportional to the footprint size; so a small footprint lidar will hardly be affected. This section will discuss the use of small footprint lidars over topography.

There has been much work investigating small footprint lidar over forests on steep slopes, both for extracting digital terrain models (James *et al.* 2007) and to measure trees (Takahashi *et al.* 2005). Arrays of small footprints can be aggregated together to get the $707m^2$ coverage needed ensure a tree top is captured (Zimble *et al.* 2003). This way many small (<1m) footprints, each unaffected by topography, can be combined to give the same signal as a large footprint system (Hofton *et al.* 2002). For this the ground position in each footprint must be known. The ground may not visible in each waveform (particularly footprints over the trunk of a tree) and so care must be taken, using data from adjacent waveforms. Even then a consistent overestimate of ground height, of the order of 1m, is reported due to saturation of the lidar beam in the canopy and understory (Næsset and Økland 2002, James *et al.* 2007).

Such pixelated recording allows some interesting multi-scale analysis; not only measuring stand height but separating individual, trees allowing height of individuals to be determined, aiding estimates of biophysical parameters (Friedlander and Koch 2000). Though it has been said that lidar is less suited for the determination of individual tree properties rather than stand characteristics (Næsset and Økland 2002).

Small footprint studies so far have used airborne scanning instruments and at present there are no plans for such an instrument to be put in space. Whether this is due to an engineering limitation or not is beyond the scope of this thesis.

An alternative method to cover an area with small footprints is to use an "imaging lidar" (Albota *et al.* 2002). That is an array of detectors recording returns from different areas of the same laser footprint. This way a single laser pulse can produce many small footprint waveforms over a large area simultaneously; an attractive prospect for a satellite.

However spreading a single pulse over a large area and splitting the returned signal across many detectors reduces the energy available for each detector, putting greater demand on the laser source output and detector efficiency. Currently true full waveform imaging lidar is not possible from space for more than a few pixels (Foster 2008).

Ground based imaging lidars have been built (Albota *et al.* 2002) and an airborne prototype for a spaceborne instrument has been proposed (Harding *et al.* 2008). These overcome the dilution of laser power by using Geiger mode APD's (introduced in section 5.6), with their very high quantum efficiencies; requiring only a single photon to make a measurement. They both overcome background noise, which can produce spurious signals as shown in figure 60(a), by taking repeat readings and averaging.

This technique works well for relatively slow moving vehicles (Albota *et al.* 2002) or over homogeneous terrain, but the heterogeneity of forests and speed of satellites prohibit this. Along with the difficulty in reconstructing a full waveform (section 5.6) it is safe to say that an imaging lidar cannot currently be used to measure forests. More efficient full waveform detectors would be needed before an imaging lidar suitable for spaceborne measurement of forests is possible.

Therefore spaceborne, waveform lidar looks set to remain large footprint for the foreseeable future and so topographic blurring cannot be avoided.

5.14 Above canopy conclusions

This chapter has discussed some of the issues an above canopy lidar faces when trying to make physically based measurements of forests. Such an approach, avoiding site specific calibration factors, is preferable when creating global datasets.

The work concentrated on separating ground and canopy returns, the first step for any physically based measurement. It was shown how this would allow estimation of stand height, canopy cover and ground slope but most end users require this to be converted to other biophysical parameters, such as biomass and LAI. Unfortunately there was not time to carry out this next step in this thesis. There are moves towards ecological models driven by variables that satellites can directly measure (Hurtt *et al.* 2004) and these would be able to make use of the forest variables

derived in the previous chapter, thereby avoiding intermediate models.

Each system parameter affecting lidar accuracy was investigated. These were tested over a range of likely target forests and optimum parameters found where possible. Some simple physical methods for removing bias without affecting accuracy were introduced.

A method for large footprint lidar (currently the only instrument proposed for space) to cope with topography has been introduced and shown to work for a range of forests and instrument characteristics. This only requires the addition of an extra wavelength to an instrument otherwise identical to current and proposed spaceborne lidars (ICESat's GLAS already has two wavelengths, 532nm and 1,064nm, but the green is only sampled every 75m making it useless for forest measurement). This would allow measurement of areas that were previously rejected (Neuenschwander *et al.* 2008) or required complex, site specific calibration (Lefsky *et al.* 2007) whilst avoiding the confusion of monochrome small footprint lidar by understory (James *et al.* 2007).

This work suggests that an ideal, large footprint spaceborne canopy lidar (within current engineering limits) would have;

Lasers at 2,300nm and 1,870nm

Range resolution finer than 1m, ideally <50cm

As short a pulse as possible, <20ns

Continuous coverage of 707m^2 to ensure measurement of a tree top

Full waveform detectors with no dead time

Record 10,000 signal photons to ensure noise does not limit accuracy

Such an instrument would allow accurate measurement of all forests except those with extreme ($> 99.5\%$, $< 1\%$) canopy covers, though accuracy falls off above 95% and below 8% canopy cover. Areas with cover below 10% are not officially classed as forest (Hansen *et al.* 2002), although there may be footprints within a forest with such covers, they are unlikely to contain whole trees, therefore this lower limit is not an issue. This is a first attempt and hopefully the accuracy can be refined. Pulse length can be corrected for by subtraction of a constant from the signal start related

to the pulse length. The multi-spectral information will ensure that the ground is distinguishable, even through topography, understory and heterogeneous canopies.

Whilst such an instrument can separate canopy from ground it cannot measure leaf angle distribution or the fraction of leaf and wood necessary to convert between canopy cover and LAI. This means that some assumptions or else field data would still be needed to obtain certain biophysical parameters for calibration and to help understand the signal. Such ground based data would benefit from being range resolved.

This chapter has concentrated on tree height, but a full waveform lidar would be capable of measuring the complete vertical distribution of a canopy. Whilst it has not yet been determined how best to use such data in ecological models, with the increasing availability of lidar data it should not be too long until that is the case. Therefore a fast (and so cost effective) method to validate range resolved measurements will be needed.

Chapter 6: Below canopy lidar

The previous chapter demonstrated that spaceborne, large footprint, full waveform lidar can be used to produce global estimates of forest height that do not saturate until very high canopy covers. Such an instrument would be a great advantage to the mapping of biomass and the modelling and understanding of ecological processes, however all variables inverted from remotely sensed data require validation before they can be used with confidence.

Section 3.1 reviewed a range of methods for measuring forests from the ground. Many of the more accurate methods are too time consuming to be used for validations over anything but small areas (Bréda 2003) and some require the destruction of areas of forest, preventing validation throughout the growing season. Optical transmission methods are the fastest and most popular ground based techniques (Gower and Norman 1991) and have been routinely used to validate remotely sensed estimates of biophysical parameters. However their measurements saturate at only moderate canopy densities (Jupp and Lovell 2007) and do not provide the range resolved metrics needed to fully validate lidar signals.

Terrestrial lidar offers the potential to characterise canopy structure, allowing validation of satellite lidar signals and avoiding the saturation issues of passive optical sensors. This chapter will examine previous attempts to measure forests with terrestrial lidar, then a physically based, stand scale inversion method is proposed and the resulting accuracy tested against existing methods. Any proposed method must be practical to perform in the field and not take too much longer than existing measurement techniques. It may be necessary to make a compromise between accuracy and data collection time.

6.1 Terrestrial lidar systems

Terrestrial laser scanners have traditionally been discrete return systems. These are ideal for measuring hard targets, such as buildings, and have been used to measure tree stem diameter and stem volume (for example Watt and Donoghue (2005), see section 3.5.4). Whilst this is important for assessing standing biomass and of particular interest for commercial foresters, this is a purely geometric point cloud processing problem and so will not be covered in this thesis. Of more interest

here is the ability of lidar to measure the canopy structure and leaf area index.

Some success has been reported using discrete return terrestrial laser scanners to measure complete forest structure (Côte *et al.* 2009), however these have required external information on tree form to convert the point clouds into quantitative data and could only be used on one tree at a time. It would be very time consuming to measure an area of forest large enough to match up to remotely sensed data with such a detailed method and it would be greatly complicated by trees obscuring each other.

There have been attempts to measure stand scale properties with discrete return terrestrial lidars, using them in much the same way as a range resolved hemispherical camera (Danson *et al.* 2007, Jupp *et al.* 2009). These, more abstract, approaches require fewer external parameters. However as each beam records only a hit or miss, small objects that do not fill the field of view will be recorded as hits and so gaps smaller than the laser footprint are missed (Danson *et al.* 2007). Some discrete lidars also record the intensity of returns which may allow some estimate of the fraction of field of view filled, but no information is available on objects behind the first interaction, so a small object in front of a trunk would be recorded as a weak return although there is no gap in that direction. Thus they are particularly susceptible to occlusion (Clawges *et al.* 2007).

Full waveform lidar records returns from all visible surfaces and so avoids this "blinding". Of course the beam can still be obscured, but it is potentially possible to work out at what point the beam is fully blocked and so decide what is and is not being measured. At present there is only one true full waveform terrestrial lidar, CSIRO's experimental Echidna (Jupp *et al.* 2009), although Riegl has recently made moves towards a terrestrial scanner with full waveform digitisation in their VZ-400. At present the data is processed on board the Riegl instrument, outputting only a few discrete returns. Commercial instruments are tailored for the traditional surveying market and so true full waveform lidar, with its enormous data output, is not really needed. The rest of the chapter will focus on Echidna and its potential future developments.

Thus far Echidna has been used to extract trunk characteristics in exactly the same way as discrete return systems in order to prove that it is capable of these measurements (Yang *et al.*

2008). In addition there have been attempts to measure stand scale canopy parameters such as LAI. Current attempts have used the scanner in the same way as a hemispherical camera (Jupp *et al.* 2009), again to prove that it is capable of such measurement with comparable or better accuracy than traditional methods, before using more complex algorithms. Here full waveform systems have a large advantage over discrete because objects smaller than the field of view will be recorded but not block the measurement of surfaces behind (or lack of). As the intensity of each return is recorded it is possible to estimate the fraction of field of view filled, allowing measurement of gaps smaller than the laser footprint.

6.2 Simulated data

The Monte Carlo ray tracer, described in chapter 3.6, was used to create sets of Echidna like, full waveform lidar hemispherical scans. Beam divergences of 0.8^o were used between -100^o and 100^o zenith and 0^o and 180^o azimuth. Waveforms were sampled every 15cm and at a range of wavelengths. Each scan contained 56,250 separate beams, requiring considerable computer resources to trace. Waveforms were individually run length encoded (Golomb 1966) to prevent files from exceeding UNIX and C's 2Gbyte file navigation limit (Schildt 1997). They could then be individually uncompressed within the inversion program when needed. Run length encoding is particularly effective for full waveform lidar data due to the long sections of zero signal (in the simulator background noise is added afterwards, section 3.6).

Older trees are far larger than younger trees and so contain many more scattering elements, taking much longer to simulate. It was decided to simulate many scans within uniform aged young forests rather than far fewer in a large range of forests and so only young Sitka spruce and birch forests were used. Young and old trees have equally dense crowns, only the size changing, therefore at the scale of an Echidna scan the age of the trees should not matter. Of course any method should be tested on a comprehensive range of forest ages and densities, but this was not attempted in this thesis. A grid of overlapping scans were simulated, with separations depending on the availability of holes big enough to "place" the virtual Echidna, which was positioned so that there were no objects within 80cm of the scan centre.

In addition small sections of canopy were extracted and scans simulated from a large range of positions. These small sections contained relatively few elements and so simulations could be run quickly, allowing experiments with data volumes that would not be possible with complete canopies. These small sections were used to explore the sensitivity of inversions to different parameters and so which could be ignored. This lead to a simple inversion method, though slightly different approaches were needed for Sitka spruce and birch canopies due to the different amounts of self shadowing in the two. Then the required number of separate scans (and so a rough idea of the time complete measurement) was determined.

Unless otherwise noted all results presented in this chapter come from these simulated Echidna scans.

6.3 Gap fraction

Gap fraction is a useful variable to measure and can be easily compared to more proven technologies. Previous studies have used terrestrial lidars to measure gap fraction (Danson *et al.* 2007, Jupp *et al.* 2009) and this should form the benchmark to test any new methods against. This section will implement the gap fraction method of Jupp *et al.* (2009) and assess its accuracy when used with the simulated scans described in the previous section. Along the way the sensitivity of inversion accuracy to various factors will be explored.

Echidna's footprints are larger than the pixels of digital cameras (at fine resolution Echidna scans equate to one mega pixel but beams overlap and start with a diameter of 3cm and so have a diameter of 6.9cm at a range of 10m), too big to fit through many gaps and so a simple fraction of beams that do not record hits will lead to an underestimate of gap fraction. Even for very small footprint lidar this effect causes an overestimate of LAI (Danson *et al.* 2007) and so the sub pixel gaps must be found from returned intensity. A lidar measures returned radiant flux, Φ which can be found by integrating the intensity, I over the solid angle of the detector's field of view Ω (Slater 1980)

$$\Phi = \int I \delta\Omega \tag{46}$$

The intensity I depends upon the range to the target, r, outgoing power, I_o, detector efficiency, $K(r)$ and the properties of the target summarised in its apparent reflectance η and can be found from the lidar equation (Wagner *et al.* 2006).

$$I = \int I_0 \frac{K(r)\eta(r)}{r^2} dr \tag{47}$$

Note that the detector efficiency $K(r)$ may vary with range as the area of overlap of the fields of view and illumination can vary; the two will never be perfectly aligned for all ranges (Jupp *et al.* 2009). The returned intensity is the integral of returns over range to allow for diffuse targets. Of these factors all except for the apparent reflectance, $\eta(r)$, are engineering considerations that can be easily calibrated against laboratory measurements or, in the case of range, from the lidar's own measurements. The apparent reflectance depends upon the target's properties through the fraction of projected area (or gap fraction) P_{gap}, the canopy element reflectance, ρ_c and the phase function, $\Gamma(\theta)$ at a zenith angle, θ.

$$\eta = (1 - P_{gap})\rho_c \Gamma(\theta) \tag{48}$$

Here the gap fraction is related to the ratio of the projected area, A_p, to footprint area, A_f, which in turn is related to the surface area, A_s, and the Ross-G function, $G(\theta)$. Figure 131 shows a sphere and a lidar beam with these three areas illustrated.

$$P_{gap} = 1 - \frac{A_p}{A_f} = 1 - \frac{A_s G(\theta)}{A_f} \tag{49}$$

Solving equation 48 for gap fraction gives;

$$P_{gap} = 1 - \frac{\eta}{\rho_c \Gamma(\theta)} \tag{50}$$

So to determine the gap fraction from Echidna the reflectance of canopy elements and the phase function must be known. Jupp *et al.* (2009) assumed that $\rho_c = 0.4$ for all elements at 1064nm and that $\Gamma(\theta) = G^2(\theta)$, both from laboratory measurements. They then assumed that canopy elements are spherically distributed so that $\Gamma(\theta) = \frac{1}{4}$ for all view angles. Gap fractions estimated from Echidna compared well with hemispherical photography and were even more consistent,

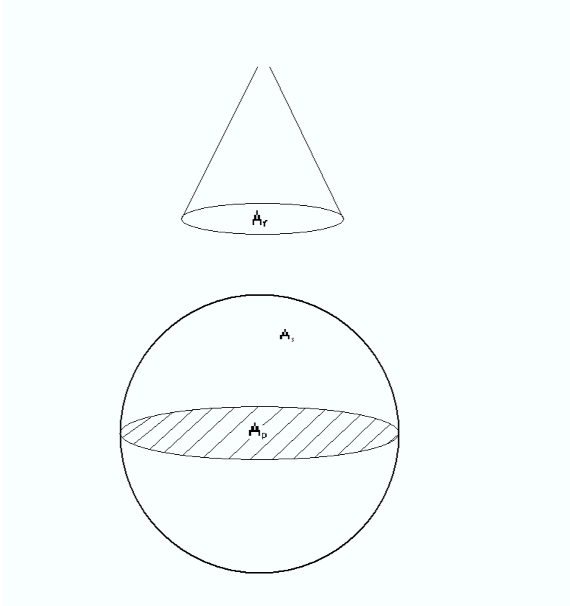

Figure 131: Illustration of areas used in derivations

being more tolerant to varying illumination conditions. The agreement of gap fractions with those from hemispherical photography does not necessarily mean that the values chosen were accurate, only that their products are correct (Jupp *et al.* 2009) and so should be considered as effective parameters (Widlowski *et al.* 2005).

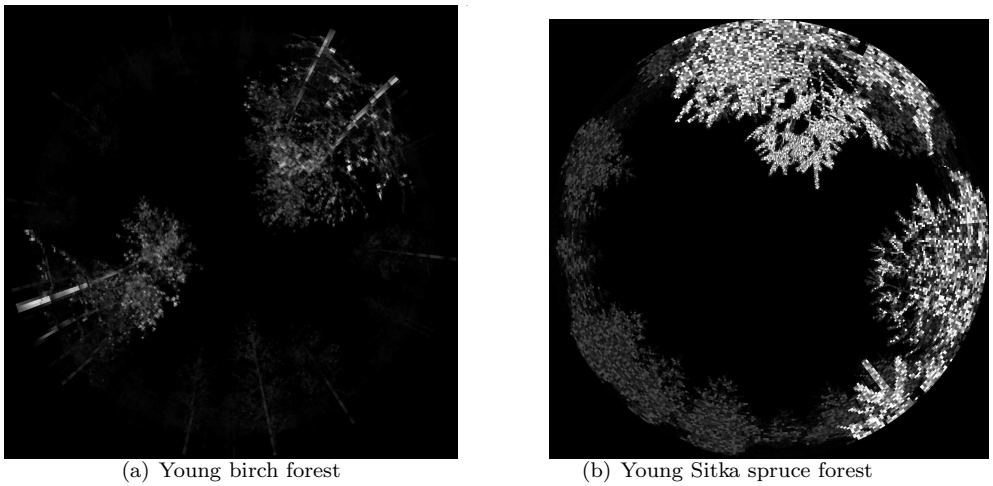

(a) Young birch forest (b) Young Sitka spruce forest

Figure 132: Hemispherical projection of two simulated Echidna scans

Equation 48 assumes that there is a linear relationship between the gap fraction and apparent reflectance for each beam with a gradient of $\frac{1}{\rho_c \Gamma(\theta)}$ and that $\Gamma(\theta)$ is spectrally invariant. In reality

the phase function will vary throughout the canopy and multiple scattering, completely ignored in equation 48, will also contribute to the apparent reflectance. Scattering varies with wavelength, as described in section 2.1.6 and so the effective phase function will have some wavelength dependence. The element reflectance may also be variable throughout the canopy and seasons (Doughty and Goulden 2008) but as the forest models used assume that all elements of a certain type had the same spectra this effect was not investigated, only the structural heterogeneity. Field measurements suggested that the reflectance within a species (taking red fir as an example, see section 4.2.2) varies by around 0.1 for a reflectance of 0.6 and Jupp *et al.* (2009) believe it to be small, therefore it seems reasonable to assume that structural effects dominate.

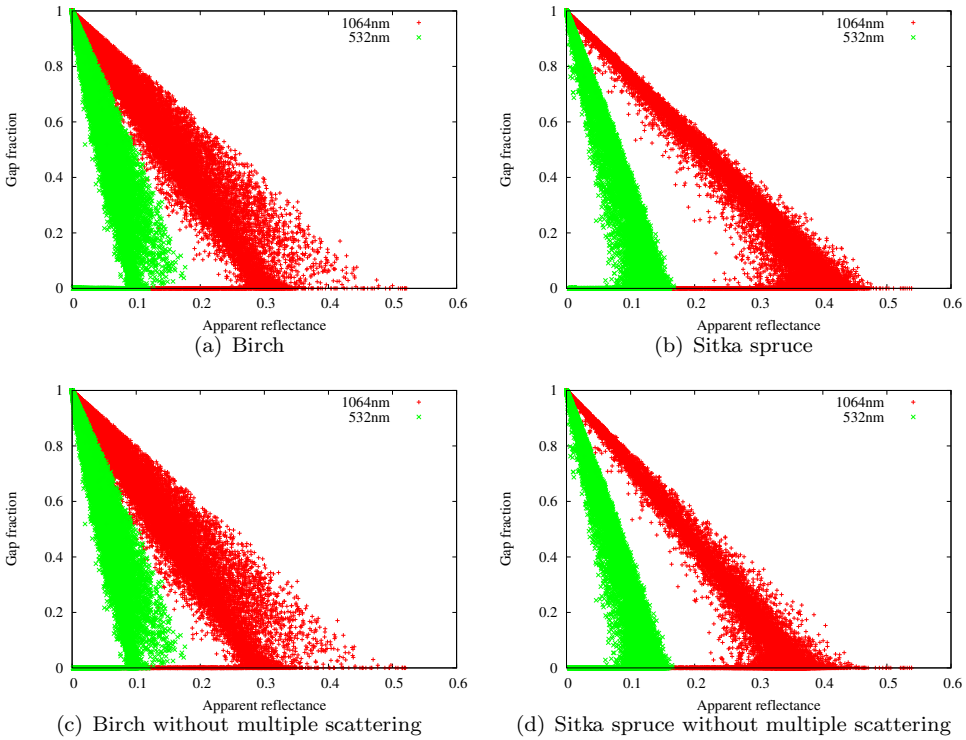

(a) Birch (b) Sitka spruce

(c) Birch without multiple scattering (d) Sitka spruce without multiple scattering

Figure 133: Gap fraction against apparent reflectance

Plotting gap fraction against apparent reflectance, shown in figure 133, suggest that the two are very closely related. Removing multiple scattering had very little effect on the signal at 532nm due, to the low element reflectance at that wavelength, but did reduce the spread at 1,064nm.

For Sitka spruce with multiple scattering, $\rho_c\Gamma = 0.41$ with a root mean square error in gap fraction of 0.061. Without multiple scattering, $\rho_c\Gamma = 0.35$ with a root mean square error in gap

fraction of 0.057. Thus for Sitka spruce the multiple scattering did make a significant contribution to the apparent reflectance (which this models subsumes into the phase function) and increased the spread of points. That the variance was not completely removed with multiple scattering shows that the heterogeneity of the structural components of the phase function were significant. A number of scans for each species were examined and all showed near identical behaviour and so this behaviour was taken as general.

For birch with multiple scattering $\rho_c\Gamma = 0.33$ with a root mean square error in gap fraction of 0.076. Without multiple scattering $\rho_c\Gamma = 0.32$ with a root mean square error in gap fraction of 0.076. Here the multiple scattering had a very small effect on the phase function and a negligible effect on the spread of data. This is due to the lower scatterer density in birch, so that the contribution from multiple scattering is less (figure 135).

The small root mean square errors are an encouraging sign and suggest that equation 48 can be used to estimate gap fraction if an appropriate value can be found for the product of the canopy element reflectance and phase function. The values found here were very different from those used by Jupp *et al.* (2009), where $\rho_c\Gamma = 0.1$. In the models used, at 1064nm $\rho_l = 0.51$ and $\rho_w = 0.57$, higher than the 0.4 used by Jupp *et al.* (2009) and it was assumed that all surfaces are perfectly Lambertian. This last assumption may not be appropriate for the forests investigated by Jupp *et al.* (2009) or their value may have been effective, taking other effects into account. Without more details on the forest these were estimated from and the appropriateness of Lambertian surfaces the cause of these differences cannot be determined for certain.

6.3.1 Separation of phase function and element reflectance

The above analysis is possible with real data through the comparison of gap fractions from Echidna and hemispherical photography, but the heterogeneity of structure, element reflectances and multiple scattering make it impossible to completely decouple the various effects.

If a single phase function, $\Gamma(\theta)$, is used to describe both leaves and wood the apparent reflectance is;

$$\eta = \Gamma(\theta)\frac{1}{A_f}(\rho_l A_l G(\theta) + \rho_w A_w G(\theta)) \tag{51}$$

Where ρ_l is leaf reflectance, ρ_w is wood reflectance, $A_l G(\theta)$ is the projected area of leaf and $A_w G(\theta)$ the same for wood. From the ray tracer only $\Gamma(\theta)$ is unknown so it can be solved for each beam.

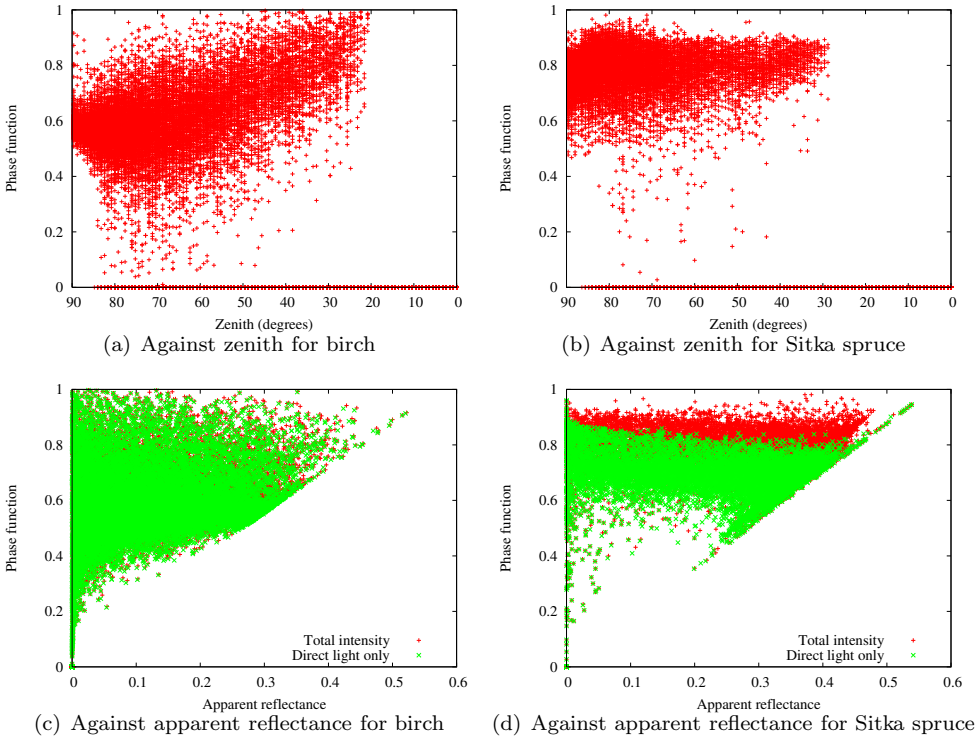

(a) Against zenith for birch

(b) Against zenith for Sitka spruce

(c) Against apparent reflectance for birch

(d) Against apparent reflectance for Sitka spruce

Figure 134: Combined phase function for all canopy elements against apparent reflectance

Figures 134(a) and 134(b) show that there was a slight increase in the phase function with decreasing zenith, suggesting a slightly planophile canopy. Table 3 shows the results of fitting straight lines to these data of the form $\Gamma(\theta) = m\theta + c$ (zenith dependent) and a flat line (no zenith dependence).

It can be seen that for Sitka spruce the phase function had very little dependence on view zenith, the sloping line would have the phase function vary from 0.84 at nadir to 0.75 horizontally. The errors on the fit for the sloping and flat line were near identical, suggesting that there is little advantage to the hemispherical gap fraction in including a zenith dependence. For birch there is a slightly stronger zenith dependence, with the phase function varying from 0.87 at nadir to 0.53 when

Species	Multiple scattering	m	c	RMSE
Birch	With	-0.0038	0.871	0.107
Birch	With	forced 0	0.608	0.125
Birch	Without	-0.0040	0.870	0.108
Birch	Without	forced 0	0.595	0.126
Sitka	With	-0.0006	0.816	0.082
Sitka	With	forced 0	0.775	0.082
Sitka	Without	-0.0012	0.776	0.118
Sitka	Without	forced 0	0.690	0.118

Table 3: Parameters of linear fits for phase function against zenith with root mean square errors with and without multiple scattering

viewed horizontally and a higher error (16% larger) when fitting a flat line compared to the sloped case. Note that removing multiple scattering only slightly decreased the phase function for birch but caused a more marked reduction for Sitka spruce, bringing the two much closer together. This undoubtedly proves that there is more multiple scattering amongst the densely packed scattering elements in a Sitka spruce shoot than for birch leaves. This increased multiple scattering seems to have a larger effect upon the differences in phase function and apparent reflectance between the two species than other structural effects. The remaining difference in phase function can only be due to angular distribution and the proportions of leaf and wood. For the sloped line, removing multiple scattering increased the slope for both species. This suggests that multiple scattering is masking some of the angular distribution effects. For these young forests, the canopies are far denser near the bottom and so more multiple scattering occurs at large zeniths than nadir (see figure 135). For older trees the canopy will be denser higher up and so this masking may not be as strong.

Due to the nature of the trees used in this set of simulations, the scans had no foliage directly above the lidar and so no estimates of phase function were available for zeniths less than 25^o. Therefore the value at nadir is an extrapolation beyond the measured bounds and may not be

reliable. To get returns from nadir, trees that overhang the lidar are needed, whilst allowing a wide view of the canopy (you would not set up a scan right against a tree trunk or within a shrub as the field of view would be greatly limited). Trees that are large enough to overhang a point whilst their trunks are far enough away not to block too much field of view (2m) are very complex, requiring far more computer time to ray trace than the younger trees used in these scans.

Taking this limited zenith range into account, for birch the phase function varied between 0.53 and 0.76 across the range tested. In this light the zenith dependence for birch does not seem so strong and the analysis can be performed assuming that the phase function is independent of view angle, $\Gamma(\theta)$ becoming Γ. It is hoped that any trend with zenith will be insignificant compared to other sources of heterogeneity and comparing figures 134(a) and 133(a) it can be seen that apparent reflectance is far more correlated to the gap fraction than phase function, suggesting that gap fraction controls the returned signal strength. To test this the difference between actual phase function and the assumed constant value was calculated, grouped in zenith bins. In addition equation 49 was used to predict a gap fraction using the constant phase function and a known reflectance (taken as the average of leaf and wood) and the error calculated.

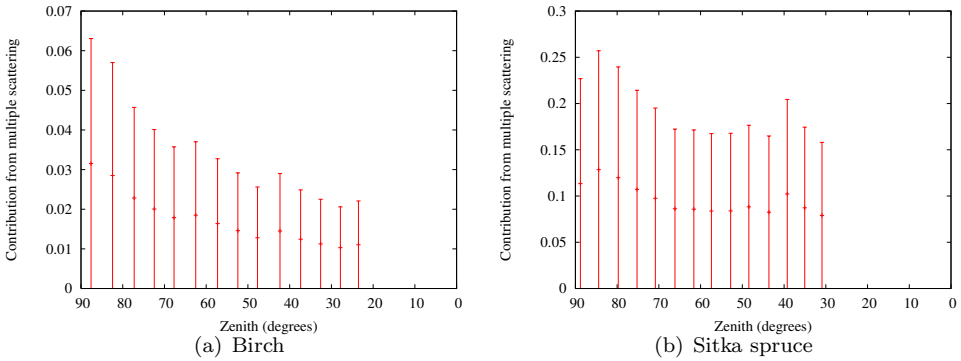

(a) Birch (b) Sitka spruce

Figure 135: Contribution from multiple scattering against zenith angle

Figure 136 shows the mean and standard deviation of the phase function over all azimuths at each zenith and the error in gap fraction resulting from assuming a constant phase function across all zeniths. The true gap fraction is shown alongside the errors to give an idea of the relative error. From figure 136(c) it can be seen that for Sitka spruce any relationship between error in the phase function and zenith was negligible compared to the errors caused by heterogeneity.

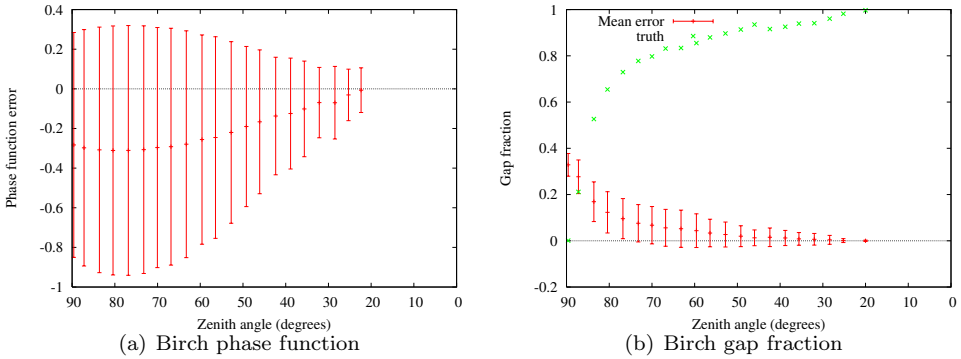

(a) Birch phase function

(b) Birch gap fraction

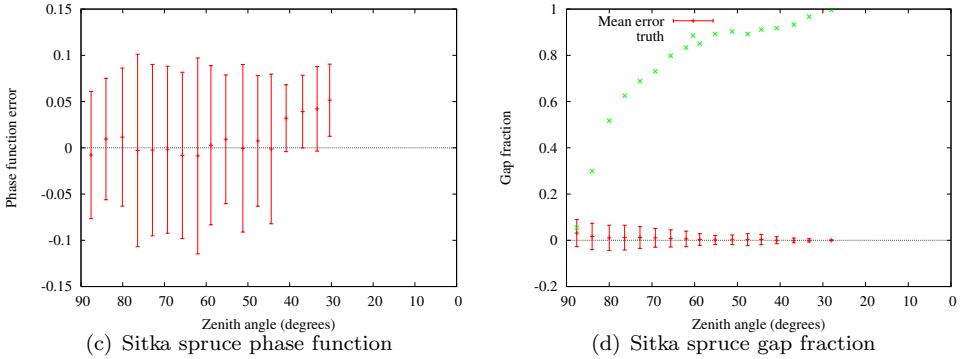

(c) Sitka spruce phase function

(d) Sitka spruce gap fraction

Figure 136: Errors from using a constant phase function against view zenith. Error bars show one standard deviation

Figure 136(a) shows that for birch the phase function error had a distinct zenith dependence, with the mean error varying from 0.3 at 80^o to 0 at 28^o and the spread of errors decreasing with zenith. However figure 136(b) shows that despite this error the predicted gap fraction was always within one standard deviation of the truth for zeniths below 70^o, though with a consistent overestimate.

Assuming a constant phase function caused significant errors in gap fraction for beams near the horizontal for both species (more than 70^o zenith). However these angles contain trunks and ground returns and have very long path lengths, so most studies ignore them. The LAI-2000 does not measure zeniths beyond 70^o (LI-COR 1992) and most users further limit this to 50^o to be sure of removing ground effects (Chen and Cihlar 1996) and so these large errors at high zeniths can be discounted. Within the restricted zenith range the errors were small, around 0.05 for gap fractions in excess of 0.8 for both species.

Interestingly for birch the predicted gap fraction showed a consistent overestimate. As the phase function was determined by fitting to the data this bias can only come from uncertainty in the element reflectance. The value used assumed that there were equal contributions from leaf and bark, this must not have been the case and the reflectance value used must be too high. An overestimate of gap will lead to an underestimate of LAI; this highlights the importance of using correct values of both phase function and canopy reflectance to extract gap fraction from Echidna.

Separating leaf and wood The slight difference between the phase functions for birch and Sitka spruce without multiple scattering must be due to other structural effects, either the angular distribution or the proportions of leaf and wood. As the projected areas of leaf and wood are recorded separately, as long as the beam contains only leaf and wood (no soil) separate phase functions can be extracted by using two wavelengths and solving a pair of simultaneous equations (see appendix D). For an apparent reflectance $\eta(\lambda)$ at a wavelength λ with a projected area of leaf A_l and wood A_w which have reflectances at λ of $\rho_l(\lambda)$ and $\rho_w(\lambda)$, with a second wavelength, ω, the phase functions for leaf Γ_l and wood Γ_w can be found from;

$$\Gamma_l = \frac{A_f}{A_l} \frac{\eta(\lambda)\rho_w(\omega) - \eta(\omega)\rho_w(\lambda)}{\rho_l(\lambda)\rho_w(\omega) - \rho_l(\omega)\rho_w(\lambda)} \tag{52}$$

$$\Gamma_w = \frac{A_f}{A_w} \frac{\eta(\lambda)\rho_l(\omega) - \eta(\omega)\rho_l(\lambda)}{\rho_w(\lambda)\rho_l(\omega) - \rho_w(\omega)\rho_l(\lambda)} \tag{53}$$

Plotting this against apparent reflectance without multiple scattering (which would only mask any structural effects) for birch and Sitka spruce gave figure 137.

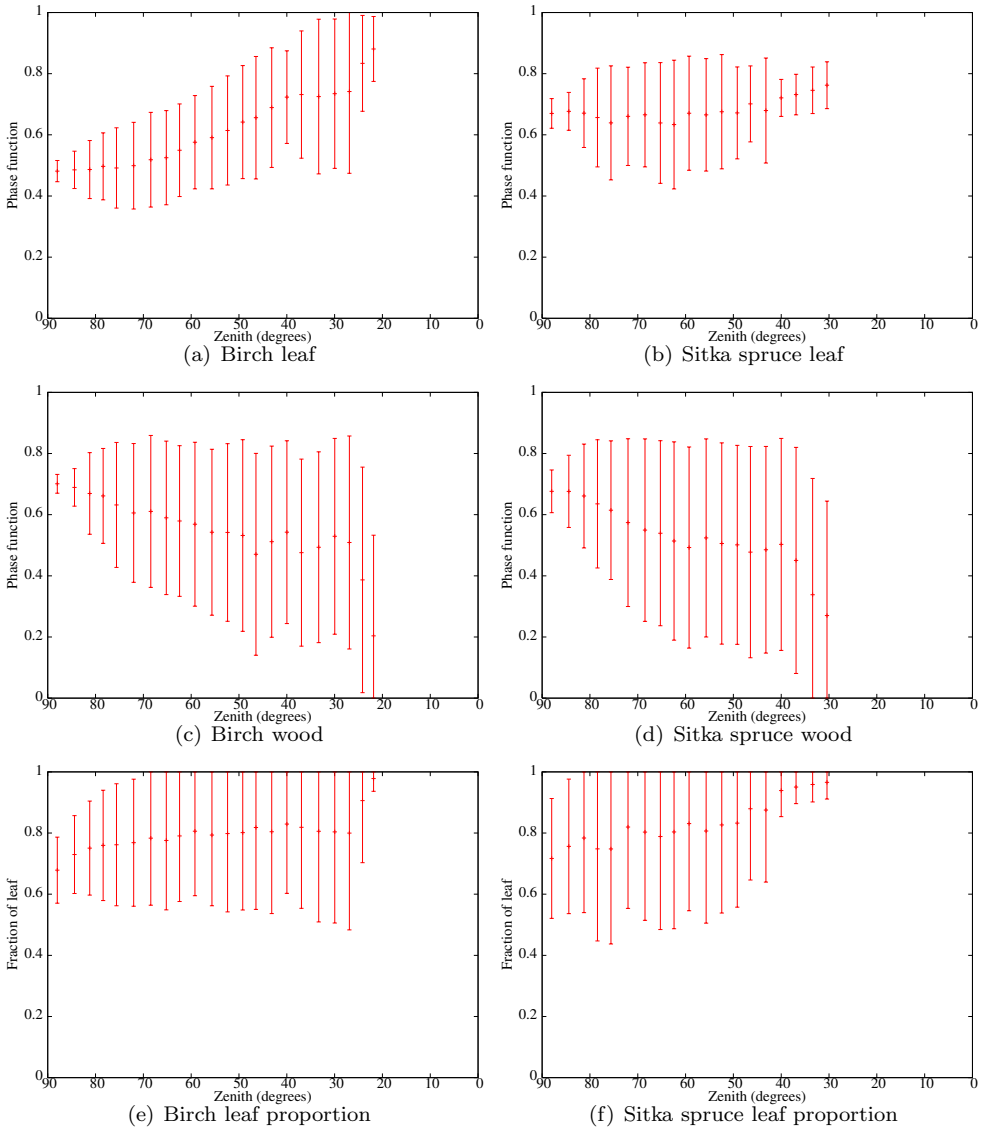

(a) Birch leaf (b) Sitka spruce leaf (c) Birch wood (d) Sitka spruce wood (e) Birch leaf proportion (f) Sitka spruce leaf proportion

Figure 137: Phase function without multiple scattering for leaf and wood and proportion of canopy made up of leaf. Error bars show one standard deviation

Figures 137(a) and 137(c) show that for birch the decreasing phase function with zenith was almost entirely due to leaves, the wood phase function did decrease a small amount with zenith but it was almost negligible compared to the variance. For Sitka spruce (figures 137(b) and 137(d)) the

leaf phase function appeared to be constant whilst the wood phase function showed a very slight tendency to increase with decreasing zenith. Figures 137(e) and 137(f) show that for both species the proportion of wood was higher nearer the horizontal, which is what would be expected as trunks become more visible. For birch this settled down to a reasonably constant value by a zenith of around 70^o whilst for Sitka spruce it was constant from 70^o to 40^o, after which it increased. This difference between species may be due to the greater tendency of pine needles to group around branches and so obscure wood than for broadleaved species. As the reflectances for leaf and bark are quite similar at these wavelengths ($\rho_l = 0.51$ and $\rho_w = 0.57$) this should not have a dramatic effect but will contribute to errors at higher zeniths (see figure 136). The gap fraction analysis used for figure 136 assumed that the proportion of leaf and wood was constant, this was not the case and as the proportion changes the canopy reflectance will also change. For the spectra used, increasing the proportion of wood will increase the canopy reflectance and so decrease the estimate of phase function, leading to an overestimate of gap fraction.

6.3.2 Accuracy of gap fraction estimates

Having determined that Echidna can be used to estimate gap fraction, provided that a value for the phase function and canopy reflectance are known, it was seen whether this could be applied across a number of scans in similar forests. The previous section found that for the forest models used, for birch $\Gamma = 0.608$ and for Sitka spruce $\Gamma = 0.776$. For both of these forests at 1064nm the reflectance was 0.51 for leaf and 0.57 for wood. Linearly mixing the two reflectances, assuming an equal proportion of leaf and wood in the absence of any more reliable data, gives a canopy reflectance, $\rho_c = 0.54$.

The above values were derived from a single scan (referred to as scan 1) after seeing that all scans were qualitatively similar these were used to calculate the gap fraction for each beam in all scans available.

Figure 138 shows that the gap fraction predicted by the above method was always within one standard deviation of the truth for zeniths below 53^o, although with a consistent overestimate. This bias is most probably from the assumption of equal proportions of leaf and wood and the resulting underestimate of canopy reflectance. Figure 137 shows that leaves dominated in this zenith range

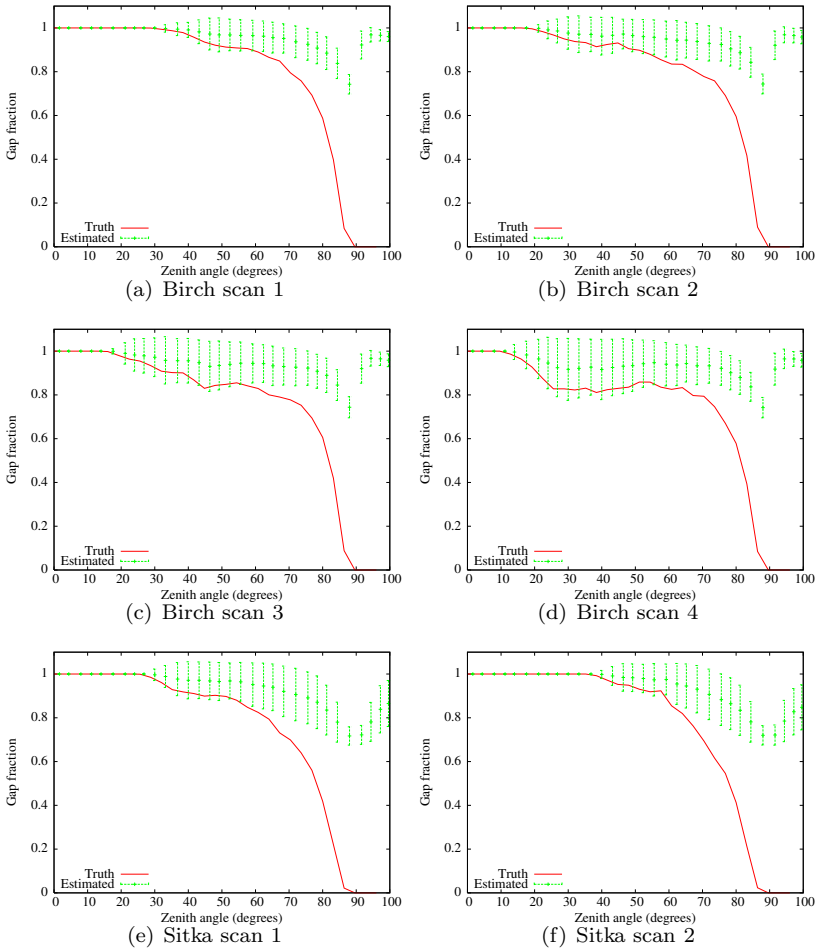

(a) Birch scan 1 (b) Birch scan 2

(c) Birch scan 3 (d) Birch scan 4

(e) Sitka scan 1 (f) Sitka scan 2

Figure 138: Gap fractions from Echidna. Error bars show one standard deviation

and so the canopy reflectance should be lower than the 0.54 used. The error introduced by using the wrong canopy reflectance was in the region of 5% and may be acceptable when compared to the errors introduced in the conversion of gap fraction to LAI, but if it is to be reduced more accurate estimates of the canopy reflectance and proportions of leaf and bark are needed. Frustratingly the hinge point of spheroidal distributions at 54.7^o (Wilson 1960), was at the very edge of this reliable range. For zeniths above 53^o the agreement worsened, most probably due to the changing proportions of leaf and wood and amount of multiple scattering (figures 137 and 135). That the error in phase function increased equally for birch and Sitka spruce suggests that it was not caused by assuming that the phase function is constant with zenith. The method completely broke down above 90^o as the ground starts to contribute. The ground was not included at all in the above method and it would be difficult to use gap fractions in this region even if they could be reliably estimated, therefore data containing ground returns must be discarded.

6.3.3 Sensitivity of gap fraction to external parameters

The method relies on knowledge of canopy reflectance and phase function, uncertainties in these values will cause errors in the estimates of gap fraction. The sensitivity of gap fraction estimate to element reflectance was explored by performing inversions for a range of canopy reflectances and phase factors. It has been shown that the gap fraction is unreliable at zeniths above 53^o, therefore only zeniths above 50^o were used for the following analysis. Within this region there was no obvious dependence of error on zenith, so the mean and root mean square errors were taken as a measure of accuracy for each scan and set of parameters.

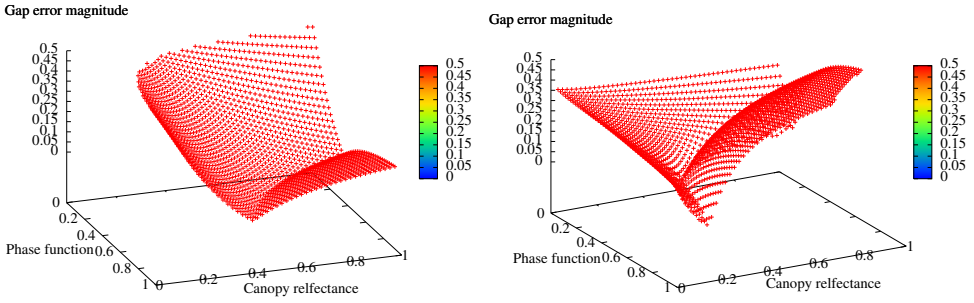

(a) Birch (b) Sitka spruce

Figure 139: Sensitivity of gap fraction from Echidna to phase function and canopy reflectance

Figure 139 shows the sensitivity of the gap fraction, estimated by equation 49, against values of the phase function and canopy reflectance. Errors over $\frac{1}{2}$ have been left out as such a result is clearly unacceptable and only the magnitude of the error is shown to make areas of zero error more apparent. It can be seen that the dependence is rotationally symmetric about $\Gamma = 1, \rho_c = 1$ and so a cross section along any radii will give a complete picture of the sensitivity at its steepest.

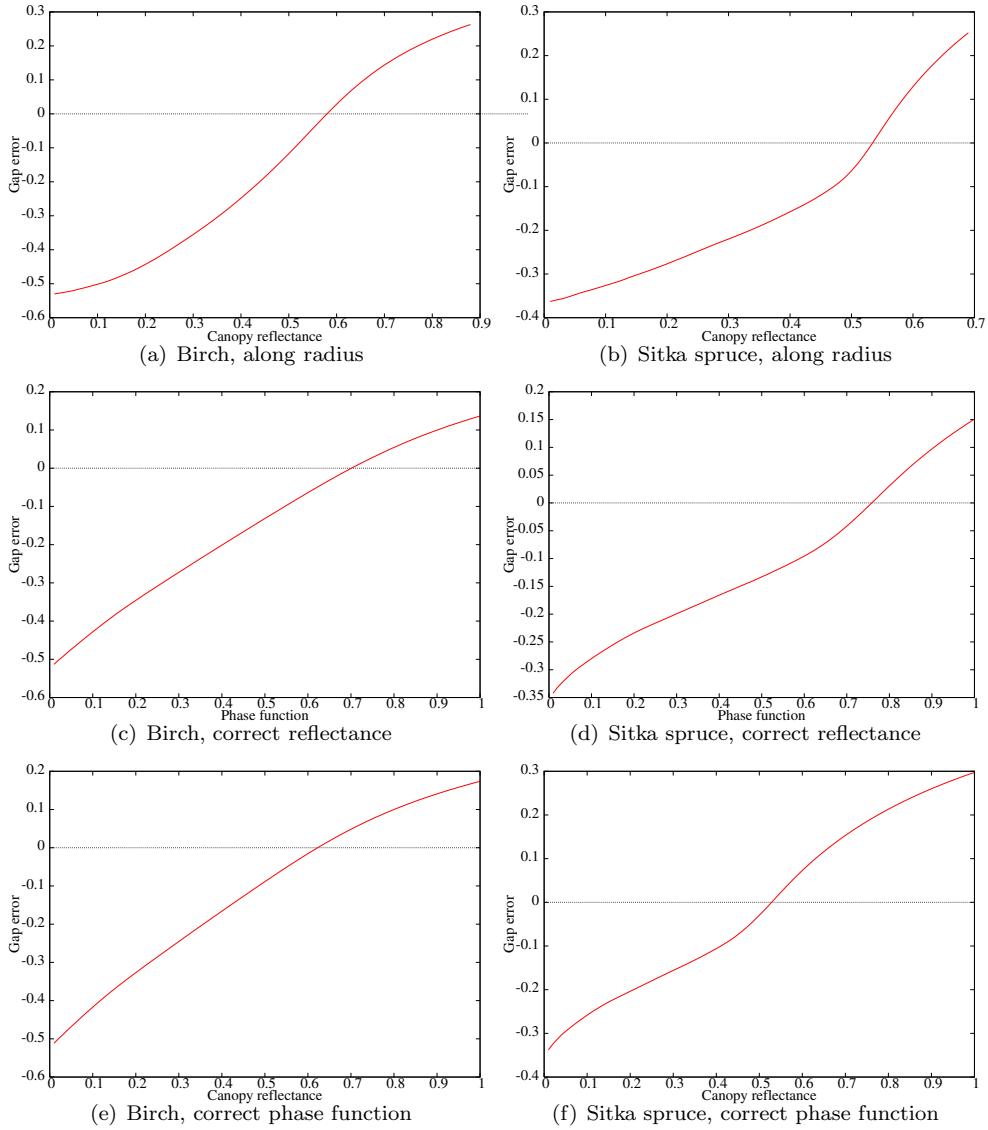

(a) Birch, along radius
(b) Sitka spruce, along radius
(c) Birch, correct reflectance
(d) Sitka spruce, correct reflectance
(e) Birch, correct phase function
(f) Sitka spruce, correct phase function

Figure 140: Slices through the error surface in figure 139

Figure 140 shows that for birch the estimated gap fraction's dependence on phase function and canopy reflectance was quite benign, with changes of only 0.1 for an uncertainty of 0.1 in one or the other. For Sitka spruce the error increase with uncertainty was more dramatic, reaching a 0.1

error in gap fraction with an uncertainty of only 0.04 in the canopy reflectance. This is a very tight tolerance and may cause errors when applied over large areas.

The gap fraction may be more sensitive for Sitka spruce than birch because for these Sitka forests the phase function was more homogeneous (indicated by figure 133 with the smaller deviation from a straight line). Therefore any deviation in phase function or canopy reflectance from the truth will cause more points to be one side of the line of the truth than the other for Sitka spruce than birch and so a larger error.

6.3.4 LAI from gap fraction

The above section has shown that Echidna can be used to accurately determine gap fraction, this can then be used to calculate LAI using the method of Jupp *et al.* (2009).

$$LAI = \frac{-\ln P_{gap}(\theta)}{k(\theta)} \tag{54}$$

Where $k(\theta)$ is an angular distribution term and also takes path length through the canopy into account. Jupp *et al.* (2009) used an approximation of the spheroidal distribution (Campbell 1986).

$$k(\theta) = \frac{1}{\cos\theta}\left(L_h \cos\theta + L_v \frac{2}{\pi}\sin\theta\right) \tag{55}$$

Where L_h is the horizontally and L_v the vertically projected LAI. Total LAI is then the sum of these terms. This is similar to the model of Suits (1972) with an added $\frac{2}{\pi}$ term. This can be rearranged and simplified into a linear form;

$$-\ln P_{gap}(\theta) = L_v \frac{2}{\pi}\tan\theta + L_h \tag{56}$$

The projected leaf area terms were found by plotting $-\ln P_{gap}$ against $\frac{2}{\pi}\tan\theta$ and fitting a straight line. L_v is then equal to the gradient and L_h the y intercept. This method was applied to the above gap fraction results to determine the LAI accuracy possible with this method.

It is not clear whether Jupp *et al.* (2009) used the mean gap fraction in each zenith ring to fit a line to or all azimuths separately and if they were combined whether the variance within a zenith ring was used in the regression. Without using the variance, these methods give different estimates

of LAI and very different certainties. in the absence of detailed knowledge on the method it was decided to use the average of each zenith ring so as to minimise noise from heterogeneity, using the standard deviation of each ring as uncertainty during the line fitting.

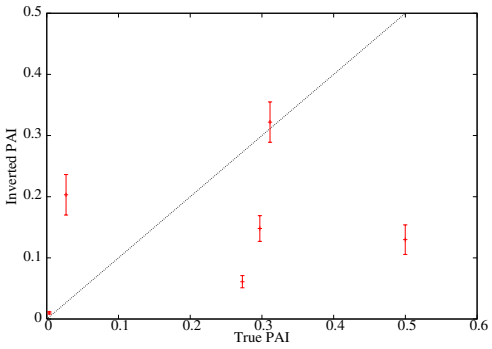

Figure 141: Inverted PAI against true PAI for inversions of birch canopies using the method of Jupp et al. (2009)

Figure 141 shows that for very low PAIs (<0.01) the method performed perfectly, but for the majority of cases the PAI was underestimated. Jupp *et al.* (2009) applied an additional correction to their phase factor in order to "prevent the canopy becoming too transparent", suggesting that the values they used for phase factor and reflectance were too low for the particular canopy tested. For the canopy tested here the same over prediction of transparency (and so gap fraction) was observed, particularly at large zeniths. An additional correction would increase estimated LAI, moving it closer to the truth. Such a fudge factor may give better results, but it has no physical basis and is not guaranteed to give the correct results. Comparing inverted gap fraction and LAI results to those found with hemispherical photography may not reveal these issues due to the common assumptions of the two methods. In addition their G function also took clumping into account (Jupp *et al.* 2009) and so would be higher than the value used here, leading to an increase in the estimate of PAI.

As well as these various correction factors, which could be applied to move the estimates closer to the truth, the plot of gap fraction against zenith angle was quite noisy due to the heterogeneity of the forest. Even with the averaging and using the standard deviation as a measure of uncertainty the algorithm struggled to fit an accurate straight line. This highlights the problems of treating a canopy as heterogeneous as a sparse birch forest as a turbid medium (Ross 1981). The method

may perform better for denser, more homogeneous canopies, but such data was not available in the thesis.

The above inversion used the gap fractions from section 6.3.2, all of which were slight overestimates. The inversion was repeated using the known truth and found to not noticeably improve the accuracy of the LAI estimation alone.

6.3.5 Sensitivity of LAI to external parameters

In section 6.3.3 it was shown that the gap fraction was sensitive to the initial estimates of canopy reflectance and phase function, particularly for Sitka spruce. The gap fraction is not the primary parameter of interest but PAI (and so LAI). This error from uncertainty will propagate through to PAI through equation 56 so that for a gap fraction estimate of "xP_{gap}", in error by a factor "x";

$$-\ln(xP_{gap}(\theta)) = L_v \frac{2}{\pi} \tan\theta + L_h \tag{57}$$

Using the logarithmic identity, $\ln ab = \ln a + \ln b$ it can be seen that any uncertainty in the gap fraction, x will become an error in the horizontally projected leaf area, L_h of magnitude $\ln x$, the gradient being unaffected. Figure 142 shows this sensitivity.

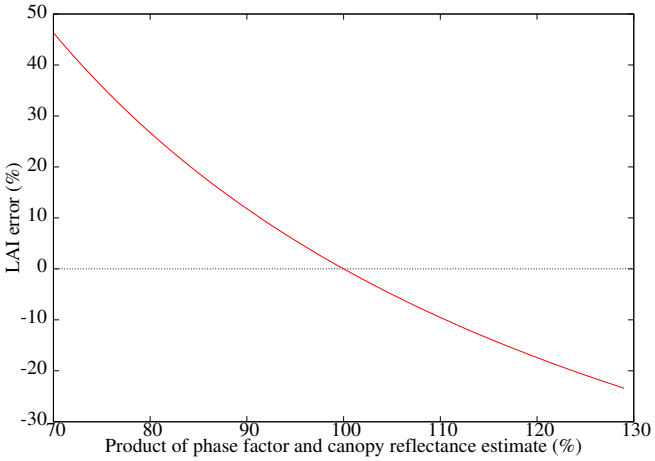

Figure 142: Sensitivity of PAI estimate to uncertainty in phase function and canopy reflectance

A 10% error in the product of the phase factor and canopy reflectance will lead to between a 9.5% and 11.5% (depending on whether it is an under or an overestimate) error in LAI. This error will be entirely in the horizontally projected LAI and so the LAD will also be in error.

6.3.6 Gap fraction conclusions

This section has shown that a full waveform terrestrial lidar can measure gap fraction accurately, with the advantage over passive optical methods of being independent of illumination conditions. This would allow measurements at any time of day or night and any sky conditions; far more of an advantage than nocturnal forestry. Unlike passive optical methods, knowledge of the reflectance and phase function of elements is required to extract gap fraction from measured intensity. Whilst authors believe these values to be fairly constant (Jupp *et al.* 2009) it is a potential source of error and bias. This investigation suggests that for Sitka spruce, small uncertainties in these external values will lead to large errors in estimated gap fractions.

Once the gap fraction has been calculated Beer-Lambert's law is needed to invert forest parameters, with all the issues of saturation, effective parameters and clumping suffered by traditional passive optical methods (see section 3.1.4). Whilst it is useful to test the new technology against an existing benchmark the gap fraction method does not take full advantage of all the possibilities of a terrestrial waveform lidar and a method that does should be the ultimate goal (Jupp and Lovell 2007).

6.4 Model inversion

Whilst Echidna can be used to extract gap fraction through equation 50 and this can be used to calculate LAI with equation 56, it is a roundabout way of arriving at a biophysical parameter. The returned intensity is related to gap fraction, but by rearranging equation 48 the lidar signal can be more directly related to canopy properties. To restate, the apparent reflectance, η, is given by;

$$\eta = (1 - P_{gap})\rho_e\Gamma(\theta) \tag{58}$$

The contact frequency ($P_{cont} = 1 - P_{gap}$) is equal to the projected area as a fraction of the field of view. For a flat plane at an angle of incidence α this will be the visible surface area multiplied by the cosine of the angle of incidence.

$$P_{cont} = 1 - P_{gap} = \frac{A_p}{A_f} = \frac{A_s}{A_f}\cos\alpha \tag{59}$$

For a flat Lambertian plane the phase function will also be equal to the cosine of the angle of incidence;

$$\Gamma(\alpha) = \cos\alpha \tag{60}$$

And so for a flat Lambertian plane at an angle of incidence α the apparent reflectance is given by;

$$\eta = \rho_e \frac{A_s}{A_f} \cos^2\alpha \tag{61}$$

Any surface can be represented as a set of small planes, each with a surface area of dA_s and so the apparent reflectance can be taken as the integral of the contributions from each of these elements.

$$\eta = \rho_e \frac{1}{A_f} \oint \cos^2\alpha dA_s \tag{62}$$

This takes no account of multiple scattering and unlike the method of Jupp *et al.* (2009) none of the structural parameters are effective factors that could be used to fudge the multiple scattering contribution. It would be possible to use an effective element reflectance that includes the multiple scattering enhancement to the single scattering value (Huang *et al.* 2007), however this was not attempted within the thesis.

The gap fraction can be found following a similar logic.

$$P_{gap} = 1 - \frac{1}{A_f} \oint \cos\alpha dA_s \tag{63}$$

The Ross-G function is simply the contact frequency divided by the surface area.

A canopy is made up of leaf and wood, each of which may have different reflectances (ρ_l and ρ_w), areas (dA_{ls} and dA_{ws}) and orientations (α_l and α_w). Therefore the apparent reflectance and gap fraction will be a sum of the above equations for each material type. Assuming that all leaves can be described by a single spectrum and all bark by another (which may be a limitation for forests with a mix of young and old trees, see section 4.2.2).

$$\eta = \frac{1}{A_f}\left(\rho_l \oint \cos^2 \alpha_l dA_{ls} + \rho_w \oint \cos^2 \alpha_w dA_{ws}\right) \tag{64}$$

$$P_{gap} = 1 - \frac{1}{A_f}\left(\oint \cos \alpha_l dA_{ls} + \oint \cos \alpha_w dA_{ws}\right) \tag{65}$$

A factor describing the proportion of total surface area made up of leaf will be useful. For leaf surface area, A_l and wood surface area, A_w, the woody correction factor, Ψ, is;

$$\Psi = \frac{A_l}{A_l + A_w} \tag{66}$$

As elements are encountered the footprint area will be reduced, affecting the intensity in subsequent ranging bins and so the above equations should be corrected for the gap fraction up to that point. A simple multiplication of the field of view area by the gap fraction will give the visible footprint area, A_{vf};

$$A_{vf} = A_f P_{gap} \tag{67}$$

Which will be the product of all gap fractions for all voxels, i, up to that point.

$$P_{gap} = \prod_i \left(1 - \frac{1}{A_f} \oint \cos \alpha_i dA_{s,i}\right) \tag{68}$$

Substituting the visible footprint area from equation 67 into equations 64 and 65 will give the true surface area at each range bin, provided that the visible elements are representative of those obscured. If there is any preferential arrangement of elements along a lidar beam (a tendency to obstruct or fill gaps) or great heterogeneity in the angular distribution this correction will lead to inaccurate estimates. The apparent reflectance then becomes;

$$\eta = \frac{1}{A_f P_{gap}}\left(\rho_l \oint \cos^2 \alpha_l dA_{ls} + \rho_w \oint \cos^2 \alpha_w dA_{ws}\right) \tag{69}$$

The solution of equation 62 requires a model to relate an element's surface area to its angle of incidence and view zenith. Cauchy's theorem (Lang 1991) could be used to measure the surface area of any convex shape from the gap fraction over all possible view angles, but this would require

an initial inversion to get the gap fractions over all angles in the first place. Instead a leaf angle distribution model can be used to perform the inversion in a single step.

Some popular models for leaf angle distributions were introduced in section 2.1.1. Whilst the beta distribution (Goel and Strebel 1984) appears to give the better representation of many canopies, it requires knowledge of the mean angle of incidence and variance, requiring measurements from all angles of incidence or else another measure to calibrate against. Unless a canopy is assumed to be homogeneous (which some claim to be inappropriate (Wilson 1959)) this would require measurements from all angles and so may not always be possible. Therefore a simpler model that can cope with gaps in the data should be used, such as a single parameter model.

Of these single parameter models the spheroidal distribution of Campbell (1986) is the most popular. Appendix C shows that, except in the special spherical case, the integral in equation 69 of such a model does not lead to a simple analytical solution and we must resort to computationally expensive numeric integration (which can be pre-computed and stored in a table) or an approximation. The choice of model is critical to the accuracy of inverted parameters.

6.4.1 Voxels

To get explicit multi-angular measurements of any part of canopy overlapping scans from different locations are needed. Processing of multiple scans requires all range bins to be matched up, which will be at different ranges and so of different sizes. The only way to match up the different range bins is to group them into volumetric pixels or "voxels", illustrated by figure 143. This is similar to the approach used in DART (Gastellu-Etchegorry *et al.* 1996) and has been applied to discrete return terrestrial lidar with some success (Hosoi and Omasa 2006).

The richness of overlapping Echidna scans would allow a DART style model to be inverted with far fewer assumptions than is necessary to invert from current remote sensing data (Gastellu-Etchegorry *et al.* 2004). Current estimates of complex models, such as DART and GORT (Ni-Meister *et al.* 2001), require an assumption of canopy form (basic shape and some dimensions, although lidar can provide height), whilst an inversion of Echidna will need a few assumptions to describe the optical properties of individual scattering elements (bidirectional reflectance and transmittance spectra), none are needed for the structure.

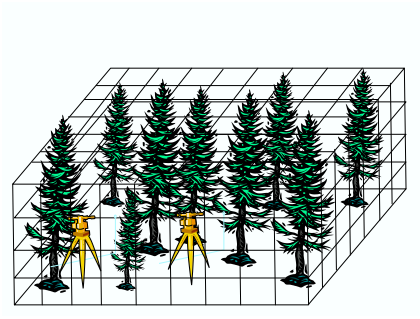

Figure 143: Illustration of a forest divided into voxels

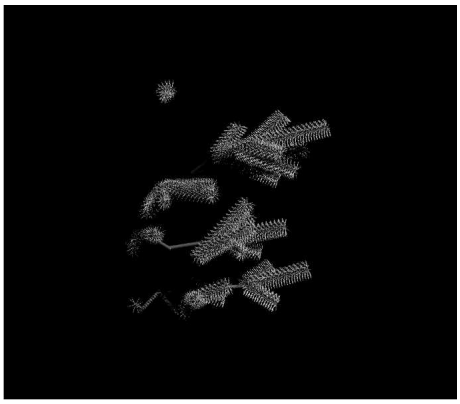

Figure 144: Image of a section of Sitka spruce canopy

6.4.2 Small scale leaf angle distribution

The models discussed in section 2.1.1 were derived from direct digitisation of whole plants or else stand scale transmission measurements. The voxel method looks at a much finer scale than these traditional methods, so to explore the angular distribution at these smaller scales cubes of different sizes (from sides of 12.5cm to 1m) of canopy elements were extracted from Sitka spruce and birch canopies. Simulated lidar measurements were made of this cube from all angles, both zenith and azimuth, to explore the heterogeneity of apparent reflectance, gap fraction and visible surface area; a process impossible in reality.

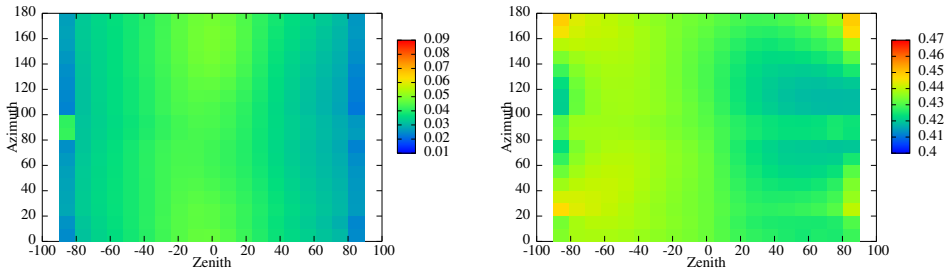

(a) Apparent reflectance against view angle

(b) Apparent reflectance per unit projected area against view angle

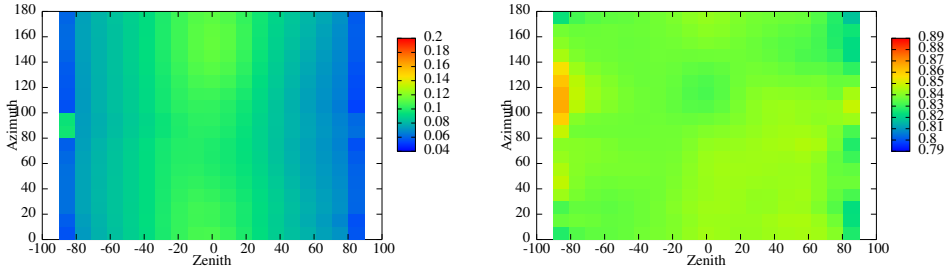

(c) Projected area against view angle

(d) Fraction of leaf against view angle

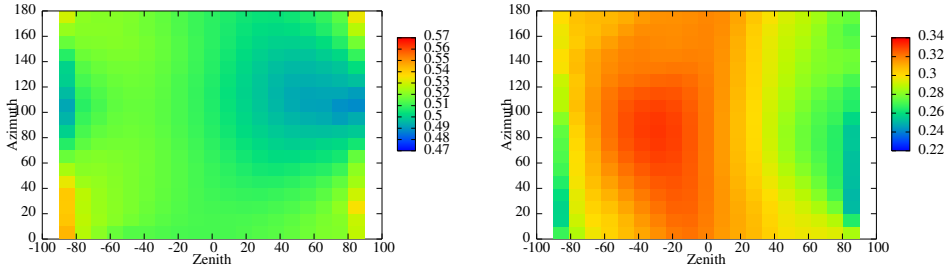

(e) Ratio of visible surface area to projected area

(f) Ratio of visible to true surface area

Figure 145: Lidar results from the section of Sitka spruce canopy shown in figure 144

Sitka spruce Figure 145 shows the apparent reflectance along with projected and surface areas from different view directions for a section of Sitka spruce canopy.

From figure 145(a) it can be seen that the apparent reflectance varied dramatically with view direction, however if the projected area is taken into account (as in figure 145(b)) this variation was greatly reduced. There was very little variation with azimuth, supporting many authors' assumption (Strebel *et al.* 1985, Weiss *et al.* 2004). The proportion of leaf was fairly constant with view direction, leaf dominating at all angles (figure 145(d)).

The ratio of visible surface area to projected area was also reasonably constant with view direction (figure 145(e)), varying between 0.48 and 0.56. There was some variation with azimuth, but as the range was so small this may be negligible. The ratio of visible surface area to actual surface area, the factor that would be taken into account by Beer-Lambert law, varied with zenith, from 0.11 to 0.19 but showed little variation in azimuth.

To see if these effects are general the above simulations were repeated for a number of sections of canopy from different trees. The data was reduced to a variance in zenith and azimuth and these results are shown in figure 146. These results suggest that whilst the assumption of azimuthal symmetry is not perfect, any variation was small (though not entirely negligible) compared to zenithal variance. For the rest of this thesis azimuthal symmetry will be assumed.

All single parameter angular distribution models assume that the angular distribution is symmetric about the vertical axis, so the visible surface area must be constant from all view directions. Of course the projected area and phase function will change, but the visible area must always be half of the total surface area. Real canopy sections will suffer from some occlusion, so the visible surface area will not be half the total surface area, but for the models to work well the ratio should be reasonably constant.

Figure 147 shows the ratio of visible surface area to total surface area for sections of canopy from different trees and locations within trees. The plot shown in figure 147(b) was by far the most common shape, the others are shown to give an idea of the behaviour in all situations. There did not seem to be any relationship between the size of a canopy section and the variance of visible surface area, nor with the location within the canopy. This difference in visible area must be

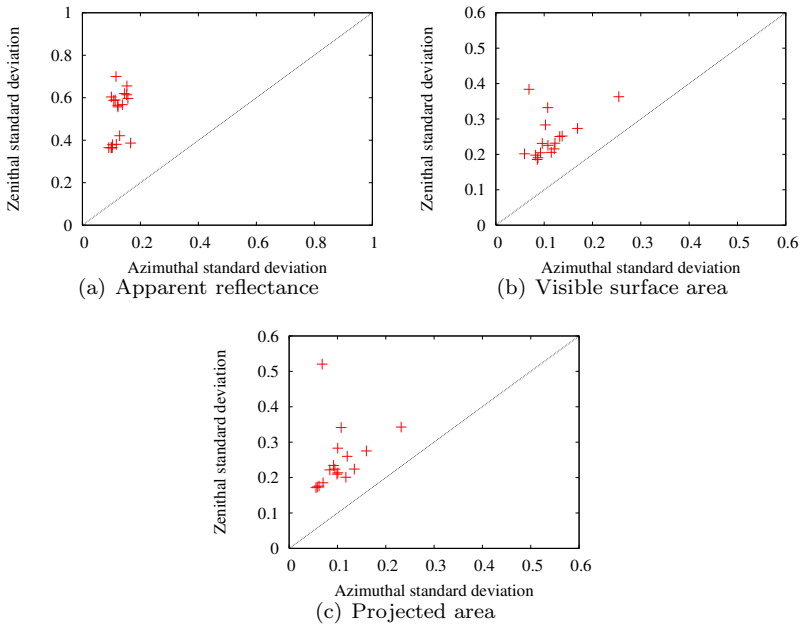

(a) Apparent reflectance (b) Visible surface area

(c) Projected area

Figure 146: Variance in azimuth and zenith for Echidna scans of a number of sections of Sitka spruce canopy

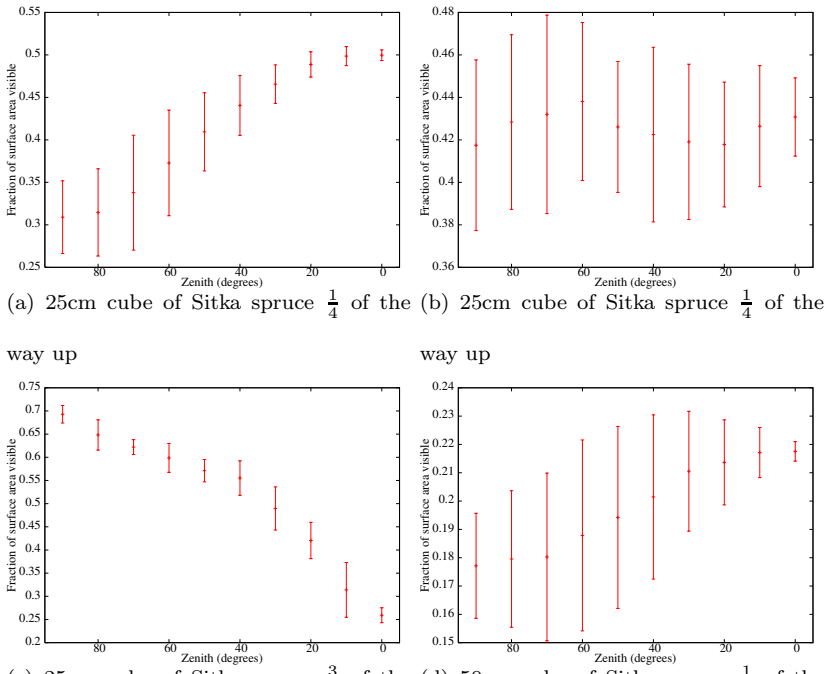

(a) 25cm cube of Sitka spruce $\frac{1}{4}$ of the way up

(b) 25cm cube of Sitka spruce $\frac{1}{4}$ of the way up

(c) 25cm cube of Sitka spruce $\frac{3}{4}$ of the way up

(d) 50cm cube of Sitka spruce $\frac{1}{4}$ of the way up

Figure 147: Fraction of surface area visible against zenith angle for a number of sections of Sitka spruce canopy

entirely due to heterogeneity of the distribution of scattering elements.

The section of canopy that led to figure 147(c) was at the top of the tree and contained a single shoot pointing near vertical. Therefore it looked the same from all azimuths (leading to a low variance) and had an increasing visible area with zenith. Whilst every coniferous tree top is likely to have a single shoot pointing upwards, this will contain a very small proportion of the canopy's total LAI. Most will be in shoots lower in the canopy, where branches tend to lie horizontally, therefore figure 147(c) can be seen as a unusual case and one need not worry too much about taking it into account.

The section used in figure 147(d) contained many shoots and branches. Most of these tended to lie flat so that when looking horizontally shoots in the same branch shadowed each other, the amount of shadowing depending upon the relative lengths of the different shoots and azimuth angle. This explains the large variance with azimuth near the horizontal and the increasing visible area with zenith.

Much like the section used in figure 147(d), that for figure 147(a) contained many shoots and branches, the majority tending to lie horizontally and in the same plane. Therefore there was more shadowing at near horizontal view directions and so the visible area increased with decreasing zenith.

The section used in figure 147(b) contained a small cluster of shoots with no preferential alignment or layering. There was an equal amount of shadowing from all view directions. In the sections tested (which were picked at random from within a number of tree canopies so can be taken as representative) this was by far the most common case, therefore it would seem to be reasonable to assume that the visible surface area is constant with view angle and so a rotationally symmetric single, parameter model can be used. Care should be taken to ensure that all voxels contain sufficient scattering elements for this assumption to hold, therefore slightly larger voxels might be preferable.

The ratio of the visible surface area to the total surface area will be needed to scale between measured surface area and LAI. Traditional transmission techniques do this with the Beer-Lambert law, but this may not apply at these small scales. For the sections tested here it would appear to

be between $\frac{1}{5}$ and $\frac{2}{5}$, but this will be explored in more detail later, once the visible surface area has been successfully measured.

Birch Birch canopy elements have a very different angular distribution to Sitka spruce elements and may show different behaviour with view direction. The above experiments were repeated using the section of birch canopy shown in figure 148.

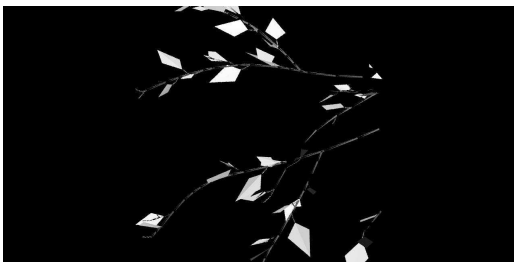

Figure 148: Image of a 25cm cube of birch canopy

Figure 149 shows that properties for birch had even less dependence on azimuth than they did for Sitka spruce. There was the same large variation in apparent reflectance with view zenith (figure 149(a)) and this was greatly reduced by accounting for projected area, though not entirely (figure 149(b)). Leaf dominated for all view angles (figure 149(d)), but not to quite the same extent as for Sitka spruce. In the Sitka spruce section leaves made up over 80% of surface area from all view directions whilst for birch this could drop to 74%; the difference may be caused by Sitka spruce needles' tendency to clump around and so obscure branches.

The ratio of projected area to visible surface surface area showed much more dramatic variation than for Sitka spruce (figure 149(e)) suggesting that the angular distribution of elements was far less uniform for broadleaved than for the coniferous trees. This is not unsurprising as in broadleaved canopies, leaves do not spiral around branches and so do not point is anything like as many directions as conifer needles. For this section, elements appear to have a planophile arrangement.

Significantly the fraction of surface area that was visible was near unity for all view angles (figure 149(f)); for Sitka spruce this fraction did not rise above a fifth. This shows that there is far less self shadowing in broadleaved canopies and so no correction factor will be needed to scale between visible surface area and true LAI. That the fraction appeared to rise above unity

(figure 149(f)) was due to rounding issues between the various programs used to extract the information. This was a small error (only significant to two decimal places) and so should not affect the validity of the conclusions and so the extra effort needed to allow the programs to store more significant figures was not expended.

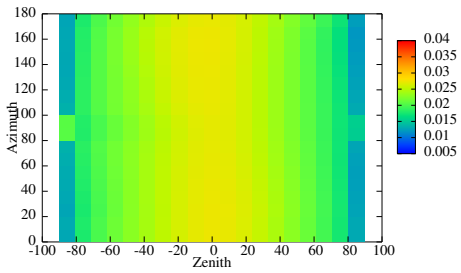

(a) Apparent reflectance against view angle

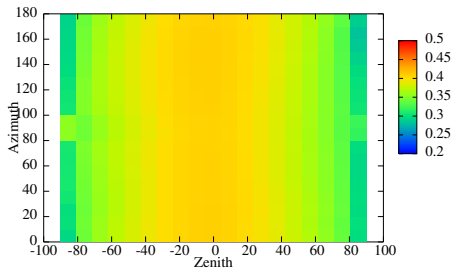

(b) Apparent reflectance per unit projected area against view angle

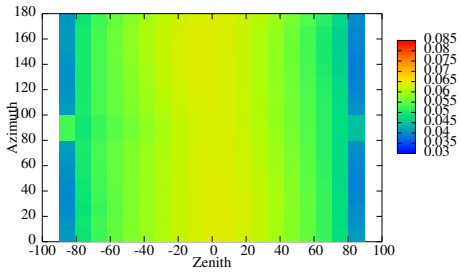

(c) Projected area against view angle

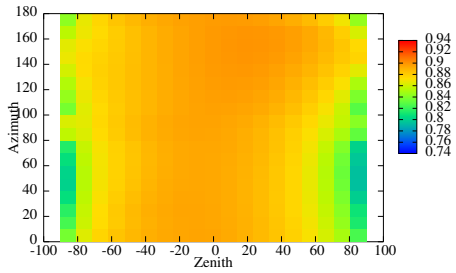

(d) Fraction of leaf against view angle

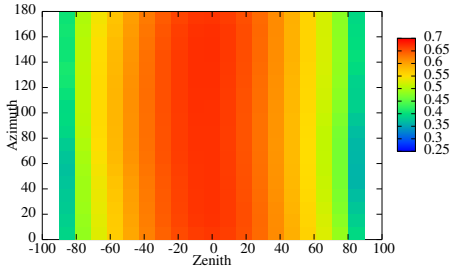

(e) Ratio of projected area to visible surface area

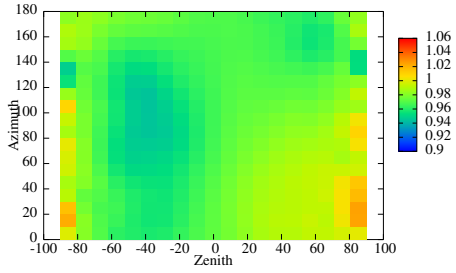

(f) Ratio of visible to true surface area

Figure 149: Lidar results for the section of birch canopy shown in figure 148

To make sure that the independence to azimuth shown in figure 149 was a general property of birch canopies the above analysis was repeated for all available birch canopy sections and the variance in zenith and azimuth calculated. Figure 150 shows that it was indeed a general property and so azimuth dependence can be discounted for the rest of this thesis.

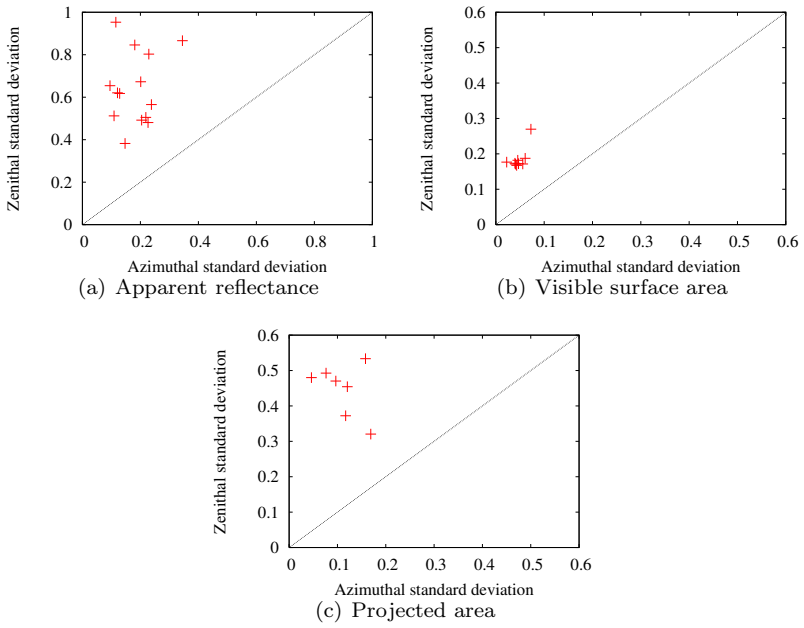

(a) Apparent reflectance (b) Visible surface area

(c) Projected area

Figure 150: Variance in azimuth and zenith for Echidna scans of a number of sections of birch canopy

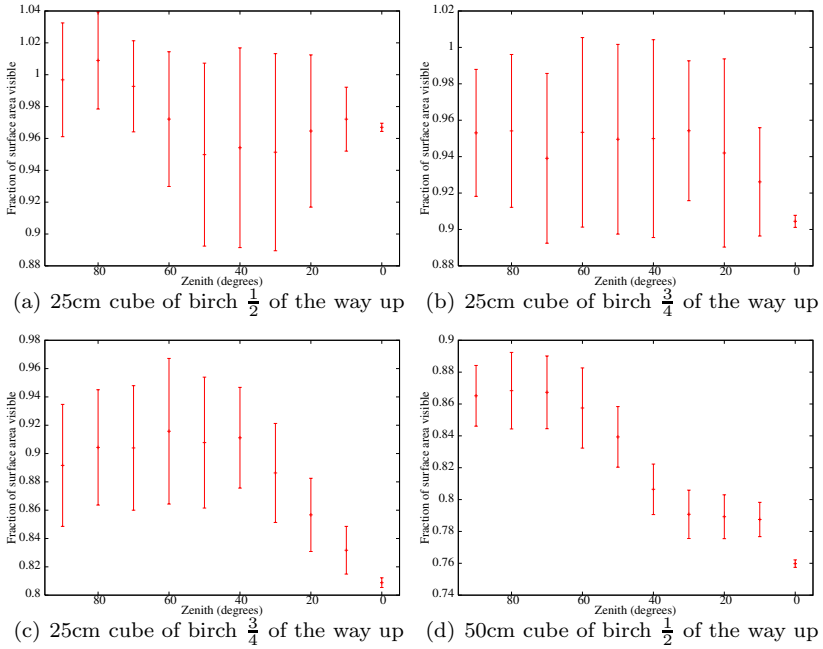

(a) 25cm cube of birch $\frac{1}{2}$ of the way up (b) 25cm cube of birch $\frac{3}{4}$ of the way up

(c) 25cm cube of birch $\frac{3}{4}$ of the way up (d) 50cm cube of birch $\frac{1}{2}$ of the way up

Figure 151: Fraction of surface area visible against zenith angle for a number of sections of birch canopy

Figure 151 shows that the fraction of surface area visible was fairly constant with view direction, suggesting that rotationally symmetric angular distribution models can be used. Note that the larger section of canopy (figure 151(d), a cube with sides of 50cm) shows slightly more self shadowing than the smaller sections. This is not surprising as the more elements a section contains the more likely they are to shadow each other. So whilst voxels should be made large enough to ensure that the contents obey any angular distribution assumptions, the larger they are the greater the correction factor needed to scale between visible and total surface area will be.

6.4.3 Choice of LAD model

Having determined that a rotationally symmetric, single parameter model is acceptable for these small scale measurements, one must be chosen. Ideally a model which can explain both the apparent reflectance and the projected area (and so the phase function and gap fraction) and relate both of these to the visible surface area or, if possible, total surface area.

Results for voxels with sides of 12.5cm were very heterogeneous. Such small voxels contain only a few elements and so the resulting behaviour is very hard to model. 25cm sided voxels would seem to be the minimum size that is well behaved enough to allow reliable modelling.

Sitka spruce The apparent reflectance, fraction of surface area projected and phase function were calculated in all view directions for each canopy section. The results area shown in figure 152, 153 and 154 respectively with error bars showing the azimuthal standard deviation.

The phase function showed a far smaller relative range than the other properties, suggesting that the projected area is the dominant factor in apparent reflectance. For sections containing more elements the phase function was near uniform (figures 160(b) and 160(d)) and so the assumption of Jupp *et al.* (2009) may be appropriate.

The only information available to constrain the surface area, angular distribution and phase function is the apparent reflectance with view angle. The simplest way would be to empirically fit values to these observations, say $\Gamma = 0.85$ and some simple form for $G(\theta)$, allowing a direct conversion from apparent reflectance over a range of angles to leaf area and angular distribution. This will not be physically based and would need site and species specific calibration to set Γ,

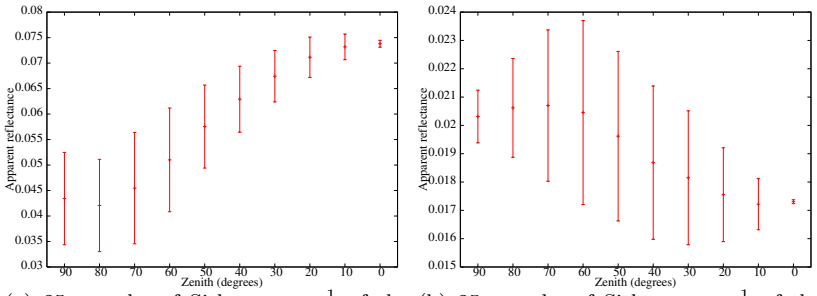

(a) 25cm cube of Sitka spruce $\frac{1}{4}$ of the way up

(b) 25cm cube of Sitka spruce $\frac{1}{4}$ of the way up

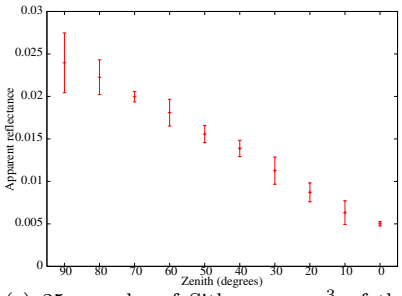

(c) 25cm cube of Sitka spruce $\frac{3}{4}$ of the way up

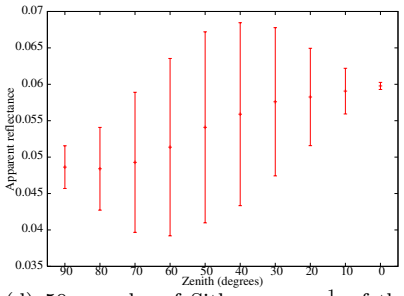

(d) 50cm cube of Sitka spruce $\frac{1}{4}$ of the way up

Figure 152: Apparent reflectance against view zenith for a number of sections of Sitka spruce canopy

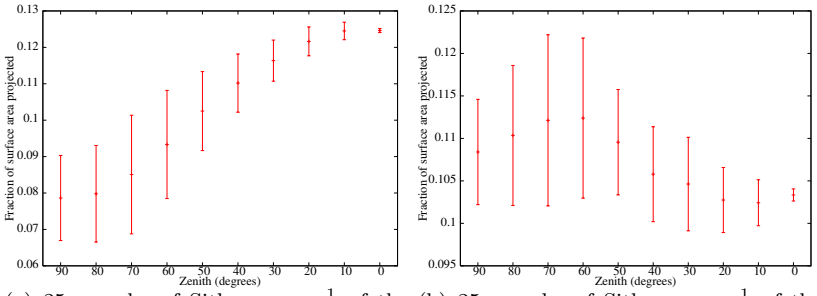

(a) 25cm cube of Sitka spruce $\frac{1}{4}$ of the way up

(b) 25cm cube of Sitka spruce $\frac{1}{4}$ of the way up

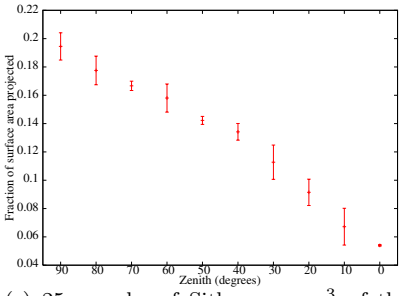

(c) 25cm cube of Sitka spruce $\frac{3}{4}$ of the way up

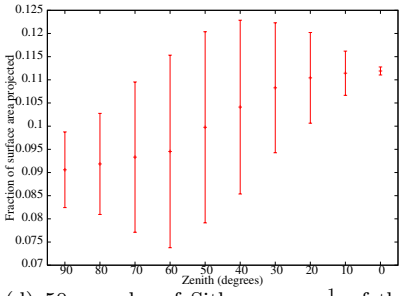

(d) 50cm cube of Sitka spruce $\frac{1}{4}$ of the way up

Figure 153: Fraction of surface area projected against view zenith for a number of sections of Sitka spruce canopy

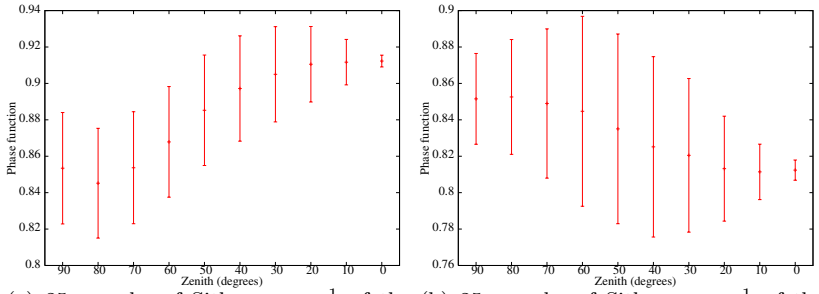

(a) 25cm cube of Sitka spruce $\frac{1}{4}$ of the way up

(b) 25cm cube of Sitka spruce $\frac{1}{4}$ of the way up

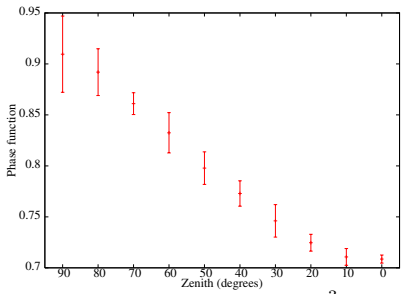

(c) 25cm cube of Sitka spruce $\frac{3}{4}$ of the way up

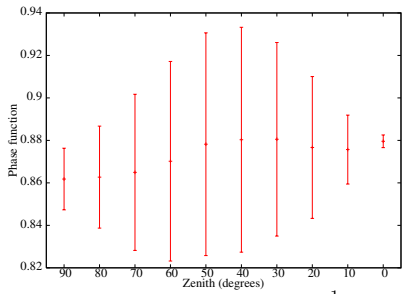

(d) 50cm cube of Sitka spruce $\frac{1}{4}$ of the way up

Figure 154: Phase function against view zenith for a number of sections of Sitka spruce canopy

assuming that it is view angle independent for all species, but it will be a good first attempt to directly link LAI to Echidna measurements.

Birch For broadleaved forests the apparent reflectance against view zenith (figure 155) showed a very similar shape for all canopy sections tested; near sinusoidal with a minimum at the horizontal.

Examining the projected area (figure 156) and phase function (figure 157) with zenith shows that the variation in apparent reflectance was a result of both, with neither showing any clear dominance. This suggests that it may be possible to describe both the projected area and phase function with a single angular distribution model.

It is not so surprising that this should be the case for birch and not for Sitka spruce. In these birch sections there was very little self shadowing so that the same surfaces are visible from all view directions and so, if all scattering elements are Lambertian, equations 69 and 65 can be used to describe both the apparent reflectance and projected area. For the Sitka spruce sections self shadowing means that the actual surfaces being observed will be different from every direction. Due to the spiralling nature of needle shoots the phase function will appear very similar from all

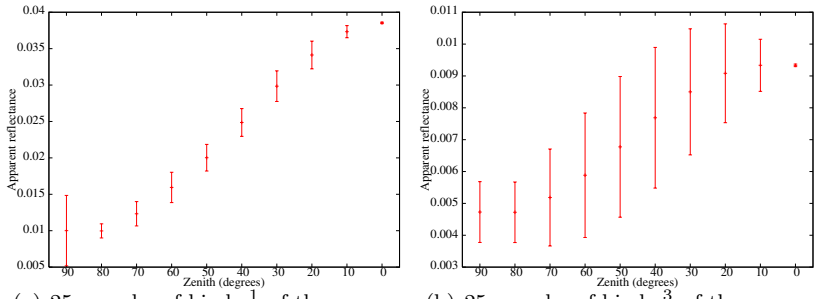

(a) 25cm cube of birch $\frac{1}{2}$ of the way up

(b) 25cm cube of birch $\frac{3}{4}$ of the way up

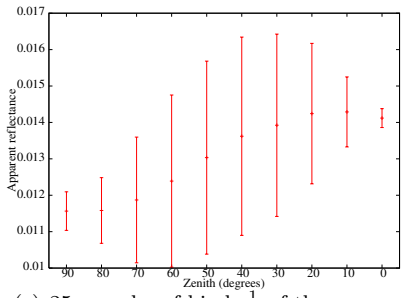

(c) 25cm cube of birch $\frac{1}{2}$ of the way up

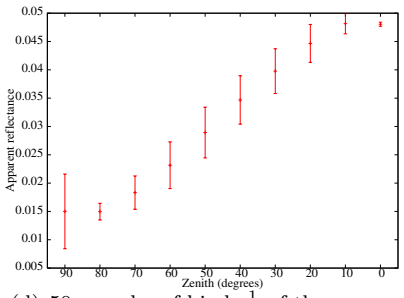

(d) 50cm cube of birch $\frac{1}{2}$ of the way up

Figure 155: Apparent reflectance against zenith angle for a number of sections of birch canopy

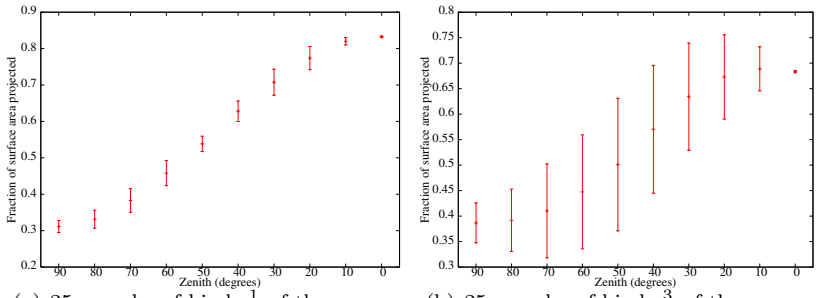

(a) 25cm cube of birch $\frac{1}{2}$ of the way up

(b) 25cm cube of birch $\frac{3}{4}$ of the way up

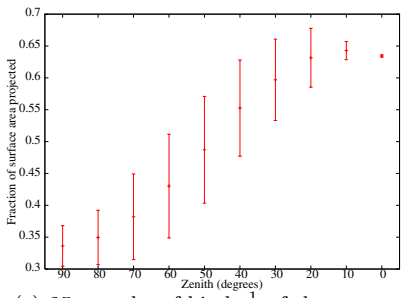

(c) 25cm cube of birch $\frac{1}{2}$ of the way up

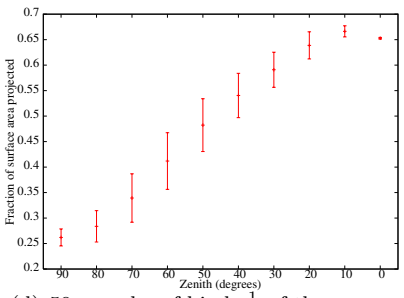

(d) 50cm cube of birch $\frac{1}{2}$ of the way up

Figure 156: Fraction of surface area visible against zenith angle for a number of sections of birch canopy

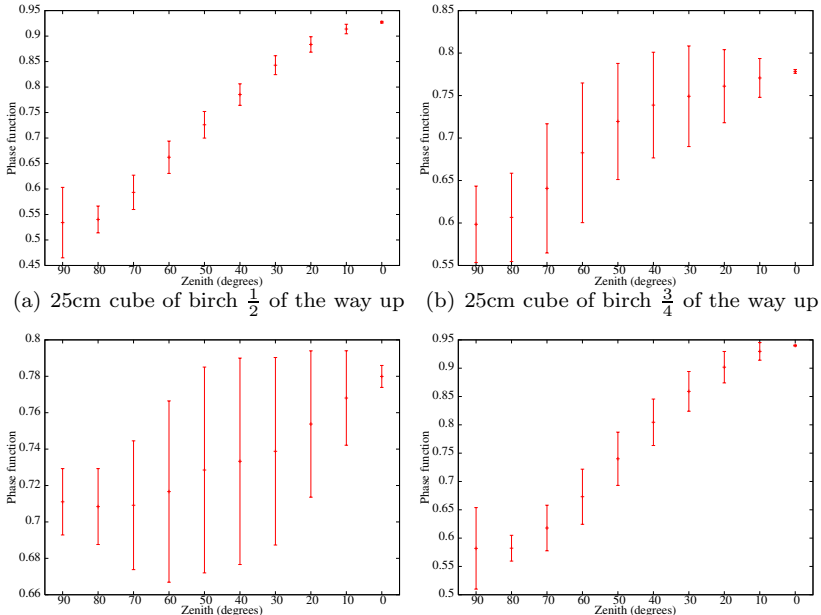

(a) 25cm cube of birch $\frac{1}{2}$ of the way up (b) 25cm cube of birch $\frac{3}{4}$ of the way up

(c) 25cm cube of birch $\frac{1}{2}$ of the way up (d) 50cm cube of birch $\frac{1}{2}$ of the way up

Figure 157: Phase function against zenith angle for a number of sections of birch canopy

view directions whilst the projected area will depend upon the arrangement and self shadowing of objects.

Comparing the above graphs for projected area and phase function to the values predicted by the spheroidal model (Campbell 1986), introduced in section 2.1.1 and derived from equation 3 (shown in figures 158 and 159) suggests that this may be able to describe both effects. These canopy sections are similar to very oblate spheroids and both sets agree that for a given eccentricity, the projected area will vary over a larger range than the phase function, with a narrowing of the range at the hinge point of 54.75^o.

6.4.4 LAD model choice conclusions

It may be necessary to use different models to describe Sitka spruce and birch as assuming a constant phase function will clearly not be appropriate for broadleaved forests. For canopies that are likely to contain many scattering elements, all shadowing each other, a constant phase function can be assumed (the value of which will be species specific) and a simple angular distribution model can be used. For canopies which are unlikely to self shadow within a voxel, the same simple angular distribution model can be used to describe the projected area and the phase function. An

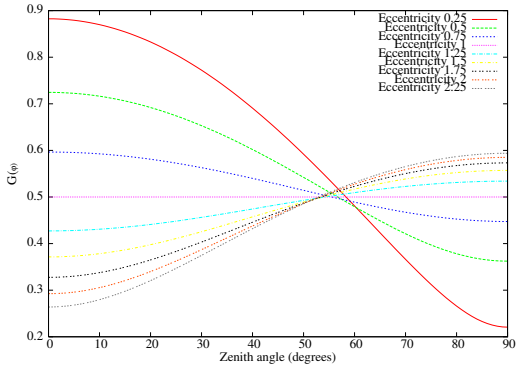

Figure 158: Ratio of projected area to surface area, or $G(\theta)$ against zenith for Lambertian spheroids of different eccentricities

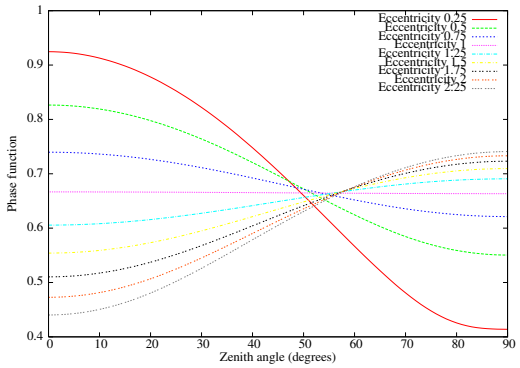

Figure 159: Phase function against view zenith for Lambertian spheroids

average value could be used for Γ, making the G function effective, but figure 157 suggests there would be too much variation within a canopy to use this to predict gap fraction with view angle.

For canopies without significant self shadowing the spheroidal distribution (Campbell 1986), or a more computational efficient approximation (Jupp *et al.* 2009), would seem to be capable of predicting both the projected area and phase function.

6.5 Self shadowing canopies

For canopies that suffer from self-shadowing within a voxel, the apparent reflectance is given by;

$$\eta = \rho_e \Gamma G(\theta) \frac{A_s}{A_f} \tag{70}$$

At first it will be assumed that both ρ_e and Γ are known so that we need only solve for $A_s G(\theta)$. Measurements of apparent reflectance may only be available over a limited range of angles so Cauchy's theorem cannot be used to extract A_s (Lang 1991). As has already been mentioned, much of the total surface area within a voxel will be obscured and as $G(\theta)$ describes the fraction of visible surface area projected in a given direction, the angular distribution model should be chosen to fit the visible area rather than the total area.

Figure 160 shows the fraction of visible surface projected in a given direction. Normalising by the visible surface area has removed much of the variation, suggesting that the small changes in visible surface area, shown in figure 147, may be very important for some sections of canopy.

Figure 160 suggests that the Ross-G function can be modelled as a straight line, a relationship of the form;

$$G(\theta) = m\theta + c \tag{71}$$

Where m is the gradient and c the y axis intercept. That the cross over point holds for these realistic canopy sections is surprising as it is a property of simple convex shapes such as frustums and spheroids and takes no account of self shadowing at all. It is certainly a great advantage in the quest for a simple, physically based model. To verify the cross over point the G function was calculated for all canopy sections and plotted on a single graph.

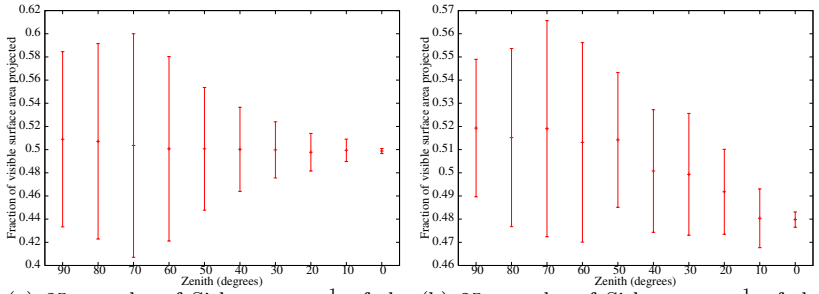

(a) 25cm cube of Sitka spruce $\frac{1}{4}$ of the way up

(b) 25cm cube of Sitka spruce $\frac{1}{4}$ of the way up

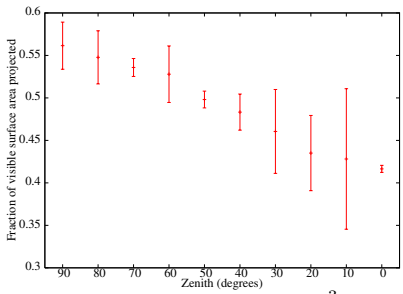

(c) 25cm cube of Sitka spruce $\frac{3}{4}$ of the way up

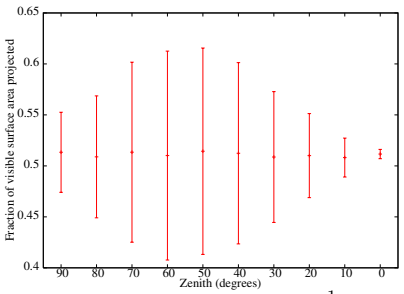

(d) 50cm cube of Sitka spruce $\frac{1}{4}$ of the way up

Figure 160: Fraction of visible area projected against zenith angle zenith for a number of sections of Sitka spruce canopy

Comparing the results for all sections (figure 161) suggests that the cross over point found for simple frustum models (Wilson 1960) holds. Though it is far from perfect there is a hint of a decrease in variation around 55^o zenith. This could provide a known tie in point, reducing the two parameter straight line equation to a single parameter model.

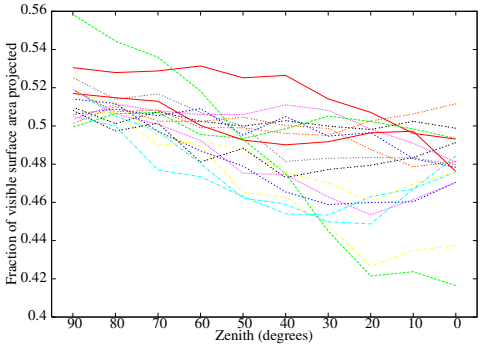

Figure 161: Ross G function against view zenith for all Sitka spruce canopy sections. The colours have no significance and are included for legibility

The cross over point in figure 161 is a little too poorly defined to pick a value for the fraction

of area projected or the cross over angle, so it was taken from an idealised spheroidal case, appendix C.3 figure 184, so that at a zenith angle of 54.75^o the projected area is 0.5 of the visible surface area.

Forcing the straight line in equation 71 through the cross over point ($\theta_c = 54.75^o$) gives the single parameter leaf angle distribution;

$$G(\theta) = m(\theta - \theta_c) + \frac{1}{2} \tag{72}$$

The apparent reflectance than becomes;

$$\eta = \rho_e \Gamma \frac{A_s}{A_f} \left(m(\theta - \theta_c) + \frac{1}{2} \right) \tag{73}$$

Plotting η against θ and fitting a line of best fit will allow the two unknowns, m and A_s to be determined. For a straight line with a gradient $\frac{d\eta}{d\theta}$ and y intercept, $\eta(0)$, the surface area is;

$$A_s = \frac{2}{\rho_e \Gamma} \left(\eta(0) + \frac{d\eta}{d\theta} \theta_c \right) \tag{74}$$

The spread of values around the hinge point is caused by the variation in the visible surface area with view direction and it may even be possible to use it to determine the amount of self shadowing within a voxel. Alternately the y intercept could be allowed to vary, changing it to a two parameter LAD model. Neither of these models will be attempted here and the spread and resulting errors will have to be accepted.

Even though the Ross G function is near linear, the apparent reflectance is not, due in part to other factors. Therefore it may be necessary to use a form for $G(\theta)$ that can take these into account; an effective G function. Looking at the graphs of apparent reflectance against zenith angle they appear to follow a sinusoidal shape with a period of π. This suggests a Ross G function of the form;

$$G(\theta) = m \cos 2\theta + c \tag{75}$$

Which is still linear in terms of $\cos 2\theta$. This can be forced through the cross over point to give;

$$G(\theta) = m(\cos 2\theta - \cos 2\theta_c) + \frac{1}{2} \tag{76}$$

and so surface area is given by;

$$A_s = \frac{2}{\rho_e \Gamma} \left(\eta(0) + \frac{d\eta}{d \cos 2\theta} \cos 2\theta_c \right) \tag{77}$$

The angular distribution parameter, m, is given by;

$$m = \frac{1}{\rho_e \Gamma A_s} \frac{d\eta}{d \cos 2\theta} \tag{78}$$

Both of these models will be tested, acknowledging that neither is physically based and the sinusoidal model will take more than just the G function into account. This should provide a better fit but may hide physical effects.

The model of Jupp *et al.* (2009), given by equation 55, is similar to the form in equation 76 except that it has a period of 2π rather than π. Thus it will provide a better fit for extremophile canopies, where all elements are near horizontal or near vertical, but the version in equation 76 will give a better fit for angular distributions in between (compare figures 3 and 158). Even the G functions of most extreme canopies tested here flattened off around nadir and the horizontal, suggesting that the less extreme equation would be more suitable.

6.5.1 Simple Echidna inversion model

The model for the leaf angle distribution given in equation 76 was used to extract LAI and LAD from overlapping Echidna scans. Multi-spectral lidar was be used to determine the fractions of leaf and wood, assuming that the two materials have the same phase function and angular distribution and different reflectances in the two bands. This may not be an entirely appropriate assumption, but as has been shown in the above section, leaves tend to dominate the signal and so the amount of wood will be insignificant. For areas without leaves the wood area may be incorrectly determined, but that would be best determined by point cloud based volume finding methods rather than these radiance inversions.

The proportion of surface area made up from leaf can be found from the apparent reflectance at two wavelengths, η_λ and η_ω which have different ratios for the reflectance of leaf, $\rho_{\lambda,l}$ and wood, $\rho_{\lambda,w}$. Figure 162 shows a false colour image of simulated dual wavelength scan of a forest (green is 1064nm, red and blue 532nm), demonstrating that it should be possible to separate leaf from bark.

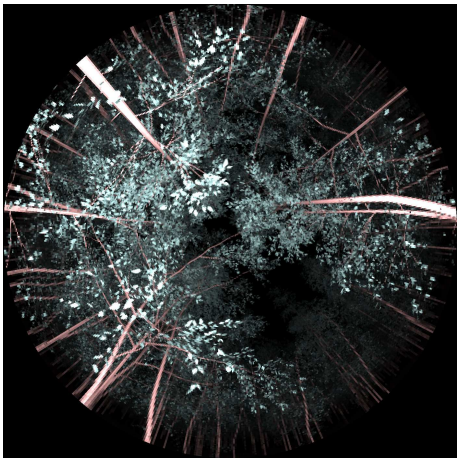

Figure 162: False colour image of a dual wavelength Echidna simulation

The woody correction factor can be found by substituting in equation 66 into equation 79 and solving simultaneously.

$$\eta_\lambda = \frac{1}{A_f}\Gamma G(\theta)(\rho_{\lambda,l}A_l + \rho_{\lambda,w}A_w) \tag{79}$$

to give;

$$\Psi = \frac{\eta_\omega \rho_{b,\lambda} + \eta_\lambda \rho_{b,\omega}}{\eta_\lambda(\rho_{l,\omega} - \rho_{b,\omega}) + \eta_\omega(\rho_{b,\lambda} - \rho_{b,\omega})} \tag{80}$$

Apparent reflectance was plotted against either zenith angle, θ or $\cos 2\theta$ and the gradient and y intercept of a line of best fit determined. The leaf proportion, Ψ was used to mix the known leaf and wood reflectances to get the canopy reflectance. This was combined with the known phase factor, Γ, to extract surface area and angular distribution equations 77 and 78.

6.5.2 Inversion of a voxel

The inversion method was tested on a small section of canopy. This removed the extra complication of attenuation of the signal by elements in other voxels. Initially this was run with twenty scans from different angles, picked randomly from between -90^o to +90^o zenith and 0^o to 180^o azimuth. This would be an unrealistic number to collect in the field but it will show whether the method works.

Using the section of canopy shown in figure 163, a section which was not used to derive the phase factor, it was determined that all scattering elements have an average visible surface area over all viewing directions of 386cm^2. Figure 164(b) shows that this varied with view zenith, but in a sinusoidal manner and so may be taken into account in the G function parameters (which will be effective).

Inverting surface area with the above method and a linear G function predicted a total area of 345cm^2, an error of only 11%, a far higher accuracy than is reported with traditional transmission methods. That the error was small shows that the changing fraction of visible surface area was taken into account in the G function factors, and it seems to have coped well with the deviation from the assumptions. Using the sinusoidal form of the G function gave an area of 328cm^2; an error of 15%, therefore in this case the linear form for the G function appears to be more appropriate. More sections of canopy should be tested before either model can be discarded.

This section of canopy had a total surface area of 923cm^2, so only 37% of the actual surface area was visible and a way to scale between these two is still needed to extract LAI.

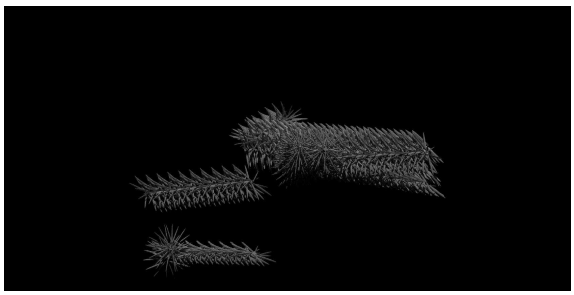

Figure 163: Image of a section of Sitka spruce forest

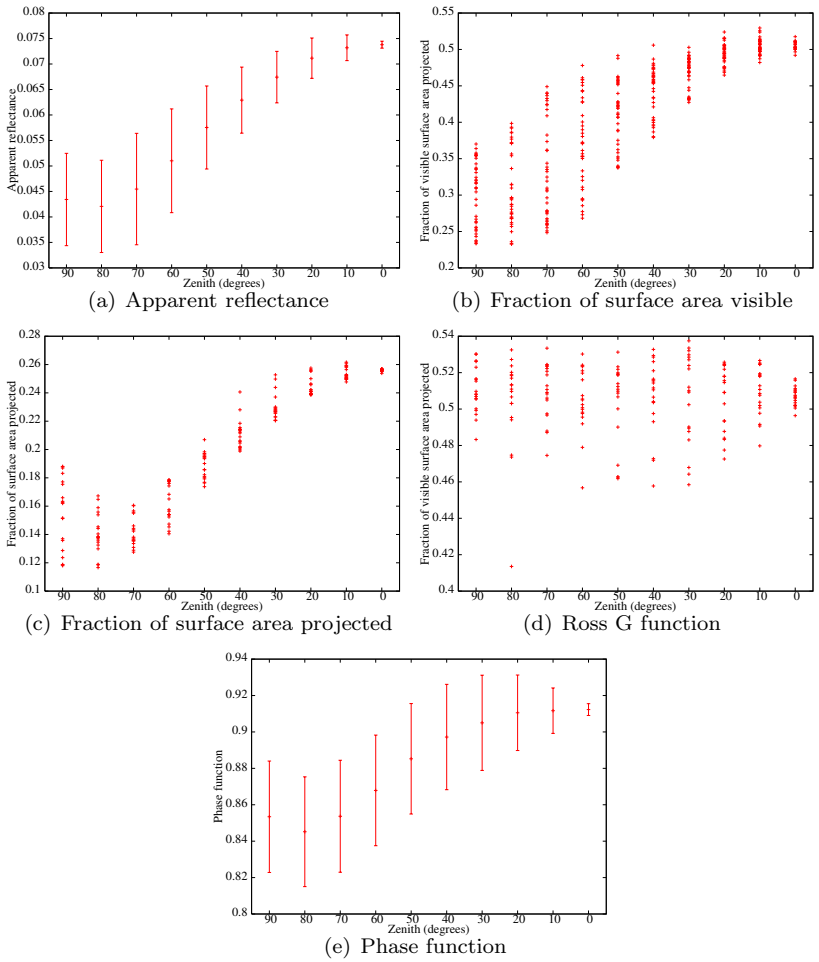

(a) Apparent reflectance

(b) Fraction of surface area visible

(c) Fraction of surface area projected

(d) Ross G function

(e) Phase function

Figure 164: Properties of the section of canopy shown in figure 163

6.5.3 Woody correction

These areas are for all scattering surfaces, separating into leaf and bark revealed visible surface areas of 364cm^2 of leaf and 22cm^2 of bark whilst the total surface areas were 877cm^2 of leaf and 46cm^2 of bark. Inverting these with dual wavelength lidar (1064nm and 532nm) gave estimated surface areas of 168cm^2 of leaf and 153cm^2 of bark. So whilst the total surface area has only a 16% error, the estimated LAI has a 54% error, a large level of uncertainty, though no worse than current transmission methods (Chen and Cihlar 1996). This failure to separate leaf and bark could have been caused by differences in the phase function of the two materials (they were assumed equal in the derivation of equation 80) or by multiple scattering contributions.

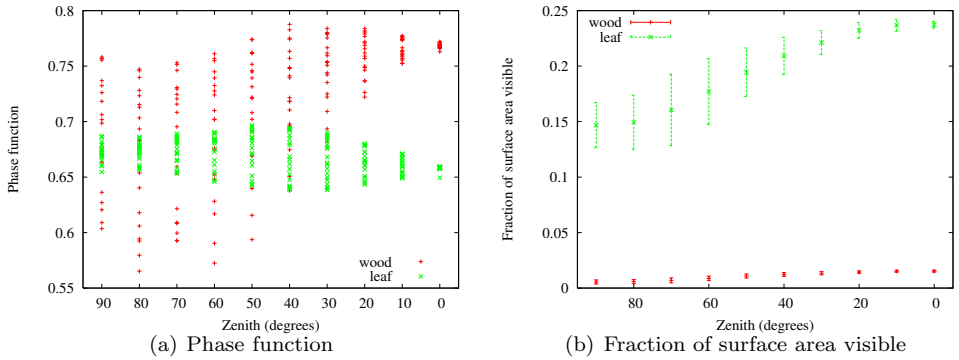

(a) Phase function

(b) Fraction of surface area visible

(c) Ross G function

Figure 165: Properties of a section of Sitka spruce, separated by material

From the phase functions for leaf and wood, shown in figure 165, it is apparent that the phase of wood was a little higher than that of leaves, which is what would be expected as woody objects tend to be large, reasonably flat shapes rather than many small elements for leaf. Wood's phase function also showed much more dependence on view zenith than leaf, again this is most probably because the wood is made up of a few relatively large (compared to the needles) twigs which lie

flat whereas the needles spiral around and so are more uniform with view angle.

Figure 165(c) shows that the Ross G functions for the two materials were slightly different, with that for leaf being almost flat whilst that for wood has a definite zenith dependence. It may be possible to correct for this effect by using separate leaf and wood angular distributions if it is deemed a limiting factor. The G functions would be effective and so gap fraction predictions may suffer, but any angular variations in phase function will be taken into account.

Whilst the contribution from multiple scattering was small (<2%) it was different for the two wavelengths, altering the relative reflectances and so potentially altering the leaf fraction estimate. The above analysis was repeated without multiple scattering to determine the contribution of this effect to the final error.

Removing multiple scattering altered the estimate of leaf area to 234cm^2 and wood area to 14cm^2, giving the correct proportion (6%), although the total visible surface area was underestimated. This underestimate is because the phase function value; ($\Gamma = 0.85$) was chosen in the presence of multiple scattering and will be slightly lower in its absence. Γ is an effective parameter rather than the true spectral invariant it is supposed to be. If the correct value had been used for Γ without multiple scattering the areas would have been correctly determined.

It would seem that the primary cause of the error in converting PAI to LAI was from the larger multiple scattering contribution to the wavelength at which canopy reflectance was higher (the near infra-red). This could be corrected for by either an enhanced reflectance (including the contribution from multiple scattering) a vastly more complex model or an external woody correction term. Data from different shoot types and scatterer densities are needed to fully understand the scattered contribution and so enhanced reflectance's dependence on canopy structure. This was not carried out as part of the thesis.

6.5.4 Predicting gap fraction

The model has been shown capable of accurately predicting surface area, although it struggles to differentiate leaf from bark. Surface area is the main biophysical parameter of interest, along with its distribution through a canopy. In a real canopy returns from any given voxel may be attenuated by other objects, decreasing the apparent reflectance from that voxel. In order to invert the correct

areas this attenuation must be accounted for by division by the gap fraction up to that point.

This requires that not only the total surface area of each voxel be correctly calculated but the gap fraction with view direction. The gap fraction was measured at a range of view angles, the apparent reflectances from those same directions were used to provide parameters for the above equations and these used to predict gap fraction.

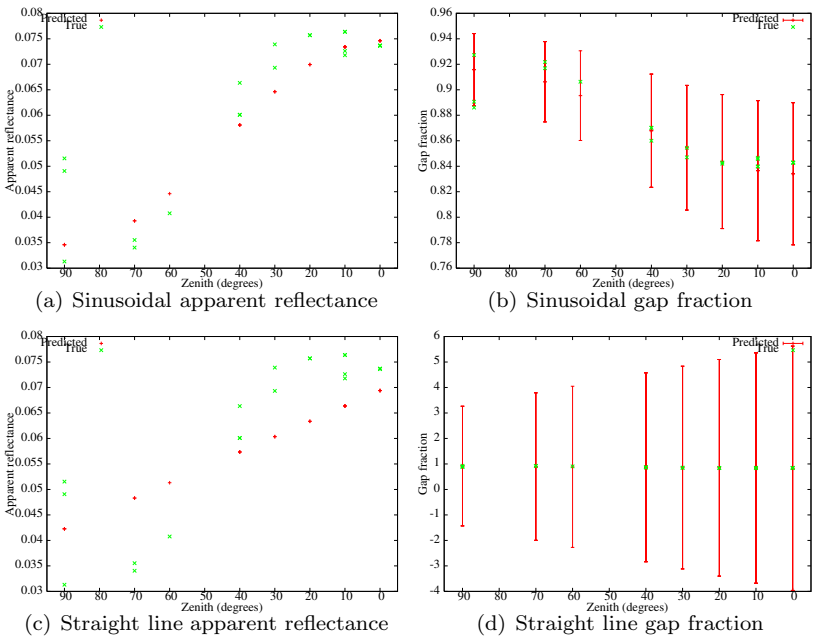

(a) Sinusoidal apparent reflectance (b) Sinusoidal gap fraction

(c) Straight line apparent reflectance (d) Straight line gap fraction

Figure 166: Predicted canopy properties against view zenith using twenty view directions for a section of Sitka spruce

Figure 166 shows that whilst the linear model gave the better prediction of surface area, the sinusoidal model gave better predictions of gap fraction at all angles (except the hinge point where all are forced to agree). Error bars show uncertainty, calculated from the standard deviation returned from the estimated LAD parameters (Press *et al.* 1994, page 665). The surface area estimates will be very sensitive to gap fraction predictions, therefore the sinusoidal model appears to be the most suitable, despite its slightly lower accuracy for surface area. All further analysis will be with this model.

6.5.5 Acceptable number of scans

It would be prohibitively time consuming (though not quite as bad as direct measurement) to collect the twenty separate scans used above and so for the method to be practical it must work with fewer view directions. The above analysis was repeated with different numbers of beams, drawing them at random from the available data (scans were simulated across the whole hemisphere every 10^o) and the error assessed for each set. This was repeated twenty times for each number of scans and the mean error and standard deviation calculated.

Figure 167(a) shows that errors could become very large (and always an underestimate) for small numbers (less than five) of scans. The results suggest that beams from at least nine different view directions would be needed to guarantee an extraction of PAI with better than 80% accuracy. Whilst this seems a large number, beams from each scan location will intersect any voxel at a range of angles. This may mean that the nine beams need not come from nine different locations, perhaps reducing the number to a figure which can easily be collected in around the same time it would take to characterise a site with traditional techniques (tape measure, compass and hemispherical photography) whilst delivering far more information.

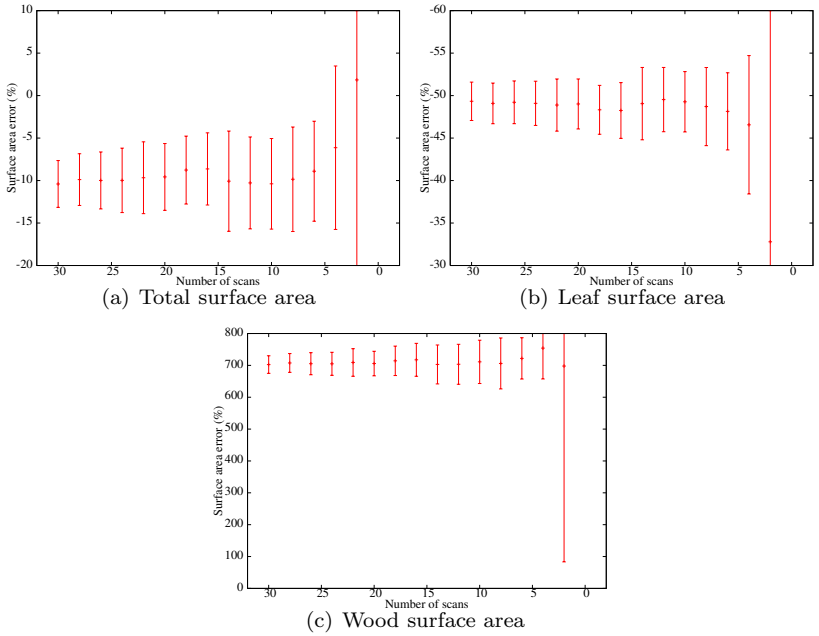

(a) Total surface area (b) Leaf surface area

(c) Wood surface area

Figure 167: Surface area error against number of scans for small sections of Sitka spruce canopy

Figure 168 shows the error against zenith range (maximum minus the minimum) and standard

deviation. There was a smaller error for large zenith ranges, suggesting that the range of zenith angles used is the main factor in inversion accuracy rather than the number of rays. Therefore it may be possible to use few (around five) separate scans as long as the zenith angles of the beams cover a wide enough range. Five scans can easily be collected in little over an hour (although the current prototype keeps overheating, slowing this down somewhat, but it should be possible) and it should be possible to arrange them so that every tree crown has beams separated by at least 60^o zenith passing through it, perhaps making use of topography.

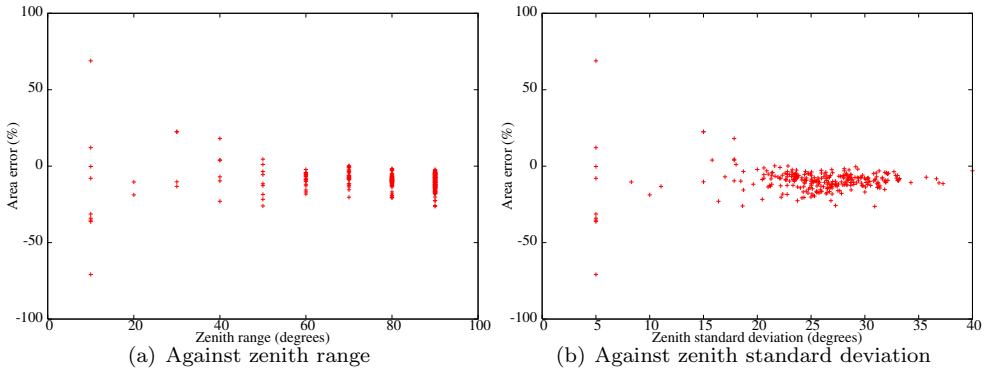

(a) Against zenith range (b) Against zenith standard deviation

Figure 168: Surface area error against angular range of scans for small sections of Sitka spruce canopy

Examining the results used to create figure 168 showed that whilst inversions using scans from less than five different directions could lead to accurate inversions if they are taken from a wide range of zeniths, this is not guaranteed. Using five scans gives reasonable results, tending to lie within 25% of the truth as long as the highest and lowest scans were at least 40^o apart. By nine different view directions errors were down to 15% with the same angular separation.

The initial results suggest that a canopy could be measured with a 25% accuracy in little over an hour and to 15% within two hours; neither of which seems particularly onerous for the accuracy achieved compared to existing methods. These timings are based on the current Echidna prototype and it is hoped that future developments will be much easier to use, faster and lighter.

6.6 Non shadowing canopies

For canopies with large, relatively sparse scattering elements, the same surfaces in a given voxel will be visible from any view angle and so the phase function is not constant and must be described by

an angular function. There will still be shadowing between voxels, but not within a single voxel. If the phase function shows a clear cross over point, as it should if it follows a spheroidal distribution, it can can be combined with the G function into a single angular distribution term.

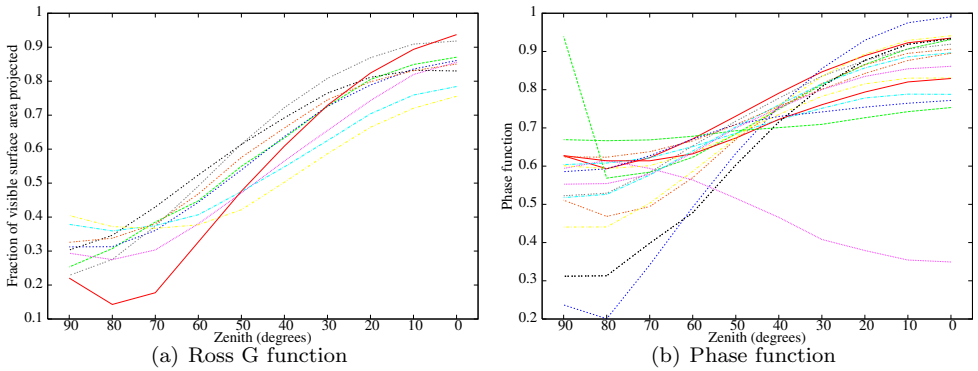

(a) Ross G function (b) Phase function

Figure 169: Birch canopy properties against view zenith to illustrate the cross over point

The birch canopies did not show as wide a range of angular distributions as was displayed by the Sitka spruce canopies. For this reason the crossover of the Ross G function is not obvious in figure 169(a), though the spread at the crossing point was as narrow as for Sitka spruce. Figure 169(b) shows that the phase function had a slight narrowing somewhere between 42^o and 55^o, except for one outlier. If the distribution were spheroidal this cross over should be at $\frac{2}{3}$ (see appendix C), which it appears to be. Therefore a spheroidal distribution may be suitable for both the G function and phase function. The product of the two was given the same sinusoidal form used for $G(\theta)$ in self shadowing canopies. Here a sinusoidal model is clearly more appropriate.

$$G(\theta)\Gamma(\theta) = m\cos 2\theta + c \tag{81}$$

Forcing the line to pass through $\frac{1}{3}$ at a cross over angle, θ_c the combined phase G function becomes;

$$G(\theta)\Gamma(\theta) = m(\cos 2\theta - \cos 2\theta_c) + \frac{1}{3} \tag{82}$$

The spread of values at the crossing point would appear to be due to the change in the ratio of projected to visible surface area and this is a real property of spheroids (see appendix C.3).

Using this form the apparent reflectance, surface area and angular parameter are;

$$\eta = \rho_e \frac{A_s}{A_f} \left(m(\cos 2\theta - \cos 2\theta_c) + \frac{1}{3} \right) \tag{83}$$

$$A_s = \frac{3A_f}{\rho_e} \left(\eta(0) + \frac{d\eta}{d\cos 2\theta} \cos 2\theta_c \right) \tag{84}$$

$$m = \frac{1}{\rho_e} \frac{A_s}{A_f} \frac{d\eta}{d\cos 2\theta} \tag{85}$$

6.6.1 Inversion of a voxel, self shadowing

The above inversion for non shadowing canopies was tested on a section of birch canopy which played no part in the method's derivation. For a section with a total surface area of 160cm^2, of which 151cm^2 was visible, the method predicted 147cm^2, an error of only 2.6% of the visible area and 8% of the total surface area, using twenty view directions.

Of the total area, 132cm^2 was leaf and 25cm^2 was bark. Of this 133cm^2 of leaf was visible and 18cm^2 of bark and the method predicted 115cm^2 of leaf and 32cm^2 of bark. Whilst the fraction of bark was slightly overestimated it was far closer to the truth than for Sitka spruce because there was much less multiple scattering amongst the large, sparse elements in a broadleaved forest than a needle leaf and so the apparent reflectance was not significantly increased.

These results suggest that the above method can determine LAI to unprecedented accuracy in birch canopies, provided that the element reflectances are known.

6.6.2 Acceptable number of scans, self shadowing

The surface area errors were calculated for inversions with different numbers of scans. For each number of scans, a set of beams was randomly chosen from the hemisphere and an inversion performed. This process was repeated twenty times for each number of scans and the mean and standard deviations of the errors calculated.

Figure 170 shows that the errors were much smaller than for Sitka spruce. Errors in total surface area stayed below 7% until only nine view directions. The errors could be up to 80% if only five view directions were used, but again the spread of view zeniths seemed to be more important than the number of view directions.

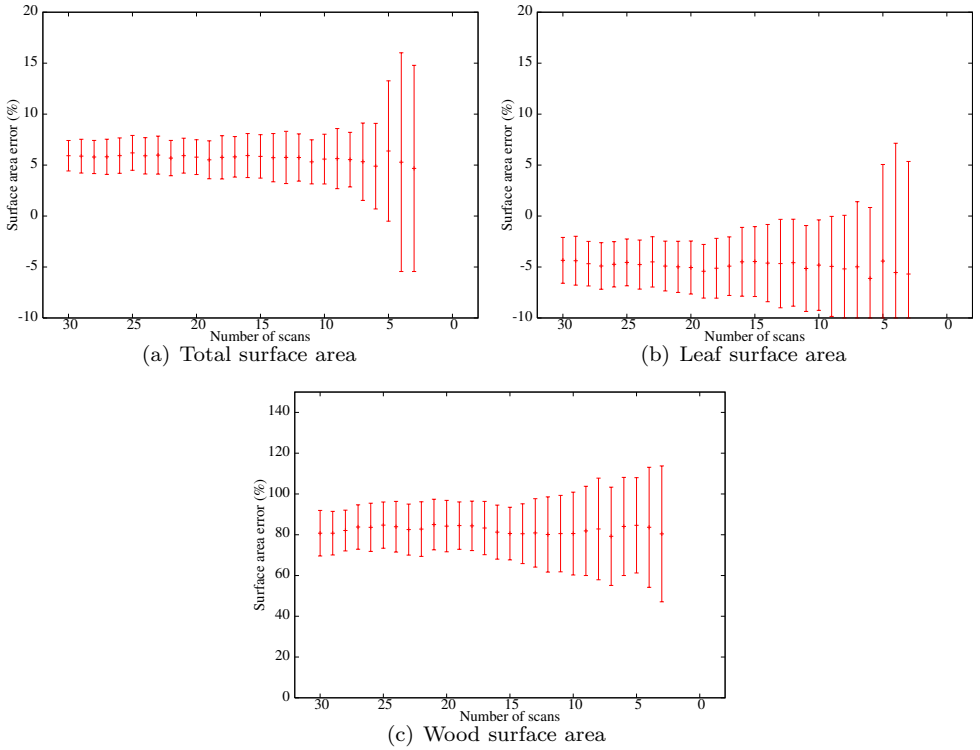

(a) Total surface area (b) Leaf surface area

(c) Wood surface area

Figure 170: Error in surface area against number of scans for sections of birch canopy

The proportion of wood was slightly overestimated for all cases and some estimate of multiple scattering would be needed to correct for this. Measurements spread over at least 70^o guaranteeing estimates within 50% of the truth no matter many beams are used in the inversion (though at least two are needed to fit a straight line to). Therefore accurate inversions are possible with five scans, if they cover a wide range of view zeniths.

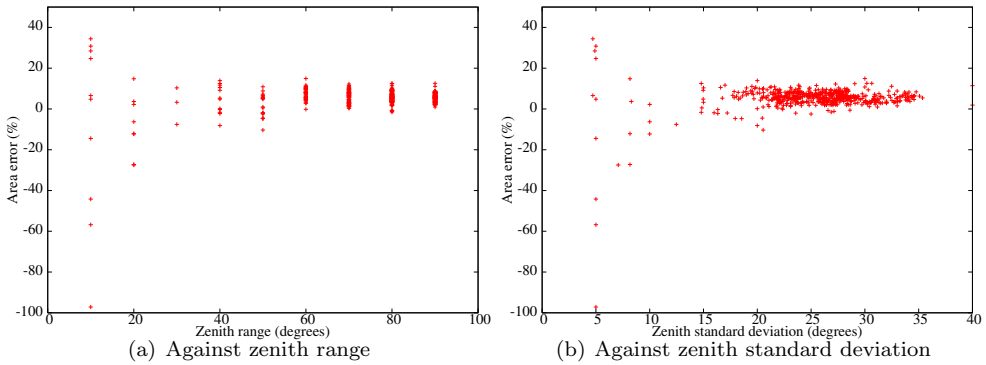

(a) Against zenith range (b) Against zenith standard deviation

Figure 171: Error in surface area against zenith range for sections of birch canopy

6.6.3 Gap fraction, self shadowing

To determine the gap fraction the G function must be decoupled from the phase function. The G and phase functions for a spheroid have been shown in figures 158 and 159.

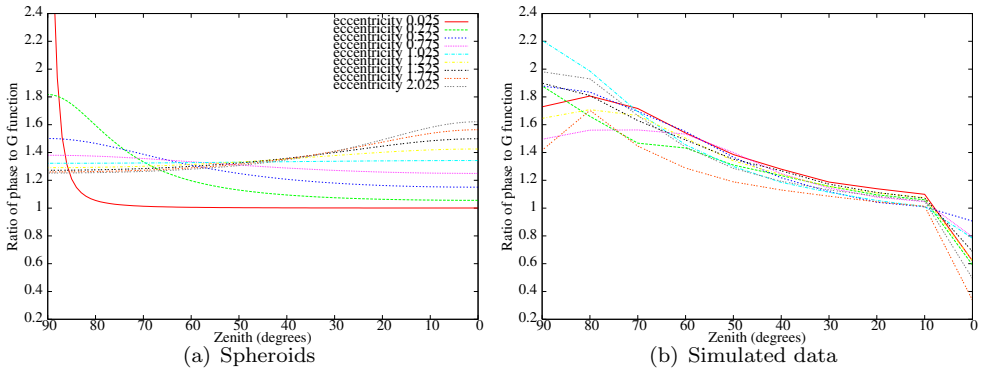

(a) Spheroids (b) Simulated data

Figure 172: Ratio of phase function to G function

Figure 172 shows that the sections tested behaved similarly to ideal spheroids, with a cross over of $\frac{4}{3}$ at 54.75^o. The dip beneath unity at nadir in figure 172(b) is a little worrying, but at all other angles the agreement was good. This dip must have been due to decreased self shadowing near nadir. The exact calculation of G and Γ for a spheroid is very computationally expensive and so a simple approximation is needed. As there is no obvious form for the lines in figure 172(a) it was decided to calculate a look up table giving the value of Γ for a range of values of m and θ using Lambertian spheroids. This requires m to be related to spheroid eccentricity. The phase function was used rather than going direct to the G function because it has a smaller range for all eccentricities and so errors are likely to be smaller.

As m is found from an approximation of true spheroid behaviour it must be related to ideal spheroids by either fitting to an ideal apparent reflectance or else by another approximation. Any approximation will introduce additional errors and so spheroid eccentricity was related to m by fitting equation 83 to synthetic data. This process need only be run once to create the look up table and should not adversely affect the method's practicality. Figure 173 shows that using this method the gap fraction has been accurately calculated at all view angles, though the uncertainties were large.

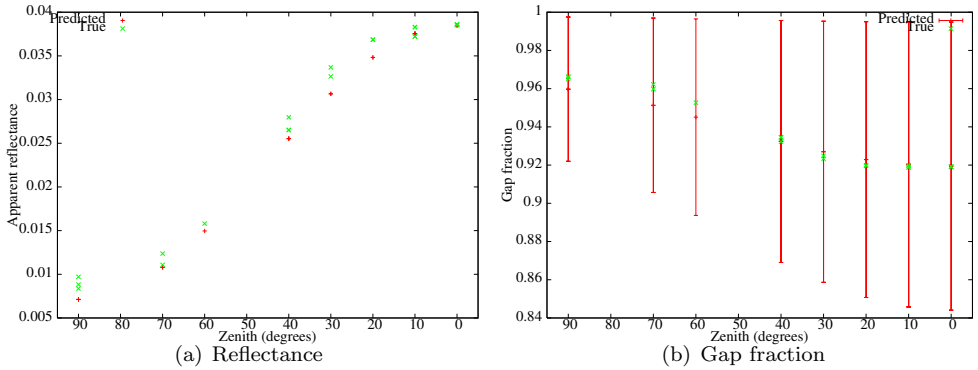

(a) Reflectance (b) Gap fraction

Figure 173: Birch gap fraction

6.7 Testing the ground based inversion

The inversions presented above were repeated over a number of different sections of canopy and voxel sizes to test the generality of the method.

6.7.1 Sitka spruce

For all sections tested the error in total surface area did not exceed 20%; the section used above had the lowest accuracy of all tested. This suggests that the method will work for any Sitka spruce canopy, provided that reasonable estimates for the phase function and element reflectance are available. It struggled to extract separate leaf and bark areas, the proportion of bark being overestimated in all cases. Figure 178 shows a scatterplot of the error for all sections and voxel sizes whilst tables 5 and 4 present the numbers for a few sections representative of the whole.

The error was not dependent on voxel size, suggesting that any cube with sides between 25cm and 1m would be suitable. Of course the larger the voxel the greater the self shadowing but the more samples will be available for inversion per voxel. Inversions of complete canopies would be needed to choose the optimum size.

Gap fractions were also correctly determined in all cases, the sinusoidal form of the LAD providing the best estimate over all zenith angles. Root mean square errors in gap fraction were less than 1% for all section of Sitka spruce canopy tested with a mean bias of less than 1.5%. Figure 174 shows scatter plots of predicted gap fraction against true gap fraction for all sections and zenith angles. The plots are separated into zenith above and below the cross over angle as

gaps are forced to be correct at that angle, any bias would occur either side of this angle, with each side likely to have opposite bias. Thus it should be possible to accurately correct measured reflectance for attenuation and so measure LAI for a whole forest stand.

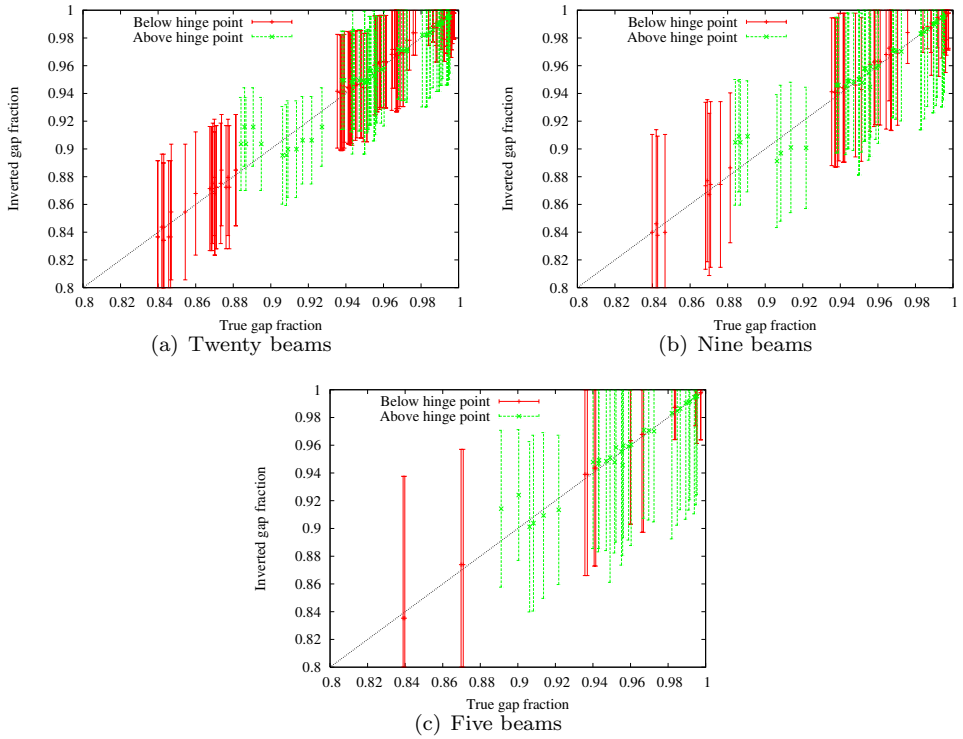

(a) Twenty beams (b) Nine beams

(c) Five beams

Figure 174: Scatter plot of predicted gap fraction against truth separated for zeniths above and below the hinge point for Sitka spruce canopies. Error bars show one standard deviation of uncertainty

Therefore this model can be taken as general for Sitka spruce. The main equations are summarised below.

$$G(\theta) = m(\cos 2\theta - \cos 2\theta_c) + \frac{1}{2} \tag{86}$$

$$\eta = \rho_e \Gamma \frac{A_s}{A_f} \left(m(\cos 2\theta - \cos 2\theta_c) + \frac{1}{2} \right) \tag{87}$$

Fitting a straight line through a plot of η against $\cos 2\theta$ to get the gradient, $\frac{d\eta}{d\cos 2\theta}$ and y intercept $\eta(0)$;

$$A_s = \frac{2A_f}{\rho_e \Gamma} \left(\eta(0) + \frac{d\eta}{d\cos 2\theta} \cos 2\theta_c \right) \tag{88}$$

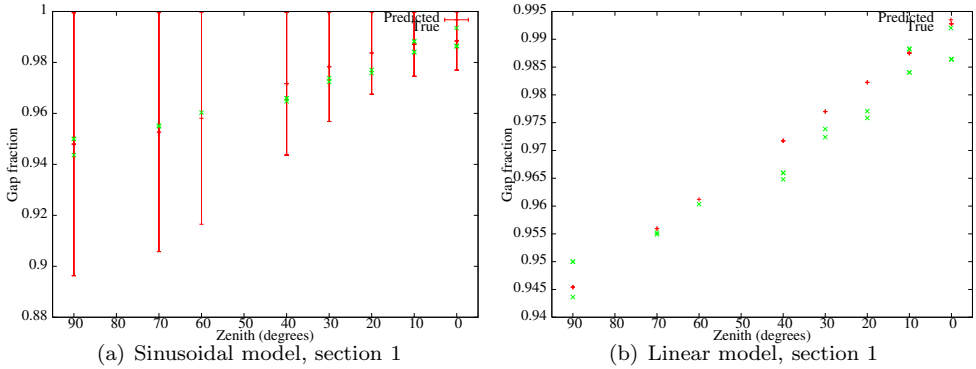

(a) Sinusoidal model, section 1

(b) Linear model, section 1

(c) Sinusoidal model, section 2

(d) Linear model, section 2

Figure 175: Predicted gap fraction for linear and sinusoidal models for a range of Sitka spruce canopy sections

$$m = \frac{1}{\rho_e \Gamma} \frac{A_f}{A_s} \frac{d\eta}{d \cos 2\theta} \tag{89}$$

6.7.2 Birch

To test the method over a range of non-shadowing canopies (within a single voxel), the inversion method was applied to all sections of birch canopy available. It was found to give similar accuracies to the single inversion described above, with a mean error in total surface error of only 6cm^2 for an average visible surface area of 78cm^2 within a cube of sides 25cm. The maximum relative error was a 20% underestimate in a section containing 82cm^2. In all cases the proportion of wood was slightly overestimated due to multiple scattering, but only by a few cm^2 at most.

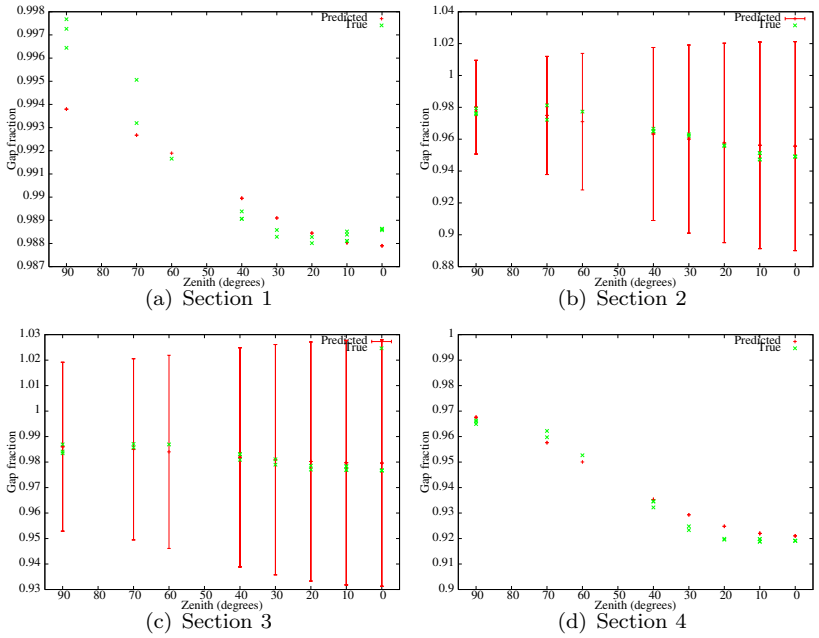

(a) Section 1 (b) Section 2

(c) Section 3 (d) Section 4

Figure 176: Predicted and measured gap fraction against zenith for a number of sections of birch canopy

Figure 176 shows that the predicted gap fractions were close to the truth in all cases. In particular they were all correct at the hinge point, proving that no bias was introduced by $\Gamma(\theta)$. This suggests that the look up table of values is correct and that birch follows the spheroidal distribution near perfectly. Two plots included error bars to show uncertainty and two without. This shows that whilst the gap fractions were correctly determined the uncertainties from the line fitting were large.

Root mean square gap fraction errors were less than 0.4% for all sections tested with a mean bias of less than 0.7%. Figure 177 shows a scatter plot of inverted gap fraction against true gap fraction for all birch sections tested. It can be seen that inverting with only nine view directions did not limit accuracy compared to using twenty and so this should be taken as the maximum number of intersecting beams needed to fully characterise a voxel. Reducing further to five caused slightly higher deviations, but all within a few percent of the truth and so perfectly acceptable.

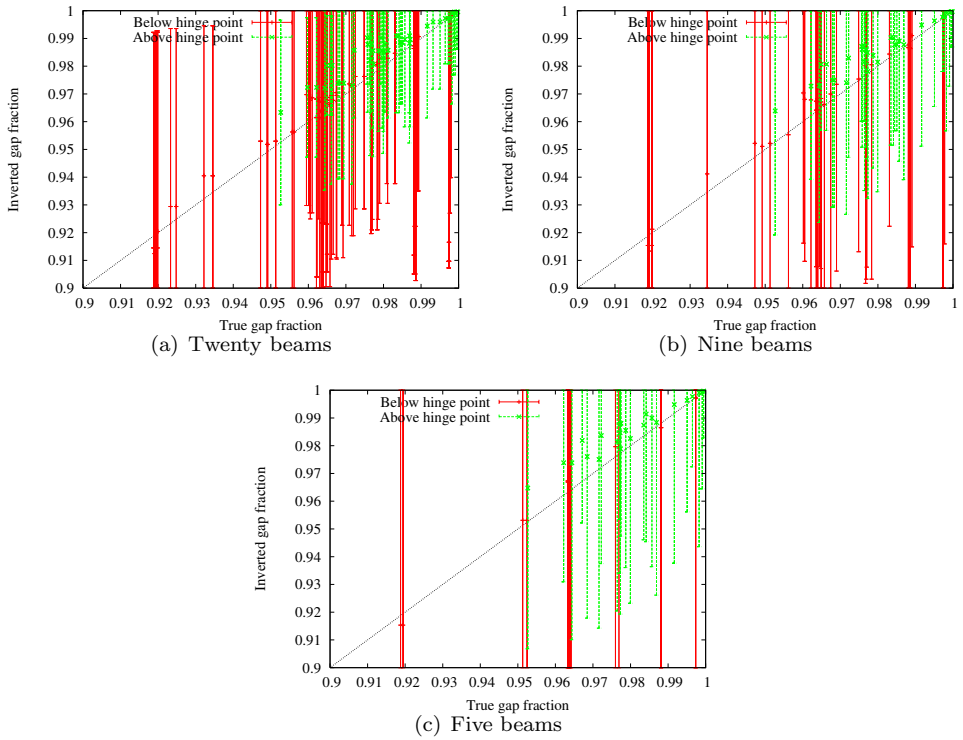

(a) Twenty beams

(b) Nine beams

(c) Five beams

Figure 177: Scatter plot of predicted gap fraction against truth separated for zeniths above and below the hinge point for sections of birch canopy

The main equations for birch are summarised below;

$$G(\theta)\Gamma(\theta) = m(\cos 2\theta - \cos 2\theta_c) + \frac{1}{3} \tag{90}$$

$$\eta = \rho_e \frac{A_s}{A_f}\left(m(\cos 2\theta - \cos 2\theta_c) + \frac{1}{3}\right) \tag{91}$$

$$A_s = \frac{3A_f}{\rho_e}\left(\eta(0) + \frac{d\eta}{d\cos 2\theta}\cos 2\theta_c\right) \tag{92}$$

$$m = \frac{1}{\rho_e} \frac{A_s}{A_f} \frac{d\eta}{d\cos 2\theta} \tag{93}$$

The gap fraction is found by separating $G(\theta)$ from $\Gamma(\theta)$ using a look up table of Γ calculated for Lambertian spheroids (see appendix C).

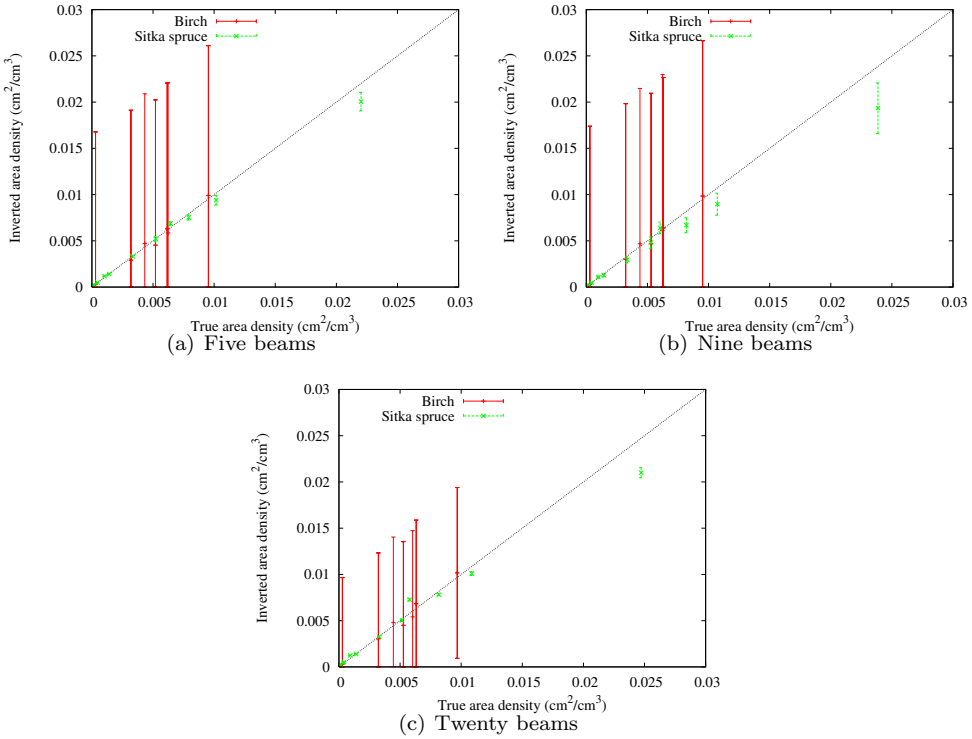

(a) Five beams (b) Nine beams (c) Twenty beams

Figure 178: Scatter plot of visible surface area against inverted for all canopy sections tested. Error bars show uncertainty

Table 4 shows that using beams from twenty view directions will ensure visible surface area errors of less than 34% in all cases and 15% in the majority of inversions. For non shadowing canopies this is very nearly equal to the total surface area and so further corrections are not necessary. For self shadowing canopies around 40% ($\pm 5\%$) of the total surface area is visible and this seems to be independent of voxel size. At least with the Sitka spruce trees tested, a simple factor of $\frac{5}{4}$ may be acceptable to convert inverted area to true surface area.

In all cases the uncertainties estimated from the errors in line fitting are smaller than the errors and so would not be useful as indicators of accuracy. This must be due to bias causing errors that are not apparent in the spread of the data.

Species	Size	Total	Visible	Inverted	Uncertainty	Error
Sitka	25cm	198cm^2	90cm^2	113cm^2	2%	26%
Sitka	25cm	309cm^2	128cm^2	122cm^2	1%	5%
Sitka	50cm	3454cm^2	1358cm^2	1261cm^2	2%	7%
Sitka	50cm	266cm^2	116cm^2	155cm^2	2%	34%
Sitka	75cm	3444cm^2	1391cm^2	1374cm^2	1%	1%
Sitka	75cm	377cm^2	178cm^2	217cm^2	2%	22%
Sitka	1m	3468cm^2	1413cm^2	1395cm^2	1%	1%
Sitka	1m	377cm^2	177cm^2	213cm^2	2%	20%
Birch	25cm	160cm^2	151cm^2	159cm^2	1%	5%
Birch	25cm	126cm^2	99cm^2	107cm^2	2%	8%
Birch	25cm	56cm^2	50cm^2	47cm^2	4%	6%
Birch	25cm	103cm^2	82cm^2	70cm^2	5%	15%
Birch	25cm	111cm^2	94cm^2	85cm^2	6%	10%
Birch	25cm	73cm^2	70cm^2	75cm^2	1%	7%

Table 4: Table of results using a simple model inversion and twenty view directions. Error is relative to the truth, the uncertainty comes from the fitting of the line of best fit

Species	Size	Total	Visible	Inverted	Uncertainty	Error
Sitka	25cm	923cm^2	344cm^2	313cm^2	5%	9%
Sitka	25cm	309cm^2	124cm^2	118cm^2	4%	5%
Sitka	50cm	1612cm^2	653cm^2	650cm^2	6%	0.5%
Sitka	50cm	266cm^2	130cm^2	147cm^2	4%	13%
Sitka	50cm	3454cm^2	1270cm^2	1174cm^2	6%	8%
Sitka	75cm	3444cm^2	1405cm^2	1398cm^2	3%	0.5%
Sitka	75cm	377cm^2	194cm^2	203cm^2	4%	5%
Sitka	1m	3468cm^2	1413cm^2	1420cm^2	3%	0.5%
Sitka	1m	377cm^2	195cm^2	202cm^2	4%	4%
Birch	25cm	160cm^2	149cm^2	155cm^2	2%	4%
Birch	25cm	126cm^2	96cm^2	98cm^2	4%	2%
Birch	25cm	56cm^2	50cm^2	45cm^2	3%	4%
Birch	25cm	103cm^2	81cm^2	71cm^2	8%	12%
Birch	25cm	73cm^2	68cm^2	74cm^2	5%	9%
Birch	25cm	19cm^2	19cm^2	22cm^2	8%	16%

Table 5: Table of results using a simple model inversion and five view directions. Error is relative to the truth, the uncertainty comes from the fitting of the line of best fit

The errors were actually lower when using five beams than twenty. This must be due to outliers amongst the twenty beams causing inaccuracies. The five beams must have included fewer or none of these outliers. Errors were all less than 16% with the majority being less than 10% with no bias, a very acceptable result.

The errors were all much smaller than those found by inverting gap fraction and using Beer-Lambert's law (section 6.3.4). This suggests that the more direct linking of measured reflectance to surface area is worthwhile, certainly the model is no more complicated to implement and makes no more assumptions than the gap fraction method. It does require more scans, needing a minimum of five spread over 60^o zenith compared to the gap fraction method's single scan, but this brings

the additional benefit of capturing the PAI and angular distribution's heterogeneity. The only potential downfall would be heterogeneous attenuation when used in complete canopies, leading to inaccurate corrections of apparent reflectance and so inverted properties. The method would have to be tested on a complete canopy before it can be stated for certain whether it can perform as well as the traditional passive optical transmission methods.

6.8 Complete canopy

The work thus far has concentrated on small sections of canopy to avoid the extra complication of beam attenuation. Now that the method has been shown to work well for the cases tested, it can be expanded to forest stands.

The apparent reflectance from a voxel depends not only on the surface area and angular distribution in that voxel but also the gap fraction between beam origins and that voxel, which in turn depends upon the contents of voxels earlier in the beam path. Because of this interdependence the inversion must be iterative, refining voxel contents until the predicted lidar returns match those measured.

The first step was to divide the scene into voxels and determine which range bins are contained within which voxels. As each Echidna scan will contain over 49,000 beams, each with around 720 range bins, this sorting can be computationally expensive. To speed the inversion process a map was created at the start of inversion, saving future searches. The map could also be used in subsequent inversions, saving processing time.

Next an initial set of voxel surface areas, angular distributions and leaf proportions were set. The fraction of leaf and bark can be calculated from the ratio of the reflectances in two bands, η_λ and η_ω of any beam using equation 80. If leaf and bark have the same angular distribution and phase function then no other parameters should affect this value and it will provide a reasonable estimate (although multiple scattering was shown to cause errors in the previous section). Both wavelengths should be equally affected by any orientation effects.

It was first assumed that all elements have a uniform angular distribution ($m = 0$), so that an estimate of surface area could be obtained from a single view zenith (taking the closest as a first

guess and not bothering to correct for gap fraction so that it was an underestimate).

After the initial estimates had been determined the function stepped through voxels, calculating the apparent reflectance from each view direction. For this the measurements from bins along each beam were summed, then the average apparent reflectance of beams from each scan centre calculated. Without this summing and averaging step the heterogeneity of the distribution of elements within each voxel caused the plot of apparent reflectance against $\cos 2\theta$ to be too messy for a line of best fit to be reliably found.

The fraction of leaf and wood was determined by comparing the reflectance from two bands and so giving a value for the average reflectance of elements within the voxel, ρ_e. The gap corrected apparent reflectance was plotted against the cosine of twice the zenith angle and Powell's method (Press *et al.* 1994) used to find the gradient and y-intercept of a line of best fit. As well as the deviation from measured apparent reflectances the error function included a cubic penalty for non-physical results; the predicted apparent reflectance was forced to be between zero and the average canopy reflectance, the maximum reflectance that can be measured if a target completely fills the field of view, ignoring multiple scattering. This maximum reflectance is unlikely to be exceeded because if a target happens to completely fill the field of view and have a significant contribution from multiple scattering, the surface is likely to be curved and folded and so the phase factor low.

As rays are attenuated the returns will become less representative of subsequent objects, in addition dividing by a small P_{gap} in equation 69 can lead to very large values which may skew line fitting. To avoid this the error function calculated in the least squares fitting was weighted by the gap fraction in that range bin (ignoring shadowing within that particular voxel). At the same time the LAD parameter, m, was determined.

Once this had been carried out for all voxels the error between predicted and measured reflectance was calculated and the process repeated until either a certain number of iterations was reached, the error dropped below a threshold or the error stayed constant for a number of iterations. No state vector as such was used and so no clever iteration method was employed.

6.8.1 Accuracy

The above method was applied using five scans from within a birch canopy. Due to computer memory requirements it was decided to limit the voxel resolution to 1m. At 50cm, even with memory mapping of the actual lidar data, the voxel and lidar bin map and results arrays for a 10m by 10m plot exceeded the computer's file navigation limit of 2 Gbytes. Higher resolution inversions and larger stands would require either more powerful computers or more extensive use of memory mapping.

The plot was centred on the scan for which the gap fraction method of Jupp *et al.* (2009) gave the best match (see figure 141 in section 6.3.4). A 10m radius plot about here with zeniths below 55^o had a PAI of 0.31 and the method of Jupp *et al.* (2009) predicted 0.32, a 3% error. The true PAI within the square plot, extending from the floor to canopy top, was 0.24. Inversion of five Echidna scans spaced throughout this plot predicted a PAI of 0.97, a factor of four different and clearly unacceptable.

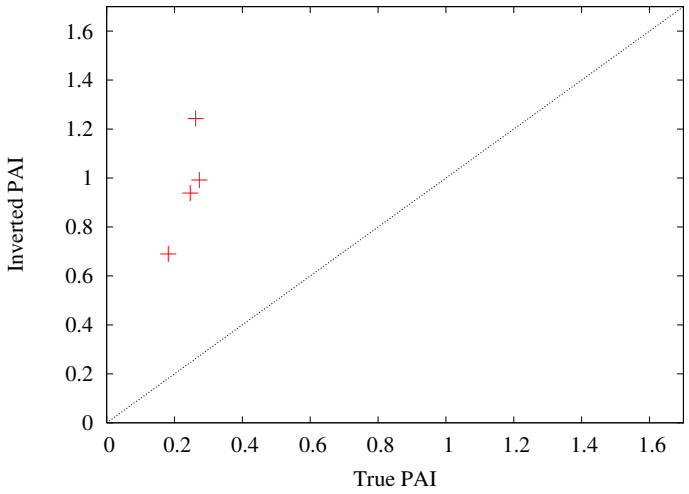

Figure 179: Inverted PAI against the truth for 5m by 5m sections within a birch canopy

The plot was further broken down into 5m by 5m sections. Figure 179 shows a scatter plot of the inverted PAI values against the truth for these sub sections. Interestingly all the points appear to lie on a straight line through the origin with a gradient of four (ratios of inverted to true PAI lay between 3.63 and 4.74).

The overestimate could be due to the obscuration correction used (described in section 6.4),

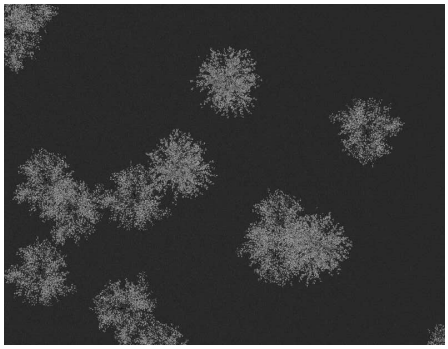

Figure 180: Image of the 10m by 10m section of birch canopy used for inversion

simplicity of the lidar bin to voxel mapping or the multiple scattering enhancement to element reflectance. For the first of these it may be the case that elements in different voxels are preferentially filling gaps (though this would be unlikely for every view angle). Therefore the visible elements are not representative of the shadowed elements and so dividing by the gap fraction up to a point overestimates the intensity of light that would be returned were it not for the obscuring elements. It may also be due to an underestimate of gap fraction, leading to an excessive correction.

The mapping of lidar bins to voxels was very rough, making no attempt to calculate the fractional overlap. Therefore the radiant flux of a lidar contributed to all intersecting voxels and energy was not conserved. In this example lidar bins were much smaller than voxels and so whilst it will have caused a slight overestimate in surface area, unless every lidar bin intersected four separate voxels on average, this would not be enough to cause the deviation alone. Multiple scattering will increase the apparent reflectance and so, as surface area is inversely proportional to element reflectance (through equation 88), cause an overestimate. However section 4.1 showed that for a single voxel the area could be accurately found and so multiple scattering is unlikely to be a significant source of error. With such a small footprint (0.8^o beam divergence) multiple scattering makes up a very small part of the signal and so the lack of error due to multiple scattering for a single voxel is likely to hold for a full canopy.

For these reasons it is likely that the gap fraction correction dominated the PAI errors. Unfortunately there was insufficient time to carry out the extra analysis needed to determine the cause of the errors. However the systematic nature of the bias (albeit over a small PAI range) suggests that it is a correctable effect.

This is far from a comprehensive error analysis but suggests that the method can return accurate values, although the current implementation needs much improvement before it can be considered the equal of the gap fraction method of Jupp *et al.* (2009). If the improvements suggested did fix the limitations then the method would have the advantage of being able to measure all canopy elements off the ground (all beams that contain no soil returns) rather than being limited to the 0^o to 55^o zenith range. All vegetation that contributes to a satellite signal will be characterised, allowing better linking with above canopy measurements. Law *et al.* (2001) believed that missing understorey vegetation was a major source of error when comparing LAIs found with hemispherical photography and satellite NDVI.

6.8.2 Future improvements

The experiments used to test the inversion of a voxel canopy model from overlapping terrestrial lidar scans were very limited. Whilst it was shown that the method works for small sections of canopy, it gives large overestimates when used on complete canopies. This is most likely to be due to the gap fraction corrections, however whether this is due to inaccurate predictions of gap fraction or non-randomness of canopy elements was not determined.

The iterative scheme to determine the voxel properties was very naïve, making no attempt to control the size or direction of voxel property adjustments. Instead they were left to their own devices, hoping that eventually the surface areas and angular distributions would settle down to the correct value. A more intelligent method should be employed once the basic idea has been shown to have value, such as the "simplex" or "Levenberg-Marquardt" methods (Press *et al.* 1994). Constructing the matrix for these methods, with the interdependence of voxel properties on adjacent voxels, would be non-trivial but once implemented should give a more accurate and much more robust solution.

One use of Echidna data would be to predict above canopy reflectance. This would require a DART type model (Gastellu-Etchegorry *et al.* 2004) to be created from the voxel inversion, then multi angular and range resolved measurements to be simulated over the canopy model and the original geometric forest model. Comparing these two data sets would determine the inversion's ability to predict above canopy reflectance. With the correct surface area, angular distributions

and gap fractions the single scattered radiation would be correctly determined however multiple scattering would require some form of model (such as that of Knyazikhin *et al.* (1992)) as it would be far more significant at the scale of the remotely sensed data than the Echidna measurements.

The number of unknowns in the method could be reduced by placing targets of known reflectance and phase function (ideally perfect Lambertian) throughout the canopy. The measured intensity from these targets would be equal to the product of the contact frequency and surface reflectance, allowing the gap fraction up to that point to be directly solved. With a few of these intersecting beams at different angles it may be possible to detect any deviations in canopy reflectance or phase factor (for coniferous canopies) from the assumed value, as well as giving a more reliable estimate of the G function. Carrying a few foldable targets and extendable poles should not add too much weight and effort to the fieldwork.

6.9 Below canopy conclusions

This chapter has outlined the current efforts to characterise forests with full waveform terrestrial lidars. There have been many studies using more common discrete return instruments, but these suffer from the problem of being blinded by the first return (Danson *et al.* 2007) and are only a stop-gap until full waveform sensors become widely available.

The initial studies with the first terrestrial waveform lidar, Echidna, have concentrated on extracting trunk characteristics (a purely geometric problem) and LAI through traditional gap fraction methods (Jupp *et al.* 2009). The ray tracer was used to assess the accuracy of such an approach. It was found to correctly predict gap fraction, though with some sensitivity to the external estimates of canopy reflectance and phase function. This will suffer from the same saturation issues as traditional transmission techniques, although the range of canopies tested here did not approach the LAI of 4 that is generally taken as the saturation point (Jupp and Lovell 2007). Clumping corrections may improve the estimate, particularly canopy scale clumping. Also Jupp *et al.* (2009) applied correction factors to their estimates of gap fraction to prevent non-physical results (such as gaps through the ground) and this may increase the PAI estimate.

Whilst gap fraction can be extracted from lidar returns and that used to estimate PAI, in theory

surface area (and so PAI) can be linked to measured intensity as directly as gap fraction can. Such an approach would allow measurement of the spatial distribution of LAI and LAD throughout the canopy and should be the ultimate aim of work with terrestrial waveform lidar (Jupp and Lovell 2007).

An angular distribution model was developed, based upon a simplification of the spheroidal model of Campbell (1986). Slightly different approaches were needed for coniferous and broadleaved canopies (as they are for any method (Chen and Cihlar 1996)). The increased self shadowing within conifer needle shoots meant that the phase function appeared constant from all view directions and so this value must be supplied from external data. For the birch canopies tested there was very little shadowing within voxels with sides of up to 1m, so the phase function could be extracted alongside the angular distribution. Both methods required an estimate of canopy reflectance, in the case of birch this was the only external data needed.

For broadleaved forests the agreement between observations and the spheroidal angular distribution model was startling. It is not known exactly how Onyx (Onyx Computing Inc 2009) set the leaf distribution within the birch canopies and this may have given a better agreement than would be observed in nature. However the tests performed here, with small sections extracted from complete canopies, would be impossible in reality; leaves would droop without the supporting branches and so it can only be stated that the tree models look correct and produce realistic remote sensing signals (Disney *et al.* 2009) and so may be taken as accurate.

In the absence of shadowing between adjacent voxels, so that corrections of gap fraction are not needed, this model predicted surface area and gap fraction with angle to a high degree of accuracy. This required at least five overlapping beams covering a 60^o zenith range and ideally nine beams, that amount of data could be collected in an hour or two.

The sensitivity of surface area and gap fraction estimates to the external values of element reflectance and, for Sitka spruce, phase factor was not explicitly calculated. Surface area is inversely linearly related to both of these factors so that any error in these values will directly scale through to surface area and gap fraction. For example a 10% underestimate of canopy reflectance would become an 11% overestimate of surface area. This is a similar sensitivity to that found for the gap

fraction method of Jupp *et al.* (2009). Measuring element reflectance in the field could be easily done with a portable spectrometer, such as the LI-1800 (LI-COR 1988) but estimation of the phase factor for coniferous canopies would be more problematic. Placing targets of known reflectance through the canopy would allow the gap fraction to be decoupled from apparent reflectance and so, providing that it is constant throughout the canopy, give an estimate of the phase factor.

Woody correction Dual wavelength lidar should allow the separation of leaf and bark areas, so the extraction of LAI from PAI independently of illumination conditions that complicate attempts with passive instruments so (Gower *et al.* 1999). This was successfully performed for birch forests, but in Sitka spruce the multiple scattering enhancement to the brighter return caused a large overestimate of wood fraction. This issue could be resolved by using an enhanced reflectance rather than element reflectance (Huang *et al.* 2007). This is a reflectance that takes the multipe scattering contribution to the shoot scale signal into account and would be dependent upon needle shoot structure.

Complete canopies It should be possible to extend the method to complete canopies as surface area and gap fractions are correctly determined for small canopy sections. The greatest potential for error here is in the gap fraction correction; if the visible elements are not representative of the obscured elements within a voxel the correction can lead to an over or underestimate of apparent reflectance which in turn will confuse the line fitting used to determine the canopy properties. The potential for error would be dependent upon canopy density and the separation between scan centres. A far more detailed analysis of errors in a range of different canopies with various scan densities would be needed before the method proposed in this chapter can be said to work reliably and provide results as useful as traditional gap fraction methods. The gap fraction methods avoid this issue by using Beer-Lambert's law and the results here are not strong enough to show that PAI can be accurately derived without resorting to it.

There was only time to do a direct comparison of the method presented here against the gap fraction method of Jupp *et al.* (2009) for a single stand. More stands would be needed to determine relative accuracies and the reasons for disagreements. A more detailed examination of

the predicted and true gap fractions along each lidar beam will reveal whether it is an error in the predicted gap fraction or a non-random arrangement of elements that caused the largest errors. Within the simulator it would be possible to determine the visible and hidden surface area within each beam field of view, however it would require a significant modification of the ray tracer. Inversions with more scans (up to twenty) should also provide more accurate estimates but would require significantly more computer time and memory to run. In the absence of these experiments it cannot be said for certain whether the method will work reliably in complete canopies.

As well as providing estimates of LAI non-destructively, these measurements have the potential to create complex canopy reflectance models, such as DART (Gastellu-Etchegorry *et al.* 1996), requiring only a fraction of the assumptions normally made. Such a model could be used to predict above canopy multi-angular and range resolved measurements, aiding the understanding of remote sensing signals, though this was beyond the scope of the thesis.

Realism These below canopy simulations used infinitely short laser pulses and did not include noise. As Echidna measurements are taken at much shorter ranges than spaceborne instruments they will have much higher signal to noise ratios, therefore it is likely that noise will play a far smaller part in inversion accuracy than canopy heterogeneity and deviations from assumptions. This omission should not limit the results' realism.

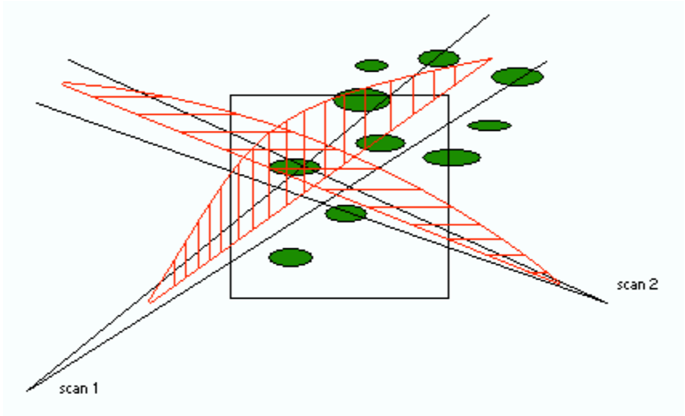

Figure 181: Illustration of the effect of pulse length on a voxel inversion method. Green ellipses are leaves and red hashed areas represent the laser intensity for a return centred on the voxel for two scans

Echidna has a 25.3ns laser pulse (Jupp *et al.* 2009) which will blur the signal over 3.8m. The

pulse length may limit the minimum voxel size as beams from different directions will contain returns from outside the voxel, as illustrated in figure 181. Whilst the impact of using smaller voxels than the pulse length on accuracy was not quantified it would seem sensible to ensure that the pulse length is shorter than the voxel sides. For $1m^3$ voxels this would be 3.3ns which table 1 shows is easily achievable with current technology. An inversion with 3.8m or larger voxels was not attempted as this would be the same size as the tree crowns used and likely to suffer from self shadowing.

Due to the failure of the current implementation of the method with complete canopies there was little point including these extra levels of detail for the time being.

Chapter 7: Conclusions

Climate change is currently one of the most pressing issues and a picture of what will happen under different scenarios, with a high degree of certainty, is needed for effective policies to be made. This requires an accurate measure of the current state of the Earth and a clear understanding of the processes that govern change and how they will themselves be affected by climate change.

One of the key factors is the land vegetation, being one of the most dynamic elements in the natural carbon cycle (Defries *et al.* 2000). Forests make up the largest part of terrestrial vegetation by mass and so an accurate map of forest characteristics and how they change through the seasons and years is essential to understand the Earth's climate. Chapter 1.3 reviewed the theory used to measure forests and chapter 2.4 presented current attempts to extract biophysical parameters using that theory.

The conclusion was that spaceborne instruments are needed to make the globally consistent and frequent measurements required. In addition it would be best to avoid site specific calibration and so a physically based method would be preferable. There has been much work in this area, however all instruments suffer from some form of limitation. Passive optical sensors offer the best spatial and temporal coverage (MODIS offers daily global coverage with 250m ground resolution whilst the Landsat series make 30m resolution measurements every 16 days and have done since 1972) but these saturate at only moderate canopy densities (LAIs of 5-6, when values of 10 are not uncommon), potentially biasing any climatic predictions. Short wavelength radars suffer the same problem of saturation as passive optical whilst longer wavelength radars suffer from significant atmospheric distortion and engineering challenges to get usable ground resolutions from space. Even if these could be overcome, the relationship between radar signals and forest properties are not direct or easily invertable (Sexton *et al.* 2009).

Lidar, specifically full waveform, offers the potential to make non-saturating measurements (up to canopy covers of 98%) that are more directly related to forest characteristics than with any other instrument (Dubayah and Drake 2000). Due to the relative immaturity of the technology and higher energy requirements they cannot achieve the spatial and temporal coverage of passive optical or radar sensors. It may be possible to use their physically based and non-saturating

measurements to calibrate passive optical or radar estimates and so "upscale" the measurements (Hyde *et al.* 2006), though with some saturation beyond the lidar measurements.

Lidar is a relatively new technology and its interaction with forest canopies is not yet fully understood. There have been several studies to validate lidar derived measurements against ground data, but these are complicated by having to match up the remotely sensed and ground observations. The errors from mismatching may well dominate over others, preventing a full understanding of the processes contributing to the signal (Harding and Carabajal 2005). Monte-Carlo ray tracing with geometrically explicit forest models (as described in section 2.2.3) allows realistic simulations of remote sensing data with a fully controlled and known set of ground truth values. This allows new techniques to be validated with confidence.

The ray tracing library of Lewis (2006) was modified to allow the simulation of any current or foreseeable lidar instrument. A library of Sitka spruce and birch forests with a variety of ages, densities and slopes were created. These were used as a virtual laboratory (Lewis 1999) to explore the effect of instrument parameters on accuracy and an optimum spaceborne lidar for forestry was proposed, the properties of which are given in section 5.14. Using these would ensure that the lidar system itself will not limit inverted parameter accuracy. In addition a method to avoid introducing bias to the tree top range estimate by noise removal was introduced in section 5.1.1. This was shown to improve the accuracy (if not the precision) of tree height estimates in all cases tested. These simulations exposed some situations that might lead to inaccurate height estimates, such as those shown in figures 102 and 108; situations that have not been apparent from real data due to other complications.

Some shortcomings of using current lidars for global measurements were addressed. All current and proposed spaceborne lidars are large footprint (10m-100m) and whilst these can be sure to measure the range to a tree top and ground, allowing tree height estimates, they are particularly susceptible to topographic blurring (see section 3.5.3). Forests on steep slopes are not uncommon (Takahashi *et al.* 2005) and so an instrument that cannot measure such areas will have considerable blind spots.

In the thesis it was proposed to use dual wavelength lidar to detect the start and end of the

ground return, no matter how great the topographic blurring, long the laser pulse duration or in the presence of understorey vegetation. This method was tested with the simulator and shown to give more accurate results than current globally applicable methods and required no site specific calibration or prior information.

Currently the highest accuracy that has been reported over topography is a root mean square error of 2.99m, reported by Rosette *et al.* (2008) over slopes up to 20^o using ICESat. However this required a 10m horizontal resolution terrain model to determine the ground position, which is not available at a global scale (Rosette *et al.* 2007), as well as some site specific calibration from ground data. Even then the accuracies were not significantly better than the method presented in section 5.12, which requires no calibration or site specific parameters. Therefore the dual wavelength method proposed here should be a considerable improvement over current tree measurement techniques, only struggling with extremely dense (>98%) and extremely sparse (<10%) canopy covers. All areas of the globe within these bounds should be measurable to a better accuracy than currently available, that is better than 5m accuracy in all cases and generally sub-metre.

Such an instrument would require two wavelengths, either through two lasers or by shifting the frequency of a single laser. Whilst this would be slightly more expensive and complex than current mono-chromatic lidars it is well within current technological reach (Foster 2008, Morsdorf *et al.* 2008b, Kaasalainen 2007).

As well as the optimum canopy lidar described above, a method to use an instrument designed for atmospheric measurements over forests was proposed (section 5.9). In particular a method to extract tree information from long duration laser pulses was presented based on the deconvolution method of Gold (1964). This was shown to be capable of retrieving accurate biophysical parameters but no robust convergence criterion was found for the iterative deconvolution. Since those experiments were carried out the instrument around which they were based (ESA's A-scope (ESA 2010)) has been cancelled (or at least put on hold) and so there seems little point in pursuing a convergence criterion for the time being.

7.1 Above canopy future work

Whilst the various methods were shown to work under certain conditions, the experiments performed were not exhaustive and more would be needed before it could be said for certain whether this is a truly global method.

7.1.1 Gappy canopies

The dual wavelength method was shown to work well for completely blurred waveforms (with no break from beginning to end, as in figure 103), however it struggled with waveforms that included a gap (see section 5.12.13). Such a gap could be due to a clear separation between canopy and ground, shadows or a break in a vertically heterogeneous canopy (such as figure 102). The first of these should be easy to solve for and this was demonstrated for the flat ground cases throughout chapter 4.3. However for the other two cases the ground start will be at one side or another of the waveform break and so a method needs to be able to determine which.

The change in spectral ratio from pure canopy to pure ground can be very small (see section 5.12) and so it may not be easy to decide which side of the gap the transition occurs from the absolute change in the ratio. It should be possible to identify the transition by "filling in" gaps and so turning the gappy waveform into a completely blurred waveform. That is to remove the gap by either ignoring those ranges or else filling in with intensity values from either side of the gap. The point of inflection of the spectral ratio can then be found in the same way as for completely blurred waveforms.

In none of the forest models used in this investigation was the intensity drop due to shadows so severe as to cause a break in the intensity. Whether this is true for all tree species and situations is not clear, but it is likely to be far less common than gaps due to breaks in the canopy. Therefore the priority should be to develop a method to cope with canopy to ground transitions above or either side of waveform gaps.

This extra processing should be relatively simple to implement, requiring an extra step to identify gaps and decide how best to deal with them, either by filling them in and looking for a turn in spectral ratio or else use the simple flat ground method. Care would be needed not to shift

the spectral ratio inflection across the gap as this would lead to large errors (section 5.12.13).

7.1.2 Dual wavelengths

Several possible wavelength combinations for the dual wavelength lidar were proposed using the spectra described in section 5.12.4. Whilst the spectra covered a broad range of vegetation types they were not comprehensive by any means, particularly the soil spectra. Therefore the experiments should be repeated with a larger number of spectra, particularly different forest floors (see section 4.2.2). If it is found that no combination meets the criteria set out in section 5.12.4 the results could be weighted by the relative proportions of each spectra on the Earth and their importance in the various ecological processes. This only requires access to more data.

More accurate engineering information would be needed to decide whether an instrument could be built at those wavelengths and meet the required system characteristics (laid out in section 5.14). Such engineering concerns were beyond the scope of this thesis but would be needed for a full instrument design.

Throughout this thesis only dual wavelength lidars were investigated. More wavelengths should provide more information and so allow further analysis, however it is not clear how best to use this additional information and much more work would be needed.

7.1.3 Biophysical parameters

This thesis concentrated on the estimation of tree height, which requires the ground's position to be found. This separation of canopy from ground returns is the first step to any physically based inversion and so tree height accuracy will be related to whether or not other parameters can be successfully inverted. The errors in these other parameters are unlikely to be linearly related to tree height error and so as these are currently the parameters of interest for ecological models it would be useful to determine how accurately they can be determined.

A method proposed by Lewis (within Hancock *et al.* (2008)) was to use the ratio of energy returned from the canopy and ground in a self calibrating method. If it is assumed that within a given area the canopy, ρ_c, and ground, ρ_g, reflectances are reasonably constant, the total waveform intensity for each footprint, E, will be a linear mix of the energy returned from the canopy, E_c,

and from the ground, E_g, weighted by the canopy cover, c.

$$E = cE_c + (1 - c)E_g \tag{94}$$

For a given area, the gradient, Δ, of a line fitted to a graph of E_c against E_g is equal to the negative of the ratio of their reflectances (ρ_c for canopy and ρ_g for ground) whilst the y-intercept, E_0, is equal to canopy reflectance.

$$\Delta = -\frac{\rho_c}{\rho_g} \tag{95}$$

$$E_0 = \rho_c \tag{96}$$

If the parameters for this line are known the canopy cover can be determined from the total waveform reflectance alone;

$$c = \frac{1}{\Delta + 1}\left(\frac{\Delta E}{E_0} + 1\right) \tag{97}$$

Therefore as long as it is possible to separate canopy from ground returns in a few waveforms the canopy cover can be determined for all, irrespective of blurring or its source. It does rely on the absolute intensities and so care must be taken to correct for any shot to shot gain variation (Harding and Carabajal 2005) but this would be a great improvement over the method of Lefsky *et al.* (1999) where a constant value of the ratio must be assumed. There was not time to perform such inversions within the thesis and its success would rely on the homogeneity of canopy and ground reflectance, effects that can only be determined from real data such as that collected by LVIS (Hofton *et al.* 2000).

Models are being developed to make use of direct lidar measurements (Hurtt *et al.* 2004), but due to the immaturity of the technology these are not yet widespread.

7.1.4 Impact on ecological models

Whilst it was shown in chapter 4.3 that the methods and instruments proposed in this thesis are able to provide tree height with better accuracy than previous attempts, there was not time to

assess the impact that this would have on ecological models.

The first step would be to determine what proportion of the Earth's surface is covered by forests with LAIs of over 7 (the saturation limit (Myneni *et al.* 2002)) and what proportion of forests are on what slopes. The global LAI products derived from MODIS and MISR could be used to find the proportion at the current saturation limit throughout the growing season. Finding which areas of forests for which it would not be possible to use large footprint monochromatic lidar over due to slope would not be simple as it depends on the separation of the crowns and ground, a value which is not readily available. Global digital elevation models are available and whilst they may not give accurate ground positions in forests (Dowman 2004) they should allow estimates of ground slope. This would give an idea of the proportion of forests at slopes over a certain angle.

To quantify the impact the values would have to be run through a global ecological model such as JULES (Clark and Harris 2010), once with currently derived estimates of biomass and LAI then again with the higher values likely to exist but not captured by current systems and comparing outputs. It would not be certain what values to use for the "non-saturated" inputs as a multi-spectral lidar does not yet exist and so there would be a large degree of uncertainty in the second output. It would however give a rough idea of whether there would be a significant difference in future climate predictions due to measurement methods.

7.2 Terrestrial lidar

Whilst spaceborne instruments are essential for globally consistent measurements, more direct, ground based measures are needed to validate and understand remote signals. Forests have been directly measured, with rulers and equivalent, but it is a tedious and expensive process impossible for anything but a few small plots. More rapid methods were reviewed in section 3.1 and whilst they have popularity due to their ease, they saturate at LAIs of 3 to 4. This is similar to the passive optical saturation point and so will bias any validation attempt and potentially obscure physical processes. In addition they cannot make the range resolved measurements of the canopy profile needed to validate spaceborne lidar measurements.

Terrestrial lidar is the only way to quickly collect range resolved measurements from the ground

and so will be a valuable tool for validating spaceborne lidar signals. Ground based lidar has been shown to be capable of explicit measurements of forest structure, particularly the solid trunks and large branches. This thesis concentrated on the distribution of foliage rather than the point cloud processing methods of wood architecture, which are not able to extract leaf area without extensive external measurements (see section 3.5.4).

A method to fully characterise a site (to some resolution) is needed. This would give the biophysical parameters of the stand as well as allowing predictions of all remote sensing signals, both range resolved, multi-angular and traditional passive optical at nadir. As a first attempt Jupp *et al.* (2009) have used terrestrial lidar to estimate gap fraction and this should form a benchmark to test other methods against.

The method was implemented (section 6.3) and shown to give accurate estimates of gap fraction (though with a slight bias that could be solved by tweaking effective parameters). This did not translate to a particularly accurate estimate of LAI in all cases, but again tweaking the effective parameters (phase and angular distribution functions) should correct these errors. The authors of the initial study admit that this is only a rough first attempt and that more detailed structural measurements should be possible with a terrestrial waveform lidar (Jupp and Lovell 2007).

The richness of hemispheric, full waveform lidar data should allow the inversion of a volumetric canopy model, giving biophysical parameters and allowing the prediction of remote sensing signals. Various experiments were performed to determine what details need to be included in such an inversion scheme and which can be safely ignored. This led to a relatively simple inversion method and this was shown to work well for small sections of canopy from a number of overlapping scans. The greater the number of scans the higher the precision but usable results were obtained with only five as long as their zeniths covered a range of 60^o.

Using two wavelengths allowed the separation of leaf and bark areas in birch forests and so the estimation of LAI rather than PAI. In Sitka spruce forests the multiple scattering enhancement to the higher reflectance wavelength prevented this separation with only the single scattering albedo. It may be possible to use an enhanced reflectance and so take multiple scattering into account (Huang *et al.* 2007) and so separate leaf from bark, but there was not time to pursue this.

7.3 Ground based future work

Due to time constraints the inversion method was only tested comprehensively on small sections of canopy. Many more tests would be needed before the value of the technique can be proven.

7.3.1 Complete canopies

A brief attempt was made to apply the method to a complete canopy and whilst it showed promise the roughness of the implementation prevented a full assessment of accuracy and so a direct comparison with the gap fraction method of Jupp *et al.* (2009). Unlike the gap fraction it did not show any specific limitations in zenith ranges and so should be able to accurately measure a complete stand, as a remote sensing instrument would see the canopy, rather than missing low lying vegetation.

One of the biggest potential errors is the gap fraction correction, given in equation 68 in section 6.4. Whilst it should be correct on average, it may lead to some large spurious values and only tests with a range of complete canopies would reveal how often and dramatically this occurs.

More comprehensive tests are needed with a much broader range of canopy types and densities. It should be possible to determine how closely the scans need to be placed to ensure the complete measurement of a given stand and so how large that stand can be. It may be the case that in taller tree stands the beam does not reach the tree tops, in which case either more scans would be needed from the ground or it may be necessary to suspend the lidar above the canopy.

7.3.2 Validating remote signals

One of the potential applications of full waveform terrestrial lidar is to provide the structural information necessary to drive a radiative transfer model and predict remotely sensed signals. In some senses this would be easier than estimating biophysical parameters, as effective values would suffice. For example no voxel scale clumping would be needed as a remote sensing instrument will also miss what a terrestrial lidar misses.

An accurate canopy model is still needed. The accuracy of this and the subsequent remote sensing predictions can be determined by comparing signals simulated over the inverted canopies

and those simulated over the original geometrically explicit forest model with the ray tracer. This would show how well they agree and highlight any potential differences.

7.3.3 Simulation realism

For the terrestrial lidar simulations a fairly idealised instrument was used. This had an infinitely short laser pulse and no noise. For complete realism these two effects should be included. Due to the short range, noise should be less of an issue than for spaceborne lidar but laser pulse duration has the potential to limit the inverted volumetric resolution (see section 6.9).

Removal of laser pulse duration was shown to be possible by deconvolution, but mathematically ill posed and so not robust (section 5.9). Therefore it may be necessary to use a laser with a pulse length shorter than the inverted canopy voxel.

This thesis dealt with lidar characteristics that cannot be avoided and so must be dealt with by inversion methods. There are potentially other effects that can change the measured lidar signal such as optical misalignment and laser "ringing" (echoes in the laser pulse), but it is assumed that these can be corrected for either during calibration or by engineering solutions. Therefore whilst the simulator could include these effects they were not dealt with in this thesis, which was primarily an investigation of the signal processing aspect.

References

Abdalati, W., Carabajal, C., Csatho, B., Dubayah, R., Fowler, D., Fricker, H. A., Hall, F., Harding, D., Joughin, I., Kimes, D., Kwok, R., Laxon, S., Lefsky, M., Luthcke, S., Martin, S., Minnett, P., Ranson, J., Sauber, J. M., Scambos, T., Spinhirne, J., Thomas, R., Urban, T., Wiscombe, W., and Zwally, J., 2007, Report from the ICESat-II workshop, NASA.

Albota, M. A., Heinrichs, R. M., Kocher, D. G., Fouche, D. G., Player, B. E., O'Brian, M. E., BF, A., Zayhowski, J. J., Mooney, J., Willard, B. C., and Carlson, R. R., 2002, Three-dimensional imaging laser radar with a photon-counting avalanche photodiode array and microchip laser. *Applied Optics*, **41**, 7671–7678.

Allen, M. T., Prusinkiewicz, and DeJong, T. M., 2005, Using L-systems for modeling source-sink interactions, architecture and physiology of growing trees: the L-PEACH model. *New Phytologist*, **166**, 869–880.

Allen, W. A., Gausman, H. W., and Richardson, A. J., 1970a, Mean effective optical constants of cotton leaves. *Journal of the Optical Society of America*, **60**, 542–547.

Allen, W. A., Gausman, H. W., Richardson, A. J., and Thomas, J. R., 1969, Interaction of isotropic light with a compact plant leaf. *Journal of the Optical Society of America*, **59**, 1376–1379.

Allen, W. A., Gayle, T. V., and Richardson, A. J., 1970b, Plant-canopy irradiance specified by the Duntley equations. *Journal of the Optical Society of America*, **60**, 372–376.

Alley, R., T, B., Bindoff, N. L., Chen, Z., Chidthaisong, A., Friedlingstein, P., Gregory, J., Hegerl, G., Heimann, M., Hewitson, B., Joos, B., Jouzel, J., Kattsov, V., Lohmann, U., Manning, M., Matsuno, T., Molina, M., Nicholls, N., Overpeck, J., Raga, G., Ramaswamy, V., Ren, J., Rusticucci, M., Solomon, S., Somerville, R., Stocker, T. F., Stott, P., Stouffer, R. J., Whetton, P.,

Wood, R. A., and Wratt, 2007, *Fourth Assessment Report: Climate Change 2007: Working Group I Report: The Physical Science Basis* (Geneva: IPCC).

Bacher, U., and Mayer, H., 2000, Automatic extraction of trees in urban areas from aerial imagery, In *ISPRS*, volume XXXIII, Amsterdam.

Baltsavias, E. P., 1999, Airborne laser scanning: basic relations and formulas. *ISPRS Journal of Photogrammetry & Remote Sensing*, **54**, 199–214.

Balzter, H., 2001, Forest mapping and monitoring with interferometric synthetic aperture radar. *Progress in Physical Geography*, **25**, 159–177.

Balzter, H., Rowland, C. S., and Saich, P., 2007, Forest canopy height and carbon estimation at Monks Wood national nature reserve, UK, using dual-wavelength SAR interferometry. *Remote Sensing of Environment*, **108**, 224–239.

Barclay, H. J., Trofymow, J. A., and Leach, R. I., 2000, Assessing bias from boles in calculating leaf area index in immature Douglas-fir with the LI-COR canopy analyzer. *Agricultural and Forest Meteorology*, **100**, 255–260.

Baret, F., Andrieu, B., and Steven, M. D., 1993, Gap frequency and canopy architecture of sugar beet and wheat crops. *Agricultural and Forest Meteorology*, **65**, 261–279.

Barnes, W. L., Pagano, T. S., and Salomonson, V. V., 1998, Prelaunch characteristics of the Moderate Resolution Imaging Spectroradiometer (MODIS) on EOS-AM1. *IEEE Transactions on Geoscience and Remote Sensing*, **36**, 1,088–1,100.

Bienert, A., Scheller, S., Keane, E., Mohan, F., and Nugent, C., 2007, Tree detection and diameter estimations by analyses of forest terrestrial laserscanner point clouds, In *ISPRS Workshop on laser scanning and Silvilaser*, Finland, pp. 50–55.

Blair, J., Coyle, D., Bufton, J., and Harding, D., 1994, Optimization of an airborne laser altimeter for remote sensing of vegetation and tree canopies, In *Geoscience and Remote Sensing Symposium, 1994. IGARSS '94. Surface and Atmospheric Remote Sensing: Technologies, Data Analysis and Interpretation., International*, volume 2, pp. 939–941.

Blair, J. B., Rabine, D. L., and Hofton, M. A., 1999, The laser vegetation imaging sensor: a medium-altitude, digitisation only, airborne laser altimeter for mapping vegetation and topography. *ISPRS Journal of Photogrammetry & Remote Sensing*, **54**, 115–122.

Bonhomme, R., and Chartier, P., 1972, The interpretation and automatic measurement of hemispherical photographs to obtain sunlit foliage area and gap frequency. *Israel Journal of Agricultural Research*, **22**, 53–61.

Borel, C. C., Gerstl, S. A. W., and Powers, B. J., 1991, The radiosity method in optical remote sensing of structured 3-D surfaces. *Remote Sensing of Environment*, **36**, 13–44.

Boudreau, J., Nelson, R. F., Margolis, H. A., Beaudoin, A., Guindon, L., and Kimes, D. S., 2008, Regional aboveground forest biomass using airborne and spaceborne LiDAR in Quebec. *Stochastic Environmental Risk Assessment*, **23**, 387–397.

Bréda, N. J. J., 2003, Ground-based measurements of leaf area index: a review of methods, instruments and controversies. *Journal of Experimental Botany*, **54**, 2403–2417.

Brooks, R., 2008, *The Handley Page Victor* (Pen & Sword publishing).

Brown, I. F., Martinelli, L. A., Thomas, W. W., Moreira, M. Z., Ferreira, C. A. C., and Victoria, R. A., 1995, Uncertainty in the biomass of Amazonian forests: An example from Rondônia, Brazil. *Forest Ecology and Management*, **75**, 175–189.

Cabrel, B., Max, N., and Springmeyer, R., 1987, Bidirectional reflectance functions from surface bump maps, In *Computers & Graphics*, volume 21, SIGGRAPH, Anaheim, pp. 273–281.

Campbell, G., 1986, Extinction coefficients for radiation in plant canopies calculated using an ellipsoidal inclination angle distribution. *Agricultural and Forest Meteorology*, **36**, 317–321.

Campbell, G., 1990, Derivation of an angle density function for canopies with ellipsoidal leaf angle distributions. *Agricultural and Forest Meteorology*, **49**, 173–176.

Cescatti, A., 1997a, Modelling the radiative transfer in discontinuous canopies of asymmetric crowns. I. Model structure and algorithms. *Ecological Modelling*, **101**, 263–274.

Cescatti, A., 1997b, Modelling the radiative transfer in discontinuous canopies of asymmetric crowns. II. Model testing and application in a Norway spruce. *Ecological Modelling*, **101**, 275–284.

Chandrasekhar, S., 1960, *Radiative Transfer* (New York, New York: Dover).

Chelle, M., 2005, Phylloclimate or the climate perceived by individual plant organs: What is it? How to model it? What for? *New Phytologist*, **166**, 781–790.

Chen, J. M., 1996, Optically-based methods for measuring seasonal variation of leaf area index in boreal conifer stands. *Agricultural and Forest Meteorology*, **80**, 135–163.

Chen, J. M., and Black, T. A., 1992, Defining leaf area index for non-flat leaves. *Plant Cell Environment*, **15**, 421–429.

Chen, J. M., and Cihlar, J., 1995, Plant canopy gap-size analysis theory for improving optical measurements of leaf-area index. *Applied Optics*, **34**, 6211–6222.

Chen, J. M., and Cihlar, J., 1996, Retrieving leaf area index of boreal conifer forests using Landsat TM images. *Remote Sensing of Environment*, **55**, 153–162.

Chen, J. M., Rich, P. M., Gower, S. T., Norman, J. M., and Plummer, S., 1997, Leaf area index of boreal forests: Theory, techniques and measurements. *Journal of Geophysical Research*, **102**, 29,429–29,443.

Ciernewski, J., 1999, *Geometrical modelling of soil bidirectional reflectance in the optical domain* (Poznan: Bogucki Scientific Publishers).

Clark, D., and Harris, P., 2010, *Joint UK Land Environment Simulator (JULES)*, Met Office, second edition.

Clark, M. L., Clark, D. B., and Roberts, D. A., 2004, Small-footprint lidar estimation of sub-canopy elevation and tree height in a tropical rain forest landscape. *Remote Sensing of Environment*, **91**, 68–89.

Clawges, R., Vierling, L., Calhoon, M., and Toomey, M., 2007, Use of a ground-based scanning lidar for estimation of biophysical properties of western larch. *International Journal of Remote Sensing*, **28**, 4331–4344.

Cohen, M. F., and Wallace, J. R., 1993, *Radiosity and realistic image synthesis* (Cambridge. MA: Academic Press).

Comas, C., Palahí, M., Pukkala, T., and Mateu, J., 2009, Characterising forest spatial structure through inhomogeneous second order characteristics. *Stochastic Environmental Risk Assessment*, **23**, 387–297.

Comrie, L. J., 1940, The use of calculating machines in ray tracing. *Proceedings of the Physical Society*, 246–252.

Coops, N. C., Hilker, T., Wulder, M. A., St-Onge, B., Newnham, G., Siggins, A., and Trofymow, J., 2006, Estimating canopy structure of Douglas-fir forest stands from discrete-return LiDAR. *Trees*, **DOI 10.1007/s00468-006-0119-6**.

Côte, J.-F., Widlowski, J.-L., Fournier, R. A., and Verstraete, M. M., 2009, The structural and radiative consistency of three-dimensional tree reconstructions from terrestrial lidar. *Remote Sensing of Environment*, **113**, 1067–1081.

Cox, P. M., Betts, R. A., Collins, M., Harris, P., Huntingford, C., and Jones, C. D., 2004, Amazon dieback under climate-carbon cycle projections for the 21st century. *Theoretical Applied Climatology*, **78**, 137–156.

Cutrona, L. J., Vivian, W. E., Leith, E. N., and Hall, G. O., 1961, A high resolution radar combat-surveillance system. *IRE Transactions on Military Electronics*, **MIL-5**, 127–131.

Dana, K. J., Ginneken, B. V., Nayar, S. K., and Koenderink, J. J., 1999, Reflectance and texture of real-world surfaces. *ACM Transactions on Graphics*, **18**, 1–34.

Danson, F. M., Hetherington, D., Morsdorf, F., Koetz, B., and Allgöwer, B., 2007, Forest canopy gap fraction from terrestrial laser scanning. *IEEE Geoscience and Remote Sensing Letters*, **4**, 157–160.

DaSheng, F., 1993, A new formula for the linear constrained matrix inversion, In *Proceedings of IEEE Topical Symposium on Combined Optical, Microwave, Earth and Atmosphere Sensing*, pp. 60–63.

Daughtry, C. S. T., Biehl, L. L., and Ranson, K. J., 1989, A new technique to measure the spectral properties of conifer needles. *Remote Sensing of Environment*, **27**, 81–91.

Davidson, G. W., Cumming, J. G., and Ito, M. R., 1996, A chirp scaling approach for processing squint mode SAR data. *IEEE Transactions on Aerospace and Electronic Systems*, **32**, 121–133.

Davies, A., Jenkins, R. M., Perrett, B. J., Leigh, R., Lawrence, J., Lewis, P., Hancock, S., Disney, M., and Quegan, S., 2008, Hollow waveguide hybrid integration technology for space borne lidar and the science case based on CO_2 and canopy measurements, Technical Report QINETIQ/AT/DEF/TR0800455, QinetiQ, NERC/CEOI contract CS/008/PR/2007.

Dawson, T. P., Curran, P. J., North, P. R. J., and Plummer, S. E., 1999, The propagation of foliar biochemical absorption features in forest canopy reflectance: A theoretical analysis. *Remote Sensing of Environment*, **67**, 147–159.

Dawson, T. P., Curran, P. J., and Plummer, S. E., 1998, LIBERTY-Modeling the effects of leaf biochemical concentration on reflectance spectra. *Remote Sensing of Environment*, **65**, 50–56.

Deblonde, G., Penner, M., and Royer, A., 1994, Measuring leaf area index with the LI-COR LAI-2000 in pine stands. *Ecology*, **75**, 1507–1511.

Defries, R. S., Hansen, M. C., Townshend, J. R. G., Janetos, A. C., and Lovelands, T. R., 2000, A new global 1-km dataset of percentage tree cover derived from remote sensing. *Global Change Biology*, **6**, 247–254.

Diner, D., Beckert, J., Reilly, T., Bruegge, C., Conel, J., Kahn, R., Martonchik, J., Ackerman, T., Davies, R., Gerstl, S., Gordon, H., Muller, J.-P., Myneni,

R., Sellers, P., Pinty, B., and Verstraete, M., 1998, Multi-angle Imaging Spectro-Radiometer (MISR) instrument description and experiment overview. *IEEE Transactions on Geoscience and Remote Sensing*, **36**, 1072–1087.

Disney, M. I., Lewis, P., and North, P. R. J., 2000, Monte Carlo ray tracing in optical reflectance modelling. *Remote Sensing Reviews*, **18**, 163–196.

Disney, M. I., Lewis, P., and Saich, P., 2006, 3D modelling of forest canopy structure for remote sensing simulations in the optical and microwave domains. *Remote Sensing of Environment*, **100**, 114–132.

Disney, M. I., Lewis, P. E., Bouvet, M., Prieto-Blanco, A., and Hancock, S., 2009, Quantifying surface reflectivity for spaceborne lidar missions via two independent methods. *IEEE Transactions on Geoscience and Remote Sensing*, **47**, 3262–3721.

Donoghue, D. N. M., and Watt, P. J., 2006, Using LiDAR to compare forest height estimates from IKONOS and Landsat ETM+ data in Sitka spruce plantation forests. *International Journal of Remote Sensing*, **27**, 2161–2175.

Doughty, Christopher, E., and Goulden, M. L., 2008, Seasonal patterns of tropical leaf area index and CO_2 exchange. *Journal of Geophysical Research*, **113**.

Dowman, I. J., 2004, Integration of lidar and IfSAR for mapping. *International Archives of Photogrammetry and Remote Sensing*, Commission II, WGII/2.

Drake, J. B., Dubayah, R. O., Clark, D. B., Knox, R. G., Blair, J. B., Hofton, M. A., Chazdon, R. L., Weishampel, J. F., and Prince, S. D., 2002, Estimation of tropical forest structural characteristics using large-footprint lidar. *Remote Sensing of Environment*, **79**, 305–319.

Drinkwater, M., Ingmann, P., Kern, M., Langen, J., Drusch, M., Davidson, M., Bensi, P., Carnicero, B., Thompson, A., Silvestrin, P., Lin, C., Heliere, F., Bezy, J., Durand, Y., Aguirre, M., and Haagmans, R., 2008, ESA's Future Earth Explorer: new candidate mission concepts. *AGU Fall Meeting Abstracts*, A683+.

Dubayah, R., Bergen, K., Hall, F., Hurtt, G., Houghton, R., Kellndorfer, J., Lefsky, M., Moorcroft, P., Nelson, R., Saatchi, S., Shugart, H., Simard, M., Ranson, J., and Blair, J. B., 2008, Global Vegetation Structure from NASA's DESDynI Mission: An Overview. *AGU Fall Meeting Abstracts*, H1+.

Dubayah, R., Blair, J. B., Bufton, J. L., Clark, D. B., JáJá, J., Knox, R., Luthcke, S. B., Prince, S., and Weishampel, J., 1997, The vegetation canopy lidar mission, In *Conference on land satellite in the next decade II. Sources and applications*, American Society for Photogrammetry and Remote Sensing, Washington.

Dubayah, R. O., and Drake, J. B., 2000, Lidar remote sensing for forestry applications. *Journal of Forestry*, **98**, 44–46.

Dufrêne, E., and Bréda, N., 1995, Estimation of deciduous forest leaf area index using direct and indirect methods. *Oecologia*, **104**, 156–162.

Duntley, S. Q., 1942, The optical properties of diffusing materials. *Journal of the Optical Society of America*, **32**, 61–70.

Elhuset, K., Andersen, P. H., Hauge, S., Isaksson, E., and Weydahl, D. J., 2003, ERS tandem InSAR processing for DEM generation, glacier motion estimation and coherence analysis on Svalbard. *International Journal of Remote Sensing*, **24**, 1415–1437.

Eriksson, H., Eklundh, L., Hall, K., and Lindroth, A., 2005, Estimating LAI in deciduous forest stands. *Agricutural and Forest Meteorology*, **129**, 27–37.

ESA, 2010, ESA earth explorer mission summaries, http://www.esa.int/esaLP/ASEWGWNW9SC_LPearthexp_0

European Commission, JRC, 2009, RAdiation transfer Model Intercomparison - IV, http://rami-benchmark.jrc.ec.europa.eu/HTML/RAMI-IV/RAMI-IV.php.

Falkowski, M. J., Smith, A. M. S., Hudak, A. T., Gessler, P. E., Vierling, L. A., and Crookston, N. L., 2006, Automated estimation of individual conifer tree height and crown diameter via two-dimensional spatial wavelet analysis of lidar data. *Canadian Journal of Remote Sensing*, **32**, 153–161.

Fassnacht, K. S., Gower, S. T., Normas, J. M., and McMurtie, R. E., 1994, A comparison of optical and direct methods for estimating foliage surface area index in forests. *Agricultural and Forest Meteorology*, **71**, 183–207.

Fisher, J. B., 1992, How predictive are computer simulations of tree architecture. *International Journal of Plant Science*, **153**, 137–146.

Foley, J. D., van Dam, A., Feiner, S. K., and Hughes, J. F., 1992, *Computer graphics; principles and practice*, second edition (Addison-Wesley publishing company).

Foster, M., 2008, Hyperspectral Imaging Lidar(LADAR) Final Report, WP1000, NERC/DIUS Contract SA-014-DJ-2007, Lidar Technologies ltd.

Frazer, G. W., Fournier, R. A., Trofymow, J. A., and Hall, R. J., 2001, A comparison of digital and film fisheye photography for analysis of forest canopy structure and gap light transmission. *Agricultural and Forest Meteorology*, **109**, 249–263.

Freeman, A., and Saatchi, S. S., 2004, On the detection of Faraday rotation in linearly polarized L-band SAR backscatter signatures. *IEEE Transactions on Geoscience and Remote Sensing*, **42**, 1607–1616.

Friedlander, H., and Koch, B., 2000, First experiment in the application of laser scanner data from the assessment of vertical and horizontal forest structures. *International Archives of Photogrammetry and Remote Sensing*, **33**, 693–700.

Fuchs, M., Asrar, G., and Kanemasu, E. T., 1984, Leaf area estimates from measurements of photosynthetically active radiation in wheat canopies. *Agricultural and Forest Meteorology*, **32**, 13–22.

Gao, X., Huete, A. R., Ni, W., and Miura, T., 2000, Optical-biophysical relationships of vegetation spectra without background contamination. *Remote Sensing of Environment*, **74**, 609–620.

van Gardingen, P. R., Jackson, G. E., Hernandez-Daumas, S., Russell, G., and Sharp, L., 1999, Leaf area index estimates obtained for clumped canopies using hemispherical photography. *Agricultural and Forest Meteorology*, **94**, 243–257.

Gastellu-Etchegorry, J. P., Demarez, V., and Zagolski, F., 1996, Modeling radiative transfer in heterogeneous 3-D vegetation canopies. *Remote Sensing of Environment*, **58**, 131–156.

Gastellu-Etchegorry, J. P., Martin, E., and Gascon, F., 2004, DART: a 3D model for simulating satellite images and studying surface radiation budget. *Internation Journal of Remote Sensing*, **25**, 73–96.

Glassner, A., 1986, Adaptive precision in texture mapping, In *Proceedings of SIGGRAPH*, SIGGRAPH, pp. 297–306.

Glassner, A., 1989, *An introduction to ray tracing* (Academic Press).

Gobron, N., Pinty, B., and Verstraete, M. M., 1997, Theoretical limits to the estimation of the leaf area index on the basis of visible and near-infrared remote sensing data. *IEEE Transactions on Geoscience and Remote Sensing*, **35**, 1438–1445.

Godin, C., Costes, E., and Sinoquet, H., 1999, A method for describing plant architecture which integrates topology and geometry. *Annals of Botany*, **84**, 343–357.

Godin, C., and Sinoquet, H., 2005, Functional-structural plant modelling. *New Phytologist*, **166**, 705–708.

Goel, N., and Strebel, D., 1984, Simple Beta distribution representation of leaf orientation in vegetation canopies. *Agronomy Journal*, **76**, 800–802.

Gold, R., 1964, An iterative unfolding method for response matrices, Technical Report NAL-6984, Argonne national laboratory.

Goldstein, R. M., Zebker, H. A., and Werner, C. L., 1988, Satellite radar interferometry: Two dimensional phase unwrapping. *Radio Science*, **23**, 713–720.

Golomb, S. W., 1966, Run-length encodings (Run-length encodings, determining explicit form of Huffman coding when applied to geometric data). *IEEE Transactions on Information Theory*, **IT-12**, 399–401.

Goodwin, N R. Coops N C. Culvenor, D. S., 2006, Assessment of forest structure with airborne LiDAR and the effects of platform altitude. *Remote Sensing of Environment*, **103**, 140–152.

Goudriaan, J., 1988, The bare bones of leaf-angle distribution in radiation models for canopy photosynthesis and energy exchange. *Agricultural and Forest Meteorology*, **43**, 155–169.

Govaerts, Y. M., Jacquemoud, S., Verstraete, M. M., and Ustin, S. L., 1996, Three-dimensional radiation transfer modeling in a dictyledon leaf. *Applied Optics*, **35**, 6585–6598.

Govaerts, Y. M., and Verstraete, M. M., 1998, Raytran: A Monte Carlo ray-tracing model to compute light scattering in three-dimensional heterogeneous media. *IEEE Transactions on Geoscience and Remote Sensing*, **36**, 493–505.

Gower, S. T., Kucharik, C. J., and Norman, J. M., 1999, Direct and indirect estimation of leaf area index, FAPAR and net primary production of terrestrial ecosystems. *Remote Sensing of Environment*, **70**, 29–51.

Gower, S. T., and Norman, J. M., 1991, Rapid estimation of leaf area index in conifer and broad-leaf plantations. *Ecology*, **72**, 1896–1900.

Graham, L. C., 1974, Synthetic interferometer radar for topographic mapping, In *Proceedings of the IEEE*, volume 62, pp. 763–768.

Grant, L., Daughtry, C. S. T., and Vanderbilt, V. C., 1993, Polarized and specular reflectance variation with leaf surface features. *Physilogia Plantarum*, **88**, 1–9.

Grier, C. C., and Waring, R. H., 1974, Conifer foliage mass related to sapwood area. *Forest Science*, **20**, 205–206.

Gurdev, L. L., Dreishuh, T. N., and Stoyanov, D. V., 1993, Deconvolution techniques for improving the resolution of long-pulse lidars. *Journal of the Optical Society of America*, **10**, 2296–2306.

Hancock, S., Lewis, P., and Disney, M., 2008, Hyperspectral Imaging Lidar(LADAR) Final Report, WP4000, NERC/DIUS Contract SA-014-DJ-2007, Centre for Terrestrial Carbon Dynamics, UCL.

Hansen, M. C., DeFries, R. S., Townshend, J. R. G., Sohlberg, R., Dimiceli, C., and Carroll, M., 2002, Towards an operational MODIS continuous field of percent tree cover algorithm: examples using AVHRR and MODIS data. *Remote Sensing of Environment*, **83**, 303–319.

Hapke, B., 1981, Bidirectional reflectance spectroscopy. I. Theory. *Journal of Geophysical Research*, **86**, 3039–3054.

Hapke, B., DiMucci, D., Nelson, R., and Smythe, W., 1996, The cause of the hot spot in vegetation canopies and soils: shadow-hiding versus coherent backscatter. *Remote Sensing of Environment*, **58**, 63–68.

Harding, D., Blair, J., Garvin, J., and Lawrence, W., 1994, Laser altimetry waveform measurement of vegetation canopy structure, In *Geoscience and Remote Sensing Symposium. IGARSS '94. Surface and Atmospheric Remote Sensing: Technologies, Data Analysis and Interpretation., International*, volume 2, pp. 1251–1253.

Harding, D. J., Abshire, J., Dabney, P., Seas, A., Shuman, C., Sun, X., Calett, S., Casliyev, A., Yu, T. Huss, T., Marzouk, and Zheng, Y., 2008, The swath imaging multi-polarization photon-counting lidar (SIMPL): A spaceflight prototype, In *IEEE International Geoscience and remote sensing symposium*, IGARSS, Boston.

Harding, D. J., and Carabajal, C. C., 2005, ICESat waveform measurements of within-footprint topographic relief and vegetation vertical structure. *Geophysical Research Letters*, **32**, L21S10.

Hofton, M. A., Minster, J. B., and Blair, J. B., 2000, Decomposition of laser altimeter waveforms. *IEEE Transactions on Geoscience and Remote Sensing*, **38**, 1989–1996.

Hofton, M. A., Rocchio, L. E., Blair, J. B., and Dubayah, R., 2002, Validation of vegetation canopy lidar sub-canopy topography measurements for a dense tropical forest. *Journal of Geodynamics*, **34**, 491–502.

Hollinger, D. Y., Aber, J., Dail, B., Davidson, E. A., Goltz, S. M., Hughes, H., Leclerc, M. Y., Lee, J. T., Richardson, A. D., Rodrigues, C., Scotts, N. A., Achuatavarier, D., and Walsh, J., 2004, Spatial and temporal variability in forest-atmosphere CO_2 exchange. *Global Change Biology*, **10**, 1689–1706.

Honda, H., 1971, Description of the form of trees by the parameters of the tree-like body: Effects of the branching angle and the branch length on the shape of the tree-like body. *Journal of Theoretical Biology*, **31**, 331–338.

Honda, H., 1978, Tree branching angle: Maximising effective leaf area. *Science*, **199**, 888–890.

Hosgood, B., Jacquemoud, S., Andreoli, G., Verdebout, J., Pedrini, G., and Schmuck, G., 1994, *Leaf Optical Properties EXperiment 93 (LOPEX93)* (Ispra, Italy: European Comission - Joint Research Centre), EUR 16095 EN.

Hosoi, F., and Omasa, K., 2006, Voxel-based 3-D modeling of individual trees for estimating leaf area density using high-resolution portable scanning lidar. *IEEE Transactions on Geoscience and Remote Sensing*, **44**, 3610–3618.

Houstoun, R. a., 1938, *A treatise on light*, 7th edition (Longmans, Green and co.).

Hu, J., Tan, B., Shabanoc, N., Crean, K. A., Martonchik, J. V., Diner, D. J., Knyazikhin, Y., and Myneni, R. B., 2003, Performance of the MISR LAI and FPAR algorithm: a case study in Africa. *Remote Sensing of Environment*, **88**, 324–340.

Huang, D., Knyazikhin, Y., Dickinson, R. E., Rautiainen, M., Stenberg, P., Disney, M., Lewis, P., Cescatti, A., Tian, Y., Verhoef, W., Martonchik, J. V., and My-

NENI, R. B., 2007, Canopy spectral invariants for remote sensing and model applications. *Remote Sensing of Environment*, **106**, 106–122.

HUETE, A., DIDAN, K., RODRIGUEZ, E. P., GAO, X., and FERREIRA, L. G., 2002, Overview of the radiometric and biophysical performance of the MODIS vegetation indices. *Remote Sensing of Environment*, **83**, 194–213.

HUETE, A. R., 1988, A soil adjusted vegetation index. *Remote Sensing of Environment*, **25**, 295–309.

HUETE, A. R., LIU, H. Q., BATCHILY, K., and VAN LEEUWEN, W., 1997, A comparison of vegetation indices over a global set of TM images for EOS-MODIS. *Remote Sensing of Environment*, **59**, 440–451.

HURTT, G. C., DUBAYAH, R., MOORCROFT, P. R., PACALA, S. W., BLAIR, J. B., and FEARON, M. G., 2004, Beyond potential vegetation: combining lidar data and a height structured model for carbon studies. *Ecological Applications*, **14**, 873–883.

HYDE, P., DUBAYAH, R., PETERSON, B., BLAIR, J. B., HOFTON, M., HUNSAKER, C., KNOX, R., and WALKER, W., 2005, Mapping forest structure for wildlife habitat analysis using waveform lidar: Validation of montane ecosystems. *Remote Sensing of Environment*, 427–437.

HYDE, P., DUBAYAH, R., WALKER, W., BLAIR, J. B., HOFTON, M., and HUNSAKER, C., 2006, Mapping forest structure for wildlife habitat analysis using multi-sensor (LiDAR, SAR/InSAR, ETM+, Quickbird) synergy. *Remote Sensing of Environment*, **102**, 63 – 73.

HYDE, P., NESLON, R., KIMES, D., and LEVINE, E., 2007, Exploring LiDAR-RaDAR synergy–predicting aboveground biomass in a southwestern ponderosa pine forest using LiDAR, SAR and InSAR. *Remote Sensing of Environment*, **106**, 28–38.

INNES, J. L., and KOCH, B., 1998, Forest biodiversity and its assessment by remote sensing. *Global Ecology and Biogeography Letters*, **7**, 397–419.

Jacquemoud, A., Baret, F., Andrieu, B., Danson, F. M., and Jaggard, K., 1995, Extraction of vegetation biophysical parameters by inversion of the PROSPECT + SAIL models on sugar beet canopy reflectance data. Application to TM and AVIRIS sensors. *Remote Sensing of Environment*, **52**, 163–172.

Jacquemoud, S., and Baret, F., 1990, Prospect: A model of leaf optical properties spectra. *Remote Sensing of Environment*, **34**, 75–91.

Jacquemoud, S., Baret, F., and Hanocq, J. F., 1992, Modeling spectral and bidirectional soil reflectance. *Remote Sensing of Environment*, **41**, 123–132.

James, L. A., Watson, D. G., and Hansen, W. F., 2007, Using LiDAR data to map gullies and headwater streams under forest canopy: South Carolina, USA. *Catena*, **71**, 132–144.

Jansson, P. A., 1997, *Deconvolution of images and spectra*, second edition (San Diego, London: Academic Press).

Jenkins, R. M., Devereux, R. W. J., and Heaton, J. M., 1992, Waveguide beam splitters and recombiners based on multimode propogation phenomena. *Optics Letters*, **17**, 991–991.

Jonckheere, I., Fleck, S., Nackaerts, K., Muys, B., Coppin, P., Weiss, M., and Baret, F., 2004, Review of methods for in situ leaf area index determination. Part I. Theories, sensors and hemispherical photography. *Agricultural and Forest Meteorology*, **121**, 19–35.

Jonckheere, I., Nackaerts, K., Muys, B., and Coppin, P., 2005, Assessment of automatic gap fraction estimation of forests from digital hemispherical photography. *Agricultural and Forest Meteorology*, **132**, 96–114.

Jupp, D. L. B., Culvenor, D. S., Lovell, J. L., Newnham, G. J., Strahler, A. J., and Woodcock, C. E., 2009, Estimating forest LAI profiles and structural parameters using a ground-based laser called Echidna. *Tree Physiology*, **29**, 171–181.

Jupp, D. L. B., and Lovell, J. L., 2007, Airborne and ground-based lidar systems for forest measurement: Background and principles, Research Paper 017, CSIRO Marine and Atmospheric Research, Canberra.

Jupp, D. L. B., and Strahler, A. H., 1991, A hotspot model for leaf canopies. *Remote Sensing of Environment*, **38**, 193–210.

Justice, C. O., 1986, Monitoring east African vegetation using AVHRR data. *International Journal of Remote Sensing*, **6**, 1,335–1,372.

Kaasalainen, S. Lindroos, T. H. J., 2007, Toward Hyperspectral Lidar: Measurement of spectral backscatter intensity with a supercontinuum laser source. *IEEE Geoscience and Remote Sensing Letters*, **4**, 211–215.

Kaiser, G., 1994, *A friendly guide to wavelets* (Boston: Birkhäuser).

Kaufman, Yoram, J., and Tanré, D., 1992, Atmospherically resistant vegetation index (ARVI) for EOS-MODIS. *IEEE Transaction on Geoscience and Remote Sensing*, **30**, 261–270.

Kauppinen, J., and Partanen, J., 2001, *Fourier transforms in spectroscopy* (Berlin: Wiley-VCH).

Kellndorfer, J., Walker, W., Pierce, L., Dobson, C., Fites, J., Hunsaker, C., and Vona, J., 2004, Vegetation height estimate from Shuttle Radar Tomography Mission and national elevation datasets. *Remote Sensing of Environment*, **93**, 339–358.

Kenyi, L. W., Dubayah, R., Hofton, M., and Schardt, M., 2009, Comparitive analysis of SRTM-NED vegetation canopy height to LIDAR-derived vegetation canopy metrics. *International Journal of Remote Sensing*, **30**, 2,797–2,811.

Kimes, D., Gastellu-Etchegorry, J., and Estève, P., 2002, Recovery of forest canopy characteristics through inversion of a complex 3D model. *Remote Sensing of Environment*, **79**, 320–328.

Kimes, D. S., and Kirchner, J. A., 1982, radiative transfer model for heterogeneous 3-D scenes. *Applied Optics*, **21**, 4119–4129.

Knyazikhin, Y., Martonchik, J. V., Myneni, R. B., Diner, D. J., and Running, S. W., 1998, Synergistic algorithm for estimating vegetation canopy leaf area index and fraction

of absorbed photosynthetically active radiation from MODIS and MISR data. *Journal of Geophysical Research*, **103**, 32,257–32,276.

Knyazikhin, Y. V., Marshak, A. L., and Myneni, R. B., 1992, Interaction of photons in a canopy of finite-dimensional leaves. *Remote Sensing of Environment*, **36**, 61–74.

Koenderink, J. J., and van Doorn, A. J., 1996, Illuminance texture due to surface mesostructure. *Journal of the Optical Society of America*, **13**, 452–463.

Koetz, B., Morsdorf, F., Sun, G., Ranson, K. J., Itten, J., and Allgöwer, B., 2006, Inversion of a lidar waveform model for forest biophysical parameter estimation. *IEEE Geoscience and Remote Sensing Letters*, **3**, 49–53.

Kovalev, V. A., and Eichinger, W. E., 2004, *Elastic Lidar; theory, practice and analysis methods* (Hoboken, New Jersey: John Wiley & Sons inc.).

Kubelka, P., and Munk, F., 1931, An article on the optics of paint layers. *Zeilschrift fur technische Physik*, **12**, 593–620.

Kucharik, C. J., Norman, J. M., and Gower, S. T., 1998a, Measurement of leaf orientation, light distribution and sunlit leaf area in a boreal aspen forest. *Agricultural and Forest Meteorology*, **91**, 127–148.

Kucharik, C. J., Norman, J. M., and Gower, S. T., 1998b, Measurements of branch area and adjusting leaf area index indirect measurements. *Agricultural and Forest Meteorology*, **91**, 69–98.

Kuga, Y., and Ishimaru, A., 1984, Retroreflectance from a dense distribution of spherical particles. *Journal of the Optical Society of America*, **1**, 831–835.

Kuusk, A., 1991, The angular distribution of reflectance and vegetation indices in barley and clover canopies. *Remote Sensing of Environment*, **37**, 143–151.

Kuusk, A., 1995, A Markov chain model of canopy reflectance. *Agricultural and Forest Meteorology*, **76**, 221–236.

Kuusk, A., 1996, A computer efficient plant canopy reflectance model. *Computers and Geosciences*, **22**, 149–163.

Lacaze, R., Chen, J. M., Roujean, J.-L., and Leblanc, S. G., 2002, Retrieval of vegetation clumping index using hot spot signatures measured by POLDER instrument. *Remote Sensing of Environment*, **79**, 84–95.

Lang, A. R. G., 1991, Application of some of Cauchy's theorems to estimation of surface areas of leaves, needles and branches of plants, and light transmittance. *Agricultural and Forest Meteorology*, **55**, 191–212.

Lang, A. R. G., and Xiang, Y., 1986, Estimation of leaf area index from transmission of direct sunlight in discontinuous canopies. *Agricultural and Forest Meteorology*, **37**, 229–243.

Lang, A. R. G., Xiang, Y., and Norman, J. M., 1985, Crop structure and the penetration of direct sunlight. *Agricultural and Forest Meteorology*, **35**, 83–101.

Law, B. E., Van Tuyl, S., Cescatti, A., and Baldocchi, D. D., 2001, Estimation of leaf area index in open-canopy ponderosa pine forests at different succesional stages and management regimes in Oregon. *Agricultural and Forest Meteorology*, **108**, 1–14.

Leblanc, S. G., Chen, J. M., and Kwong, M., 2002, *Tracing Radiation and Architecture of Canopies TRAC MANUAL Version 2.1.3*, Natural Resources Canada, Ontario, Canada.

Lefsky, M. A., Cohen, W. B., Acker, S. A., Parker, G. C., Spies, T. A., and Harding, D., 1999, Lidar remote sensing of the canopy structure and biophysical properties of Douglas-fir and western hemlock forests. *Remote Sensing of Environment*, **10**, 339–361.

Lefsky, M. A., Cohen, W. B., Parker, G. G., and Harding, D. J., 2002, Lidar remote sensing for ecosystem studies. *BioScience*, **52**, 19–30.

Lefsky, M. A., Keller, M., Yong, P., de Camargo, P. B., and Hunter, M. O., 2007, Revised method for forest canopy height estimation from Geoscience Laser Altimeter System waveforms. *Journal of Applied Remote Sensing*, **1**, 1–18.

Levy, R. H. M., and Madden, E. A., 1933, The point method of pasture analysis. *New Zeland Journal of Agriculture*, **46**, 267–279.

Lewis, P., 1999, Three-dimensional plant modelling for remote sensing simulation studies using the Botanical Plant Modelling System. *Agronomie*, **19**, 185–210.

Lewis, P., 2006, Rat library, http://www2.geog.ucl.ac.uk/ plewis/bpms/src/start/tests/lidar.

Li, X., and Strahler, A. H., 1985, Geometrical-optical modeling of a conifer forest canopy. *IEEE Transactions on Geoscience and Remote Sensing*, **23**, 705–721.

Li, X., and Strahler, A. H., 1988, Modeling the gap probability of a discontinuous vegetation canopy. *IEEE Transactions on Geoscience and Remote Sensing*, **26**, 161–167.

Li, X., and Strahler, A. H., 1992, Geometric-optical bidirectional reflectance modeling of the discrete crown vegetation canopy: Effect of crown shape and mutual shadowing. *IEEE Transactions on Geoscience and Remote Sensing*, **30**, 276–292.

Li, X., Strahler, A. H., and Woodcock, C. E., 1995, A hybrid geometric optical-radiative transfer approach for modeling albedo and directional reflectance of discontinuous canopies. *IEEE Transactions on Geoscience and Remote Sensing*, **33**, 466–480.

LI-COR, 1988, *1800-12 integrating sphere instruction manual*, LI-COR inc., Lincoln, Nebraska, Publication No. 8305-0034.

LI-COR, 1992, *LAI-2000 plant canopy analyzer instruction/operating manual*, LI-COR inc., Lincoln, Nebraska.

Liang, S., 2004, *Quantitative remote sensing of land surfaces* (John Wiley & Sons, Inc.).

Liang, S., and Strahler, A. H., 1993, Calculation of the angular radiance distribution for a coupled atmosphere and canopy. *IEEE Transactions on Geoscience and Remote Sensing*, **31**, 491–502.

Lim, K., Treitz, P., Wulder, M., St-Onge, B., and Flood, M., 2003, LiDAR remote sensing of forest structure. *Progress in Physical Geography*, **27**, 88–106.

Lindenmeyer, A., 1968a, Mathematical models for cellular interactions in development. I. Filaments with one-sided inputs. *Journal of Theoretical Biology*, **18**, 280–299.

Lindenmeyer, A., 1968b, Mathematical models for cellular interactions in development. II. Simple branching filaments with two-sided inputs. *Journal of Theoretical Biology*, **18**, 300–315.

Liu, Q., Huang, H., Qin, W., Fu, K., and Li, X., 2007, An extended 3-D radiosity-graphics combined model for studying thermal-emission directionality of crop canopy. *IEEE Transactions on Geoscience and Remote Sensing*, **45**, 2900–2918.

Lovell, J. L., Jupp, D. L. B., Culvenor, D. S., and Coops, N. C., 2003, Using airborne and ground-based ranging lidar to measure canopy structure in Australian forests. *Canadian Journal of Remote Sensing*, **29**, 607–622.

MacArthur, R. H., and Horn, H. S., 1969, Foliage profile by vertical measurements. *Ecology*, **50**, 802–804.

Mack, R. N., and Pyke, D. A., 1979, Mapping individual plants with a field-portable digitizer. *Ecology*, **60**, 459–461.

Maier, S. W., Lüdeker, W., and Günther, K. P., 1999, SLOP: A revised version of the stochastic model for leaf optical properties. *Remote Sensing of Environment*, **68**, 273–280.

Marshall, J. D., and Waring, R. H., 1986, Comparison of methods of estimating leaf-area index in old-growth Douglas-fir. *Ecology*, **67**, 975–979.

McShane, M. C., Carlile, D. W., and Hinds, W. T., 1983, The effect of collector size on forest litter-fall collection and analysis. *Canadian Journal of Remote Sensing*, **13**, 1037–1042.

Means, J. E., Acker, S. A., Harding, D. J., Blair, J. B., Lefsky, M. A., Cohen, W. B., Harmon, M. E., and McKee, W. A., 1999, Use of large-footprint scanning airborne lidar to estimate forest stand characteristics in the western cascades of Oregon. *Remote Sensing of Environment*, **67**, 298–308.

Metropolis, N., and Ulam, S., 1949, The Monte Carlo method. *Journal of the American Statistical Association*, **44**, 335–341.

Miller, E. E., and Norman, J. M., 1971, A sunfleck theory for plant canopies. I Lengths of sunlit segments along a transect. *Agronomy Journal*, **63**, 735–738.

Monsi, M., and Saeki, T., 1953, Über den Lichtfaktor in den Pflanzengesellchaften und seine Bedeutung für die Stoffproduktion. *Japanese Journal of Botany*, **14**, 22–52.

Morsdorf, F., Frey, O., Meier, E., Itten, I., and Allgöwer, B., 2008a, Assessment of the influence of flying altitude and scan angle on biophysical vegetation products derived from airborne laser scanning. *International Journal of Remote Sensing*, **29**, 1387–1406.

Morsdorf, F., Nichol, C., Malthus, T. J., Patenaude, G., and Woodhouse, I. H., 2008b, Modelling multi-spectral LIDAR vegetation backscatter - assessing structural and physiological information content, In *proceedings of Silvilaser*, Edinburgh, pp. 257–265.

Myneni, R. B., Asrar, G., and Hall, F. G., 1992, A three-dimensional radiative transfer method for optical remote sensing of vegetated land surfaces. *Remote Sensing of Environment*, **41**, 105–121.

Myneni, R. B., Hoffman, S., Knyazikhin, Y., Privette, J. L., Glassy, J., Tian, Y., Wang, Y., Song, X., Zhang, Y., Smith, G. R., Lotsch, A., Friedl, M., Morisette, J. T., Votava, P., Nemani, R. R., and Running, S. W., 2002, Global products of vegetation leaf area and fraction absorbed PAR from year one of MODIS data. *Remote Sensing of Environment*, **83**, 214–231.

Myneni, R. B., Maggion, S., Iaquinta, J., Privette, J. L., Gobron, N., Pinty, B., Kimes, D. S., Verstraete, M. M., and Williams, D. L., 1995, Optical remote sensing of vegetation; Modeling, caveats and algorithms. *Remote Sensing of Environment*, **51**, 169–188.

Myneni, R. B., and Ross, J., 1989, A review on the theory of photon transport in leaf canopies. *Agricultural and Forest Meteorology*, **45**, 1–153.

Næsset, E., and Økland, T., 2002, Estimating tree height and crown properties using airborne scanning laser in a boreal nature reserve. *Remote Sensing of Environment*, **79**, 105–115.

Neckel, H., and Labs, D., 1984, The solar radiation between 3300 and 12500 Å. *Solar Physics*, **90**, 205–258.

Nelson, R., Krabill, W., and Maclean, G., 1984, Determining forest canopy characteristics using airborne laser data. *Remote Sensing of Environment*, **15**, 201–212.

Neuenschwander, A. L., Urban, T. J., Gutierrez, R., and Schutz, B. E., 2008, Characterization of ICESat/GLAS waveforms over terrestrial ecosystems: Implications for vegetation mapping. *Journal of Geophysical Research*, **113**, G02S03.

Ni, W., Li, X., Woodcock, C. E., Caetano, M. R., and Strahler, A. H., 1999, An analytical hybrid GORT model for bidirectional reflectance over discontinuous plant canopies. *IEEE Transactions on Geoscience and Remote Sensing*, **37**, 987–999.

Ni-Meister, W., Jupp, D. L. B., and Dubayah, R., 2001, Modeling lidar waveforms in heterogeneous and discrete canopies. *IEEE Transactions on Geoscience and Remote Sensing*, **39**, 1943–1958.

Ni-Meister, W., Strahler, A. H., Woodcock, C. E., Schaaf, C. B., Jupp, D. L. B., Yao, T., and Yang, X., 2008, Modeling the hemispherical scanning, below-canopy lidar and vegetation structure characteristics with a geometric-optical and radiative-transfer model. *Canadian Journal of Remote Sensing*, **34**, S385–S397.

Nilson, T., 1971, A theoretical analysis of the frequency of gaps in plant stands. *Agricultural and Forest Meteorology*, **8**, 25–38.

North, P., Rosette, J., Suarez, J., and Los, S., 2008, A Monte Carlo radiative transfer model of satellite waveform lidar, In *Proceedings of SilviLaser*, SilviLaser, Edinburgh, pp. 189–198.

North, P. R. J., 1996, Three-dimensional forest light interaction model using a Monte Carlo method. *IEEE Transactions on Geoscience and Remote Sensing*, **34**, 946–956.

Oker-Blom, P., and Smolander, H., 1988, The ratio of shoot silhouette area to total needle area in Scots pine. *Forest Science*, **34**, 894–906.

Omasa, K., Hosoi, F., and Konishi, A., 2007, 3D lidar imaging for detecting and understanding plant responses and canopy structure. *Journal of Experimental Botany*, **58**, 881–898.

Omasa, K., Qiu, G. Y., Watanuki, K., Yoshimi, K., and Akiyama, Y., 2003, Accurate estimation of forest carbon stocks by 3-D remote sensing of individual trees. *Environmental Science & Technology*, **37**, 1198–1202.

Onyx Computing Inc, ., 2009, Onyx tree professional, www.onyxtree.com, accessed 13th June 2009.

Oppenheimer, P. E., 1986, Real time design and animation of fractal plants and trees, In *Computers & Graphics*, volume 20, SIGGRAPH, Dallas, pp. 55–64.

Ozanne, C. M. P., Anhuf, D., Boulter, S. L., Keller, M., Kitching, R. L., Körner, C., Meinzer, F. C., Mitchell, A. W., Nakashizuka, T., Silva Dias, P. L., Stork, N. E., Wright, S. J., and Yoshimura, M., 2003, Biodiversity meets the atmosphere: A global view of forests canopies. *Science*, **301**, 183–186.

Parker, G. G., and Brown, M. J., 2000, Forest canopy stratification — Is it useful? *The American Naturalist*, **155**, 473–484.

Parker, G. G., Harding, D. J., and Berger, M. L., 2004, A portable LIDAR system for rapid determination of forest canopy structure. *Journal of Applied Ecology*, **41**, 755–767.

Paschotta, R., Collett, M., Kürz, P., Fiedler, K., Bachor, H. A., and Mlynek, J., 1994, Bright squeezed light from a singly resonant frequency doubler. *Physical Review Letters*, **72**, 3807–3811.

Patenaude, G., HIll, R. A., Milne, R., Gaveau, D. L. A., Briggs, B. B. J., and Dawson, T. P., 2004, Quantifying forest above ground carbon content using LiDAR remote sensing. *Remote Sensing of Environment*, **93**, 368–380.

Peterson, D. L., and Waring, R. H., 1994, Overview of the Oregon TransecT Ecosystem Research project. *Ecological Applications*, **4**, 211–225.

Pfeifer, N., Gorte, B., and Winterhalder, D., 2004, Automatic reconstruction of single trees from terrestrial laser scanner data. *ISPRS XX th Congress. Istanbul. Turkey. 12.07.-23.07.2004 Pitas, I*, 0–47137739.

Pinty, B., Gobron, N., Widlowski, J.-L., Gerstl, S. A. W., Verstraete, M. M., Antunes, M., Bacour, C., Gascon, F., Gastellu-Etchegorry, J.-P., Goel, N., Jacquemond, S., North, P., Qin, W., and Thompson, R., 2001, Radiation transfer model intercomparison (RAMI) exercise. *Journal of Geophysical Research*, **106**, 11937–11956.

Pinty, B., Verstraete, M. M., and Dickinson, R. E., 1990, A physical model of the bidirectional reflectance of vegetation canopies. 2. Inversion and validation. *Journal of Geophysical Research*, **95**, 11767–11775.

Pinty, B., Widlowksi, J.-L., taberner, M., Gobron, N., Verstraete, M. M., Disney, M., Gascon, F., Gastellu-Etchegorry, J.-P., Jiang, L., Kuusk, A., Lewis, P., Li, X., Ni-Meister, W., Nilson, T., North, P., Qin, W., Su, L., Tang, S., Thompson, R., Verhoef, W., Wang, h., Wang, J., Yan, G., and Zang, H., 2004, Radiation transfer model intercomparison (RAMI) exercise: Results from the second phase. *Journal of Geophysical Research*, **109**, D06210.

Pitman, A. J., 2003, Review. The evolution of, and revolution in, land surface schemes designed for climate models. *International Journal of Climatology*, **23**, 479–510.

Press, W. H., Tuekolsky, S. A., Vetterling, W. T., and Flannery, B. R., 1994, *Numerical Recipes in C*, second edition (Cambridge: Cambridge University Press).

Price, J. C., 1990, On the information content of soil reflectance spectra. *Remote Sensing of Environment*, **33**, 113–121.

Prusinkiewicz, P., and Lindenmeyer, A., 1990, *The algorithmic beauty of plants* (Springer-Verlag).

Qin, W., and Gerstl, S. A. W., 2000, 3-D scene modeling of semidesert vegetation cover and its radiation regime. *Remote Sensing of Environment*, **74**, 145–162.

Qin, W., and Xiang, Y., 1994, On the hotspot effect of leaf canopies: Modeling study and influence of leaf shape. *Remote Sensing of Environment*, **50**, 95–106.

Raab, F. H., Blood, E. B., Steiner, T. O., and Jones, H. R., 1979, Magnetic position and orientation tracking system. *IEEE transactions on Aerospace and Electronics Systems*, **AES-15**, 709–718.

Rautiainen, M., Mõttus, M., and Stenberg, P., 2009, On the relationship of canopy LAI and photon recollision probability in boreal forests. *Remote Sensing of Environment*, **113**, 458–461.

Rayner, P. J., Scholze, M., Knorr, W., Kaminski, T., Giering, R., and Widmann, H., 2005, Two decades of terrestrial carbon fluxes from a carbon cycle data assimilation system (CCDAS). *Global Biogeochemical Cycles*, **19**, GB2026.

Reitberger, J., Krzystek, P., and Stilla, U., 2008, Analysis of full waveform LIDAR data for the classification of deciduous and coniferous trees. *International Journal of Remote Sensing*, **29**, 1407–1431.

Renker, D., 2006, Geiger-mode avalanche photodiodes, history, properties and problems. *Nuclear Instruments and Methods in Physics Research*, **567**, 48–56.

Reulke, R., and Haala, N., 2004, *Tree species recognition with fuzzy texture parameters*, Lecture notes in computer science (Berlin/Heidelberg: Springer), pp. 607–620.

Richter, T., and Fukshansky, L., 1996, Optics of a bifacial leaf: 1. A novel combined procedure for deriving optical parameters. *Photochemistry and Photobiology*, **63**, 507–516.

Rochdi, N., Fernandes, R., and Chelle, M., 2006, An assessment of needles clumping within shoots when modeling radiative transfer within homogeneous canopies. *Remote Sensing of Environment*, **102**, 116–134.

Rodell, M., Houser, P. R., Jambor, U., Gottschalck, J., Mitchell, K., Meng, C.-J., Arsenault, K., Cosgrove, B., Radakovich, J., Bosilovich, M., Entin, J. K., Walker, J. P., Lohmann, D., and Toll, D., 2004, The global land data assimilation system. *Bulletin of the American Meteorological Society*, **85**, 381–394.

Rogers, A. E. E., and Ingalls, R. P., 1969, Venus: Mapping the surface reflectivity by radar interferometry. *Science*, **165**, 797–799.

Rosenqvist, Å., Milne, A. A., Lucas, R., Imhoff, M., and Dobson, C., 2003, A review of remote sensing technologies in support of the Kyoto Protocol. *Environmental Science and Policy*, **6**, 441–455.

Rosette, J. A., North, P. R. J., and Suarez, J. C., 2007, A method of directly estimating stemwood volume from GLAS waveform parameters, In *Proceedings of Silvilaser*, Helsinki.

Rosette, J. A. B., North, J, P. R., and Suarez, J. C., 2008, Vegetation height estimates for a mixed temperate forest using satellite laser altimetry. *International Journal of Remote Sensing*, **29**, 1475–1493.

Ross, J., 1975, *Radiative transfer in plant communities: In. Vegetation and the atmosphere* (Academic Press).

Ross, J., 1981, *The radiation regime and architecture of plant stands* (The Hague-Boston-London: Dr W. Junk Publishers).

Ross, J., and Nilson, T., 1965, The extinction of direct radiation in crops. In: questions on radiation regime of plant stands. *Academy of science ESSR, Institute of physics and astronomy, Tartu (Russian)*.

Ross, J. K., and Marshak, A. L., 1988, Calculation of canopy bidirectional reflectance using the Monte Carlo method. *Remote Sensing of Environment*, **24**, 213–225.

Ross, R. A., Hinsley, S. A., Gaveau, D. L. A., and Bellamy, P. E., 2004, Predicting habitat quality for great Tits (Parus major) with airborne laser scanning data. *International Journal of Remote Sensing*, **20**, 4851–4855.

Saatchi, S. S., Houghton, R. A., Dos Santos Alvalá, R. C., and Soares, J. V., 2007, Distribution of aboveground live biomass in the Amazon basin. *Global Change Biology*, **13**, 816–837.

Santoro, M., Askne, J., Smith, G., and Fransson, J. E. S., 2002, Stem volume retrieval in boreal forests from ERS-1/2 interferometry. *Remote Sensing of Environment*, **81**, 19–35.

Sarabandi, K., 1997, Δk-radar equivalent of interferometric SAR's: A theoretical study for determination of vegetation height. *IEEE Transactions on Geoscience and Remote Sensing*, **35**, 1267–1276.

Schildt, H., 1997, *Teach yourself C*, third edition (Berkely, California: Osborne).

Schutz, B. E., Zwally, H. J., Shuman, C. A., Hancock, D., and DiMarzio, J. P., 2005, Overview of the ICESat mission. *Geophysical Research Letters*, **32**, L21S01.

Seeliger, H., 1895, Theorie der Beleuchtun staubformiger kosmishen Masses insbesondere des Saturinges. *Abhandl. Bayer. Akad. Wiss. Math-Nature. Kl. II*, **18**, 1–72.

Sellers, P. J., Hall, F. G., Kelly, R. D., Black, A., Baldocchi, D., Berry, J., Ryan, M., Ranson, K. J., Crill, P. M., Lettenmaier, P., Margolis, H., Cihlar, J., Newcomer, j., Fitzjarrald, D., Jarvis, P. G., Gower, S. T., Halliwell, D., Williams, D., Goodison, B., Wickland, D. E., and Guertin, F. E., 1997, BOREAS in 1997: Experiment overview, scientific results, and future directions. *Journal of Geophysical Research*, **102**, 28,731–28,769.

Sexton, J. O., Bax, T., Siqueira, P., Swenson, J. J., and Hensley, S., 2009, A comparison of lidar, radar, and field measurements of canopy height in pine and hardwood forests of southeastern North America. *Forest Ecology and Management*, **257**, 1136–1147.

Shimizu, R., and Ze-Jun, D., 1992, Monte Carlo modelling of electron-solid interaction. *Reports on Progress in Physics*, **55**, 487–531.

Shinozaki, K., Yoda, K., Hozumi, K., and Kira, T., 1964, A quantitative analysis of plant form - the pipe model theory I. Basic analyses. *Japanese Journal of Ecology*, **24**, 97–105.

Sinoquet, H., Sonohat, G., Phattaralerphong, J., and Godin, C., 2005, Foliage randomness and light interception in 3-D digitized trees: an analysis from multiscale discretization of the canopy. *Plant, Cell and Environment*, **28**, 1158–1170.

Slater, P. N., 1980, *Remote sensing, optics and optical systems* (Addison-Wesley Publishing Company).

Smith, D. E., Zuber, M. T., Frey, H. V., B, G. J., Head, J. W., Muhleman, D. O., Pettengill, G. H., Phillips, R. J., Solomon, S. C., Zwally, H. J., Banerdt, W. B., Duxbury, T. C., Golombek, M. P., Lemoine, F. G., Neumann, G. A., Rowlands, D. D., Aharonson, O., Ford, P. G., Ivanov, A. B., Johnson, C. L., McGovern, P. J., Abshire, J. B., Afzal, R. S., and Sun, X., 2001, Mars Orbiter Laser Altimeter: Experiment summary after the first year of global mapping of Mars. *Journal of Geophysical Research*, **106**, 23689–23722.

Smith, J. A., and Oliver, R. E., 1974, Effects of changing canopy directional reflection on feature selection. *Applied Optics*, **13**, 1599–1604.

Smolander, S., and Stenberg, P., 2003, A method to account for shoot scale clumping in coniferous canopy reflectance models. *Remote Sensing of Environment*, **88**, 363–373.

Smolander, S., and Stenberg, P., 2005, Simple parameterizations of the radiation budget of uniform broadleaved and coniferous canopies. *Remote Sensing of Environment*, **94**, 355–363.

Sommer, K. J., and Lang, A. R. G., 1994, Comparitive analysis of two direct methods of measuring leaf area index as applied to minimal and spur pruned grape vines. *Australian Journal of Plant Physiology*, **21**, 21.

Stenberg, P., 1996, Correcting LAI-2000 estimates for the clumping of needles in shoots of conifers. *Agricultural and Forest Meteorology*, **79**, 1–8.

Stephen, M. J., and Cwilich, G., 1986, Raylegh scattering and weak localization: Effects of polarization. *Physical Review B*, **34**, 7564–7572.

Stoner, E. R., Baumgardner, M. F., Biehl, L. L., and Robinson, B. F., 1980, Atlas of soil reflectance properties, Research Bulletin 962, Purdue University, West Lafayette, IN.

Strahler, A. H., and Jupp, D. L. B., 1990, Modeling bidirectional reflectance of forests and woodlands using Boolean models and geometric optics. *Remote Sensing of Environment*, **34**, 153–166.

Strebel, D. E., Goel, N. S., and Ranson, K. J., 1985, Two-dimensional leaf orientation distributions. *IEEE Transactions on Geoscience and Remote Sensing*, **23**, 640–647.

Suits, G. H., 1972, The calculation of the directional reflectance of a vegetative canopy. *Remote Sensing of Environment*, **2**, 117–125.

Sun, G., Ranson, K. J., Kimes, D. S., Blair, J. B., and Kovacs, K., 2008, Forest vertical structure from GLAS: An evaluation using LVIS and SRTM data. *Remote Sensing of Environment*, **112**, 107–117.

Takahashi, T., Yamamoto, K., Senda, Y., and Tsuzuku, M., 2005, Estimating individual tree heights of sugi (Cryptomeria japonica D. Don) plantations in mountainous areas using small-footprint airborne LiDAR. *Journal of Forest Research*, **10**, 135–142.

Tanaka, S., 1969, Estimation of sunlit leaf area in tobacco plant community by the Monte Carlo method, Estimation of direct sunlight, In *Photosynthesis and utilization of solar energy*, Japanese IBP/PP - Photosynthesis level III group, Tokyo, pp. 76–79.

Tanaka, T., Park, H., and Hattori, S., 2004, Measurement of forest canopy structure by a laser plane range-finding method. Improvement of radiative resolution and examples of its application. *Agricultural and Forest Meteorology*, **125**, 129–142.

Tanaka, T., Yamaguchi, J., and Takeda, Y., 1998, Measurement of forest canopy structure with a laser plane range-finding method - Development of a measurement system and applications to real forests. *Agricultural and Forest Meteorology*, **91**, 149–160.

Teh, C. B. S., Simmonds, L. P., and Wheeler, T. R., 2000, An equation for irregular distributions of leaf azimuth density. *Agricultural and Forest Meteorology*, **102**, 223–234.

Ter-Mikaelian, M. T., and Korzhukin, M. D., 1997, Biomass equations for sixty-five North American tree species. *Forest Ecology and Management*, **97**, 1–24.

Thomas, S. C., and Winner, W. E., 2000a, Leaf area index of an old-growth Douglas-fir forest estimated from direct structural measurements in the canopy. *Canadian Journal of Forest Research*, **30**, 1922–1930.

Thomas, S. C., and Winner, W. E., 2000b, A rotated ellipsoidal angle density function improves estimation of foliage inclination distributions in forest canopies. *Agricultural and Forest Meteorology*, **100**, 19–24.

Thompson, R. L., and Goel, N. S., 1998, Two models for rapidly calculating bidirectional reflectance: Photon spread (ps) model and statistical photon spread (sps) model. *Remote Sensing Reviews*, **16**, 157–207.

Tinney, F. W., Aamodt, O. S., and Ahlgren, H. L., 1937, Preliminary report of a study on methods used in botanical analysis of pasture swards. *Journal of the American Society of Agronomy*, **29**, 835–840.

Tipler, P. A., 1999, *Physics, for scientists and engineers*, fourth edition (W. H. Freeman and company/Worth publishers).

Turner, D. P., Acker, S. A., Means, J. E., and Garman, S. L., 2000, Assessing alternative allometric algorithms for estimating leaf area of Douglas-fir trees and stands. *Forest Ecology and Management*, **226**, 61–76.

Ulbricht, C., Wilki, A., and Purgathofer, W., 2006, Verification of physically based rendering algorithms. *Computer Graphics Forum*, **25**, 237–255.

Vanderbilt, V. C., 1985, Measuring plant canopy structure. *Remote Sensing of Environment*, **18**, 281–294.

Verhoef, W., 1984, Light scattering by leaf layers with application to canopy reflectance modeling: The SAIL model. *Remote Sensing of Environment*, **16**, 125–141.

Verhoef, W., 2002, Improved modelling of multiple scattering in leaf canopies: The model SAIL++, In *Proceedings of the first symposium on recent advances in quantitative remote sensing*, Torrent, Spain, pp. 11–20.

Verstraete, M. M., Pinty, B., and Dickinson, R. E., 1990, A physical model of the bidirectional reflectance of vegetation canopies 1. Theory. *Journal of Geophysical Research*, **95**, 11755–11765.

Wagner, W., Luckman, A., Vietmeier, J., Tansey, K., Balzter, H., Schmullius, C., Davidson, M., Gaveau, D., Gluck, M., Le Toan, T., Quegan, S., Shvidenko, A., Wiesmann, A., and Yu, J. J., 2003, Large-scale mapping of boreal forest in SIBERIA using ERS tandem coherence and JERS backscatter. *Remote Sensing of Environment*, **85**, 125–144.

Wagner, W., Ullrich, A., Ducic, V., Melzer, T., and Studnicka, N., 2006, Gaussian decomposition and calibration of a novel small-footprint full-waveform digitising airborne laser scanner. *ISPRS Journal of Photogrammetry and Remote Sensing*, **60**, 100–112.

Walker, J. C. G., Hays, P. B., and Kasting, J. F., 1981, A negative feedback mechanism for the long-term stabilization of Earth's surface temperature. *Journal of Geophysical Research*, **86**, 9776–9782.

Wang, W. M., Li, Z. L., and Su, H. B., 2007, Comparison of leaf angle distribution functions: Effects on extinction coefficient and fraction of sunlit foliage. *Agricultural and Forest Meteorology*, **143**, 106–122.

Waring, R., Law, B., Goulden, M., Bassow, S., McCreight, R., Wofsy, S., and Bazzaz, F., 1995a, Scaling gross ecosystem production at Harvard Forest with remote sensing: a comparison of estimates from a constrained quantum-use efficiency model and eddy correlation. *Plant Cell Environment*, **18**, 1201–1213.

Waring, R. H., 1983, Estimating forest growth and efficiency in relation to canopy leaf area. *Advances in Ecological Research*, **13**, 327–354.

Waring, R. H., Emmingham, W. H., Gholz, H. L., and Grier, C. C., 1978, Variation in maximum leaf area of coniferous forests and its ecological significance. *Forest Science*, **24**, 131–140.

Waring, R. H., Way, J., Hunt, E. Raymond, J., Morrissey, L., Ranson, K. J., Weishampel, J. F., Oren, R., and Franklin, S. E., 1995b, Imaging Radar for Ecosystem Studies. *BioScience*, **45**, 715–723.

Watt, P. J., and Donoghue, D. J., 2005, Measuring forest structure with terrestrial laser scanning. *International Journal of Remote Sensing*, **26**, 1437–1446.

Wegmüller, U., and Werner, C., 1997, Retrieval of vegetation parameters with SAR interferometry. *IEEE Transactions on Geoscience and Remote Sensing*, **35**, 18–24.

Weiss, M., Baret, F., Smith, G. J., Jonckheere, I., and Coppin, P., 2004, Review of methods for in situ leaf area index (LAI) determination. PART II. Estimation of LAI, errors and sampling. *Agricultural and Forest Meteorology*, **121**, 37–53.

Werner, M., 2000, Shuttle radar topography mission (SRTM) Mission overview. *EUSAR 2000; proceedings of the 3rd European conference on synthetic aperture radar, Germany. 23rd-25th May 2000*, 209–212.

White, R. L., 1994, Image restoration using the damped Richardson-Lucy method. *Proceedings SPIE*, **2198**, 1342.

Widlowski, J.-L., Pinty, B., Lavergne, T., Verstraete, M. M., and Gobron, N., 2005, Using 1-D models to interpret the reflectance anisotropy of 3-D canopy targets: Issues and caveats. *IEEE Transactions on Geoscience and Remote Sensing*, **43**, 2008–2017.

Widlowski, J.-L., Robustelli, M., Disney, M., Gastellu-Etchegorry, J.-P., Lavergne, T., Lewis, P., North, P., Pinty, B., Thompson, R., and Verstraete, M., 2008, The RAMI On-line Model Checker (ROMC): A web-based benchmarking facility for canopy reflectance models. *Remote Sensing of Environment*, **112**, 1144 – 1150.

Widlowski, J.-L., Taberner, M., Bruniquel-Pinel, V., Disney, M., Fernandes, R., Gastellu-Etchegorry, J.-P., Gobron, N., Kuusk, A., Lavergne, T., Leblanc, S., Lewis, P. E., Martin, E., Mottus, M., North, P. R. J., Qin, W., Robustelli, M., Rochdi, N., Ruiloba, R., Soler, C., Thompson, R., Verhoef, W., Verstraete, M. M., and Xie, D., 2007, Third radiation transfer model intercomparison (RAMI) exercise: Documenting progress in canopy reflectance models. *Journal of Geophysical Research*, **112**, D09111.

Williams, M., 1996, A three-dimensional model of forest development and competition. **98**, 73–98.

Williams, M., Schwarz, P. A., Law, B. E., Irvine, J., and R, K. M., 2005, An improved analysis of forest carbon dynamics using data assimilation. *Global Change Biology*, **11**, 89–105.

Wilson, J., and Hawkes, J., 1987, *Lasers, principles and applications*, first edition (Prentice Hall).

Wilson, J. W., 1959, Analysis of the spatial distribution of foliage by two-dimensional point quadrats. *New Phytologist*, **58**, 92–99.

Wilson, J. W., 1960, Inclined point quadrats. *New Phytologist*, **59**, 1–7.

de Wit, C. T., 1965, *Photosynthesis of leaf canopies* (Wageningen, The Netherlands: Pudoc Publishers).

Woodcock, C. E., Collins, J. B., Jakabhazy, V. D., Li, X., Macomber, S. A., and Wu, Y., 1997, Inversion of the Li-Strahler canopy reflectance model for mapping forest structure. *IEEE Transactions on Geoscience and Remote Sensing*, **35**, 405–414.

Xu, H., Gossett, N., and Chen, B., 2007, Knowledge and heuristic-based modeling of laser-scanned trees. *ACM Transactions on Graphics*, **26**, 19.

Yamaguchi, Y., Kahle, A., Tsu, H., Kawakami, T., and Pniel, M., 1998, Overview of Advanced Spaceborne Thermal Emission and Reflection Radiometer (ASTER). *Geoscience and Remote Sensing, IEEE Transactions on*, **36**, 1062–1071.

Yang, X., Yao, T., Strahler, A. H., Woodcock, C. E., Schaaf, C. B., Myneni, R., Liu, J., Newnham, G. J., Jupp, D. L. B., Culvenor, D. S., Lovell, J. L., Ni-Meister, W., Lee, S., Zhao, F., Schull, M., Roman, M., Wang, Z., and Shuai, Y., 2008, Validation of improved forest canopy measurement from a ground-based lidar instrument Echidna, In *IGARSS*, poster only.

Yoder, B. J., Ryan, M. G., Waring, R. H., Schoettle, A. W., and Kaufmann, M. R., 1994, Evidence of reduced photosynthetic rates in old trees. *Forest Science*, **40**, 513–527.

Zappa, F., Giudice, A., Ghioni, M., and Cova, S., 2002, Fully-integrated active-quenching circuit for single-photon detection. *28th European Solid-State Circuits Conference, September 2002, Florence, ESSCIRC*, 355–358.

Zappa, F., Lacaita, A., Cova, S., and Lovati, P., 1996, Solid-state single-photon detectors. *Optical Engineering*, **34**, 938–945.

Zarco-Tejada, P. J., Miller, J. R., Harron, J., Hu, B., Noland, T. L., Goel, N., Mohammed, G. H., and Sampson, P., 2004, Needle chlorophyll content estimation through model inversion using hyperspectral data from boreal conifer forest canopies. *Remote Sensing of Environment*, **89**, 189–199.

Zebker, H. A., and Goldstein, R. M., 1986, Topographic mapping from interferometric synthetic aperture radar observations. *Journal of Geophysical Research*, **91**, 4993–4999.

Zhang, Y., Tian, Y., Martonchik, J. V., Diner, D. J., Leroy, M., and Myneni, R. B., 2000, Prototyping of MISR LAI and FPAR algorithm with POLDER data over Africa. *IEEE Transactions on Geoscience and Remote Sensing*, **38**, 2,402–2,418.

Zimble, D. A., Evans, D. L., Carlson, G. C., Parker, R. C., Grado, C. G., and Gerard, P. D., 2003, Characterizing vertical forest structure using small-footprint airborne LiDAR. *Remote sensing of environment*, **87**, 171–182.

Zwally, H. J., Schutz, B., Abdalati, W., Abshire, J., Bentley, C., Brenner, A., Bufton, J., Dezio, J., Hancock, D., Harding, D., Herring, T., Minster, B., Quinn, K., Palm, S., Spinhirne, J., and Thomas, R., 2002, ICESat's laser measurements of polar ice, atmosphere, ocean and land. *Journal of Geodynamics*, **34**, 405–445.

A List of publications

A.1 Conference proceedings

Hancock S, Lewis P, Muller J-P, Disney M, 2007. Using Monte-Carlo ray tracing to investigate the measurement of forest parameters with the Echidna^{TM} laser scanner. The International Archives of Photogrammetry, Remote Sensing and Spatial Information Sciences, v 34.

Hancock S, Lewis P, Foster M, Disney M, Muller J-P, 2008. Extracting tree heights over topography with multi-spectral spaceborne waveform lidar. Proceedings of IGARSS, Boston.

Hancock S., Disney M., Lewis P., Muller J-P, 2008. Exploring the measurement of forests with full waveform lidar through Monte-Carlo ray tracing. Proceedings of ISPRS, Beijing, v 37 p 235-239.

Hancock S., Lewis P., Disney M., Foster M., Muller J-P. 2008, Assessing the accuracy of forest height estimation with long pulse waveform lidar through Monte-Carlo ray tracing. Proceedings of Silvilaser, Edinburgh, 17^{th}-19^{th} September, p 199-206.

A.2 Technical reports

Davies A,Jenkins R M, Perrett B J, Leigh R, Lawrence J, Lewis P, Hancock S, Disney M, Quegan S, 2008. Hollow waveguide hybrid integration technology for space borne lidar and the science case based on CO_2 and canopy measurements. QINETIQ/AT/DEF/TR0800455, NERC/CEOI contract CS/008/PR/2007. (contributed canopy lidar section)

Muller J-P, Griffiths A, Yuen P, Bentley B, Lewis P, Hancock S, Disney M, Foster M, 2008. Hyperspectral Imaging lidar (ladar), NERC Centre for Earth Observation and Instrumentation final report. NERC/DIUS Contract, SA-014-DJ-2007. (contributed canopy lidar section)

A.3 Contributions

Disney, M. I., Lewis, P., Bouvet, M., Prieto-Blanco, A. and Hancock, S. Quantifying surface reflectivity for spaceborne lidar via two independent methods. submitted IEEE Transactions on Geoscience and Remote Sensing, v 47, p 3262-3271.

Disney, M. I., Kalogirou, V., Lewis P., Prieto-Blanco A., Hancock S. and Pfeifer M. 2010. Simulating the impact of system characteristics on discrete-return lidar over conifer and broadleaf forests. Remote Sensing of Environment, v 114, p 1546-1560.

B Order of smoothing for calculating the spectral ratio

The proof that smoothing the individual waveforms before ratioing lessens the impact of noise relative to smoothing the spectral ratio of two noised waveforms is presented here.

Taking a point at which one waveform has an intensity β and the other x. The spectral ratio of the ideal waveforms would then be;

$$ratio_{ideal} = \frac{\beta}{x} \tag{98}$$

If the denominator has its intensity reduced by a noise value of α, the spectral ratio of the noised waveforms becomes;

$$ratio_{noised} = \frac{\beta}{x - \alpha} \tag{99}$$

The deviation from the truth is then the difference between equations 99 and 98;

$$error = \frac{\beta}{x - \alpha} - \frac{\beta}{x} \tag{100}$$

Which becomes;

$$error = \frac{\beta\alpha}{x(x - \alpha)} \tag{101}$$

This situation is illustrated in figure 182, with noise causing a reduction in the intensity of the denominator (the most disruptive situation for analysis). Bare in mind that the intensity will be

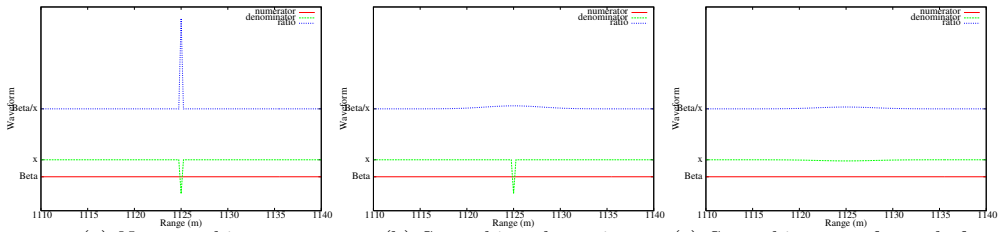

(a) No smoothing (b) Smoothing the ratio (c) Smoothing waveforms before division

Figure 182: Illustration of the magnitude of noise's effect on the spectral ratio smoothing before and after

truncated at 0, therefore $\alpha <= x$.

B.1 Post-smoothing

If the noised waveforms are ratioed and subsequent signal smoothed by a Gaussian with unit energy and width σ, the deviation from the truth is scaled by the maximum amplitude of the Gaussian;

$$error_{post-smooth} = \frac{\beta\alpha}{x(x-\alpha)} \times \frac{1}{\sqrt{2\pi}\sigma} \tag{102}$$

Here the smoothing function's width, σ, is that relative to the sampling width, therefore for a smoothing function;

$$\sigma > 1 \tag{103}$$

B.2 Pre-smoothing

If the two waveforms are smoothed by convolution with a Gaussian before calculating the spectral ratio their intensities become β and $x - \frac{\alpha}{\sqrt{2\pi}\sigma}$. The deviation from the truth is then;

$$error_{pre-smooth} = \frac{\beta}{x - \frac{\alpha}{\sqrt{2\pi}\sigma}} - \frac{\beta}{x} \tag{104}$$

Which goes to;

$$error_{pre-smooth} = \frac{\beta\alpha}{x(\sqrt{2\pi}\sigma x - \alpha)} \tag{105}$$

B.3 Comparison

Comparing the relative sizes of $error_{post-smooth}$ and $error_{pre-smooth}$;

$$error_{post-smooth} <?> error_{post-smooth} \tag{106}$$

$$\frac{\beta\alpha}{\sqrt{2\pi}\sigma x(x-\alpha)} <?> \frac{\beta\alpha}{x(\sqrt{2\pi}\sigma x-\alpha} \tag{107}$$

$$\frac{1}{\sqrt{2\pi}\sigma(x-\alpha)} <?> \frac{1}{\sqrt{2\pi}\sigma x-\alpha} \tag{108}$$

Taking the reciprocal of both sides and changing signs;

$$\sqrt{2\pi}\sigma <?> 1 \tag{109}$$

From equation 103 it can be seen that;

$$\sqrt{2\pi}\sigma > 1 \tag{110}$$

Therefore;

$$error_{post-smooth} > error_{pre-smooth} \tag{111}$$

Smoothing the individual waveforms before calculating the spectral ratio will always give smaller deviations from the truth than smoothing the ratio of noised signals, as long as the Gaussian width is greater than $\frac{1}{\sqrt{2\pi}}$ of the sampling interval.

C Angular distribution models

C.1 Sphere

As explained in section 6.4, the apparent reflectance, η any surface is given by;

$$\eta = \frac{\rho_e}{A_{foot}} \oint \cos^2(\alpha) dA_s \tag{112}$$

For a sphere of radius r annuli can be integrated over, in polar coordinates, between 0 and $\frac{\pi}{2}$.The area of an annulus, A_{ann} at a zenith angle (which for a sphere is equal to the angle if incidence), θ is;

$$A_{ann} = 2\pi r^2 \left|\sin\theta\right| d\theta \tag{113}$$

Divide this by the sphere's projected area, πr^2, to get dA_s

$$dA_s = 2\left|\sin\theta\right| d\theta \tag{114}$$

For a sphere that completely fills the field of view (ie $A_{foot} = \pi r^2$), the integral becomes;

$$\eta = \rho_e \int_0^{\frac{\pi}{2}} 2\left|\sin\theta\cos^2\theta\right| d\theta \tag{115}$$

Using the substitution $u = \cos\theta$ to solve t too;

$$\eta = \frac{2}{3}\rho_e \tag{116}$$

C.2 Spheroid

Spheroids are far less well behaved in polar coordinates than spheres, the surface normal is not equal to the angular coordinate and the radius is a function of angle. It was decided to use Cartesian coordinates instead.

The equation of a vertical cross section through a spheroid (an ellipse) with vertical radius a and horizontal radius b (as shown in figure 2) is;

$$\frac{y^2}{a^2} + \frac{x^2}{b^2} = 1 \tag{117}$$

The circumference of an annulus is $2\pi x$ with a width of $\frac{dx}{\cos\alpha}$ so;

$$dA_s = 2\pi x \frac{dx}{\cos\alpha} \tag{118}$$

For a spheroid that completely fills the field of view, the vertically projected area and so footprint is equal to $A_f = \pi b^2$. Substituting into equation 112 gives;

$$\eta = \frac{2\rho_e}{b^2} \int_0^b x\cos\alpha dx \tag{119}$$

The surface angle, α is equal to the tangent of the gradient, which can be found by differentiating equation 117.

$$\tan\alpha = \frac{dy}{dx} = -\frac{a}{b}\frac{x}{\sqrt{b^2 - x^2}} \tag{120}$$

Therefore $\cos\alpha$ can be expressed in terms of x as;

$$\cos\theta = \frac{1}{\sqrt{1 + \frac{a^2}{b^2}\frac{x^2}{b^2 - x^2}}} \tag{121}$$

And so the apparent reflectance becomes;

$$\eta = \frac{2\rho_e}{b^2}\int_0^b \frac{x}{\sqrt{1 + \frac{a^2}{b^2}\frac{x^2}{b^2 - x^2}}}dx \tag{122}$$

This can be somewhat simplified by setting $u = x^2$ and substituting;

$$\eta = \frac{\rho_e}{b^2}\int_0^{b^2} \frac{1}{\sqrt{1 + \frac{a^2}{b^2}\frac{u}{b^2 - u}}}du \tag{123}$$

Whilst this is a relatively compact equation it does not seem possible to solve analytically. The function within the integral is not continuous, being undefined when $u = b^2$.

Its numerical evaluation presents no problems, although such an approach is unsuitable for inversion it will allow us to explore the behaviour of the apparent reflectance. The apparent reflectances predicted by equation 123 exactly match those measured by the ray tracer over spheroids with a range of eccentricities.

Off-nadir So far only the special case when the lidar is looking along the vertical axis has been dealt with. To make use of Echidna's multi-angular measurements this must be generalised to the off-nadir case, for a lidar at a zenith, θ to the vertical axis. A one dimensional integral over annuli can no longer be used as the angle of incidence is now a function of a surface normal's zenith, β and azimuth, ϕ. This relationships can be derived by taking the dot product of two unit vectors, the surface normal, $\hat{n}$ and the view direction, $\hat{v}$. Here the lidar is looking along the x axis so azimuth, ϕ is taken from here; the direction is irrelevant.

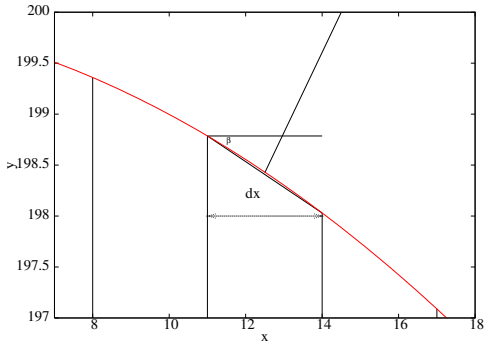

Figure 183: Cross section through a spheroid

$$\hat{n} = \begin{pmatrix} \cos\phi \sin\beta \\ \sin\phi \sin\beta \\ \cos\beta \end{pmatrix} \tag{124}$$

$$\hat{v} = \begin{pmatrix} \sin\theta \\ 0 \\ \cos\theta \end{pmatrix} \tag{125}$$

Taking the dot product gives;

$$\cos\alpha = \cos\phi \sin\beta \sin\theta + \cos\beta \cos\theta \tag{126}$$

The surface integral in equation 112 must be evaluated over radius and around the azimuth. Each element is now a segment rather than an annulus, with a surface area $dA_s = \frac{dx}{\cos\beta} x d\phi$.

$$\eta = \rho_e \frac{1}{A_f} \int_0^b \int_0^{2\pi} cos^2\alpha \frac{x}{|\cos\beta|} d\phi dx \tag{127}$$

Here β is the surface zenith angle which is equal to the angle of incidence, θ, for the nadir case and so can be calculated from equations 120 and 121. Only the magnitude of the surface normal zenith angle is of importance here so the sign of the gradient can be ignored.

$$\tan\beta = \frac{a}{b} \frac{x}{\sqrt{b^2 - x^2}} \tag{128}$$

$$\cos\beta = \frac{1}{\sqrt{1 + \frac{a^2}{b^2}\frac{x^2}{b^2 - x^2}}} \tag{129}$$

Using the trigonometric identity $\sin^2\theta + \cos^2\theta = 1$.

$$\sin\beta = \frac{ax}{\sqrt{b^2(b^2 - x^2) + a^2x^2}} \tag{130}$$

Substituting equation 126 into 127 then expanding the square and simplifying gives;

$$\eta = \rho_e \frac{1}{A_f} \int_0^b \int_0^{2\pi} x \left|\cos^2\phi \sin^2\theta \sin\beta \tan\beta + \cos\phi \sin 2\theta \sin\beta + \cos^2\theta \cos\beta\right| d\phi dx \tag{131}$$

This can be expressed in terms of x by in equations 128, 129 and 130.

The above equations were tested on a sphere which, according to the analytic solution, should have an apparent reflectance of $\frac{2}{3}\rho_e$ from all view zeniths, and it did. As an analytic solution for spheroids was not found here, the predictions had to be validated against ray traced simulations.

The apparent reflectance of spheroids with different eccentricities was measured with starat from a range of view zeniths. These results were compared to those predicted by the above equations and found to match. Confidence can be had in these equations and use them to explore the behaviour of the apparent reflectance of spheroidally distributed surfaces with view zenith, hopefully leading to a method for quick and easy inversion of LAD from Echidna data.

C.3 Effective angle of incidence

The surface integrals to determine the apparent reflectance and projected area of a spheroid are non-trivial and it may not be possible to solve them analytically, but such a solution was not found here. Instead a spheroid may be treated as a plane at an effective angle of incidence, θ_e. Section C.1 showed that for a sphere the effective reflectance is $\frac{2}{3}$ of the actual reflectance. For a plane the effective reflectance is given by equation 61, so.

$$\eta = \frac{A_s}{A_f}\rho_e \cos^2\theta_e \tag{132}$$

For a sphere that completely fills the field of view the footprint area $A_f = \pi r^2$ and the visible surface area, $A_s = 2\pi r^2$ and so evaluating to $\frac{2}{3}$ gives;

$$\eta = 2\rho_e \cos^2 \theta_e = \frac{2}{3}\rho_e \tag{133}$$

and so;

$$\theta_e = \arccos\left(\frac{1}{\sqrt{3}}\right) = 54.75^o \tag{134}$$

This is the hinge point of the LAD described by (Wilson 1960). If this effective angle of incidence holds, the projected area, $A_s G(\theta$ should also be related to it. For a sphere the Ross-G function is equal to a half so from equation 60;

$$G(\theta) = \frac{1}{2} = \cos \theta_e \tag{135}$$

Solving gives;

$$\theta_e = \arccos\left(\frac{1}{2}\right) = 60^o \tag{136}$$

The effective angle of incidence for the apparent reflectance and projected area are not equal, although they are similar and an approximate solution may be acceptable. To see how the effective angles of incidence for apparent reflectance and projected area behave they will have to be evaluate for spheroids with a range of eccentricities.

The effective angle of incidence can be found for any spheroid and view direction using the following equation;

$$\theta_e = \arccos\left(\sqrt{\frac{1}{A_s}\oint \cos^2 \theta dA_s}\right) \tag{137}$$

Figure 184 shows that the effective angle of incidence is far better behaved than either the projected surface area or the apparent reflectance. The cross over point is very clearly defined, with the curves for all eccentricities passing through an effective angle of 54.75^o at a zenith of 54.75^o. The deviation from a perfect cross over in all other properties must be due to varying projected area as a fraction of the visible surface area.

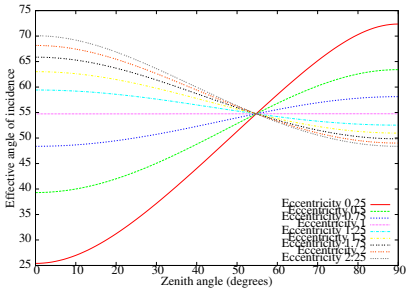

Figure 184: Effective angle of incidence for the apparent reflectance against view zenith for a range of eccentricities

This value for the cross over point was used due to its high precision, impossible to achieve with other metrics.

D Phase function

For beams that contain no soil the phase function calculations requires only two bands and the equations are greatly simplified. The measured reflectance, η_λ, at wavelength λ is;

$$\eta_\lambda = \Gamma_l A_{p,l} \rho_{l,\lambda} + \Gamma_w A_{p,w} \rho_{w,\lambda} \tag{138}$$

The same is true at any other wavelength, ω. The projected areas of leaf ($A_{p,l}$) and wood ($A_{p,w}$) are constant for all wavelengths, as are the phase functions, in the absence of multiple scattering (and in the presence if it is taken into account by another method). Simultaneously solving the equation at two wavelengths gives the phase functions;

$$\Gamma_l = \frac{\eta_\omega \rho_{w,\lambda} - \eta_\lambda \rho_{w,\omega}}{A_{p,l}(\rho_{l,\omega}\rho_{w,\lambda} - \rho_{l,\lambda}\rho_{w,\omega})} \tag{139}$$

$$\Gamma_w = \frac{\eta_\omega \rho_{l,\lambda} - \eta_\lambda \rho_{l,\omega}}{A_{p,w}(\rho_{w,\omega}\rho_{l,\lambda} - \rho_{w,\lambda}\rho_{l,\omega})} \tag{140}$$

E Multiple scattering for Echidna

The methods described used in chapter 5.14 no attempt to explicitly describe multiple scattering. For self shadowing canopies it was taken into account by the phase value, Γ whilst for non shadowing canopies it was assumed negligible. These assumptions have been shown to provide accurate estimates of surface area and gap fraction with angle, however differences in scattering at different wavelengths prevent the accurate separation of leaf from bark in highly scattering canopies.

All the simulations used a beam divergence of 15mrad but it has been shown that larger (30m footprint) beam divergences have larger contributions from multiple scattering, therefore in self shadowing canopies a Γ value calculated for 15mrad may not be suitable for different beam divergences. To investigate the method's robustness to beam divergence the contribution from multiple scattering was calculated for different beam divergences, from 2mrad to 35mrad.

Figure 185 shows that there was an increase in the average fractional contribution from multiple scattering and so a separate value of Γ should be calculated for each bream divergence. Interestingly the maximum contribution did not increase with beam divergence.

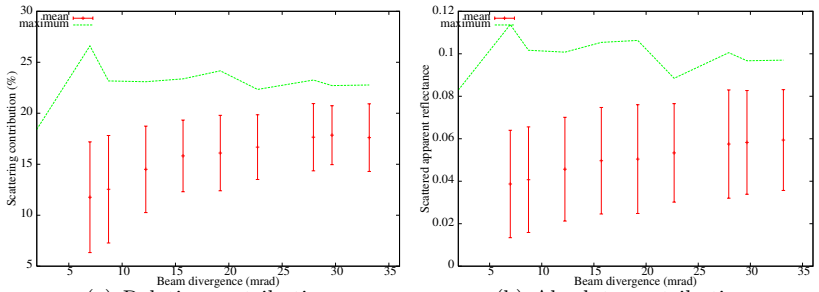

(a) Relative contribution (b) Absolute contribution

Figure 185: Contribution from multiple scattering against beam divergence for a Sitka spruce forest

In an attempt to understand multiple scattering's dependence on beam divergence the experiment was repeated using an array of small, highly reflecting spheres. Each sphere was separated by less than half the smallest beam footprint so that multiple objects would be within each return. The sphere's diameter was a quarter of their separation and they were given the same reflectance as leaves at 920nm. Figure 186 shows that the multiple scattering contribution increases almost linearly with beam divergence. This is as expected, as beam divergence increases more scattering elements are included and so the multiple scattered reflectance will increase whilst the singly

scattered stays constant.

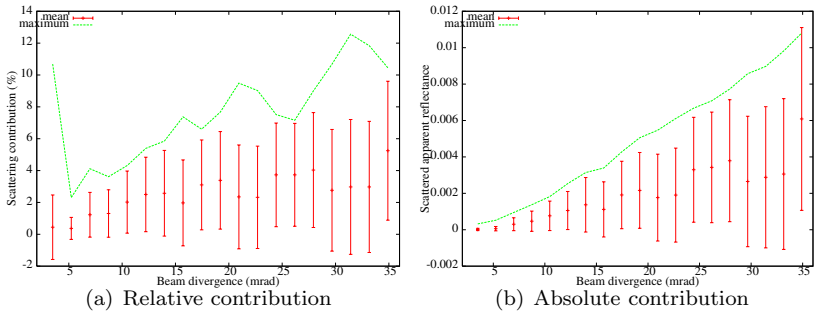

(a) Relative contribution (b) Absolute contribution

Figure 186: Contribution from multiple scattering against beam divergence for an array of small spheres

This suggests that the majority of scattering in Sitka spruce canopies is short range, within needle shoots. Within a canopy scattering elements are clumped into shoots and these clumped into branches and whorls so that increasing the beam divergence may increase the number of shoots but if a shoot is wholly within a lidar beam the multiple scattering will not be increased by including more shoots. In So that increasing the beam divergence

In addition to laser beam divergence, many lidars have broader field of views than fields of illumination. This ensures that the first interaction of all emitted energy is detected, not wasting any energy. In addition on ICESat this gives a certain amount of pointing ability, helping it to observe points of interest (Schutz *et al.* 2005). The viewed area outside the illuminated footprint cannot contain any directly reflected radiation but will contain multiple scattered light, therefore this setup will increase the contribution of multiple scattering. Simulations were run with a Sitka spruce forest with a variety of fields of view and a fixed beam divergence of 14mrad.

In a real instrument the field of view would never be smaller than the field of view, such a set up would waste energy. However simulations of this arrangement show that the contribution from multiple scattering increases in the same manner as with increasing beam divergence. As the field of view increases beyond the beam divergence the amount of singly scattered light will remain constant whilst that from multiple scattering will increase as light scattered outside the laser beam is detected. The chance of a ray of light being scattered and detected will decrease with distance from the illuminated footprint, so as the field of view becomes much larger than the laser footprint the increase in the contribution from multiple scattering should level off.

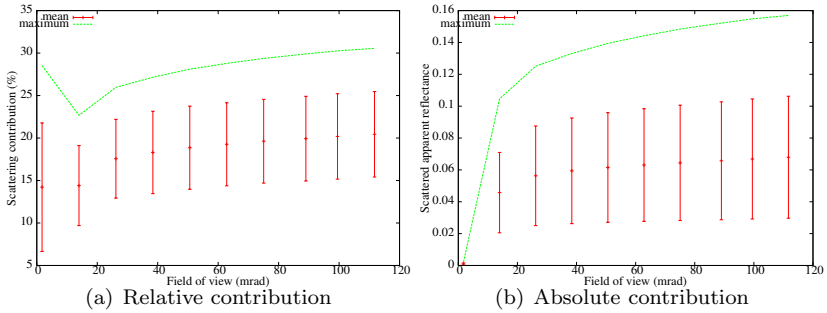

(a) Relative contribution (b) Absolute contribution

Figure 187: Contribution from multiple scattering against field of view for a fixed beam divergence in a Sitka spruce forest

Figure 187 shows that the contribution from multiple scattering did continue to increase as the field of view passed the beam divergence

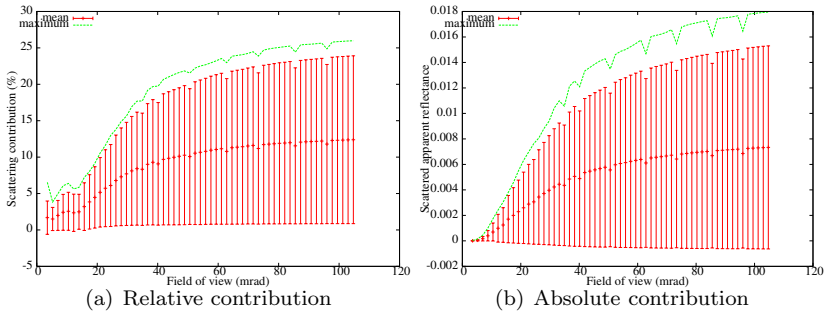

(a) Relative contribution (b) Absolute contribution

Figure 188: Contribution from multiple scattering against field of view for a fixed beam divergence over an array of small spheres

F Acknowledgements

I'd like to thank all those people who helped get this thesis finished. Glen Newnham, Darius Culvenor and David Jupp for teaching me about Echidna and letting me tag along with them on fieldtrips. To Crystal Schaaf, Alan Strahler, Ralph Dubayah and Curtis Woodcock for also letting me join them on fieldwork and seeing just what's involved in measuring forests. To Professor Charles Adams for introducing me to laser remote sensing.

To the post-docs and PhDs in Geomatic Engineering and Geography who let me interrupt them with my naïve questions, particularly Tris Quaife, Jose Gomez-Dans, Joe Bradbury and Dietmar Backes. To Chris Knell and Mike Dunderdale for fixing all the computers that stopped working whilst I was using them, sorry for the extra work I caused.

Very importantly, Martin De Kauwe for showing me that there is life in London and introducing me to most people I knew as well as helping me learn the ins and outs of the Geography Unix system. Tash MacBean for providing light relief with constant questions and not distracting me at all. To Simon and Maddy Jessop for allowing me to lodge with them during the critical final month of the write-up after my landlord's sudden change of mind.

Finally I would like to thank Lewis for teaching me everything I know about ray tracing, radiative transfer and satellites, Mat Disney for acting as a third supervisor throughout without reward and Peter Muller for proposing the project in the first place and welcoming me warmly to London. And of course my parents for making me work hard at school amongst other things.